The Photoluminescence Ensemble

Sarah C. Gillespie

2025

The Photoluminescence Ensemble

Techniques for Advanced Characterization of Metal Halide Perovskites

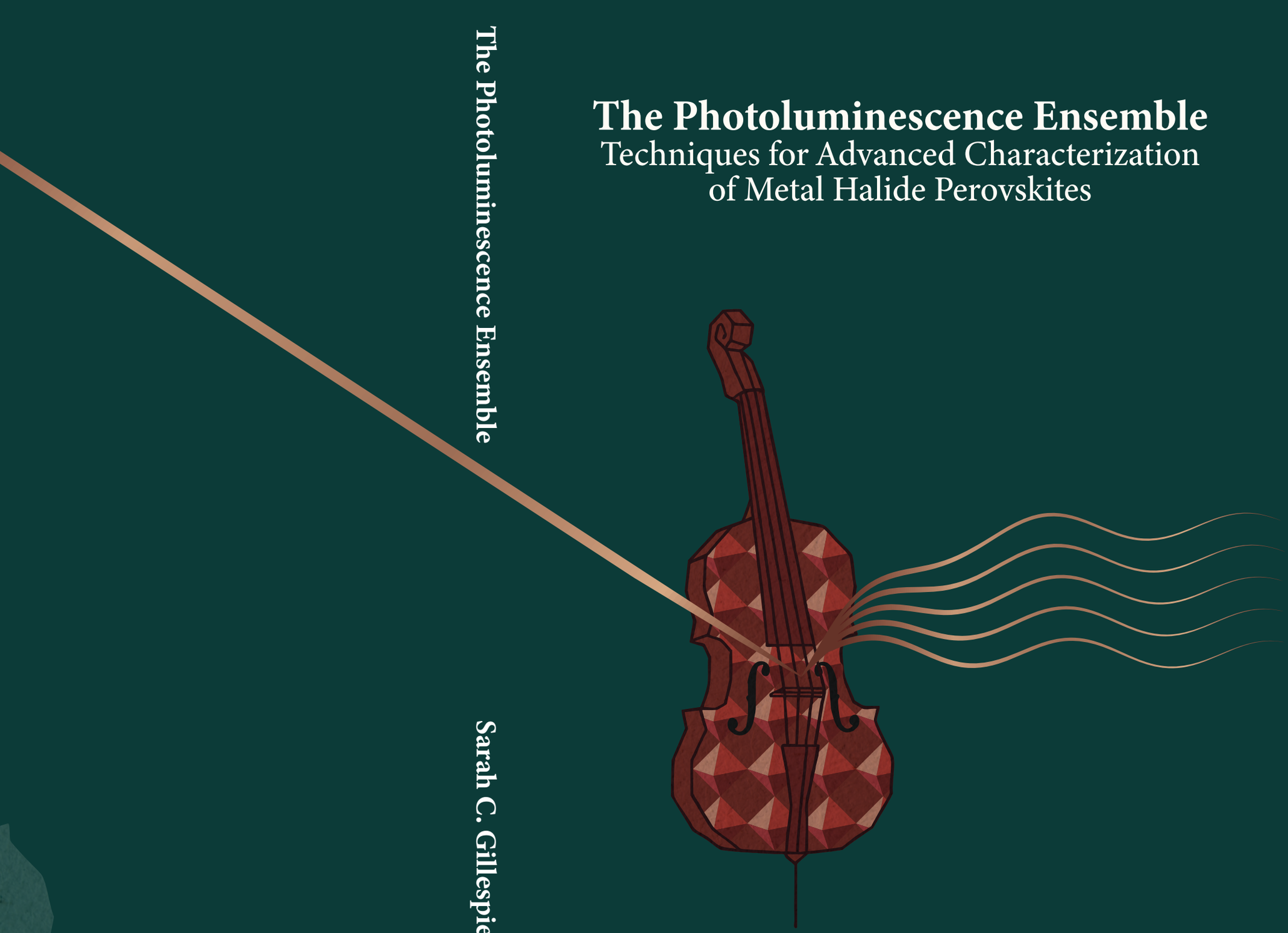

Sarah C. Gillespie

The Photoluminescence Ensemble
Techniques for Advanced Characterization
of Metal Halide Perovskites

The Photoluminescence Ensemble: Techniques for Advanced Characterization of Metal Halide Perovskites
Ph.D. Thesis, University of Amsterdam, December 2025
Sarah C. Gillespie

ISBN: 978-94-6496-494-3

Cover design: *Conceptual representation of a cello inspired by the octahedral geometry of perovskite crystals, emitting photoluminescence when bowed with a laser beam.*
Designed and created by the author.

The work described in this thesis was carried out between September 2021 and August 2025 at NWO-I Institute AMOLF, Science Park 104, 1098 XG Amsterdam, and at the TNO Solar Energy Department, Westerduinweg 3, 1755 LE Petten, The Netherlands. This work is part of the Dutch Research Council (NWO), and is partly funded through governmental funding of TNO financed by the Ministry of Climate Policy and Green Growth and Ministry of Economic Affairs.

A digital version of this thesis is available at:
https://ir.amolf.nl/ and https://www.lmpv.nl/theses/
Printed by: Gildeprint

The Photoluminescence Ensemble: Techniques for Advanced Characterization of Metal Halide Perovskites

ACADEMISCH PROEFSCHRIFT

ter verkrijging van de graad van doctor

aan de Universiteit van Amsterdam

op gezag van de Rector Magnificus

prof. dr. ir. P.P.C.C. Verbeek

ten overstaan van een door het College voor Promoties ingestelde commissie,

in het openbaar te verdedigen in de Agnietenkapel

op donderdag 11 december 2025, te 10.00 uur

door Sarah Catherine Bernadette Gillespie

geboren te Donegal

Promotiecommissie

Promotor:	prof. dr. E.C. Garnett	Universiteit van Amsterdam
Copromotor:	dr. G. Coletti	University of New South Wales
Overige leden:	prof. dr. M. Morales Masis	Universiteit Twente
	prof. dr. E.L. von Hauff	Technische Universität Dresden
	prof. dr. E. Alarcón Lladó	Universiteit van Amsterdam
	dr. J. van de Groep	Universiteit van Amsterdam
	dr. S.A. Mann	Universiteit van Amsterdam

Faculteit der Natuurwetenschappen, Wiskunde en Informatica

Contents

1

Introduction

For millennia, humans have venerated the Sun as a universal timekeeper, a source of heat, a necessity for crop growth, and even as a deity. A compelling example of this reverence is Newgrange, a Neolithic tomb in Ireland built over 5,200 years ago. The aperture above its entrance is precisely aligned with the sunrise on the winter solstice, channeling light into the inner chamber only on that day each year[1]. Beyond its cultural significance, sunlight powers oxygenic photosynthesis, the process by which plants, algae, and cyanobacteria convert solar energy into chemical energy – forming the foundation of nearly all ecosystems on Earth[2]. In the broadest sense, for most of the past 3.5 billion years, sunlight has supplied the planet with all of the energy necessary to sustain life.
It was not until the Industrial Revolution in the mid-19th century that human energy demands surpassed the basic metabolic needs. Additional primary energy sources, particularly coal, became essential to power steam engines and turbines. In 1850, the global primary energy use per capita was approximately 6.5 MWh/year[3]. Since then, the global average demand has surged to more than 22.8 MWh/year; Figure 1.1a summarizes the historical breakdown of energy consumption. This global average notably masks substantial regional disparities and significantly underestimates consumption in developed nations (35.3 MWh/year in the EU and 76.8 MWh/year in the USA; Figure 1.1b)[4]. Among other issues, our reliance on fossil fuels has driven a 51% rise in atmospheric CO_2 relative to pre-industrial levels, and has contributed to a 73% decline in the average wildlife population size since 1970[5–7]. At the current trajectory, sustainable growth is incompatible with the primary energy sources at large today.

It is therefore essential to transition to globally abundant, clean energy sources in order to meet our projected energy demands sustainably. Fortunately, the Sun provides an enormous resource, delivering on average 10^{17} W to the Earth's surface – more than 10,000 times the planet's total power consumption. Solar energy can be converted to electricity using photovoltaics (PV), which can currently deliver electricity for costs as little as €0.04/kWh[8]. Today, silicon modules dominate the global PV market. However, record silicon PV power conversion efficiencies (PCE, $\eta \sim 27.8\%$) are now approaching

the theoretical Auger recombination limit[9, 10]. In combination with silicon, higher-performing, next-generation PV technologies are essential to achieve the global targets of the sustainable energy transition[11].

Metal halide perovskites have emerged as highly promising candidates for this role. These relatively new photovoltaic materials exhibit exceptional optoelectronic properties, including high absorption coefficients and long carrier lifetimes[12, 13]. After only about 15 years of development, record perovskite PV efficiencies are on par with those of silicon (a technology refined since 1954)[9]. Moreover, when combined with silicon in tandem PV architectures, perovskites can push the theoretical PCE to η_{tandem}~45%[14]. However, unlike silicon, perovskites are mixed electronic–ionic semiconductors with unconventional ion migration and defect dynamics that can limit device performance. Understanding these dynamic material properties with appropriate characterization methods is crucial for advancing the potential of perovskites in PV applications and other semiconductor technologies.

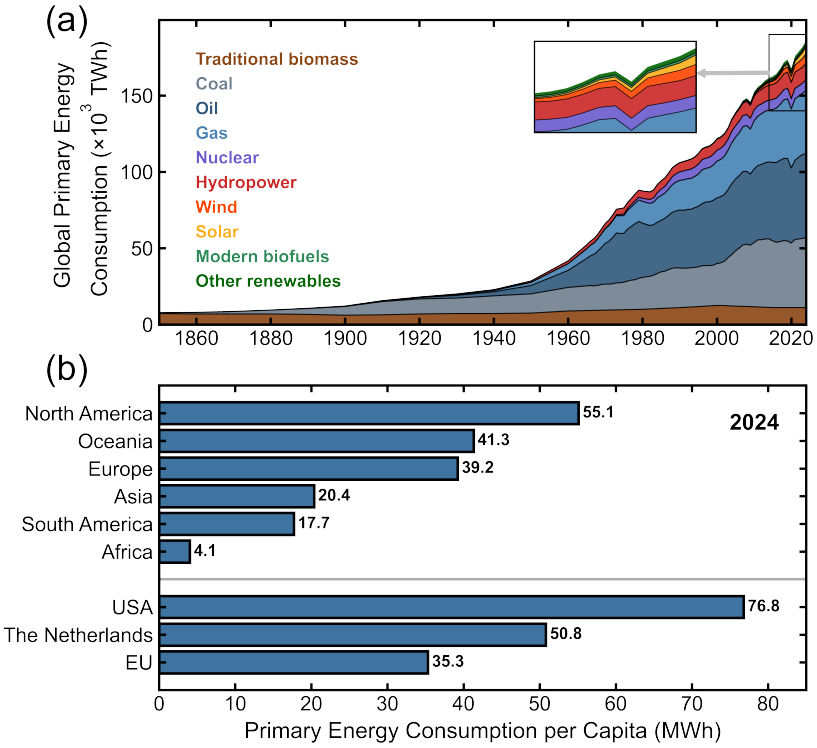

Figure 1.1: (a) Global primary energy consumption by source between 1850 and 2024. Stacked areas are color-coded by energy source. (b) Primary energy consumption per capita in 2024, shown as a continental breakdown (top), and for selected focus regions (bottom; United States, the Netherlands and the European Union). Values are given in MWh to the right of each bar. Panels (a) and (b) were constructed using publicly available datasets from Refs. [3] and [4], respectively.

Among the available characterization techniques, we argue that photoluminescence (PL) spectroscopy stands out as one of the most powerful and versatile tools for understanding the fundamental processes that govern the material's optoelectronic properties. In the following chapters of this thesis, we present a coordinated *ensemble* of PL-based techniques, designed to further advance the understanding of perovskites for PV applications. Specifically, we employ PL methods to quantify relevant electronic properties, resolve loss processes across the solar cell stack, probe ionic dynamics without the requirement of electrical contacts, and optimize device performance and stability through dynamic illumination protocols. To provide the necessary context, the remainder of this chapter presents an overview of the material properties of metal halide perovskites, the principles of photovoltaics, the dynamics of charge carriers, and the impact of mobile ions in perovskite solar cells. These aspects are then linked to PL spectroscopy, followed by a brief outline of the key PL characterization procedures employed in this work.

1.1. Metal Halide Perovskite Solar Cells

Metal halide perovskites are a class of semiconductors with the general chemical formula ABX_3, in which the B^{2+} metal cations and X^- halide anions form corner-sharing octahedra, while the smaller A^+ cations occupy the interstitial cavities between them (Figure 1.2). For PV applications, the A-site is typically occupied by methylammonium (MA^+), formamidinium (FA^+) or cesium (Cs^+); the B-site by lead (Pb^{2+}) or tin (Sn^{2+}); and the X-site by chloride, bromide or iodide (Cl^-, Br^-, I^-)[15–17]. Thin-film perovskite layers can be fabricated using a range of techniques, including solution processing, physical vapor deposition, and thermal evaporation[18–20]. A unique property of these materials is that their band gap (E_g) can be tuned by adjusting the halide ratio in the composition[15, 21, 22]. In this work, we focus primarily on lead-based triple-cation, double-halide compositions such as $Cs_{0.7}(FA_{0.83}MA_{0.17})_{0.93}Pb(I_{0.83}Br_{0.17})_3$, in which $E_g = 1.59$ eV. These mixed-cation, mixed-halide compositions are among the highest performing in terms of PCE and device stability to date[9, 17].

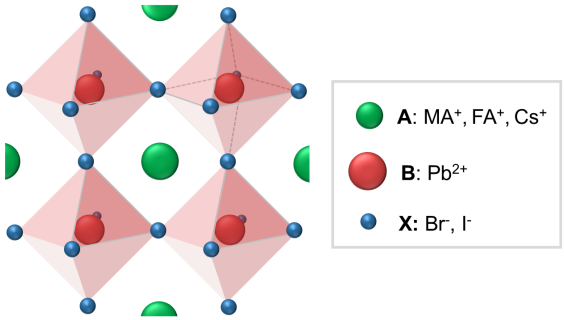

Figure 1.2: Perovskite ABX_3 crystal structure. In the context of this thesis, the A-site cations (green) are MA^+, FA^+ or Cs^+; the B-site cation (red) is Pb^{2+}; and the X-site anions (blue) are Br^- or I^-.

The device architecture of a typical planar perovskite solar cell consists of a perovskite absorber layer positioned between an electron transport layer (ETL) and a hole transport layer (HTL), connected to an external load with either metal or transparent conductive oxide electrodes. When a photon with energy $E \geq E_g$ is absorbed, an electron-hole pair is generated. The built-in electric field, together with the engineered energy-level alignment of the transport layers, directs photogenerated electrons toward the ETL and holes toward the HTL. Ideally, this enables efficient carrier separation and extraction under illumination, which generates a photovoltage. Once separated, the carriers pass through the external circuit – producing a photocurrent – before recombining at the opposite electrode.

To assess the photovoltaic performance of a solar cell, the PCE is measured under standard test conditions (STC), which specify the AM1.5G solar spectrum as the standardized incident irradiance (Figure 1.3a). The PCE is defined as the ratio of extracted electrical power to incident optical power[23]:

$$\eta = \frac{J_{MP} V_{MP}}{P_{AM1.5G}} = \frac{J_{SC} V_{OC} FF}{P_{AM1.5G}} \tag{1.1}$$

where J_{MP} and V_{MP} are the current density and the voltage measured at the maximum power point (MP, the operating point of the device), and J_{SC} and V_{OC} are the short-circuit current density and open-circuit voltage, respectively. These parameters are related through the fill factor (FF) and are indicated on the simulated JV curve in Figure 1.3b. This curve was generated assuming ideal conditions for a perovskite absorber with E_g = 1.59 eV.

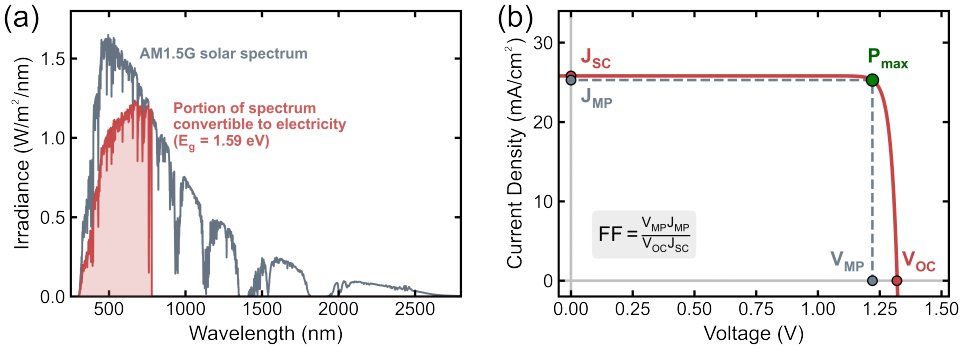

Figure 1.3: (a) AM1.5G solar spectrum (gray). The portion of the solar spectrum with photon energies above the perovskite band gap (E_g = 1.59 eV, shaded in red) represents the usable fraction that can generate electron-hole pairs and, in principle, be converted to electricity. (b) Simulated ideal JV curve at the radiative limit for the same band gap. The device operating point ideally corresponds to the maximum electrical power point, P_{max} (green marker).

The theoretical maximum PCE of a single-junction solar cell is derived from thermodynamic and detailed balance principles[24]. Under the assumptions of perfect absorption, perfect carrier extraction and purely radiative recombination, the maximum PCE for

an absorber with $E_g = 1.59$ eV is $\eta_{\max} = 30.9\%$. In practice, record perovskite device efficiencies fall short of the detailed balance limit due to additional loss processes, such as ion-induced extraction barriers at the perovskite interface, trap-assisted recombination at grain boundaries and surfaces, and resistive losses that reduce the fill factor[25–27]. While FF losses can often be mitigated through optimized device engineering, maximizing record performance fundamentally depends on effective carrier management: increasing photogeneration and carrier extraction enhance the J_{SC}, while suppressing non-radiative recombination pathways maximize the V_{OC}. A detailed understanding of charge-carrier physics is therefore essential for optimizing both the J_{SC} and V_{OC}, and consequently the overall device performance.

1.2. Charge Carrier Dynamics in Halide Perovskites

1.2.1. Carrier Concentrations under Equilibrium Conditions

For an intrinsic semiconductor, the electron (n) and hole (p) densities in the dark are equal: $n = p = n_i$. The intrinsic carrier density n_i for perovskites with compositions similar to those in this thesis is $n_i \simeq 10^5$ cm^{-3}[28, 29]. An excess of holes or electrons can occur either through intentional doping with impurities or, more typically in perovskites, from intrinsic lattice defects[30]. Following convention, we assume that our perovskite materials are p-type[30, 31]. Under equilibrium conditions, the hole density is approximately equal to the acceptor density, $p \approx N_A$, while the electron density is given by:

$$n \approx \frac{n_i^2}{N_A} \ll p \tag{1.2}$$

In this regime, the hole and electron populations are referred to as the majority and minority carrier densities, respectively[32]. If the perovskites were in fact n-type, the physics would be entirely analogous, with electrons as the majority carriers and holes as the minority carriers.

In thermal equilibrium, carrier populations are described by a single Fermi level, E_F, which corresponds to the electrochemical potential of the electrons. For intrinsic semiconductors, E_F lies close to the middle of the band gap, with a small offset due to differences in the effective densities of states between the conduction and valence bands. In p-type materials, E_F shifts toward the valence band, reflecting the higher hole density relative to electrons. While these carrier properties are well-defined under dark conditions, illumination drives the material out of equilibrium, establishing the carrier conditions required for photovoltaic operation.

1.2.2. Photogeneration of Excess Charge Carriers

Photogeneration occurs when electrons transition from the valence band to the conduction band upon photon absorption. The probability of absorption is determined by the material's absorption coefficient, $\alpha(E)$; for lead halide perovskites, α above the band gap is generally in the range of $10^4 - 10^5$ cm^{-1}[33, 34]. The local carrier generation rate, $G(x)$, at depth x in the film follows the Beer-Lambert decay law. For monochromatic illumination with incident photon flux Φ_0 and assuming unity internal quantum efficiency:

$G(x) = \Phi_0 \alpha \exp(-\alpha x)$. Integrating over the perovskite thickness W and relating to the film's absorptance A, the average generation rate per unit volume is:

$$G_{\text{tot}} = \frac{A\Phi_0}{W}. \tag{1.3}$$

Immediately after photoexcitation, excess electrons and holes are created in the conduction and valence bands. These are defined as:

$$\Delta n = n - n_0 \quad \text{and} \quad \Delta p = p - p_0 \tag{1.4}$$

where n_0 and p_0 are the equilibrium (dark) carrier concentrations.
Adhering to the principles of detailed balance, excess carrier densities must remain constant in time under steady-state illumination conditions. This implies that the generation rate of charge carriers must be the same as their rate of recombination: $G = R$, meaning the values of Δn and Δp are determined by the balance between both excess carrier generation and carrier recombination processes.

1.2.3. Charge Carrier Recombination

For photovoltaics, the three dominant mechanisms for carrier recombination are radiative recombination (R_{rad}), trap-assisted recombination (R_{trap}) and Auger recombination (R_{Auger}). The total recombination rate is the sum of these processes:

$$R_{\text{tot}} = R_{\text{rad}} + R_{\text{trap}} + R_{\text{Auger}} \tag{1.5}$$

The most fundamental of the three is radiative recombination, which is the inverse process of photogeneration (Figure 1.4a). Radiative recombination is a form of spontaneous emission, occurring when an electron-hole pair annihilates and emits a photon. Because both carriers are required, the rate scales with their product:

$$R_{\text{rad}} = k_{\text{rad}}(np - n_i^2) \tag{1.6}$$

where k_{rad} is the radiative recombination coefficient. R_{rad} is fundamentally linked to the material's PL, which will be discussed in detail later. For now, it is important to emphasize that radiative recombination is thermodynamically unavoidable in any semiconductor; it sets the lower bound for R_{tot} and defines the detailed balance limit.
In reality, $R_{\text{tot}} > R_{\text{rad}}$ because semiconductors contain defects in their lattice, often due to imperfect fabrication processes. Defects that introduce energy states within the band gap are called traps, which act as non-radiative recombination sites for charge carriers (Figure 1.4b). Shallow traps are located close to the conduction or valence band; they tend to capture only one carrier type and these trapped carriers have a high probability of being thermally re-excited back to the band. Deep traps, on the other hand, are located closer to the midpoint of the band gap, meaning both carrier types can be trapped and the probability of non-radiative recombination is high compared to thermal re-excitation. The trap-assisted recombination rate, R_{trap}, depends on the trap-state density (N_T), the carrier thermal velocity (v_{th}) and the trap capture cross-section (σ). The corresponding trap-assisted carrier lifetime is defined as $\tau_{\text{trap}} = (v_{th}\sigma N_T)^{-1}$, with the trap-assisted

recombination rate expressed in terms of this lifetime by:

$$R_{\text{trap}} = \frac{np - n_i^2}{n\tau_{\text{trap},n} + p\tau_{\text{trap},p}} \tag{1.7}$$

Since N_T is typically much higher at the surfaces of the semiconductor compared to the bulk – due to dangling bonds or interfacial reactions – surface recombination often limits the total trap-assisted carrier lifetime. When determining the major loss processes in a device, it is useful to separate bulk and surface contributions:

$$R_{\text{trap,tot}} = R_{\text{trap,bulk}} + R_{\text{trap,surf(1)}} + R_{\text{trap,surf(2)}} \tag{1.8}$$

This is extensively discussed in **Chapter 2**. Notably, the surface recombination rate further depends on the carrier diffusion coefficient D[35]. Together with the carrier lifetime, this defines the charge carrier diffusion length L_d, which effectively sets the upper limit for the perovskite absorber thickness in a solar cell.
Finally, Auger recombination is a non-radiative process that becomes significant only at high carrier densities. At these densities, the recombination energy from electron-hole pair annihilation is highly likely to be transferred to a third carrier, which is subsequently excited to a higher energy state within its band. The third carrier then relaxes back to the band edge, losing its energy through thermalization (Figure 1.4c). The rate of Auger recombination is:

$$R_{\text{Auger}} = (C_{\text{Aug},n}\, n + C_{\text{Aug},p}\, p)(np - n_i^2) \tag{1.9}$$

where C_{Aug} is the material-specific Auger recombination coefficient. While R_{Auger} can dominate during high-intensity optical characterization measurements, it is not a major loss process in perovskite solar cells operating under standard solar illumination conditions.

From the total recombination rate, we can define the *effective* charge carrier lifetime, τ_{eff}, which is, by definition, dependent on carrier density[36, 37]. In the case where $\Delta n \approx \Delta p$, the relationship between τ_{eff} and R_{tot} is:

$$\tau_{\text{eff}}(\Delta n) = \frac{\Delta n}{R_{\text{tot}}(n,p)} \tag{1.10}$$

From $G = R$, the steady-state excess carrier density can be expressed in terms of the carrier generation rate: $\Delta n = G\tau_{\text{eff}}(\Delta n)$.

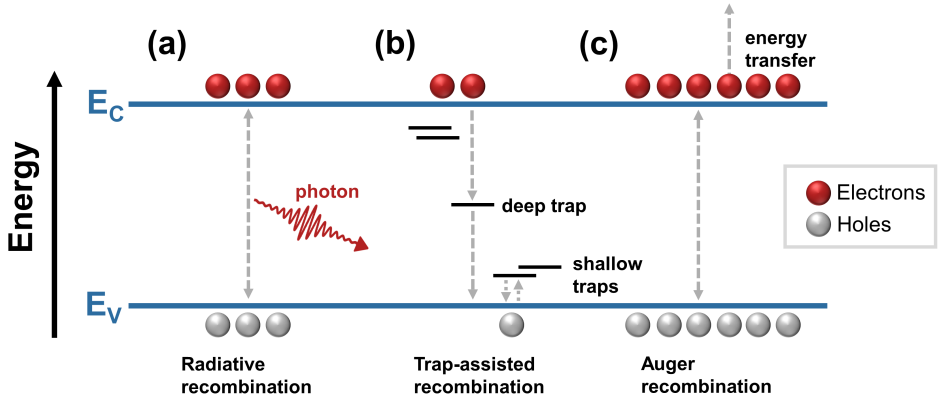

Figure 1.4: Illustration of the three dominant carrier recombination processes in semiconductors: (a) radiative recombination, where an electron-hole pair recombines and emits a photon; (b) trap-assisted recombination through defect states within the band; and (c) Auger recombination, where the recombination energy of an electron-hole pair is transferred to a third carrier.

1.2.4. Electronic Carriers Determine Photovoltaic Performance

Under illumination, $np > n_i^2$, meaning that a single Fermi level cannot describe both carrier populations. Instead, the quasi-Fermi levels $E_{F,n}$ and $E_{F,p}$ are defined for the electron and hole populations. The difference between these levels is the quasi-Fermi level splitting (QFLS), which is given by:

$$\Delta E_F = E_{F,n} - E_{F,p} = k_B T \ln\left(\frac{np}{n_i^2}\right) \tag{1.11}$$

This represents the maximum achievable photovoltage of the device: $\Delta E_F = qV_{OC}$. The QFLS therefore links the measured device performance to the excess carrier concentrations, therefore to the recombination rates and, importantly, to the PL.

The J_{SC} is primarily determined by the carrier generation rate and the efficiency with which carriers are extracted. For perovskites, large absorption coefficients and long carrier diffusion lengths enable nearly perfect photon absorption and carrier extraction in films that are on the order of several hundred nanometers. Defining ξ as the carrier extraction efficiency, J_{SC} can be expressed as:

$$J_{SC} = \xi qGW \tag{1.12}$$

Experimentally, record perovskite solar cells already achieve J_{SC} values that are ~99% of the detailed balance limit, yet the experimental $V_{OC}\times$FF product only reaches about 89% of the theoretical maximum[9, 24, 38, 39]. As a result, one might argue that further efficiency gains rely solely on suppressing non-radiative recombination to increase V_{OC} and on optimizing the FF through resistance engineering. This would indeed be true if the optoelectronic properties remained constant over time. However, in halide perovskites,

device parameters evolve over time due to mobile ionic defects in the lattice. These defects modulate internal electric fields, alter recombination rates, and affect charge extraction efficiencies[25, 40–43]. Ultimately, this means that performance optimization is not only a matter of managing electronic charge carriers, but also of understanding and controlling the complex ionic dynamics in the perovskite material.

1.3. Mobile Ions in Halide Perovskites

1.3.1. Impact of Ionic Processes on Perovskite Photovoltaics

Mobile ion dynamics in halide perovskites arise from the combination of high ionic defect concentrations ($10^{15} - 10^{19}$ cm^{-3}) and low migration barriers for halide anions and A-site cations[44–48]. While reported activation energy values for vacancy-mediated halide migration in $MAPbBr_3$ and $MAPbI_3$ range from $0.1-0.6$ eV, the prevailing consensus in the perovskite community is that halides are the fastest migrating species and that vacancy-mediated migration dominates over interstitial pathways (Figure 1.5a)[45, 49–51]. These low barriers enable ionic redistribution even under moderate illumination or electrical bias[52–54]. On device measurement timescales, the ionic redistribution manifests as *JV* hysteresis and scan-rate-dependent PCEs[50, 55–57]. However, the more contentious issue is how mobile ions contribute to long-term device instability. Under operating conditions, ions can trigger interfacial chemical degradation with charge-transport layers, or can accumulate at the perovskite interfaces to form extraction barriers that reduce the J_{SC} over time[25, 58]. Evidence for ion-induced extraction barriers comes from PCE tracking combined with scan-rate-dependent *JV* sweeps: scans performed faster than the migration rates ("ion-freeze") show that PCEs remain close to their initial values, in contrast to standard operating conditions where ions are free to migrate and form barriers (Figure 1.5b).

Conversely, ionic redistribution can be beneficial for the device V_{OC}, by modifying interfacial energy-level alignment and recombination dynamics[40, 42, 43]. Moreover, device PCEs can fully recover to their initial performance when left in the dark overnight[59]. We exploit this ion-induced dark-recovery phenomenon to stabilize perovskite PV performance in **Chapter 6**. Further complicating matters, ion migration dynamics depend on a myriad of material factors, such as perovskite grain size, composition, and applied interfaces[53, 60–63]. The net impact of mobile ions in a perovskite solar cell ultimately depends on the delicate interplay between their beneficial and detrimental effects under operating conditions. Advanced characterization is therefore essential not only to understand this interplay, but also to determine methods to mitigate the processes that lead to PV instability, and to exploit ionic effects for novel applications beyond photovoltaics[64, 65].

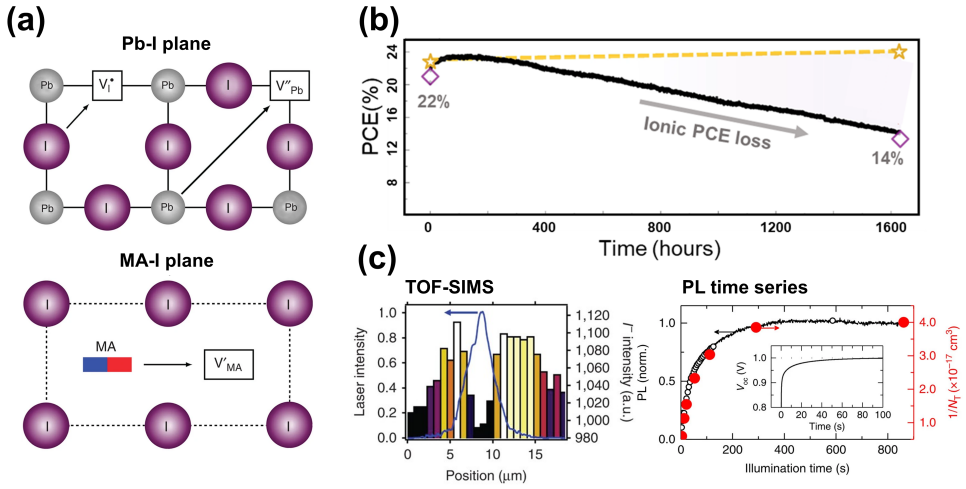

Figure 1.5: (a) Schematic illustration of vacancy-mediated ion migration pathways in $MAPbI_3$, showing I^- and Pb^{2+} migration (top) and MA^+ migration (bottom). Reproduced from Ref. [45]. (b) Set-point tracking of the PCE of a $Cs_{0.05}(FA_{0.6}MA_{0.4})_{0.95}Pb(I_{0.6}Br_{0.4})_3$ perovskite solar cell (black). Yellow stars indicate the PCEs extracted from ion-freeze JV curves, while the dashed yellow line between them is included for clarity, highlighting that the observed PCE losses arise from mobile ions. Reproduced with minor edits from Ref. [25]. (c) TOF-SIMS measurements (left) showing redistribution of I^- defects from the center of the laser illuminated spot (blue curve). This redistribution is corroborated by the local PL enhancement observed during PL time-series measurements (right). Reproduced from Ref. [41].

1.3.2. Characterization of Mobile Ions

Mobile ions can be tracked using techniques such as time-of-flight secondary-ion mass spectrometry (TOF-SIMS, Figure 1.5c, left) and nanoprobe X-ray fluorescence (XRF), often coupled with PL time-series measurements (Figure 1.5c, right)[41, 66, 67]. In particular, PL time-series measurements are widely used to monitor halide segregation in mixed halide systems and to qualitatively track ion migration[41, 68, 69]. However, quantification of key ionic properties, including the mobile ion density (N_{ion}), activation energy for ion migration (E_a) and the ionic diffusion coefficient (D_{ion}) are typically achieved through electrical methods[63, 70–74]. These include techniques in both the time domain – for example, transient photovoltage and photocurrent spectroscopies – and in the frequency domain. Frequency-domain techniques include impedance spectroscopy (IS), intensity-modulated photocurrent spectroscopy (IMPS) and intensity-modulated photovoltage spectroscopy (IMVS)[48, 54, 70, 75–77].

For frequency-domain electrical approaches, a sinusoidal perturbation with a modulation frequency f is applied as the input signal and the material's response is measured as the output. In IS, a voltage perturbation is commonly applied and the response is measured as the current (though the inverse is also possible and is still considered IS). The total voltage and current signals can be expressed as functions of time t, written as the superposition

of the sinusoidal perturbation ($\widetilde{V}, \widetilde{I}$) with their respective offsets ($\bar{V}, \bar{I}$):

$$V = \bar{V} + |\widetilde{V}|\sin(2\pi f t) \quad \text{and} \quad I = \bar{I} + |\widetilde{I}|\sin(2\pi f t + \theta) \tag{1.13}$$

where θ is the relative phase shift between these signals. The impedance transfer function is defined as:

$$Z = Z' + iZ'' = \frac{|\widetilde{V}|}{|\widetilde{I}|}\exp(i\theta) \tag{1.14}$$

where Z' and Z'' are the resistive and reactive components, respectively[78]. Equivalent-circuit (EC) models are often used to fit the frequency-domain electrical data and to extract relevant device frequency-dependent device parameters. An ideal process with a relaxation time τ can be modeled with a simple parallel resistor-capacitor (RC) circuit, for which $\tau = RC$[75]. In practice, overlapping and non-ideal processes require relatively more complex EC models to fit the data[74, 75]. As a result, different EC models can often produce similarly good fits for the same dataset. To reduce model ambiguity and improve parameter reliability, it is common to combine multiple electrical techniques and, when necessary, support them with drift–diffusion simulations[48, 70, 77].
From such optimized EC modeling, ionic properties can be quantified. For example, in single-crystal $MAPbBr_3$ perovskite devices, diffusion coefficients have been extracted from IS by including Warburg-like constant-phase elements in the EC model to account for accumulation at the perovskite interface[79]. Temperature-dependent capacitance–frequency measurements, a variant of IS, combined with drift-diffusion simulations have also been applied to extract N_{ion}, E_a and D_{ion}. For instance, in $MAPbI_3$ devices with Au and ITO contacts, capacitance-frequency measurements yielded $N_{\text{ion}} \approx 2 \times 10^{18}$ cm^{-3}, $D_{\text{ion}} \approx 4 \times 10^{-11}$ cm^2/s, and $E_a \approx 0.38$ eV, which has been attributed to iodide vacancy diffusion[48]. A benefit of IS and frequency-domain techniques in general is their high sensitivity to material changes, particularly compared to JV sweeps. Recent simulations suggest that short-term changes in IS signatures resulting from ionic processes may even provide a unique means to predict long-term perovskite device stability[80, 81].

Despite their potential, all electrical methods come with inherent limitations. Notably, they require electrical contacts, which restrict measurements to fully operational devices. Moreover, high interfacial recombination at the electrical contacts often dominates the IS signal, and the ionic response – including their reactions at the interfaces – can be challenging to disentangle from other processes[72, 82, 83]. To overcome these challenges, in **Chapters 3 - 5**, we introduce intensity-modulated photoluminescence spectroscopy (IMPLS) as a fully optical analogue to IS, which we apply to probe fundamental ionic processes in our perovskite thin films.

1.4. The Photoluminescence Spectroscopy Ensemble

1.4.1. The Photoluminescence Spectrum

The overarching theme of this thesis is the versatility of PL spectroscopy as a tool for characterizing halide perovskites. PL-based approaches are applied to probe electronic properties (**Chapter 2**) and mobile ion dynamics (**Chapters 3 - 5**), and to extract design principles for optimizing device performance (**Chapter 6**). This section introduces the fundamental principles of PL spectroscopy and the specific characterization techniques employed in this work.

Luminescence is a broad term for light emission from a material that deviates from black-body emission, while photoluminescence specifically refers to emission due to optical absorption[84]. The PL spectrum is therefore related to both the material's absorption and emission properties. Defining $a(E) = (1-r)[1-\exp(-\alpha W)]$, where r is the surface reflectivity, the PL spectrum can be modeled using the generalized Planck's law[85]:

$$\Phi_{\mathrm{PL}}(E) = \frac{2\pi E^2}{h^3 c^2} \frac{a(E)}{\exp[(E-\Delta E_F)/k_B T]-1} \tag{1.15}$$

We exemplify this PL model in Figure 1.6a, using $E_g = 1.59$ eV. Equation 1.15 shows that the material's PL is directly related to the QFLS; thus the PL is a proxy of the material quality in terms of its carrier recombination processes. Moreover, the QFLS can be directly determined from PL spectrum fitting[86]. However, fitting to the full spectrum requires prior knowledge of additional parameters such as α, W and r[87, 88]. An alternative approach to determining the QFLS is to integrate the PL spectrum over all photon energies and infer the QFLS directly from the material's photoluminescence quantum yield (PLQY)[89].

1.4.2. Photoluminescence Quantum Yield

The PLQY of a material is defined as the ratio of the radiative recombination rate to the total recombination rate or, equivalently, it is the ratio of the emitted photon flux to the absorbed photon flux:

$$\mathrm{PLQY} = \frac{\Phi_{\mathrm{PL}}}{\Phi_{\mathrm{abs}}} = \frac{R_{\mathrm{rad}}}{R_{\mathrm{tot}}} \tag{1.16}$$

Applying detailed balance principles under illumination and in thermal equilibrium, this expression can be rearranged with Equation 1.11 to yield:

$$\Delta E_F = \Delta E_{F,\mathrm{rad}} + k_B T \ln(\mathrm{PLQY}) \tag{1.17}$$

This emphasizes that the PLQY is a direct measurement of non-radiative recombination losses in the material, thereby a measure of maximum possible V_{OC} that the perovskite material can achieve assuming all other components of the PV device are perfect[89]. As a rule of thumb, an order-of-magnitude reduction in the PLQY at $T = 300$ K corresponds to a QFLS loss of approximately 60 meV. Because both the absolute photon flux and the sample's absorptance must be measured to determine the PLQY, these measurements are typically performed with the sample placed inside a highly reflective integrating sphere, with the excitation and PL signals collected by calibrated photon detectors[90].

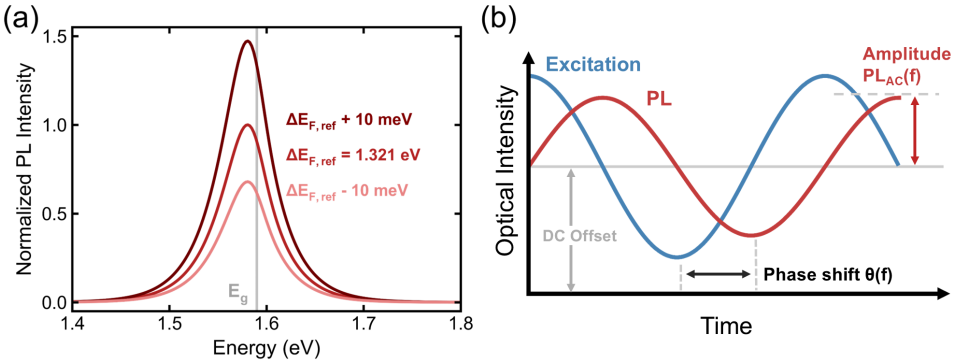

Figure 1.6: (a) Modeled PL spectra from Equation 1.15 for a semiconductor film of thickness $W = 500$ nm, assuming perfect antireflection ($r = 0$) and an absorption coefficient $\alpha(E) \propto \exp[(E - E_g)/E_U]$. An Urbach energy of $E_U = 13.5$ meV is applied, consistent with measured values for triple-cation, mixed-halide perovskite films[91]. The reference QFLS is $\Delta E_{F,\mathrm{ref}} = 1.321$ eV and the band gap $E_g = 1.59$ eV. (b) Schematic of intensity-modulated photoluminescence spectroscopy (IMPLS) at a fixed modulation frequency f. The PL intensity (red) is tracked in time under sinusoidally modulated optical excitation (blue). For each frequency, the relative phase shift $\theta(f)$ and the PL amplitude $\mathrm{PL}_{\mathrm{AC}}(f)$ are extracted.

1.4.3. Time-Resolved Photoluminescence Spectroscopy

While PLQY is an excellent measure of material quality, it does not directly quantify individual charge-carrier recombination processes such as the recombination coefficients or effective carrier lifetimes. These parameters can instead be determined using time-resolved photoluminescence (TRPL) spectroscopy. Once illumination is removed ($G = 0$) and assuming $n \approx p$, the rate of change of the excess carrier density is:

$$\frac{\mathrm{d}\Delta n(t)}{\mathrm{d}t} = -R_{\mathrm{tot}}(t) = -k_{\mathrm{rad}} n(t)^2 - n(t)/\tau_{\mathrm{trap}} - C_{\mathrm{Aug}} n(t)^3 \tag{1.18}$$

This can be combined with the effective lifetime definition (Equation 1.10) to yield:

$$\tau_{\mathrm{eff}}(\Delta n) = -\left(\frac{\mathrm{d}\ln \Delta n(t)}{\mathrm{d}t}\right)^{-1} = -\left(\frac{1}{m}\frac{\mathrm{d}\ln \Phi_{\mathrm{PL}}}{\mathrm{d}t}\right)^{-1} \tag{1.19}$$

where $m = 1$ under low injection levels (since $\Phi_{\mathrm{PL}} \propto n$) and $m = 2$ under high injection levels ($\Phi_{\mathrm{PL}} \propto n^2$)[37]. Tracking the PL decay after a pulsed excitation allows one to probe the recombination dynamics as a function of excess carrier density. From Equation 1.19, a constant $\tau_{\mathrm{eff}}(\Delta n)$ as a function of time (equivalently, as a function of excess carrier density) corresponds to the trap-assisted lifetime, τ_{trap}. Further fitting to the TRPL decay trace allows for the determination of the radiative and Auger recombination coefficients (**Chapter 2**). Experimentally, TRPL is commonly measured using a time-correlated single-photon counting (TCSPC) system, in which the PL decay is recorded following excitation by a pulsed laser source. To maximize the signal-to-noise ratio, the decay trace is typically averaged over millions of excitation pulses.

1.4.4. Intensity-Modulated Photoluminescence Spectroscopy

While PLQY and TRPL provide valuable insights into electronic processes, we resolve ionic dynamics in this thesis using a novel PL-based technique called intensity-modulated photoluminescence spectroscopy (IMPLS). High-frequency IMPLS has previously been used to study charge-carrier lifetimes in silicon and other semiconductors[92–94]. However, to the best of our knowledge, low-frequency IMPLS has not yet been applied to probe ionic-timescale processes, as we do in the coming chapters of this work.
The principle of IMPLS is analogous to impedance spectroscopy, where the sinusoidally modulating PL signal is tracked with respect to the modulating optical excitation (Figure 1.6b). The IMPLS transfer function P is defined as:

$$P = P' + iP'' = \frac{|\widetilde{\phi}_{\mathrm{PL}}|}{|\widetilde{\phi}_{\mathrm{exc}}|}\exp(i\theta) \tag{1.20}$$

Here, $|\widetilde{\phi}_{PL}|$ is the amplitude of the modulated PL intensity signal and $|\widetilde{\phi}_{\mathrm{exc}}|$ is the amplitude of the modulated excitation intensity. The frequency-dependent amplitude change and phase shift can be analyzed using equivalent circuit proxies, which we refer to as optical equivalent circuits (OECs), to extract key information such as the characteristic lifetimes of the probed ionic processes. Key advantages of IMPLS include its simple, contact-free implementation and versatility. For instance, it allows for full-field illumination (**Chapter 3**) as well as localized point probing and sample mapping (**Chapter 4**). Furthermore, IMPLS can be extended to *spectrally* resolve the PL response in the frequency domain, and can separate distinct features across different sample compositions (**Chapter 5**).

1.5. Thesis Outline

The aim of this thesis is to extract the maximum information from an ensemble of PL-based characterization methods, with a particular focus on advancing the potential of perovskite photovoltaics. To frame this work, each chapter title alludes to a musical term that mirrors the central experimental concept. The thesis is structured as follows:

• **Chapter 2 – Light Refrains**: Building on established methods in the silicon community, we apply TRPL to disentangle bulk and surface trap-assisted recombination by systematically varying the perovskite film thickness. Surface recombination velocities (SRVs) are quantified for 17 interfacial contacts relevant to photovoltaic devices, together with those of air and SiO_2. The recombination properties determined from TRPL are converted to the implied V_{OC}, and benchmarked against full device JV parameters. This chapter highlights the importance of identifying the dominant loss channels to ensure that optimization strategies are not misdirected towards regions of the device that are already near-optimal. *"Light Refrains"* is inspired from the repeated pulses and PL decays in TRPL analysis, analogous to recurring lines in many musical works.
• **Chapter 3 – Key Signatures**: We introduce IMPLS for probing ionic dynamics and demonstrate, as a proof of concept, its application to perovskite thin films and solar cells. Optical equivalent circuit models are introduced and fit to the IMPLS data. From the OEC fits, we resolve two distinct processes ($\tau_{\mathrm{char}} \approx 2$ ms and 77 s) which we attribute to ionic

defect formation and diffusion. The IMPLS response of both the perovskite thin film and the corresponding full device are compared with the responses obtained from the similar electrical techniques of IMVS and IMPS.
The title *"Key Signatures"* stems from the principle of IMPLS. By sweeping the modulation frequency, IMPLS identifies the "key" of the ionic processes – much like an orchestra tuning to the oboe's concert A (440 Hz) before a performance.
• **Chapter 4 – Dynamic Contrasts**: We adapt the IMPLS experimental configuration for single-spot probing across a high dynamic range of applied optical excitation. By correlating the IMPLS phase shift with PLQY, we propose a model linking both characterization techniques to ion diffusion processes. This analysis suggests that IMPLS can be applied to estimate lateral diffusion coefficients of mobile ions entirely optically. We then spatially map the IMPLS phase shift and PL intensity for two beam spot sizes. According to our model, the difference between the phase and intensity signals delineates regions dominated by mobile versus fixed (or very slowly mobile) traps. We quantify and spatially resolve this separation using a parameter we term the "defect contrast coefficient".
"Dynamic Contrasts" reflects the musical texture of crescendos and diminuendos, where variations in volume add depth, just as our maps reveal contrasts between mobile and fixed ionic defects.
• **Chapter 5 – Theme & Variation**: With PL spectra collected as a function of modulation frequency, we expand IMPLS and demonstrate the concept of spectral Bode and Nyquist plots. These spectral features indicate that the dominant IMPLS response is due to the halide composition. To verify this, we perform a compositional analysis, comparing four sample types: $MAPbI_3$, $MAPb(I_{0.8}Br_{0.2})_3$, $MAPb(I_{0.5}Br_{0.5})_3$ and $MAPbBr_3$. From this comparison, we verify that iodide is the dominant mobile species responsible for the observed IMPLS responses across the relevant frequency measurement window.
"Theme & Variation" alludes to two aspects in this chapter: it captures both the variation of IMPLS into a new spectral dimension, and the compositional variation of our perovskite films.
• **Chapter 6 – Interludes**: Finally, we systematically study PL time-series dynamics across various perovskite compositions, excitation intensities, and dark times between illumination cycles. Importantly, allowing brief dark intervals significantly enhances PL intensity, which we correlate with higher PCEs in complete devices. Ultimately, this chapter suggests that leveraging ionic processes through unconventional illumination protocols may offer a viable pathway to enhancing perovskite PV performance.
The title *"Interludes"* naturally refers to the intervals of light and darkness applied to films and devices, in analogy with the pauses and transitions that shape a musical performance.

The main title of this thesis, *"The Photoluminescence Ensemble"*, emphasizes the central message of this work: while each PL technique – like a soloist – offers valuable insights on its own, it is their combined application – the ensemble – that yields a much deeper understanding of halide perovskite physics.

2

Light Refrains
Quantifying Carrier Recombination Processes in Perovskite Photovoltaics

Perovskite solar cells have reached an impressive certified efficiency of more than 27%, yet carrier recombination at interfaces remains a major source of performance loss. In this chapter, we demonstrate how time-resolved photoluminescence spectroscopy (TRPL) can locate and quantify these recombination losses, analogous to well-established approaches in silicon photovoltaics. This TRPL analysis enables separation of bulk and surface lifetimes, extraction of surface recombination velocity (SRV), determination of the recombination parameter (J_0), and calculation of the implied open-circuit voltage (iV_{OC}) for any perovskite device configuration. We apply this framework to compare 18 carrier-selective and passivating contacts for perovskite photovoltaics. Furthermore, the calculated iV_{OC} values are directly compared to those calculated from photoluminescence quantum yields and to the corresponding solar cell V_{OC}. This simple technique serves as a practical guide for screening and selecting multifunctional, passivating perovskite contact layers. As with silicon solar cells, most of the material and interface analysis can be done without fabricating full devices or measuring efficiency. These purely optical measurements are even preferable when studying bulk and interfacial passivation approaches, since they remove complicating effects from poor carrier extraction.

This chapter is based on:

Sarah C. Gillespie, Jérôme Gautier, Julia S. van der Burgt, John Anker, L.J. (Bart) Geerligs, Gianluca Coletti, and Erik C. Garnett. Silicon-Inspired Analysis of Interfacial Recombination in Perovskite Photovoltaics. *Advanced Energy Materials* **14**, 2400965 (2024).

Author contributions:

SCG fabricated the perovskite samples and devices, performed TRPL, XRD, PL, absorbance, SEM and photoconductance decay measurements, characterized the solar cells, carried out the data analysis, and wrote the manuscript. JG measured the carrier diffusion length using SSPG and provided feedback on the manuscript. JSB and SCG measured the PLQY. JA fabricated the silicon samples. LJG, GC and ECG provided experimental and analytical guidance, contributed to interpretation of the results, and reviewed the manuscript.

2.1. Introduction

The remarkable progress of perovskite solar cells in recent years has brought certified device efficiencies to 27.3% – now within one percent of the silicon record[9]. Comparing record device parameters to the detailed balance (DB) limit, successful mitigation of the remaining losses should primarily proceed via further carrier management improvements (experimental records are ~91% $V_{OC,DB}$ and ~93% FF_{DB}), rather than from light management optimization (~99% $J_{SC,DB}$)[24, 38, 95]. However it is not trivial to identify the significant carrier recombination pathways across the stack's layers based on device V_{OC} and FF alone; supplemental characterization is generally required to locate and ultimately eliminate the major recombination losses to further improve device performance.
Particularly in the perovskite community, films and half-fabricated cells are widely assessed using purely optical techniques. For example, the photoluminescence quantum yield (PLQY) and the minority carrier lifetime (τ) are frequently measured and included in perovskite photovoltaic reports[96–100]. These non-electrical assessment tools make it easier to compare film or half-stack quality without needing to fabricate full devices – but these measurements alone will not answer the key question: are the carrier recombination losses coming from the bulk of the perovskite layer, from one or both of the perovskite-contact interfaces, or from somewhere else in the device? If this question is not addressed, the community may be misdirected to make erroneous assumptions and focus on optimizing regions within the stack that are already nearly perfect.
Conversely, the silicon PV community has been utilizing well-established techniques for isolating recombination processes for the past 30 years[101–104]. Specifically, the photoconductance decay method enables the fast and simple determination of the minority carrier lifetime – similar to what is typically extracted from time-resolved photoluminescence (TRPL) decays for perovskite films. With the lifetime easy to quantify, further methods such as thickness-variation measurements have enabled the separation of bulk and surface recombination contributions in silicon and germanium wafers[105–107]. Moreover, it is typical for the silicon community to quote the recombination current density, J_0, or the implied open-circuit voltage, iV_{OC}, of the wafer rather than its minority carrier lifetime[108–110]. Reporting these parameters can be exceedingly more practical than reporting lifetime alone as they can easily be compared to the properties of the equivalent device's current-voltage curve.

In this chapter, we propose a framework to experimentally locate and separate trap-assisted recombination processes as they occur across any perovskite stack, with inspiration drawn from the longstanding silicon techniques. This framework emphasizes how one can extend from the archetypal TRPL spectroscopy measurements to separate bulk and surface recombination losses at either interface. We describe how the surface recombination velocity (SRV) can be extracted at either contact by measuring τ_{eff} as a function of perovskite thickness, W_{pvk}, provided the carrier diffusion length is known[35, 105]. Using this framework, this work provides the experimentally-determined SRVs of 18 different passivating and carrier selective contacts with $Cs_{0.06}(MA_{0.2}FA_{0.8})_{0.94}Pb(Br_{0.2}I_{0.8})_3$[17]. We further compare SRVs when the perovskite stack is inverted.
We continue by explaining the utility of using the recombination parameter J_0 and the separated bulk and surface J_0 components either in addition to, or instead of, quoting

the SRV or PLQY in reports. In line with the argument that determining the J_0 can aid in the understanding of solar cell performance, we finish by detailing how the implied V_{OC} extracted from the proposed framework compares to the implied V_{OC} extracted from PLQY, and to the true V_{OC} measured for full devices, highlighting the losses predicted from the framework analysis and losses from other sources not included in the analysis. Experimentally, we determine that the limiting region due to trap-assisted recombination in our solar cells is at the perovskite-C_{60} interface, which accounts for ≈90% of the total non-radiative open-circuit voltage losses. We further show that for perfectly passivated cells, the maximum iV_{OC} that can be achieved is ≈1.29 V, signifying that the perovskite bulk quality is already exceptionally high in this case.
Finally, we show that reporting full device efficiencies is not strictly necessary for analyzing current and next-generation perovskite contact layer passivation properties. Indeed, we argue that focusing on high efficiencies alone can be detrimental to perovskite solar cell progress as, even with a high quality perovskite active layer and state-of-the-art contacts, device efficiencies can remain limited due to hidden additional losses. Without a separate analytical procedure in place to identify and quantify each loss process, device optimization can be limited. This argument has already been established in the silicon community – here we simply extend the rationale to perovskite photovoltaics.

2.2. The Minority Carrier Lifetime

Deviation from the detailed balance limit for any trap-containing photovoltaic material is, by definition, partially attributed to trap-assisted recombination which can occur within the bulk of the material or at its surface (depending on the location and nature of the trap)[24, 111]. For perovskite solar cells in particular, trap-assisted recombination is still a major energy loss pathway which limits device efficiencies[112, 113]. Consequently, the material quality of any photovoltaic layer can be quantified by determining the trap-assisted recombination rate, which is proportional to the trap density in the material. By means of convention, it is not the trap-assisted recombination rate, R_{trap}, that is quoted and compared in literature, but the effective trap-assisted lifetime – a proxy of the inverse recombination rate – given as:

$$\tau_{trap,eff} = \frac{\Delta n}{R_{trap}} \tag{2.1}$$

for p-type semiconductors ($\tau_{trap,eff} = \Delta p / R_{trap}$ for n-type semiconductors). The effective trap-assisted lifetime, shortened to τ_{eff}, is related to the trap-assisted bulk and surface lifetimes by:

$$\frac{1}{\tau_{eff}} = \frac{1}{\tau_{bulk}} + \frac{1}{\tau_{surf}} \tag{2.2}$$

Separation of these lifetimes and further analysis are described in Sections 2.3 and 2.4. Before that, it is first necessary to discuss the standard methods applied to determine the effective lifetime. While experimental methods can vary between photovoltaic materials, such as between silicon and perovskite samples, the underlying theory and the lifetime meaning are the same.

2.2.1. Measuring the Minority Carrier Lifetime in Silicon Wafers

In silicon photovoltaics, the effective minority carrier lifetime of a wafer is generally determined using the photoconductance decay technique. This technique, for many researchers and industrial testers, is carried out using the Sinton WCT-120 assessment tool[101, 102]. To illustrate this technique, we fabricated and measured the lifetime of an n-type Czochralski silicon wafer with symmetric nitric acid oxidized silicon (NAOS) tunneling layers and with 20 nm of n-type polysilicon deposited symmetrically on top of the oxide. Fabrication details are listed in the Supporting Information, Section 2.6.1, at the end of this chapter.

In the measurement, the symmetric n-poly/SiO_2/silicon wafer was placed on top of the induction coil and a flash from a standing lamp briefly illuminated the wafer, as schematically shown in Figure 2.1a. The raw photovoltage decay was measured as a function of time (Figure 2.1b) and was converted to the photoconductance decay ($\Delta\sigma_G$) based on a predefined calibration curve[103]. The excess carrier concentration as a function of time was then obtained based on the relation: $\Delta\sigma_G = qW\Delta p(\mu_n + \mu_p)$, where mobilities are known for silicon (typically, electron mobilities are $\mu_n \approx 1100$ $cm^2V^{-1}s^{-1}$ and hole mobilities are $\mu_p \approx 400$ $cm^2V^{-1}s^{-1}$), and the thickness is a measured input – in this case $W_{Si} = 180$ µm[102].

The effective carrier lifetime is generally obtained using the standard continuity equation with the assumption that the carrier concentration is spatially uniform across the sample. Under this assumption, the continuity equation is reduced to:

$$\frac{d\Delta p(t)}{dt} = G(t) - R(t) \tag{2.3}$$

Where *G(t)* and *R(t)* are the total time-dependent carrier generation and recombination rates, respectively. There are three analysis modes which can be selected based on the expected lifetime[104]. For high quality and well-passivated wafers, the transient mode is most commonly applied; when the carrier lifetime of the symmetric silicon sample is longer than the flash time. Under this condition, $G(t) \approx 0$ can be assumed and the continuity equation simply becomes:

$$\tau_{CD}(\Delta p) = -\frac{\Delta p}{d\Delta p(t)/dt} \tag{2.4}$$

Wherein the variable or carrier-dependent lifetime is defined as:

$$\frac{1}{\tau_{CD}} = \frac{1}{\tau_{eff}} + \frac{1}{\tau_{rad}} + \frac{1}{\tau_{Auger}} \tag{2.5}$$

We plot the carrier-dependent lifetime both as a function of carrier concentration and of time for our illustrative silicon sample in Figure 2.1c. Conventionally, the reported lifetime is given at the minority carrier density (MCD) corresponding to one-tenth of the wafer doping density (N_D), typically at 10^{15} cm^{-3}[114]. In our case, τ_{CD}@MCD = 7.2 ms, as indicated by the blue marker in Figure 2.1c. This marker is located approximately at the plateau of the carrier-dependent lifetime curve, which is an indication that trap-assisted recombination is the dominant recombination process, signifying that at this point, $\tau_{CD} \approx$

τ_{eff}; this is the underlying justification of reporting lifetimes at $0.1 \times N_D$. At higher carrier concentrations, τ_{CD} is much shorter, which is of course the consequence of radiative and Auger recombination processes becoming increasingly dominant[115].

2.2.2. Measuring the Minority Carrier Lifetime in Perovskite Films

Comparatively in perovskite photovoltaics, the carrier lifetime is typically determined by using time-correlated single-photon counting (TCSPC) to obtain the PL decay trace[116]. We similarly provide an illustrative case by measuring the PL decay of a perovskite film on glass with the composition $Cs_{0.06}(MA_{0.2}FA_{0.8})_{0.94}Pb(Br_{0.2}I_{0.8})_3$. In the standard TCSPC experimental procedure, which is schematically shown in Figure 2.1d, a pulsed laser excites the film and an emitted photon from the sample is detected some time later typically with a single photon counter. The time of travel of the photon to the detector is subtracted such that only the time difference between excitation and emission is recorded. This process is repeated several million times to build up a histogram of the decay curve, similar to what is shown in Figure 2.1e. Notably, the repetition rates, RR, for all TRPL measurements in this work were selected by ensuring that $\tau_{eff} \ll RR^{-1}$. This ensures that in every case the full decay was captured[13, 31, 117].

In many works, researchers generally obtain the minority carrier lifetime by fitting a n^{th} order (usually n=2) exponential to the TRPL decay: $PL(t) = \sum_{i=1}^{n} A_i \exp(-t/\tau_i)$. Generally, the long time constant obtained from the fit is quoted as the effective minority carrier lifetime, since the solution to the continuity equation at the trap-assisted limit is a monoexponential decay[118–120]. However, there are some nuances in fitting such an arbitrary function to the decay, namely that while the solution of the continuity equation for the trap-assisted component is a monoexponential, other processes — radiative, Auger, extraction, re-injection and so forth — generally are not, making the biexponential fitting procedure quite groundless. This has already been eloquently described in other works[37, 121]. In the same works, it has instead been proposed that the "differential lifetime":

$$\tau_{diff}(\Delta n) = -\left(\frac{d\ln \Delta n(t)}{dt}\right)^{-1} = -\left(\frac{1}{2}\frac{d\ln PL(t)}{dt}\right)^{-1} \tag{2.6}$$

should be used to analyze TRPL decays to find the more accurate effective trap-assisted lifetime (see **Chapter 1**, Equation 1.19). Δn is applied here as it is assumed that our perovskite layer is p-doped. The factor of 2 in Equation 2.6 arises from measuring under high injection levels, $PL \propto n^2$. By the differential lifetime definition, the point of saturation of the differential lifetime is the effective lifetime, provided no other injection or extraction processes are occurring and that first order radiative recombination is negligible. It is noted that while there has already been some adoption of applying the differential lifetime technique for TRPL analysis, it has not yet been heavily popularized[13, 28, 122, 123].

In this study, we apply the differential lifetime analysis technique to extract the effective lifetime of the perovskite sample. The differential lifetime – for sake of comparison, redefined as the carrier-dependent lifetime – of the illustrative perovskite sample is plotted as function of carrier concentration and as a function of time in Figure 2.1f. The carrier concentration of the perovskite, shown along the primary x-axis in Figure 2.1f,

was not directly measured but approximated using the laser fluence, laser spot size and absorption, as described in Section 2.6.2. From the plateau of the curve, the effective lifetime of the perovskite sample was determined to be τ_{eff} = 196 ns. Similar to the silicon lifetime analysis, the drop off in the carrier-dependent lifetime is a consequence of radiative and Auger recombination dominating at high carrier concentrations. We exemplify this by also plotting the radiative and Auger lifetimes as a function of minority carrier concentration in Figure 2.1f, which we determined in this work by simply fitting the curve to Equation 2.5. Notably, the extracted values strongly agree with the reported values of a similar perovskite composition[28]. The figure highlights that radiative recombination accounts for the carrier-dependent lifetime transition at 2×10^{17} cm^{-3} $<\Delta n<10^{18}$ cm^{-3}, while Auger dominates at $\Delta n>10^{18}$ cm^{-3}.
It is noted that, upon illumination, the effective Auger and radiative lifetimes tend to vary over time due to local material changes such as halide segregation occurring within films; we further discuss such variations and the effect on the shape of Figure 2.1f in Section 2.6.2. Importantly, we measured all perovskite samples only under high injection level conditions, in which case the effective lifetime is the sum of the electron and hole lifetimes, $\tau_{eff} = \tau_p + \tau_n$. For low injection levels, the plateau would correspond to either τ_p or τ_n, depending on the polarity of the dopant; see Section 2.6.2 for further details.

2.3. Decoupling Bulk and Surface Recombination

2.3.1. Thickness-Dependent Effective Lifetime Measurements

We now return to Equation 2.2 and discuss the means of separating the bulk from surface recombination processes from the measured effective lifetime. While the bulk lifetime is a reasonably simple parameter, the surface lifetime is less straightforward. This is due to the fact that the surface lifetime depends on more than simply the rate of trap-assisted recombination at the surface; it also depends on the layer thickness and carrier diffusivity, both of which can of course vary between similar sample types. It is therefore more appropriate to determine and quote the surface recombination velocity, which depends only on the surface properties, such as the surface trap density and the carrier concentration at the surface[125].

Relating the surface lifetime to SRV has previously been outlined in literature, where it was noted that a direct relation is not trivial; the generalized form can only be solved numerically[35]. However, the boundary conditions can be approximated analytically, which provide upper and lower limits to the determined SRV. Defining the effective SRVs of either interface to be S_1 and S_2, we can write that at the limit wherein $S_1 \gg S_2$ ($S_2 \approx 0$):

$$\tau_{surf} = \frac{2W}{S_1} + \frac{4}{D}\left(\frac{W}{\pi}\right)^2 \tag{2.7}$$

For the limit of $S_1 = S_2$, the relationship is approximated as:

$$\tau_{surf} = \frac{2W}{S_1 + S_2} + \frac{1}{D}\left(\frac{W}{\pi}\right)^2 \tag{2.8}$$

In the above expressions, W is the thickness of the photoactive layer and D is the ambipolar diffusion constant (under high injection levels). The factor of 2 in each of the first

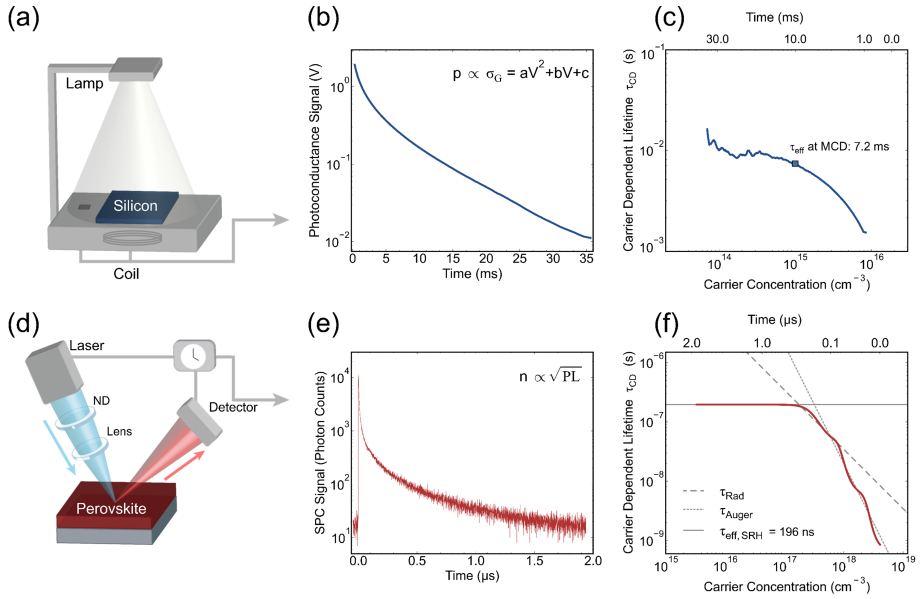

Figure 2.1: (a) Schematic of the Sinton WCT-120 lifetime assessment tool for silicon PV. (b) The raw photovoltage decay signal as a function of time for a symmetric n-poly Si/SiO_2 on n-Si wafer. (c) The carrier-dependent lifetime as a function of carrier concentration (primary x-axis) and as a function of time (secondary x-axis), calculated from Equation 2.4. The reported τ_{eff} is at the standard MCD of 10^{15} cm^{-3}. (d) Schematic of the typical TCSPC setup for TRPL measurements. In this work, λ_{exc} = 485 nm ($\lambda_{em} \approx$ 780 nm after ~2 minutes of continuous illumination). (e) The cumulative photon signal collected over time for the perovskite on glass sample. (f) The carrier-dependent lifetime (differential lifetime) as a function of carrier concentration and as a function of time, calculated from Equation 2.6. τ_{eff} is determined at the saturation point of the curve. The radiative carrier lifetime (dashed) and Auger carrier lifetime (dotted) are also plotted based on our fit and on reported coefficients for a similar perovskite composition; $k_{rad} = 2.9\times10^{-11}$ cm^3s^{-1}, $C_{Auger} = 5\times10^{-29}$ cm^6s^{-1}[28, 124].

terms arises from the assumption that the effective SRV at either interface, S, is equivalent to both the hole SRV and electron SRV – that is, $S_e + S_h = 2S$[37].

For perovskites, several works argue that as the carrier diffusion length (related to D by $L_d = \sqrt{D\tau}$) is much longer than the typical film thickness, so the second term in Equations 2.7 and 2.8 is negligible[26, 37, 121, 126]. This assumption would enable the convenient case of:

$$\tau_{surf} \approx \frac{2W}{S_1 + S_2} \tag{2.9}$$

This assumption can be somewhat justified on the basis that there are many reports finding L_d to be at least 5 μm for polycrystalline perovskite thin films[127–130]. However, the true diffusion length of any perovskite film depends on a myriad of factors including

polycrystallinity and chemical composition. Consequently, mixed-halide perovskite films have been reported in other works to have diffusion lengths much closer to the typical film thickness[12, 131–133]. To this extent, we argue that this assumption should be approached with caution; in any case, entirely neglecting the diffusivity term and still obtaining reasonable surface lifetimes only holds for relatively low SRVs.

To ascertain whether the second term can be omitted to simplify our analytical procedures, we solved for the effective lifetime when either Equations 2.7 or 2.8 are used to find τ_{surf}, and compared the results to when Equation 2.9 is used to find τ_{surf}. We present the results in Figure 2.15. In Section 2.6.3, we also discuss the limiting scenarios for when the diffusivity term is necessary for a range of different SRVs and diffusion lengths. Based on the experimentally obtained effective lifetimes in this work and comparing with the analytical results, we deduced that the transverse carrier diffusion length must be ≥1 µm. We supplement this calculation by experimentally measuring the lateral carrier diffusion length of our triple-cation mixed-halide perovskite thin film on glass using a home-built steady-state photocarrier grating (SSPG) setup, the experimental details of which are described in our previous work[134]. Typically for perovskite films, the transverse carrier diffusion length is significantly longer than the lateral diffusion length[135]. From these measurements, we obtained an in-plane carrier diffusion length of $L_{d,\text{lat}} \approx 500$ nm.

With the diffusion length considered, it is now reasonable to confirm and utilize the relationship of the effective lifetime with surface recombination velocities and bulk lifetime:

$$\frac{1}{\tau_{\text{eff}}} = \frac{1}{\tau_{\text{bulk}}} + \frac{S_1 + S_2}{2W_{\text{pvk}}} \tag{2.10}$$

Drawing inspiration from similar techniques applied in the silicon community, we separated the bulk and surface recombination parameters by varying the thickness of unencapsulated perovskite films on glass and plotting the inverse effective lifetime as a function of the inverse thickness (Figure 2.2a)[105–107]. Using Equation 2.10, the inverse of the y-intercept from the linear fit corresponds to τ_{bulk}, while the slope is $(S_{\text{air}} + S_{\text{glass}})/2$. The unencapsulated perovskite linear fit yields a bulk lifetime of $\tau_{\text{bulk}} \approx 1$ µs. However, as the associated statistical uncertainty of the intercept is high (± 4 µs, represented by the gray region Figure 2.2a), there are clearly issues with this initial approximation, which we attribute to interfacial reactions such as oxidation at the perovskite-air interface. To reduce this uncertainty, we further measured the effective lifetime as a function of thickness for perovskite films encapsulated with trioctylphosphine oxide (TOPO, shown in green), and with electron-beam evaporated SiO_2 (shown in red). As shown in Figure 2.2a, the data spread – thereby the associated uncertainty – is reduced in both cases, enabling a more reliable estimation of τ_{bulk}. We determined from the TOPO-encapsulated dataset that $\tau_{\text{bulk}} \approx 2 \pm 1$ µs.
Furthermore, as TOPO has been shown to passivate the dangling bonds incredibly well when deposited on top of perovskite films, the SRV of the perovskite-TOPO interface is near zero, allowing one to determine the SRV of the rear perovskite-glass interface as simply twice the slope of the best linear fit[26, 37, 136]. The SRV of the perovskite-glass interface was determined to be $S_{\text{glass}} = 200 \pm 80$ cm/s. This is in agreement with the

slope from the SiO_2-encapsulated dataset (S_{glass} = 300 ± 150 cm/s), the latter calculated under the assumption that the SRVs of the top and rear SiO_2 interfaces are equal. Using the former value for S_{glass}, the SRV between the perovskite and air was subsequently determined: S_{air} = 1100 ± 500 cm/s.

This thickness-variation method can be applied to all perovskite structures of interest and, particularly when using encapsulants such as TOPO or SiO_2, the bulk lifetime and the SRVs become experimentally straightforward to determine. Moreover, if the assumption is made that the perovskite bulk carrier lifetime does not substantially differ when deposited on different contacts, one can then use the bulk lifetime obtained from the fits in Figure 2.2a and extend its use to rapidly determine the SRV of layers that are of greater interest in the photovoltaic community. We highlight that such an assessment has already been implemented for the extraction of the SRVs of several selective contacts on $MAPbI_3$ films in the past[26]. The assumption that bulk lifetime does not drastically change is somewhat reasonable considering that, while the bulk lifetime may slightly differ when the perovskite film is formed over different substrates, it does not span orders of magnitude. Furthermore, it has been shown in literature the bulk rarely limits the measured effective lifetime[126, 133, 137]. As a result, the extracted values for τ_{bulk} and S_{air} (or indeed S_{glass} if SiO_2 encapsulation is applied) can be used to determine the $S_{contact}$, the SRV of the rear contact, using the above relations.

2.3.2. SRVs for Relevant Contacts

The effective lifetimes of the substrate-contact-perovskite stacks were measured for 17 additional thin contacts of interest for photovoltaic applications. The SRVs of the 7 hole transport layers (HTLs), 7 electron transport layers (ETLs) and 3 additional materials were then obtained using Equation 2.10 and the predetermined τ_{bulk} and S_{air} values, with the uncertainty range determined from the limits of $S_1 \gg S_2$ and $S_1 = S_2$. The effective lifetimes and corresponding SRVs are plotted in Figure 2.2b. The extracted SRV values are of course sensitive to the nature of the perovskite (composition, deposition, method, treatment) – as such, different works may report slightly different values. However, despite the compositional variation, it is emphasized that the SRVs determined in this work are in agreement with the SRVs of similar contacts but on $MAPbI_3$ films[26].

We first emphasize the caveats of directly measuring the passivation of a contact with the intent of relating the results to a full device. By inspecting the graph, it is clear that NiO_x, deposited as Ni by electron-beam evaporation followed by high-temperature annealing in air, exhibits by far the lowest SRV of ≈80 cm/s. From purely a passivation viewpoint, one would expect NiO_x to serve as the most effective HTL under a single junction pin configuration. It is however emphasized that passivation does not automatically infer effective carrier extraction; poor band alignment or the formation of a passivating inert layer by redox reactions at the oxide-perovskite interface will, and do, limit effective carrier extraction[138]. Indeed, in our previous work we found that the NiO_x interface was limiting the performance in our back-contact perovskite solar cells, due to the formation of a substantial carrier extraction barrier[100]. As a second caveat, significant variations from the perovskite-glass reference should be tracked with supplemental optical and morphological characterization, such as with XRD, SEM, UV-Vis and PL (all of which

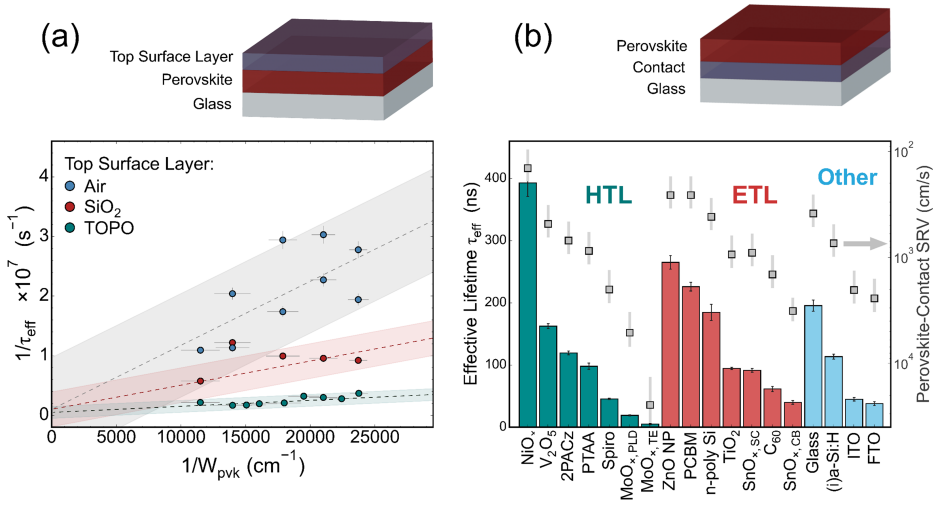

Figure 2.2: (a) Above: schematic depicting the standard sample configuration used for thickness-dependent lifetime measurements. Below: the inverse effective lifetime as a function of inverse perovskite thickness, with linear fits applied to the data (dashed lines). The fits were used to determine the bulk lifetime (intercept^{-1}) and the surface recombination velocities ($S_1 + S_2 = 2\times$slope) for unencapsulated perovskite films (blue), SiO_2-encapsulated films (red) and TOPO-encapsulated films (green). The shaded regions correspond to the statistical uncertainty of the fitted intercept. All perovskite films were fabricated on glass substrates. (b) Above: schematic of the sample configuration applied to determine SRVs of the PV-relevant contacts. Below: corresponding histogram of the effective carrier lifetimes (read from the left y-axis) measured for 18 different contacts of interest, grouped into HTLs (green), ETLs (red) and remaining contacts not typically used as transport layers (blue). The corresponding determined SRVs for each contact are shown as the gray markers and read from the right y-axis. The gray errorbars indicate the SRV range determined from the boundary conditions defined using Equations 2.7 and 2.8.

are presented in Section 2.6.2). Should significant deviations occur for a test sample compared to the glass reference – for example if an excess of PbI_2 is present as determined from XRD – it is recommended that a thickness-dependent effective lifetime dataset is collected for that sample, and the SRV is extracted instead from the slope. With the caveats known, we argue that this method serves as a reasonable and efficient screening technique to determine the passivation properties of any contact located on the rear of the perovskite film.

In addition to directly comparing the passivation performance of different contact materials using this technique, the influence of deposition method can also be established. For example, we compared 10 nm films of MoO_x, deposited by either pulsed laser deposition (PLD) or by thermal evaporation (TE)[139]. As shown in Figure 2.2b, the passivation of MoO_{xTE} (SRV $\approx 2.5\times10^4$ cm/s) is much worse than that of MoO_{xPLD} (SRV $\approx 5.1\times10^3$ cm/s). Similarly, we show that the SRV of the SnO_x ETL is higher when fabricated using chemical

bath deposition (SRV ≈2.3×10^3 cm/s) compared to the standard spin-coating method (SRV ≈900 cm/s)[96]. Furthermore, we can apply this method to screen for prospective passivating, carrier selective contacts for single junction and tandem perovskite devices. The case in point for this work is highlighted with the SRV measurements of intrinsic amorphous silicon, (i)a-Si:H, and n-type polysilicon (n-poly Si) – both are comparable to state-of-the-art perovskite contacts.

As the SRV of the perovskite-glass substrate interface is known, the PV-relevant contact position in the stack can be inverted, enabling one to also obtain the SRV of the contact when it is employed as a superlayer rather than a sublayer. This extends the applicability of this technique and enables us to compare different contacts under realistic device configurations. We selected four common contacts of interest, namely the HTLs of Spiro-OMeTAD (Spiro) and PTAA, and the ETLs of C_{60} and the related PCBM. These contacts were selected as they are extensively used as typical transport layers in perovskite solar cells, and they additionally can be easily spin-coated or evaporated either on the substrate or on the perovskite film without major sample alterations. It is widely known that PTAA and C_{60} are preferentially utilized in the pin configuration, while Spiro and PCBM are generally utilized in the nip configuration[140, 141]. With the exception of the high SRV of C_{60} when deposited on top of the perovskite layer, we find that such common preferential configurations agree with the differences in our experimentally determined SRVs, which we compare in Figure 2.3[142, 143]. The underlying reasons for differing SRV values between the same contacts but with an inverted stack order are complex. We propose that a key reason is likely due to the different nucleation and growth mechanisms of the deposited layers which are highly dependent on the substrate beneath; such surface variability has been shown to occur for perovskite films grown upon different substrates[137, 144]. We further postulate that dry deposition methods, such as evaporation, will likely lead to less intermixing of the contacts at the surface compared to wet processing methods. Whether this intermixing is beneficial or detrimental for the device likely depends on the precise contact composition.

The determination of the SRV of any contact regardless of their position in the perovskite stack enables one to calculate the effective total SRV for any hypothetical perovskite configuration – with any two contacts placed on either side of the film. The benefit of this calculation is that it can then be converted to the corresponding upper limit for the open-circuit voltage, provided that extraction beyond the carrier transport layer is perfect. These calculations can therefore be used to determine and optimize the limiting contact(s) in current and next-generation perovskite photovoltaic devices, and further indicate whether additional significant losses occur beyond carrier extraction and separation into the transport layers.

2.4. Implied V_{OC} and Solar Cell Comparisons

We now focus on addressing the question: how do the trap-assisted recombination properties, determined using the above methodology, translate to full device open-circuit voltages and cell efficiencies? To address this relationship, we first consider the simple perovskite half-stack configuration schematically portrayed in the upper half of Figure

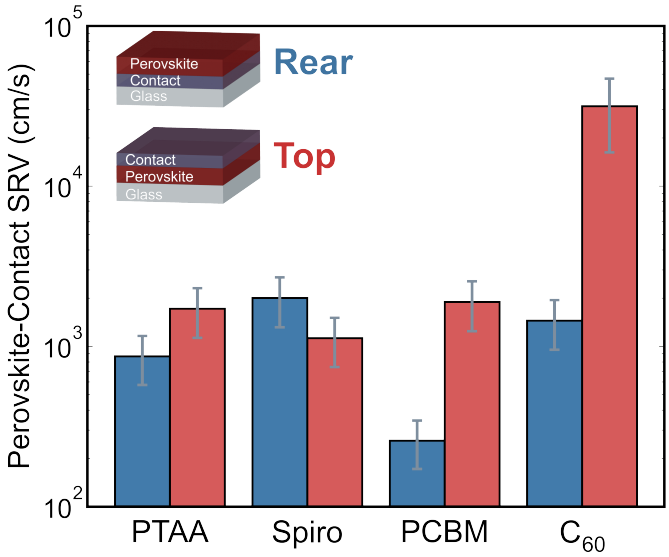

Figure 2.3: The differences between the measured SRVs for the perovskite-PTAA, -Spiro, -PCBM and -C_{60} interfaces when the contacts were deposited at the rear (blue) or on top (red) of the perovskite film.

2.2b.
We begin by assessing whether the extracted SRVs agree with a second material property that directly relates to minority carrier recombination – the PLQY. As the PLQY is simply the ratio of the radiative to total recombination rate in a semiconductor material, it is inversely proportional to the non-radiative recombination rate and, by extension, the measured SRV of the same sample. We exemplify this relationship by plotting the inverse percentage PLQY against the perovskite-contact SRV for a subset of 11 contacts in Figure 2.4a. We omit FTO, ITO, the silicon-based contacts, MoO_x and SnO_{xCB} as these contacts currently are not widely applied directly as an interfacial layer to the perovskite film in PV technologies. With the exception of two outliers, the samples containing Spiro and V_2O_5, the results follow the expected inverse linear relationship. The outlier discrepancy was attributed to degradation between measurements and local differences across the samples. Specifically in the case of Spiro, the wettability of the perovskite was poor on the contact which in turn implied regional differences in the film formation and quality (this argument is supported by the low solar cell performance which is shown later in this section).

While the conversion from the measured PLQY to the sample's implied open-circuit voltage is relatively straightforward: i$V_{OC} = V_{OC,rad} + V_{therm} \ln(\text{PLQY})$, in which $V_{OC,rad}$ is the open-circuit voltage at the radiative limit and V_{therm} is the thermal voltage (25.85 mV at room temperature), the direct relationship between the minority carrier lifetime and open-circuit voltage is slightly more nuanced. We consider an approach with two varia-

tions in converting τ_{eff} to iV_{OC}: the first variation is that we directly apply a previously derived expression specifically for perovskite materials and their properties[31]. The second variation is by more generally converting the trap-assisted recombination parameters to their corresponding J_0 values and summing all the recombination components[145]. Of course, both of these variations are derived from first principles – as such they should yield the same result (this is verified and further discussed in Section 2.6.4). However, each calculation relies on different perovskite properties; the variation one chooses therefore will depend on which properties are known.

Beginning with the first method, it has previously been shown that the iV_{OC} can be determined from τ_{eff}, provided that the background doping density (equivalent to N_A), the carrier generation rate G, the radiative recombination coefficient k_{rad}, the probability of escape (P_e) and summation of P_e with probability of parasitic absorption ($P = P_e + P_a$) are known[31, 111, 146]. Reproducing this relationship, i$V_{OC} = V_{OC,rad} + V_{therm} \ln(Q)$, where Q is defined as the external luminescence quantum efficiency:

$$Q = \frac{2k_{rad}P_e\tau_{eff}(N_A + G\tau_{eff})}{1 + k_{rad}\tau_{eff}P(N_A + 2G\tau_{eff}) + \tau_{eff}\sqrt{4Gk_{rad}P + \frac{(1+k_{rad}N_AP\tau_{eff})^2}{\tau_{eff}^2}}} \tag{2.11}$$

In this analysis, voltage losses due to Auger recombination are neglected. Based on the TRPL fluence conditions in our work, we set $G \approx 4.2\times10^{18}$ cm^{-3}s^{-1}, which we determine from the absorbed photon flux and perovskite thickness. The radiative recombination coefficient is set as $k_{rad} = 2.9\times10$ cm^{3}s^{-1}, which agrees with the carrier-dependent lifetime trend of the perovskite in Figure 2.1d and agrees with previous reports[28]. Following realistic literature values, we set P_e to be 0.13 and P_a to be 0.07[147–150]. With these parameters and measuring the perovskite band gap to be E_g = 1.6 eV, we plot the iV_{OC} as a function of effective minority carrier lifetime for three different doping densities in Figure 2.4b[151]. For reference, the experimentally measured effective carrier lifetimes and the corresponding iV_{OC} derived from PLQY are plotted in the same figure. Accounting for the differences in carrier generation rates between the measurements (solid versus dashed lines), the implication from the position of the experimental data is that the background doping density of the triple-cation perovskite used in this work is on the order of 10^{16} - 10^{17} cm^{-3}. Furthermore, as shown at sufficiently high effective lifetimes, the maximum achievable V_{OC} is ~11 mV below that of the radiative limit; this is a consequence of the notably strong influence of parasitic absorption (absorbing 7% of the total incoming light) in such high-quality hypothetical devices.

Of course, the corresponding open-circuit voltages for the plotted samples do not correlate to true device parameters, as these are half-stack samples and contain only one transport layer of interest. However, as we have already predetermined τ_{bulk} and the SRVs of several contacts of interest in their relevant configuration in the stack, we can combine Equations 2.10 with 2.11 to estimate the upper limit to the open-circuit voltage for full device stacks, assuming that losses beyond the transport layers are negligible. Using τ_{bulk} = 2 µs, we plot the iV_{OC} as a function of SRV = S_1 + S_2, shown as the green dashed line Figure 2.4c. It is evident that at SRVs beyond ~100 cm/s, surface recombination limits the iV_{OC}. At negligibly low SRV values, the total non-radiative iV_{OC} loss is 27 mV. The 27

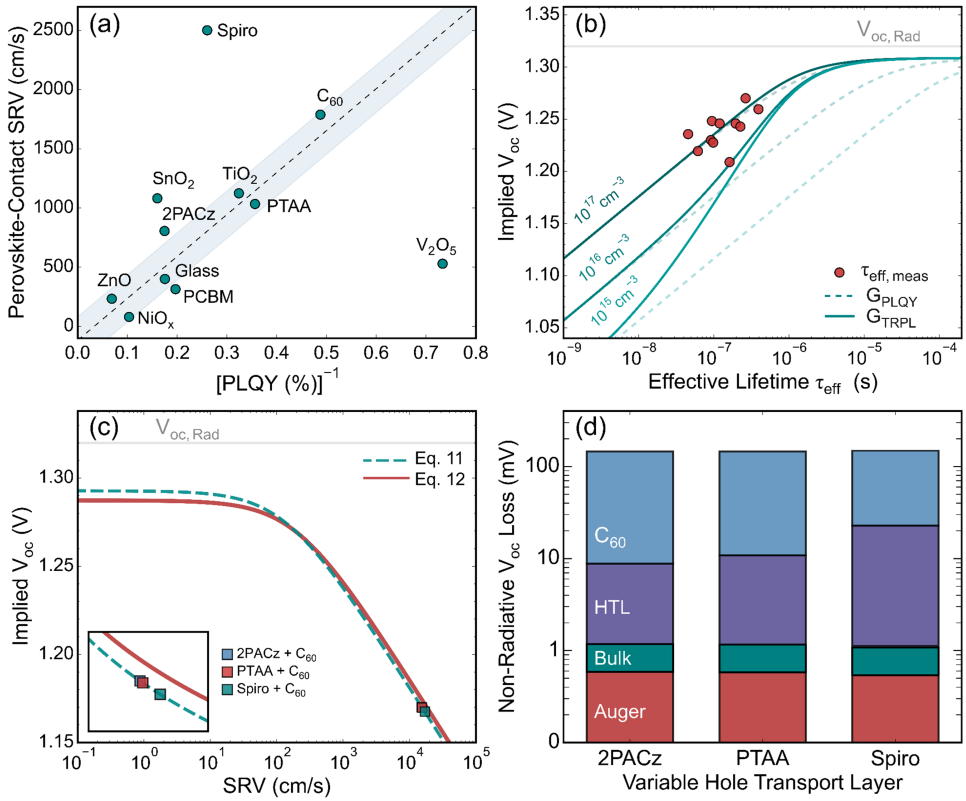

Figure 2.4: (a) SRV plotted against the inverse PLQY of 11 contacts, in which the contacts were deposited on the rear of the unencapsulated perovskite film. (b) Calculated implied open-circuit voltage using Equation 2.11 for different doping densities of $N_A = 10^{15}$, 10^{16} and 10^{17} cm^{-3}. The solid line represents the carrier generation under TRPL conditions. For reference, the dashed line corresponds to the PLQY carrier generation rates in this work; $G_{PLQY} = 2.24 \times 10^{14}$ cm^{-3}s^{-1}. The radiative limit is also indicated with the solid gray line, $V_{OC,rad} = 1.32$V. (c) Plotting iV_{OC} as a function of SRV = $S_1 + S_2$ for $N_A = 10^{17}$ cm^{-3} and $\tau_{bulk} = 2$ µs. The green dashed line corresponds to iV_{OC} determination from the first discussed method, and the red solid line corresponds to the curve determined from the J_0 method. Inset: zoomed region which resolves the marker positions of the three hypothetical solar cell configurations. (d) Visualization of the total non-radiative iV_{OC} losses for the three solar cell configurations, solved by determining the ratio of the total voltage loss due to each J_0 term (note that the losses are presented on a logarithmic voltage scale).

mV loss in this case is due to both parasitic absorption, as described above, and to bulk recombination within the sample; this is effectively the iV_{OC} limit in which $\tau_{bulk} = \tau_{eff} = 2$ µs.

In the same figure, we also indicate the predicted open-circuit voltages for three different pin solar cell configurations, in which C_{60} is the common ETL and with different HTLs, namely 2PACz, PTAA and Spiro. As expected from the previously shown exceedingly high

SRV of the perovskite-C_{60} interface, we see that in all cases C_{60} accounts for an additional voltage loss of 127 mV. This interface is clearly the voltage-limiting component in each hypothetical device. This limitation has been observed in other works using different methods; within the past three years, there has been a heightened focus in the perovskite community to understand and to mitigate the observed losses at the C_{60}-perovskite interface[142, 152, 153]. Additional losses due to the HTL are consequently minimal, as evident by the proximity of the markers. This of course does not imply that they do not limit the device in any way; should C_{60} be replaced with a highly passivating ETL, one finds that the HTL in each case then becomes the limiting point of recombination, which is evident from simply following the trend in Figure 2.4c.

We now consider the second and more generalized variation to predict iV_{OC} and estimate the voltage losses at each region of the device. From the trap-assisted recombination parameters calculated in previous sections, it is also possible to make an estimation of the recombination parameter J_0, the reverse saturation current density[145]. J_0 is widely used in silicon PV as a means to assess the quality of the silicon (half-fabricate) wafers; J_0 is notably automatically calculated in the Sinton WCT-120 analysis software and the value is generally returned with the lifetime and the iV_{OC}[109, 110]. The benefit of using J_0 is that each loss component can simply be added up to determine the total dark recombination current density: $J_{0,\text{tot}} = J_{0,\text{rad}} + J_{0,\text{surf}} + J_{0,\text{bulk}} + J_{0,\text{Auger}}$. This makes the determination of the key loss mechanisms relatively more straightforward than using Equation 2.11. The total iV_{OC} can then be simply determined using the standard expression:

$$\text{i}V_{OC} = V_{\text{therm}} \ln\left(\frac{J_{SC}}{J_{0,\text{tot}}}\right) \tag{2.12}$$

For the perovskite band gap of 1.6 eV, $J_{0,\text{rad}} = 1.43 \times 10^{-27}$ A/cm^2 (Section 2.6.4). We once more draw inspiration from silicon methods to convert τ_{bulk} into a reasonable estimation for $J_{0,\text{bulk}}$[125]:

$$J_{0,\text{bulk}} = \frac{W_{\text{pvk}}}{\tau_{\text{bulk}}} \frac{q n_i^2}{N_A + \Delta n} \tag{2.13}$$

It similarly follows that for surface recombination, with $S = S_1 + S_2$, that:[154]

$$J_{0,bulk} = \frac{S}{2} \frac{q n_i^2}{N_A + \Delta n} \tag{2.14}$$

For a generalized trap-assisted recombination expression, each of the above bulk and surface components can simply be summed: $J_{0,\text{eff}} = J_{0,\text{bulk}} + J_{0,\text{surf}}$. The intrinsic carrier concentration for this perovskite is calculated to be $n_i = 7.03 \times 10^4$ cm^{-3} (see Section 2.6.4 for the calculation). As with the first variation, we also account for the probabilities of escape and of parasitic absorption by scaling the J_0 components accordingly. We account for the probability of emission by scaling the non-radiative J_0 terms with the inverse of P_e, and by scaling the radiative J_0 term with P/P_e[31]. Using this approach, we determine $J_{0,\text{bulk}} = 1.90 \times 10^{-24}$ A/cm^2. While the Auger recombination is neglected in Equation 2.11, we show that it can easily be implemented in this generalized approach to predict a more accurate open-circuit voltage. Using an Auger coefficient of $C_{\text{Auger}} = 5 \times 10^{-29}$

cm^6s^{-1}, we calculate $J_{0,Auger} = 1.90 \times 10^{-24}$ A/cm^2[28]. We argue it is good practice to incorporate the losses due to Auger, should high injection levels be required or applied in different measurements and test conditions, as is the case in this work. The predicted open-circuit voltage determined from Equation 2.12 is plotted as the red solid line in Figure 2.4c. Indeed, the difference in the green and red curves at low SRVs is the effect of including Auger in the latter variation. Auger accounts for an additional iV_{OC} loss of 5 mV (this is the difference in the plateaus of the curves at low SRVs in Figure 2.4c). Otherwise, the similarities between the solid and dashed curves emphasizes the minimal differences in the calculation variations to convert the trap-assisted lifetime properties to predicted open-circuit voltages.

To emphasize the benefit in resolving each J_0 component, we visualize the extent of open-circuit voltage loss due to Auger and trap-assisted recombination for the three hypothetical cells in Figure 2.4d. The extent of the iV_{OC} loss, which is logarithmically visualized along the y-axis, is calculated by assessing the relative contribution that each non-radiative recombination process has upon to the total non-radiative component of J_0. The benefit of this visualization is that relative contributions from non-limiting contacts can also be clearly resolved, rather than by simply noting the further minor losses as in Figure 2.4c. Inspecting the scale of Figure 2.4d highlights that in all cases, ~90% of the total non-radiative iV_{OC} losses is due to the limiting perovskite-C_{60} interface. Evidently, to further improve the implied open-circuit voltage of these configurations, some ETL addition or substitution is required. However, we note that as each of these losses are derived from the percentage of the total non-radiative recombination, reducing, for example, the surface recombination at the C_{60} contact will in turn increase the relative contribution in other non-radiative loss mechanisms. Therefore, in order to optimize contacts for full devices, one requires information from both Figures 2.4c and 2.4d to understand the full picture of the stack.

We highlight that applying an optical assessment like the procedure described here is already a proven technique to optimize the photovoltage in perovskite solar cells. A notable example is shown in the work of Ginger and co-workers, where (3-aminopropyl)-trimethoxysilane (APTMS) was applied as a passivating layer between the perovskite and the C_{60} interface. The group measured more than an order of magnitude reduction in the SRV when the APTMS layer was added compared to the perovskite/C_{60} control, corresponding to a 100 mV improvement in the iV_{OC} and a 60 mV increase in the measured V_{OC}. The advantage of the prior optical assessment is clearly showcased in this work, as the characterization ultimately led to a cell efficiency enhancement from 15.9% to >18%[155, 156].

Finally, we compare our open-circuit voltage predictions with fully fabricated devices. We prepare three different test device configurations which are schematically shown in Figure 2.5a. As with our hypothetical devices, we only vary the HTL in each of the tested cells. The corresponding JV curves for each of the three devices are shown in Figure 2.5b, with device statistics presented in Figures 2.5c - 2.5f. Notably, the open-circuit voltages extracted from the JV curves are significantly lower than the implied open-circuit voltages

as calculated above. The differences in the median V_{OC} with the iV_{OC} for the 2PACz-, PTAA- and Spiro-based devices are 267 mV, 106 mV and 829 mV, respectively. With the exception of the PTAA-based device, V_{OC} losses from factors that we have not yet accounted for are substantially higher than losses simply from non-radiative recombination in and at the interface of the perovskite film (Figure 2.5g). The poor device performances and JV parameters justify the argument that analyzing the device statistics alone may result in the erroneous conclusion that the low J_{SC} combined with lower than anticipated V_{OC} may be a consequence of high recombination at the perovskite-contact interface, or indeed due to high recombination rates within the bulk of the film. As we have shown with the long τ_{bulk} and high PLQY, it is not the bulk quality that is influencing the device performance, nor the interfaces that can account for such extensive losses. Therefore, some additional loss mechanisms are occurring beyond the photoactive layer. The device resistances extracted from the JV curves and from fitting the curves to the ideal diode equation notably show detrimentally low shunt resistances in both the 2PACz-based and Spiro-based cells ($R_{sh,2PACz}$ ≈2.5 KΩcm^2, $R_{sh,Spiro}$ ~0.3 KΩcm^2), while all devices suffer losses due to high series resistances ($R_{s,2PACz}$ ≈6 Ωcm^2, $R_{s,PTAA}$ ≈12 Ωcm^2, $R_{s,Spiro}$ ≈5.5 Ωcm^2). We further explore the loss mechanisms based on the extracted resistances, and discuss optimization strategies in Section 2.6.4. Notably, we find that the device performances are likely due to poor carrier mobilities in the transport layers.

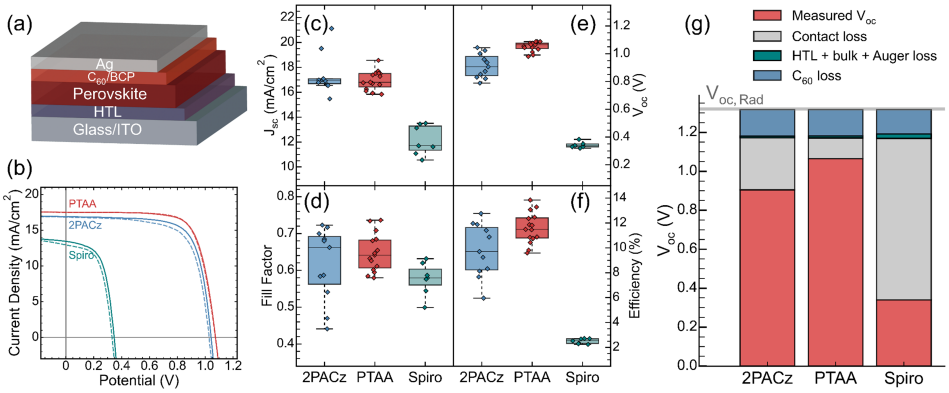

Figure 2.5: (a) Schematic of pin stack, with variable HTLs, fabricated in this work. (b) Measured light JV curves of the devices, using PTAA (red), 2PACz (blue) and Spiro-OMeTAD (green) as the different hole transport layers. The solid and dashed lines represent the forward and reverse scans, respectively. (c) - (f) Corresponding JV cell statistics of the tested devices. (g) The complete breakdown of the measured open-circuit voltage and the resolved photovoltage losses for each of the tested device configurations in this work. Resolving each loss highlights the combined detrimental effects of the C_{60} interface and recombination issues beyond the transport layers (contact losses), compared to losses due to bulk, Auger and HTL recombination losses.

2.5. Conclusion

In summary, we have shown that simple thickness-dependent effective lifetime measurements of perovskite half-stacks can resolve the total trap-assisted recombination losses, within the perovskite bulk and at both interfaces. We have drawn upon established silicon assessment methods to quantify the resolved trap-assisted recombination processes in terms of τ_{bulk} and SRV, experimentally determined the SRVs of 18 different contacts and confirmed our findings with supplemental PLQY characterization. Extending this analytical framework to full perovskite stacks relevant for photovoltaics, we find that C_{60} – while possibly the most popular ETL in perovskite photovoltaics – accounts for ~90% of the total non-radiative losses within the photoactive layer in typical device configurations. We present how the trap-assisted parameters can be combined and converted to obtain an upper limit to the open-circuit voltage for effectively any device configuration. Despite the high SRV of C_{60}, we show that archetypal devices containing common HTLs such as 2PACz and PTAA can in principle achieve implied open-circuit voltages beyond 1.15 V. We furthermore highlight that solving for the iV_{OC} using the common recombination parameter J_0 enables one to neatly resolve and visualize not only each trap-assisted recombination process, but also the influence of Auger at relevant injection levels. We emphasize that using this framework in addition to fabricating full devices can lead to a much stronger insight into device losses. We have evidently shown that even with a high quality perovskite film (τ_{bulk} = 2 µs) and reasonable perovskite interfaces, efficiencies of full devices can remain low due to detrimental processes beyond the photoactive layer. In our case, we note that the predominant losses likely arise from poor mobilities in the transport layers, or indeed simply a poor connection to the electrodes and external circuit. With the framework proposed, device optimization can be easily directed to the relevant limiting processes which may have been otherwise overlooked.

2.6. Supporting Information

2.6.1. Methods

Chemicals

Dimethyl sulfoxide (DMSO, anhydrous ≥99.9%), N,N-dimethylformamide (DMF, anhydrous ≥99.8%), chlorobenzene (CB, anhydrous ≥ 99%), toluene (anhydrous, ≥ 99.8%), acetonitrile (anhydrous, ≥ 99.8%), ethanol, isopropanol (IPA), acetone, hydrochloric acid (HCl, 37%), 4-tert-butylpyridine (TBP, ≥ 98%) and thioglycolic acid (TGA, ≥ 90%) were purchased from Sigma-Aldrich. Methylammonium bromide (MABr, CH_3NH_3Br, 99%), formamidinium iodide (FAI, CH_5IN_2, ≥99%) lead iodide (PbI_2, ≥99.99%), lead bromide ($PbBr_2$, ≥98%) and 2-(9H-carbazol-9-yl)ethyl)-phosphonic acid (2PACz, >98%) were purchased from TCI. Cesium iodide (≥ 99.99%), (6,6)-phenyl C_{61} butyric acid methyl ester (PCBM, ≥99.5%), poly[bis(4-phenyl)(2,4,6-trimethylphenyl)amine] (PTAA, ≥95%), fullerene-C_{60} (>99.5%), molybdenum(VI) oxide (MoO_x, ≥99.9%),vanadium(V) oxide (V_2O_5, ≥99.9%), tin(II) chloride dihydrate ($SnCl_2.2H_2O$, ≥99.99%), titanium(IV) isopropoxide, zinc oxide nanoparticle ink (0.8 g/mL), urea (≥99.5%), bis(trifluoromethane)sulfonimide lithium salt (Li-TFSI, >99%) and trioctylphosphine oxide (TOPO, >99%) were purchased from Sigma-Aldrich. Bathocuproine (BCP, ≥99.5%) was purchased from Ossila. 2,2',7,7'-tetrakis(N,N-di-p-methoxyphenylamine)-9,9'- spirobifluorene (Spiro-OMeTAD, >99.5%) was purchased from Derthon.

Sample Fabrication

Glass substrates (1.5 × 1.5 cm^2) were first scrubbed then ultrasonically cleaned successively with a 1% Hellmanex III solution in 70 °C water, acetone and IPA for 15 minutes each, followed by drying under a N_2 gas flow. The samples were then UV-ozone treated for 40 minutes immediately before the contact or perovskite was spin-coated on top. ITO and FTO on glass substrates were similarly cleaned and treated before subsequent processes. The perovskite solution was prepared by first stirring separate 1.5 M solutions of PbI_2 and $PbBr_2$ in DMF:DMSO (4:1) overnight. The PbI_2 solution was added to pre-weighed FAI to achieve a 1.24 M $FAPbI_3$ solution (with an 10% excess of PbI_2). Similarly, the $PbBr_2$ solution was added to pre-weighed MABr to achieve a 1.24 M $MAPbBr_3$ solution (with no excess of $PbBr_2$). These solutions were separately stirred for 2 hours at 70 °C before they were combined in a 80:20 ratio of $FAPbI_3$:$MAPbBr_3$. Finally, CsI in DMSO (1.5 M, stirred for 2 hours at 70 °C) was added in a 6% ratio to the mixed perovskite solution and stirred for a subsequent 2 hours at the same temperature to achieve the desired mixed-halide perovskite solution. Before any deposition, the solution was cooled and filtered with a 0.45 µm PTFE filter. For all depositions, 120 µL of the perovskite precursor solution was spin-coated for 30 seconds with a ramping time of 5 seconds before full speed. At 15 seconds into the spin-coating at full speed, the samples were quenched with 170 µL of CB. The samples were then annealed on a hotplate at 100 °C for 45 minutes. To obtain a 622 nm film, the spin speed was set at 4000 RPM. For the thickness-dependent measurements, the spin speed was varied and the perovskite thickness was measured using profilometry. The relationship between the spin speed and thickness is shown in Figure 2.6.

For the films that had been encapsulated for the thickness dependent lifetime measurements in Figure 2.2a, they were either capped with TOPO or with electron-beam

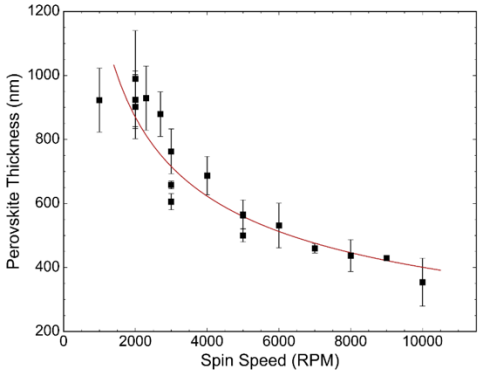

Figure 2.6: Perovskite film thickness as a function of the rotational speed (RS) of the spin-coater, in rotations per minute. For rotational speeds (RS) between 2000 - 10000 RPM, the perovskite thickness (W_{pvk}, in nanometers) followed the empirical power law of $W_{pvk} = 33654 \times RS^{-0.481}$ (shown in red).

evaporated SiO_2. The 0.025 M TOPO solution was prepared in CB and 80 µL was spin-coated on top of the perovskite film at 2000 RPM for 60 seconds with a ramping time of 4 seconds. This process was repeated two additional times to achieve a full TOPO film. The 60 nm SiO_2 films were deposited with a Polyteknik Flextura M508E electron-beam evaporator under vacuum and with an SiO_2 source, at an evaporation rate of 0.2 nm/s.

The additional contact layers presented in Figure 2.2b and Figure 2.3 were fabricated as follows:
NiO_x (~10 - 15 nm) films were fabricated by evaporating 10 nm of Ni using the same electron-beam evaporator listed above, at a rate of 0.04 nm/s. The films were then annealed at 300 °C for 1 hour under atmospheric conditions.
V_2O_5 (10 nm), MoO_{xTE} (10 nm) and C_{60} (10 nm) were thermally evaporated using an Angstrom Engineering glovebox-integrated thermal evaporator, at rates of 0.1 Å/s for both of the oxide layers, and 0.2 Å/s for the C_{60} layer. Chamber pressures were kept below 10^{-7} mbar in each case.
MoO_{xPLD} (10 nm) was deposited with a Solmates PLD, with a 98.9% neon, 1% krypton, 0.1% fluorine (KrF) laser, with an emission wavelength of 245 nm, at a laser fluence of 1.55 J/cm^2 and a repetition rate of 10 Hz. The chamber pressure was maintained at 0.2 mbar with an O_2:Ar gas flow ratio of 1:4 (10 sccm: 40 sccm).
SnO_{xCB} compact films were fabricated similarly to what has been outlined in other works[96]. The substrates were treated for 4 hours in a 90 °C chemical bath containing 625 mg of urea, 12.5 µL of TGA, 625 µL of HCl, 135.5 mg of $SnCl_2.2H_2O$ in 50 mL of water, then rinsed in IPA and annealed for 1 hour at 170 °C.
SnO_{xSC} films were prepared by preparing a 0.1 M solution of $SnCl_2.2H_2O$ in ethanol, filtering using a 0.45 µm PTFE filter and spin-coated onto the substrate for 30 seconds at a spin speed of 3000 RPM, with a ramp time of 4 seconds. The samples were then annealed for 1 hour at 180 °C.

TiO_2 films were prepared by spin-coating a solution containing 369 µL of TTIP and 35 µL of HCl in IPA. The solution was spin-coated for 30 seconds at 3000 RPM with a 4 second ramp time. The films were then annealed for 30 minutes at 500 °C.
ZnO nanoparticle layers were prepared by spin-coating 30 µL of the as-purchased ink onto the substrates, at 4000 RPM for 40 seconds with a 5 second ramp time, followed by a 10 minute anneal at 100 °C.
The 2PACz monolayers were formed by preparing a solution containing 0.9 mg of 2PACz in 3 mL of ethanol, and spin-coating the solution onto the substrates at 3000 RPM for 30 seconds with a 5 second ramp time, followed by a 10 minute anneal at 100 °C.
The PTAA solution contained 10 mg of PTAA, 7.5 µL of Li-TFSI (170 mg/1 mL in acetonitrile) and 4 µL of TBP in 1 mL of toluene. PTAA films were fabricated by spin-coating the solution was onto the substrates at 3000 RPM for 30 seconds, with a 5 second ramp rate, followed by a 10 minute anneal at 100°C.
The Spiro-OMeTAD (Spiro) solution contained 72.3 mg of Spiro, 17.5 µL of Li-TFSI (520 mg/1 mL acetonitrile) and 28.8 µL of TBP in 1 mL of CB. Spiro films were fabricated by spin-coating the solution at 4000 RPM for 20 seconds, followed by a 15 minute anneal at 100°C.
PCBM films were formed by spin-coating a 0.025 M solution of PCBM in CB onto the substrates, at 1200 RPM for 40 seconds with a 3 second ramp time, followed by a 10 minute anneal at 100 °C.
It is noted that all solution-processed films were subjected to filtration with a 0.45 µm PTFE filter prior to deposition. The n-polysilicon layers and hydrogenated intrinsic amorphous silicon, i(a)-Si:H, layers were both formed using plasma enhanced chemical vapor deposition (PECVD), on polished n-type Cz silicon substrates. The polysilicon films were symmetrically deposited as amorphous silicon (20 nm) onto M2 size silicon wafers. The wafers were previously RCA cleaned and a thin tunneling oxide was formed using the standard NAOS treatment, at room temperature for 2 minutes. The samples were then annealed at 900 °C for 25 minutes in a tube oven with a 5% O_2 gas flow. The wafers were then cut to 1.5 × 1.5 cm^2 samples and again RCA cleaned and the native oxide was removed before the perovskite was deposited on top. 14 nm of i(a)-Si:H films were similarly symmetrically deposited on the n-type wafers with the tunnel oxide layer using PECVD, without subsequent annealing.

Moving to the fabrication procedure of the complete solar cells, the ITO on glass substrates were cleaned and treated in a same manner as the bare glass substrates. The HTLs were similarly deposited as discussed above, with the same perovskite composition spin-coated on top of the HTLs. 25 nm of C_{60} and 7 nm of BCP were sequentially thermally evaporated on top of the perovskite film at evaporation rates of 0.2 Å/s and 0.1 Å/s, respectively. Finally, 100 nm of Ag was thermally evaporated through a mask such that each substrate contained four solar cell pixels, using the same evaporator as for the other thermally evaporated materials. Ag was evaporated at a rate of 0.1 Å/s for the first nanometer deposited, and then at 1 Å/s for the remaining 99 nanometers.

2.6.2. Characterization

Time-Resolved Photoluminescence Spectroscopy

TRPL decay curves were obtained using a customized time-correlated single-photon counting (TCSPC) system, consisting of a PicoQuant PDL 828 Sepia II, a PicoQuant HydraHarp, a 485 nm LED laser and an Olympus ×60 Plan Apochromat water objective. The repetition rate of the laser was varied depending on the sample; generally following the rule that $1/f_{RR} \geq 8\tau_{\text{eff}}$, such that the full decay was captured but the resolution was not compromised for each sample. Due to limitations of the system, the decay histogram was limited to 4000 bins regardless of the repetition rate. The f_{RR} varied from 200 kHz to 5 MHz across different sample measurements. 80 µm × 80 µm maps at 400 nm intervals were obtained for each sample, containing a full decay trace at each pixel. The final raw decay trace in every case was taken as the average of all of the decays measured at each pixel. This is exemplified in Figure 2.1e and again in Figure 2.7a, below.

To determine the differential lifetime, the PL peak was first zeroed along the time axis, and the noise floor was subtracted from each raw signal (Figure 2.7b). An arbitrarily high order exponential or polynomial was applied to each normalized, corrected decay to obtain the best possible fit of the data. This fit was applied such that the noise associated with each trace was eliminated (Figure 2.7c). The fitted curve then was converted to the differential lifetime using Equation 2.6. We generally found that using the conventional procedure of applying a biexponential fit to the decay trace can lead to differences of up to 20 - 25% in the extracted carrier lifetime. These lifetime differences were attributed to both the non-physical meaning of the biexponential fit itself and to the relatively poor quality of the fit from the biexponential procedure, compared to the arbitrary fit used to determine the differential lifetime.

As mentioned in Section 2.2.2, the effective radiative and Auger recombination rates generally locally vary over time due to halide segregation and photobrightening occurring within the film. Evidence of halide segregation was observed to occur within the first two minutes in both continuous and pulsed laser excitation, evident with a concurrent red-shift in the PL peak and PLQY improvement (the PLQY of the pristine perovskite on glass improved from ~5% to ~15% when under continuous illumination for 30 minutes). This implies that the perovskite composition locally changed and over time and in the end resembled an iodide-rich halide perovskite. Consequently, the fundamental material properties, namely the radiative and Auger rates, naturally slightly differ at this region after illumination.

The appropriate injection level was obtained by adjusting the total power of the laser (maximum CW power of 16 mW) and applying the relevant ND filters. The fluence was calculated by measuring the laser spot size using the standard knife edge technique[157]. From here, the approximate density of photons incident per pulse was calculated, and an approximation of the initial minority carrier density and the carrier density decay trace was made. In the illustrative perovskite sample case, the effective power was 4.27 µW. From the obtained laser spot width of 2 µm, and f_{RR} = 500 kHZ, the fluence was calculated to be 0.1359 mJ/cm^2. With the corresponding perovskite thickness, W_{pvk} = 622 nm, and knowing that 80% of the incident photons are absorbed (as measured from UV-Vis and PLQY), this means that the approximate generated charge carriers at time t = 0 s would be approximately 4.25 × 10^{18} cm^{-3}. The decay of carriers over time could then be related to

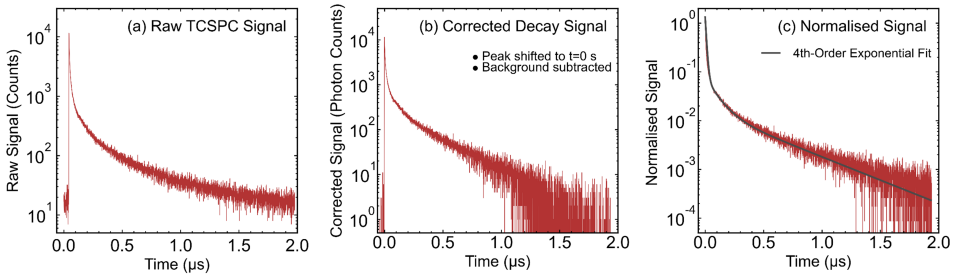

Figure 2.7: (a) The raw TCSPC signal of the bare perovskite film on glass. The noise floor is evident as the signal before the peak and the signal at the end are both greater than zero. The peak PL is also positioned at time t > 0 s. (b) The TCSPC signal after the signal is zeroed along the time-axis and the noise floor is subtracted from the decay. (c) The corrected signal after normalization. The applied high-order exponential fit that was then used to calculate the differential lifetime is also shown in gray.

the PL emission as under high injection levels, the PL $\propto n^2$.
The PL decay as a function of carrier concentration is shown in Figure 2.8a. The low injection to high injection transition is visualized from where the PL $\propto$ n (Figure 2.8b) changes to where PL $\propto n^2$ (Figure 2.8c). This transition point supports the extracted value of $N_A \sim 10^{17}$ cm^{-3}. An estimation of the low injection carrier lifetime ($\tau_{\text{eff}} \approx \tau_n \approx 130$ ns) was determined by fitting a biexponential function to the low injection level region of the PL decay. Based on the earlier point of discussion, if we allow for a 20% uncertainty in this value, then a reasonable estimation range of the electron carrier lifetime would be 104 ns $< \tau_n <$ 156 ns. Taking the lower lifetime limit, this approximation implies a slight asymmetry in the charge carrier lifetimes, where if the sum of the electron and hole lifetimes is indeed approximately 196 ns, then $\tau_p \approx 92$ ns.

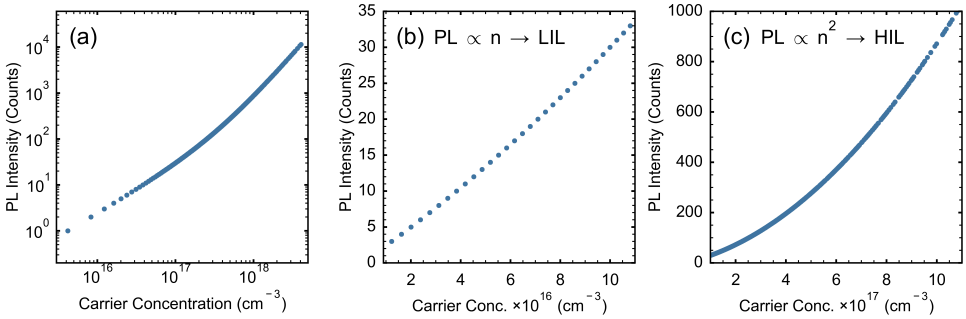

Figure 2.8: (a) The PL decay as a function of carrier concentration. (b) The PL decay scales linearly at carrier densities below ~ 10^{17} cm^{-3}, signifying that the sample was under the low injection level (LIL) regime at this point. (c) The PL decay scales quadratically at carrier densities above ~ 10^{17} cm^{-3}, signifying the high injection level (HIL) regime.

Photoluminescence Quantum Yield

The PLQY of each sample was obtained using a home-built optics setup containing a coupled supercontinuum laser, integrating sphere, 50:50 beam splitter, beam monitor photodetector, reflection photodetector, transmission photodetector (each linked to a separate lock-in amplifier), NIR objective and a 3D piezo stage mounted inside the integrating sphere. The system configuration and details are described in our previous work[158].

The PLQY of each sample was obtained by taking 40 µm × 40 µm maps at 200 nm pixel steps, and averaging the PLQY across the entire map. The laser was set to 620 nm and pulsed on the sample at a repetition rate of 20 kHz. With the system, the absolute incident flux, emitted PL flux (therefore absorptance and PLQY) were tracked and mapped. Typical maps using this measurement are shown in Figure 2.9.

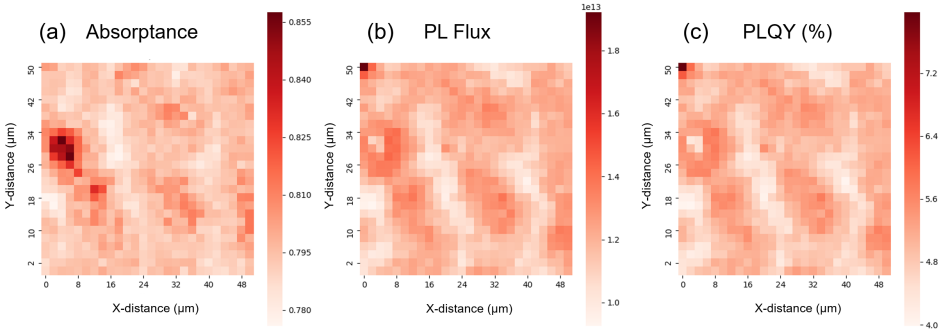

Figure 2.9: The (a) absorptance, (b) PL emission and (c) PLQY maps obtained for the unencapsulated perovskite on glass sample. Note: the high PLQY in the top left pixel is a consequence of photobrightening before the measurement started, therefore this pixel was omitted when determining the average PLQY.

Solar Cell Characterization

The light JV curves for all solar cells were measured in the glovebox using a Keithley 2401 SMU and a G2V Pico LED solar simulator under standard AM1.5G test conditions. The photoactive area of each solar cell was defined using a photomask such that the effective solar cell area was 6.25 mm^2. A cyclic (combined forward and reverse) scan was run for each cell from -1.3 V to 0.3 V in 301 steps, with a 1 ms step delay. Dark JV scans were subsequently obtained for each cell under the same sweep conditions.

In addition to extracting the standard JV parameters, approximate series and shunt resistances of the devices were obtained by calculating tangents to the curves near the J_{SC} and V_{OC} limits (Figure 2.10a). The exceedingly low shunt resistance obtained for the Spiro-based sample indicates that there is some major alternative carrier pathway that is limiting the device performance and indeed is why Spiro is not commonly applied in pin single junction cell configurations. Focusing specifically on on the difference between the

PTAA-based and 2PACz-based contacts, the series resistance was resolved as a function of applied potential by:

$$R_s(V) = \frac{V_{dark} - V_{light}}{J_{SC}} \tag{2.15}$$

The results of which are shown in Figure 2.10b[159]. By further comparing the current density in the light minus the short-circuit current density ($J(Vl) - J_{SC}$) with the dark current density ($J(Vd)$), one can identify whether shunts appear as a consequence of applied light. We visualize the differences in the curves for PTAA-based and 2PACz-based cells in Figures 2.10c and 2.10d, respectively. In the 2PACz case, the shunt is clear in both the dark and under illumination, signifying that there likely is a problem with an incomplete 2PACz film, or something else that is light-independent. Interestingly, the PTAA-based device exhibits a photoshunt only, which corresponds to slow charge extraction occurring at J_{SC} – this therefore can be translated to a low hole mobility in the PTAA layer itself, a low electron mobility in the C_{60} film, or both.

The JV curves in the light were also fitted the ideal diode equation to verify the resistances and to extract the ideality factor for the cells:

$$J = J_{SC} - J_0\left[\exp\frac{V + JR_s}{n_{id}V_{therm}} - 1\right] - \frac{V + JR_s}{R_{sh}} \tag{2.16}$$

For the PTAA-based cells, the ideality factor, $n_{id} = 1.83$, for Spiro-based cells, $n_{id} = 1.44$, and for the 2PACz-based cells, $n_{id} = 2.5$.

The devices were stored under inert conditions (in a nitrogen-filled glovebox in the dark) for four months and were then remeasured. Figure 2.11a shows the JV of the same PTAA-based cell as presented in Figure 2.10a, measured after it had been aged. Upon comparison, the aged cell's efficiency was measured to be 83.2% of the starting efficiency (the efficiency dropped from 12.5% to 10.4%). The reduction in the overall efficiency is predominantly the consequence of a significant further decrease in the measured short circuit current density (from 17.3 mA/cm^2 to 15.04 mA/cm^2) rather than from substantial changes in the open-circuit voltage (from 1.087 V to 1.066 V) or in the fill-factor (from 0.667 to 0.646).
External quantum efficiency (EQE) spectra were obtained using the same setup that had been used to measure the JV curves, but by sweeping individual LED channels and measuring the current. The spectra were determined both with and without a white light bias while the incident photon flux was monitored using a calibrated power meter and further referenced against a silicon reference cell. The corresponding EQE spectrum of the solar cell presented in Figure 2.11a is shown in Figure 2.11b. The ~13% difference in the J_{SC} when extracted from the EQE compared to the JV measurement falls within the expected variability between JV curves and EQE spectra for perovskite solar cells; differences are generally between 10-20% for such devices[160].

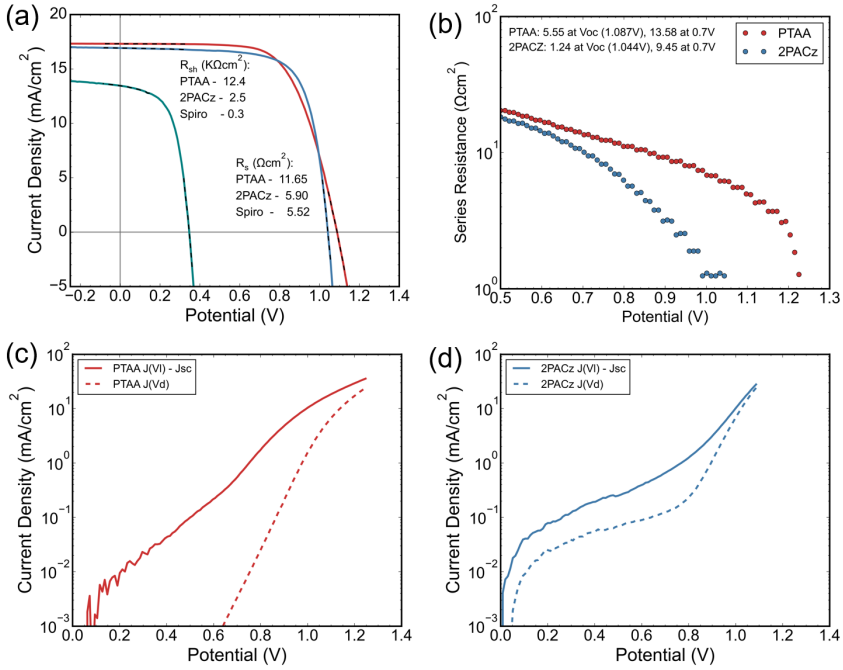

Figure 2.10: (a) Extracting values for the series resistance and shunt resistance for each of the three tested device configurations. (b) Series resistance as a function of applied potential for the 2PACz-based (blue) and PTAA-based (red) cells. (c) Plotting the current density in the light minus the short-circuit current density (solid line) with the dark current density (dashed line) for the PTAA-based cell. (d) Similarly showing the current density differences under light and in the dark for the 2PACz-based cell.

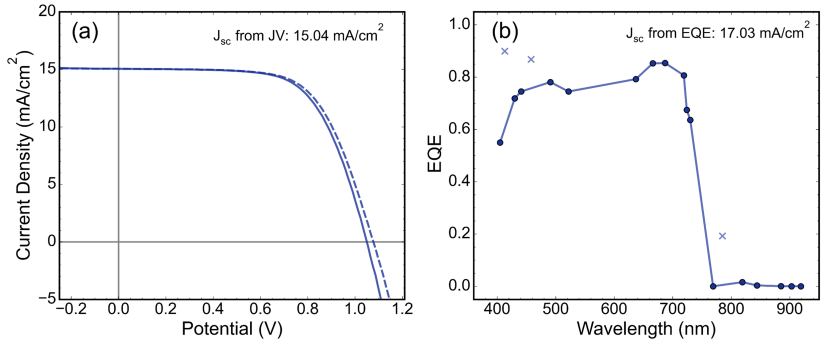

Figure 2.11: (a) *JV* curve of an aged PTAA-based solar cell, measured 4 months after fabrication. The device was stored under inert conditions in the dark between fresh and aged measurements. (b) The corresponding EQE spectrum for the same cell also measured 4 months after fabrication. The J_{SC} extracted from the EQE spectrum was obtained by integrating the data along the solid blue line. The crosses indicate the experimental outliers not considered in the J_{SC} determination.

Supplementary Characterization

XRD signals were recorded using a Bruker D2 Phaser with a Cu Kα tube. These diffractograms of all substrate-contact-perovskite samples are shown in Figure 2.12.

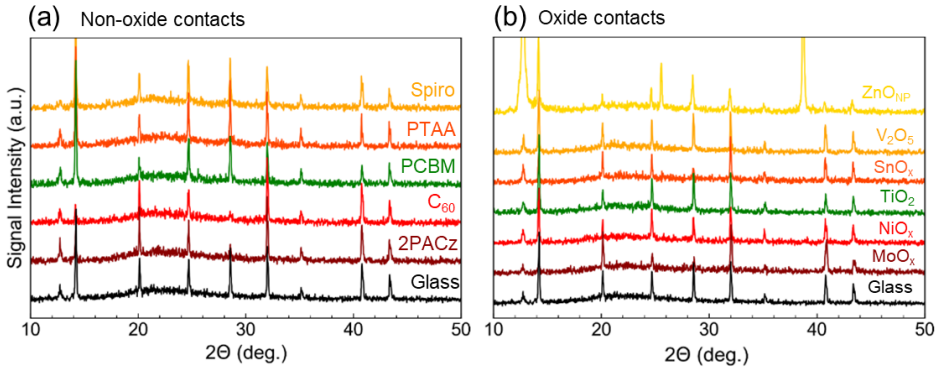

Figure 2.12: XRD diffractograms obtained of the unencapsulated glass-contact-perovskite samples, separated into (a) the non-oxide based contacts and (b) the oxide based contacts.

Absorbance spectra were obtained using a PerkinElmer LAMBDA 750 UV/Vis/NIR Spectrophotometer. PL spectra were collected using a coupled WITec alpha300 SR confocal imaging microscope and a Thorlabs S1FC405 405 nm CW diode laser. The absorbance and PL spectra of the same samples as for the XRD diffractograms are shown in Figure 2.13. For clarity, only the samples that are visibly different from the reference spectrum (perovskite on glass, in black) are labeled. The Tauc procedure was applied to determine the perovskite band gap in every case (E_g of the perovskite on glass reference was 1.596 eV). The fitted band gaps, in addition to the percentage absorptance, and percentage PLQY for the 11 samples in Figure 2.13a are tabulated in Table 2.1.
Scanning electron microscopy images were obtained using a Thermo Fischer Scientific Verios 460 SEM. Sample SEM images are shown in Figure 2.14.

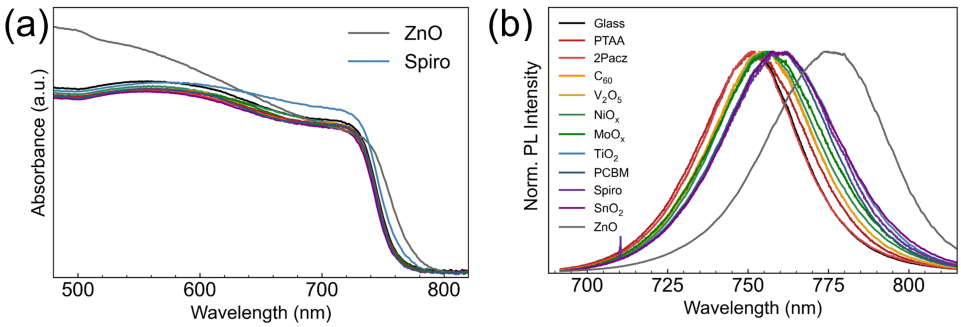

Figure 2.13: (a) Absorbance and (b) PL spectra obtained for the same samples as shown in Figure 2.12.

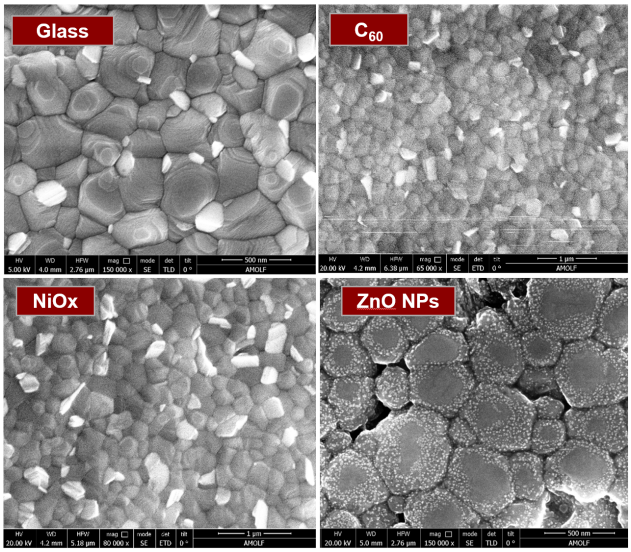

Figure 2.14: Top-view SEM images of the perovskite film on four different sublayers: glass, C_{60}, NiO_x, and ZnO nanoparticles.

It is evident that the samples containing ZnO nanoparticles are quite different to the perovskite on glass reference, shown by the >2.5% difference in measured band gap, excessive PbI_2 peaks shown in XRD and an unusual film structure as observed by SEM. We postulate that the nanoparticles or the ligands aid in passivating the grain boundaries with an excess of PbI_2, which increases the PLQY of the material. This in turn would increase the bulk lifetime of the perovskite film, though we argue likely not beyond the associated uncertainty of the obtained bulk lifetime of the perovskite reference. We include the ZnO nanoparticles in the main analysis to extract the SRV, because a higher than anticipated bulk lifetime would in turn mean that we obtain a surface lifetime that is lower than the true value. Therefore, the quoted SRV for ZnO nanoparticles is a reasonable conservative estimate for the true SRV in this particular case.

2.6.3. Surface Lifetime and Carrier Diffusion Length

As discussed in Section 2.3, the surface recombination velocity a proxy of the trap-assisted recombination rate at the surface; it is simply the boundary condition for trap-assisted recombination at the extremities of the film. In the bulk film, of course, the rate of recombination depends on the trap density per unit volume, N_T, the thermal velocity of the charge carrier, v_{th}, the carrier capture cross-section, σ_n (for electrons) or σ_p (for holes), and the excess minority carrier concentration, Δn (for p-type semiconductors). That is:

$$R_{\text{trap}} = \sigma_n v_{th} N_T \Delta n \tag{2.17}$$

At the surface, trap density is per unit area – hence the units of cm/s for SRV, and the associated use of the term “velocity”.

Table 2.1: Summary of measured band gap, absorptance and PLQY of 11 samples in the unencapsulated glass-contact-perovskite configuration as in Figure 2.4a. The statistical uncertainty of the extracted band gap was ±0.02 eV. The associated uncertainties of the absorptance and PLQY were on the order of ±0.05%.

Contact	E_g (eV)	Abs. (%)	PLQY (%)
Glass	1.596	79.65	5.71
NiO_x	1.600	81.44	9.69
TiO_2	1.597	79.77	3.09
V_2O_5	1.598	79.56	1.36
ZnO NP	1.556	82.14	14.58
SnO_x	1.600	77.03	6.25
Spiro-OMeTAD	1.582	85.46	3.84
PCBM	1.595	83.55	5.09
C_{60}	1.599	79.77	2.05
PTAA	1.598	81.60	2.81
2PACz	1.601	80.31	5.73

The surface lifetime naturally depends on both how carriers migrate to the surface (represented by the carrier diffusion coefficient, D) and by this surface recombination rate. The generalized solution of the surface lifetime can be described as $1/\tau_{surf} = \alpha_0^2 D$, wherein the solution is:

$$\tan \alpha_0 W = \frac{\alpha_0 D(S_1 + S_2)}{\alpha_0^2 D^2 - S_1 S_2} \tag{2.18}$$

Which has the approximate solutions of Equations 2.7 and 2.8 at the limiting cases of $S_1 \gg S_2$ and $S_1 = S_2$[35].
We argue that the omission of the second term in either of the limiting cases of Equation 2.7 or Equation 2.8 can only be justified at low surface recombination velocities. We plot percentage difference of the determined τ_{surf} based on whether we regard the second term to be negligible or not for the limiting cases of $S_1 \gg S_2$ and $S_1 = S_2$ cases in Figures 2.15a and 2.15b, respectively. These figures show that indeed at high SRVs, one cannot simply neglect the second term without first determining what the diffusion length and thereby diffusion coefficient would be for the perovskite. We further consider what influence the carrier diffusion length has upon the total effective carrier lifetime, for when L_d = 100 nm, 1 µm, 10 µm and for when $L_d \gg W_{pvk}$. The analytical results are shown for the two limiting cases in Figures 2.15c and 2.15d. In these calculations, it is assumed that the majority of carriers are generated near the center of the perovskite film. Hence, for low diffusion lengths, the generated carriers feel no influence on the surface and recombine as a consequence of bulk trap-assisted recombination only. Of course, this would increase the bulk lifetime, but would imply that effectively no carriers would be separated when the same film is implemented into a full device.

Importantly, we make the argument that the carrier diffusion length must be substantially

greater than the film thickness based on the differences in the measured effective lifetimes for perovskite films fabricated on the same substrate but with different top contacts. As in Figure 2.2a, the different top layers has little influence on the bulk lifetime, thus in each case we can assume that the bulk lifetime is the same. Specifically, we measured τ_{eff} ≈ 4 ns when C_{60} was evaporated as a top contact. This incredibly low effective lifetime is a consequence of the high SRV at the perovskite-C_{60} interface. However, for carriers generated at the center of the film, and assuming that the L_d would be at the maximum 1 µs, the effective lifetime would be approximately two orders of higher than what had been actually measured (Figures 2.15c and 2.15d). As we measure much lower lifetimes, this implies that the carriers generated closer to the center of the film are also limited by the C_{60} interface – therefore, the carrier diffusion length must be ~ 10 µm, rather than ~ 1 µm. In this sense, we can omit the diffusivity terms to simplify the relationship between the surface lifetime and SRV.

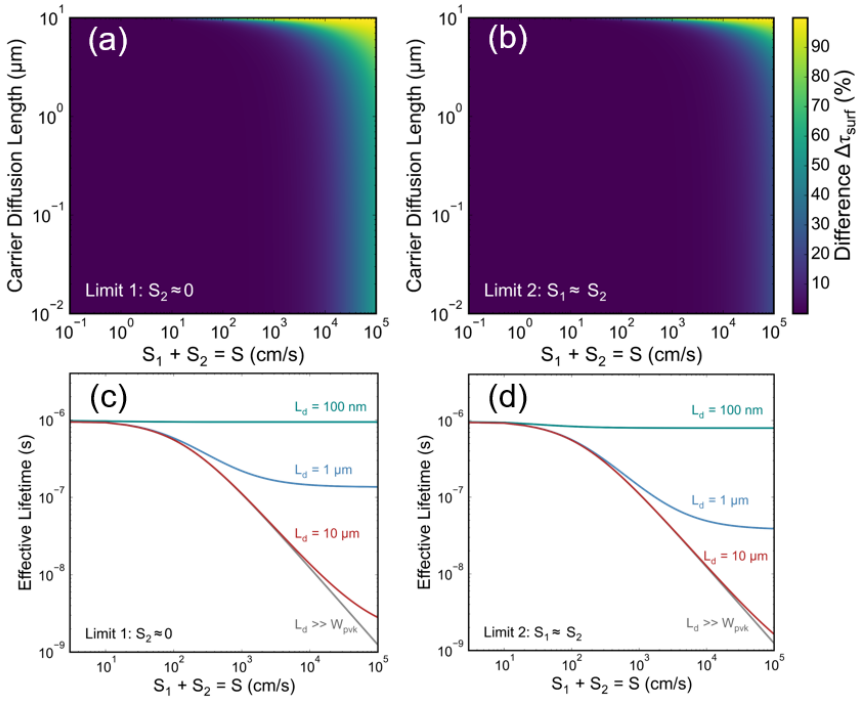

Figure 2.15: The influence of the carrier diffusion length and surface recombination velocity on the surface lifetime and the effective lifetime, for the specific case of when W_{pvk} = 622 nm, and when τ_{bulk} = 2 µs. (a) The percentage difference in the extracted τ_{surf} when the second term in Equation 2.7 is either included or excluded. (b) The same percentage difference, but when Equation 2.8 is applied rather than Equation 2.7. (c), (d) The effective carrier lifetime as a function of SRV for four specific cases of typical carrier diffusion lengths for the limiting cases of $S_1 \gg S_2$ and when $S_1 = S_2$, respectively.

However, for completeness, we also consider what the SRV differences would be if the transverse carrier diffusion length would be precisely that of the measured lateral carrier diffusion length, $L_d = 500$ nm. We argue that it is quite unlikely that the transverse L_d would be substantially shorter than the lateral L_d; thus the comparison tabulated below can be considered as a proxy for the associated uncertainty in the SRV and iV_{OC} values reported in this work (at the extreme limit). We show the SRV and the iV_{OC} differences for NiO_x and MoO_{xTE}, the respective lowest and highest SRVs plotted in Figure 2.2b. The accompanying iV_{OC} comparisons assume a perfectly passivating contact on the opposite side of the perovskite.

Table 2.2: Comparison of the extracted SRV and iV_{OC} values of NiO_x and MoO_{xTE} for when $L_d \gg W_{pvk}$ and when $L_d = 500$ nm.

	SRV, $L_d \gg W_{pvk}$ (cm/s)	**SRV, $L_d = 500$ nm (cm/s)**	**iV_{OC}, $L_d \gg W_{pvk}$ (V)**	**iV_{OC}, $L_d = 500$ nm (V)**	**ΔiV_{OC} (mV)**
NiO_x	144 ± 48	236 ± 55	1.273	1.267	6
MoO_x	24704 ± 11279	47800 ± 18483	1.162	1.145	17

2.6.4. Further Calculations on the Implied V_{OC}

Here, we briefly discuss the parameters used obtain the implied open-circuit voltages as a function of the SRV and separating the iV_{OC} loss components due to radiative, SRH and Auger recombination mechanisms.

$J_{0,rad}$ as derived in the detailed balance limit is dependent only on the variable properties of temperature and the material band gap[24]. The emission rate per photon energy (E) is given as:

$$b(E,T) \approx \frac{2\pi}{h^3c^2}E^2 \exp\left(\frac{-E}{k_BT}\right)\mathrm{d}E \tag{2.19}$$

Integrating this relationship over all energies gives the total photon emission rate and subsequently multiplying by the elementary charge yields the emission current density:

$$J_{0,rad} = qk_BT\frac{2\pi}{h^3c^2}\exp\left(\frac{-E_g}{k_BT}\right)[E_g^2 + 2k_BTE_g + 2(k_BT)^2] \tag{2.20}$$

The intrinsic carrier concentration, n_i was calculated using the expression that relates $J_{0,rad}$ to k_{rad}:

$$n_i = \sqrt{\frac{J_{0,rad}}{qW_{pvk}k_{rad}}} \tag{2.21}$$

To confirm the agreement between Equation 2.11 and Equation 2.12, we can substitute our calculated values into the generalized expression for the implied open-circuit voltage (Equation 2.22) and compare the extracted values for when the Auger recombination term is neglected (as in Equation 2.11) or included (as in Equation 2.12). This comparison is

straightforward as each of the terms in the generalized form has already been derived in the main analysis.

$$\mathrm{i}V_{\mathrm{OC}} = V_{\mathrm{OC,rad}} + V_{\mathrm{therm}} \ln\left(\frac{P_e k_{\mathrm{rad}} np}{n/\tau_{\mathrm{eff}} + P k_{\mathrm{rad}} np + C_{\mathrm{Auger}} n^2 p}\right) \tag{2.22}$$

At the negligibly low SRV limit ($\tau_{\mathrm{eff}} = \tau_{\mathrm{bulk}}$) and substituting in the values, $\mathrm{i}V_{\mathrm{OC}} = 1.293$ V when the Auger term is omitted – this is the same value that was obtained when Equation 2.11 was used. When the Auger term is included, $\mathrm{i}V_{\mathrm{OC}} = 1.283$ V, compared to 1.287 V as derived using Equation 2.12 (the small 4 mV difference is attributed to minor rounding errors between each of the two calculation methods). This simple comparison verifies the validity between both approaches in the determination of the $\mathrm{i}V_{\mathrm{OC}}$.

Lastly, we would like to remark upon the simplicity of comparing our implied open-circuit voltage calculations with experimentally determined open-circuit voltages in other works. As an example, we provide a brief but varied list of the measured V_{OC} values of various perovskite solar cells in Table 2.3. In this list, each perovskite has the same band gap, and each are of similar composition (triple-cation, mixed-halide of similar ratios), to the perovskite that was analyzed in this work. By assuming that these devices exhibit similar bulk and Auger losses to our own perovskite film, we identify varying degrees of additional losses that may be due to heightened surface recombination compared to what was found in this report. The losses may additionally be due to recombination beyond the perovskite's interface, suggesting possible extraction or contacting issues.
Furthermore, this brief summary highlights the V_{OC} differences when contacts are applied under their standard configuration versus their more unconventional configuration. Specifically, when applying Spiro-OMeTAD in the typical nip configuration (as listed in the table), the measured V_{OC} is substantially higher than when it is used as a HTL under the pin configuration, as in this work.

Table 2.3: A brief comparison of some experimentally determined open-circuit voltages with their corresponding implied open-circuit voltages calculated from the analysis in this work. We specifically selected device structures that we did not fabricate ourselves to highlight the wide applicability of the analytical process.

Configuration	**HTL**	**ETL**	**Reported V_{OC} (V)**	**iV_{OC} from this work (V)**	**ΔV_{OC} (mV)**	**Reference**
NIP	Spiro	TiO_2	1.13	1.22	90	[161]
NIP	Spiro	SnO2	1.15	1.21	60	[162]
NIP	Spiro	PCBM	1.13	1.23	100	[163]
NIP	PTAA	TiO2	1.03	1.22	190	[164]
PIN	NiO_x	C_{60}	1.07	1.16	90	[165]
PIN	PTAA	PCBM	1.12	1.21	90	[166]
PIN	V_2O_5	C_{60}	0.89	1.15	260	[167]

3

Key Signatures

Intensity-Modulated Photoluminescence Spectroscopy for Revealing Ionic Processes in Halide Perovskites

Mobile ions limit perovskite solar cell performance, yet quantifying ionic properties remains challenging. Frequency-domain electrical techniques are restricted to operational devices, and the resulting signals are often dominated by interfacial processes, which obscure ionic contributions. In this chapter, we introduce intensity-modulated photoluminescence spectroscopy (IMPLS) as a fully optical alternative, where the amplitude and phase of the photoluminescence intensity are measured as functions of the excitation modulation frequency. As a proof of concept, IMPLS is demonstrated on a $Cs_{0.07}(FA_{0.83}MA_{0.17})_{0.93}Pb(I_{0.83}Br_{0.17})_3$ *film. Fitting the data with an optical equivalent circuit (OEC) model reveals two characteristic lifetimes:* τ_{char} *= 2.1 ms and 77 s, likely corresponding to ionic defect formation and ion diffusion, respectively. The diffusion feature is consistent with intensity-modulated photocurrent/photovoltage spectroscopy (IMPS/IMVS) measurements on corresponding full devices. Importantly, this chapter highlights how IMPLS enables contact-free characterization of slow processes in all perovskite sample types – including films and devices – thereby significantly expanding the techniques available for understanding mobile ions in these materials.*

This chapter is based on:

Sarah C. Gillespie, Agustin O. Alvarez, Jarla Thiesbrummel, Veronique S. Gevaerts, L.J. (Bart) Geerligs, Bruno Ehrler, Gianluca Coletti, and Erik C. Garnett. Intensity-Modulated Photoluminescence Spectroscopy for Revealing Ionic Processes in Halide Perovskites. *ACS Energy Letters* **10**, 3122-3131 (2025).

Author contributions:

SCG fabricated the perovskite samples, performed all measurements and analyses beyond IMPLS and wrote the manuscript. SCG and AOA performed the IMPLS measurements; AOA developed the OEC model. JT fabricated the devices. VSG, LJG, BE, GC and ECG provided supervision. All authors contributed feedback on the manuscript.

3.1. Introduction

Perovskite solar cells have shown rapid improvement in power conversion efficiency, reaching values comparable to those of silicon solar cells[168, 169]. However, their widespread commercialization is still hindered, predominantly due to the instability of the perovskite material itself[170, 171]. While many of the external instability issues, such as heat- and moisture-induced degradation, can largely be prevented through effective device engineering and encapsulation strategies[172–175], the intrinsic perovskite instability – arising from ion migration within the perovskite film and ionic reactions at the interfaces – cannot be easily mitigated[25, 176–178]. At the same time, this ionic reactivity is often reversible and not always detrimental to the overall device performance. Ionic reversibility can often lead to perovskite healing and even performance enhancements in some cases[54, 179, 180]. Moreover, the influence of moving ions is pivotal in the wider application of perovskite materials in other technologies, such as in transistors, artificial synapses and self-tracking solar concentrators[181–184]. Ionic effects can be observed over a large range of timescales, from milliseconds to hours, and up to even years; understanding the influence of ions is therefore crucial for optimizing stability while also exploiting the self-healing effects in perovskite solar cells, LEDs and all other perovskite applications[53, 75, 82].

There are various electrical techniques, both in the time and frequency domains, to characterize ions in metal halide perovskites. Probably the most well-known technique in the frequency domain is impedance spectroscopy (IS), with additional methods including intensity-modulated photovoltage spectroscopy (IMVS), intensity-modulated photocurrent spectroscopy (IMPS) and capacitance-voltage (CV) measurements[70, 75, 76, 185]. Corresponding techniques in the time domain include transient (photo)current, transient (photo)voltage and transient capacitance techniques[72, 186, 187]. However, each of these methods – indeed, all electrical characterization methods – are inherently limited by their requirement for electrical contacts, restricting their applicability to operational devices. The electrical response can be strongly influenced by the contacts and interfaces, making it challenging to disentangle the intrinsic properties of the perovskite film from the overall device measurements[72, 82, 83]. Recently, it has been shown that combining these techniques on transport-layer free devices may elucidate properties such as mobile ion densities and activation energies, but chemical reactions and electrical effects at the contacts still remain[48]. Furthermore, these methods are unsuitable for non-electrical perovskite technologies, such as phosphors for next-generation LEDs and down-conversion systems[188, 189]. These techniques similarly cannot be applied as in-line characterization tools for each step of device fabrication processes in pilot lines and factories[190].

Alternatively, there are various purely optical characterization techniques which can be applied to study perovskite thin films, half-stacks of devices, nanocrystals and other samples. One of the most popular among these techniques is time-resolved photoluminescence spectroscopy (TRPL), where the PL decay is tracked immediately after an optical excitation pulse, as described in **Chapter 2**. However, due to constraining factors in typical TRPL systems, including that the repetition rates are typically limited to high frequencies in single photon counting setups, this method is only useful for measuring

relatively fast processes, such as electronic carrier recombination and diffusion, rather than capturing slower ionic processes or chemical reactions[13, 29, 191]. Even using TRPL systems with a high dynamic range, such as gated charge-coupled devices, the captured carrier lifetimes have thus far only been on the order of hundreds of microseconds – much shorter than typical characteristic lifetimes of ionic processes[13, 53, 75]. PL changes can also be tracked in time under continuous illumination which can provide qualitative insight into, for example, iodide interstitial migration rates and halide phase segregation rates in mixed halide systems. However, over the PL time-series, it is difficult to isolate and quantify any single process; understanding the various entangled processes which overlap in time typically requires several supplemental techniques[41, 67, 68].

In this work, we introduce and validate a purely optical measurement technique in the frequency domain that enables the characterization of slow processes particularly in metal halide perovskites. We call this method intensity-modulated photoluminescence spectroscopy (IMPLS). Just as impedance spectroscopy is considered the frequency-domain counterpart to transient current or transient voltage measurements, or as IMPS is to transient photocurrent, IMPLS can be viewed as the frequency-domain analog of TRPL and PL time-series measurements[70, 186].

3.2. Modulated Techniques

Modulated methods (IS, IMVS, IMPS and more) broadly rely on applying an input signal to the device consisting of a small sinusoidal perturbation (AC) superimposed on a steady background (DC). The amplitude of the response signal and the relative phase shift between the input and response are then measured across relevant frequencies. The main difference between each of the modulated techniques is simply which property is perturbed and which is measured[77]. These methods are compared in Table 3.2 in the Supporting Information (Section 3.8) at the end of this chapter.

In IMPLS, the input signal is optical excitation above the sample's band gap. The excitation is provided by a light source with a fixed background intensity, $\bar{\phi}_{\text{exc}}$, and a small modulated intensity, $\tilde{\phi}_{\text{exc}}$. The total illumination intensity is then:

$$\phi_{\text{exc}} = \bar{\phi}_{\text{exc}} + \tilde{\phi}_{\text{exc}} \tag{3.1}$$

The measured property in IMPLS is the photoluminescence emission from the sample, ϕ_{em}, which similarly consists of both an AC and a DC component:

$$\phi_{\text{em}} = \bar{\phi}_{\text{em}} + \tilde{\phi}_{\text{em}} \tag{3.2}$$

During a measurement, both the excitation and PL signals are tracked in time for a number of cycles at a fixed frequency, f. From the tracked data, the DC offsets and the amplitudes of both the excitation and emission signals ($|\tilde{\phi}_{\text{exc}}|$, $|\tilde{\phi}_{\text{em}}|$), along with the relative phase shift between these signals (θ), can be determined. This measurement is then repeated over the entire relevant frequency range. The parameters are visualized in Figure 3.1a.

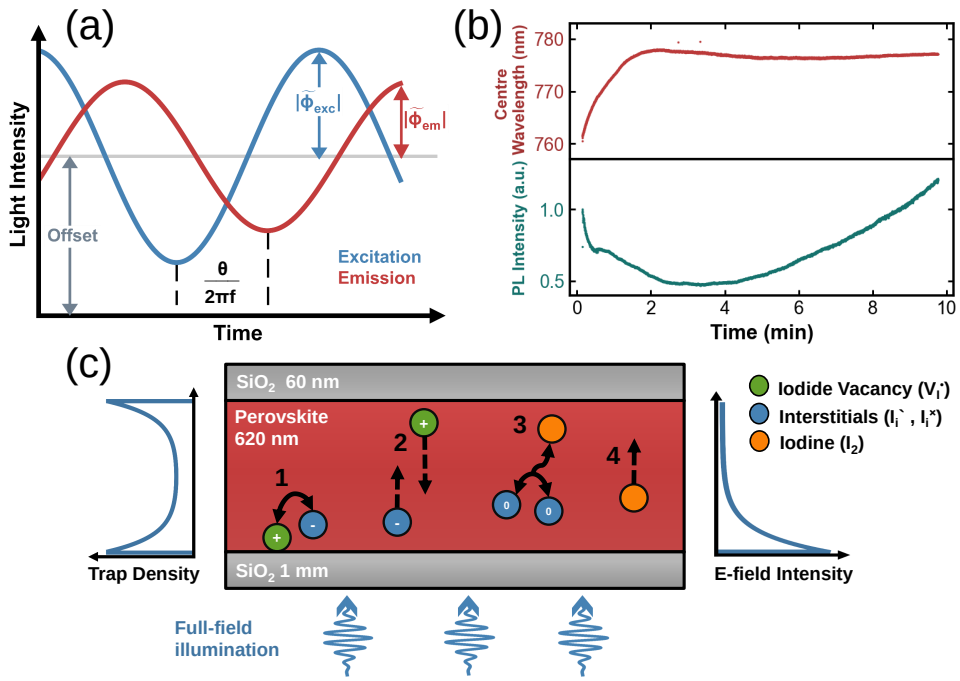

Figure 3.1: (a) Conceptual illustration of IMPLS. The schematic shows the tracking of excitation (blue) and emission (red) intensities over time at an arbitrary frequency. The key extracted parameters include the DC offset intensity for both signals, their amplitudes ($|\widetilde{\phi}_{\text{exc}}|$, $|\widetilde{\phi}_{\text{em}}|$), and the relative phase shift (θ) between them. For readability, the DC offsets are scaled to the same intensity value. (b) Tracking of the PL center-wavelength (top) and integrated PL intensity (bottom) of a SiO_2-encapsulated $Cs_{0.07}(FA_{0.83}MA_{0.17})_{0.93}Pb(I_{0.83}Br_{0.17})_3$ thin film under continuous illumination for 10 minutes. (c) Simplified schematic of various ionic processes occurring in halide perovskite films under illumination[41, 69]. (1) Reversible formation and recombination of $V_I^{\bullet}/I_i'$ Frenkel pairs; (2) diffusion of mobile ion species, where I_i' interstitials ($V_I^{\bullet}$ vacancies) are repelled from (attracted to) the surface[41]; (3) reversible formation of iodine (I_2) via recombination of uncharged iodine interstitials ($I_i^{\times}$)[69]; (4) iodine diffusion to the surface. Other mechanisms not depicted include atmospheric reactions and halide segregation[68, 192].

In electrically modulated methods, the data is commonly presented using either Bode plots or Nyquist plots[75]. In Bode plots, properties such as the amplitude, phase and capacitance are plotted against the modulating frequency. In Nyquist plots, the imaginary component of the data is plotted against the real component – for which a transfer function must be defined. Here, we define the IMPLS transfer function, P, to be proportional to the AC equivalent of the photoluminescence quantum yield ($\widetilde{\text{PLQY}}$; assuming constant absorptance)[193]:

$$\text{P} = \frac{\widetilde{\phi}_{\text{em}}}{\widetilde{\phi}_{\text{exc}}} \propto \widetilde{\text{PLQY}} \tag{3.3}$$

Expanding the transfer function to resolve the real and imaginary components results in

$$\mathrm{P} = P' + iP'' = \frac{|\widetilde{\phi}_{\mathrm{em}}|}{|\widetilde{\phi}_{\mathrm{exc}}|}\exp(i\theta) = \frac{|\widetilde{\phi}_{\mathrm{em}}|}{|\widetilde{\phi}_{\mathrm{exc}}|}\big(\cos\theta + i\sin\theta\big) \tag{3.4}$$

It is conventional in IS, IMVS and IMPS to plot the negative of the imaginary component on the y-axis[194]. To maintain consistency, we present all IMPLS Nyquist plots as $-iP''$ against P'.

Modulated PL is not a new concept; a high-frequency variation of modulated PL has previously been applied as a means to extract the minority carrier lifetime in silicon wafers, where the relative phase shift between carrier generation and relaxation depends on the carrier lifetime[92, 93, 195, 196]. A related technique known as frequency-resolved spectroscopy has also been applied to measure the electronic lifetimes in amorphous silicon and chalcogenide glasses[197–200]. More recently, a theoretical model was developed that enables additional parameters, such as surface recombination velocities, to be determined from modulated PL data obtained for Cu(In,Ga)Se_2 (CIGS) semiconductors[94, 201].
To date, IMPLS has not been applied to investigate ionic, chemical or any other relatively slow process in metal halide perovskites, as we propose to do so here. These slow ionic and chemical effects are observable through PL time-series measurements[41, 69, 202, 203]. As shown in Figure 3.1b, we observe complex PL dynamics on a silicon-oxide (SiO_2)-encapsulated high-performance halide perovskite thin film with a chemical composition of $Cs_{0.07}(FA_{0.83}MA_{0.17})_{0.93}Pb(I_{0.83}Br_{0.17})_3$ (sample fabrication and characterization details are listed in Section 3.8). The PL dynamics observed over a period of 10 minutes of continuous illumination include a red shift in the PL peak wavelength, and competing photobrightening and photodarkening processes. Proposed mechanisms for various slow PL processes include Frenkel pair formation and annihilation, ion migration, reversible interfacial passivation due to the atmosphere, reversible iodide formation within the film, formation of superoxide species, morphological influences and many more[41, 68, 69, 192, 204–208]. As we are measuring a fully encapsulated perovskite film in a N_2 atmosphere in this work, we do not consider atmospheric effects to play a dominant role in the measured PL behavior. Rather, these features are more likely the result of a combination of ionic defect formation, annihilation and diffusion events (Figure 3.1c). Since these processes can be observed with PL in the time domain, they should also be observable in the PL frequency domain. Low-frequency IMPLS should therefore enable the extraction of key ionic properties, such as diffusion rates and accumulation times.

3.3. Experimental Proof of Concept

To validate IMPLS, we performed a proof-of-concept measurement on the same encapsulated perovskite film as described before. Figure 3.2a shows a schematic of the system used to measure IMPLS, which was housed inside a nitrogen-filled glovebox. A 465 nm LED was used as the excitation source and a 650 nm long-pass filter was used to block the LED light from being detected by the photodiode. The LED DC illumination power density was set to approximately 10 mW/cm^2 and the AC modulation amplitude was set to 10% of its DC intensity. All IMPLS measurements consisted of running 15 sinusoidal waves of light emission from the LED at a fixed frequency, while simultaneously recording the LED current (j_{LED}) and photodiode current (j_{PL}) before moving to the next frequency point. We exemplify this procedure by plotting the LED and photodiode currents for four of the 15 cycles at f = 100 Hz in Figure 3.2b.

Before measuring the perovskite sample, two reference measurements were performed. First, the system response was determined by measuring the photodiode current directly against the LED current (represented by the solid gray line in Figures 3.2c and 3.2d). Then, the extent of light leakage through the long-pass filter was determined by measuring the photodiode current against the LED current when only the long-pass filter was placed in the path between them. The results of both references for modulating frequencies up to 1 MHz are shown in Figure 3.7. Since there is no measurable system or leakage response between 1 kHz and 1 Hz, any processes observed within this frequency range must originate from the sample. At frequencies below 1 Hz, a small phase response is measured (Figure 3.2c), but as the amplitude response remains unchanged in this range (Figure 3.2d), the dominant sample response can be distinguished from this minor system contribution.
The perovskite thin film was then measured; the results of the IMPLS measurement are shown in the phase and amplitude Bode plots in Figures 3.2c and 3.2d, respectively. The corresponding IMPLS Nyquist curve, calculated using Equation 3.3, is visualized in Figure 3.2e. Two distinct features, shaded in red and blue in the phase plot, indicate that at least two dynamic processes are captured in this measurement. The approximate characteristic frequencies of these processes are at 100 Hz (red) and 10 mHz (blue). For now, we will refer to these processes simply as the “fast process” (100 Hz) and the “slow process” (10 mHz) in our sample. Figure 3.8 shows that the fast process quenches under prolonged light exposure times. Therefore, to analyze the processes individually, the IMPLS measurement was separated into two parts, where the processes were independently probed and demonstrated reversibility (Figure 3.9). This requirement of reversibility follows from the analogy with IS, where a process must remain stable while it is probed to ensure the data can be fitted to appropriate models[209]. More information on these measurements is provided in Section 3.8.

3.4. Optical Equivalent Circuits to Model IMPLS

To quantify the observed processes, an optical equivalent circuit (OEC) model was developed and applied to separately fit the fast and slow processes. Equivalent circuit models have been used extensively in modulated electrical techniques (IS, IMPS, IMVS) to pro-

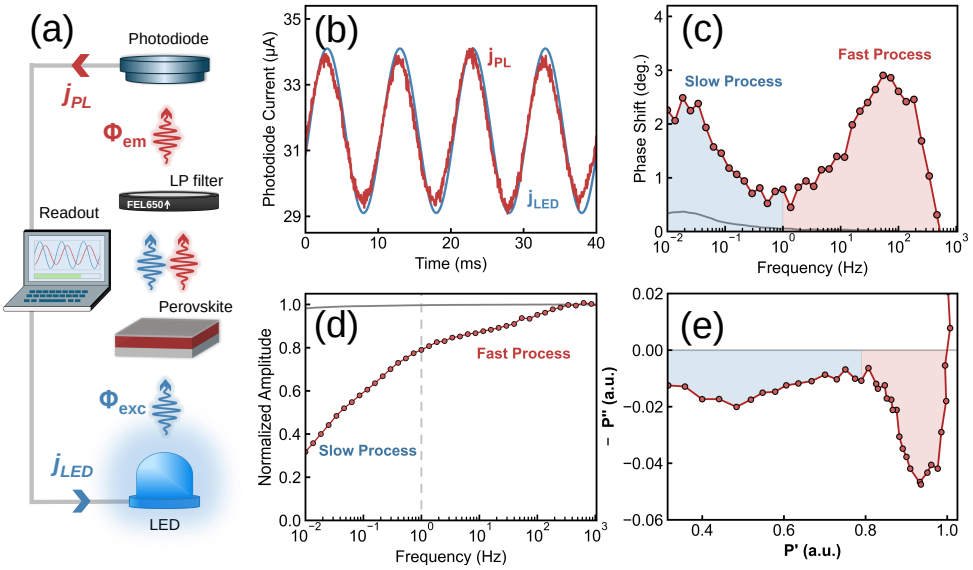

Figure 3.2: (a) The IMPLS experimental setup used in this work is housed inside a nitrogen-filled glovebox. (b) The measured photodiode current (red) resulting from the PL, plotted over the LED current (blue) for four sine wave cycles at a modulating frequency of 100 Hz. The LED current is scaled for readability. (c) The relative phase shift between the PL and the LED for frequencies ranging from 10 mHz to 1 kHz (red) and the relative phase shift of the system response (gray). (d) The corresponding amplitude of the PL intensity (red) and of the system (gray) for the same frequency range. (e) The amplitude-normalized Nyquist plot generated from the amplitude and phase data of the perovskite (note: for clarity, this exemplary Nyquist plot is not scaled 1:1; however, all subsequent Nyquist plots in this work are scaled 1:1).

vide a deeper understanding of the underlying processes[75, 77]. Although we do not have electrical contacts, we can still use the optical emission as a proxy for the electrical circuit. This is done extensively in photovoltaics in a common measurement known as Suns-iV_{OC}[210–212]. In that case, the excitation intensity is a proxy for the current of the device and the PL intensity is a proxy for the voltage, since both rely on the ratio between radiative and non-radiative recombination. Here, we also equate the excitation intensity to the generated current, represented by the current generator element (blue) in Figure 3.3a, and use a combination of resistors and inductors across different branches to represent the various recombination processes in the perovskite.

Before applying the optical equivalent circuit model in Figure 3.3a to fit the IMPLS data, we will first walk through the physical interpretation of this model for different modulating frequencies. At sufficiently high frequencies, all of the “current" flows only through the high-frequency (HF) branch, which contains one resistor, R_{HF}. This resistor represents all of the carrier recombination processes – radiative recombination, Auger recombination and trap-assisted recombination – which are frequency-independent for the frequency window relevant to this work. In other words, the corresponding carrier lifetimes of these

processes (τ_{rad}, τ_{Auger}, τ_{trap}) are much shorter than the measurement range (denoted by the frequency f_{range}) of our setup:

$$\frac{1}{2\pi f_{range}} \gg \tau_{rad}, \tau_{Auger}, \tau_{trap} \tag{3.5}$$

This is a valid assumption as the highest frequency of interest in our measurements is f = 1 kHz (corresponding to a lifetime of 159 µs), and we have previously determined in **Chapter 2** that the effective trap-assisted carrier lifetime of this perovskite material is approximately three orders of magnitude shorter, $\tau_{trap} \approx 200$ ns[29].
As the modulating frequency is reduced, the "current" can also pass through the low-frequency (LF) branch. The relevant frequency at which this occurs is determined by the values of the low-frequency resistor (R_{LF}) and of the inductor (L), using the relationship:

$$\tau_{char} = \frac{1}{2\pi f_{char}} = \frac{L}{R} \tag{3.6}$$

Where f_{char} is the characteristic frequency of the process and τ_{char} is the corresponding characteristic lifetime. Whether this frequency-dependent pathway increases or reduces the PL depends on the nature of the process itself – for example, formation or annihilation of Frenkel pairs will either decrease or increase the PL, respectively[41, 204].
The OEC shown in Figure 3.3a was applied to fit to the IMPLS data collected for the fast process in Figure 3.12. The amplitude was normalized so that the value of R_{HF} = 1, allowing for the relative losses due to the LF branch to be quantified. The fits of the Nyquist, amplitude and phase plots of the reverse scan are shown in green in Figure 3.3 (similar forward scan fits are shown in Figures 3.12c and 3.12d). The extracted quantities of the relative resistances (in arbitrary units) and the inductance (in seconds) of this process are summarized in Table 3.3. From these parameters, τ_{char} and f_{char} were determined using Equation 3.6. Averaging the values between the forward and reverse scans, $f_{char,fast}$ = 76±8 Hz, corresponding to a lifetime of τ_{fast} = 2.1±0.2 ms. The ratio between R_{HF} and R_{LF} provides insight into how many carriers recombine via the LF branch at sufficiently low frequencies. The ratio between these resistances is R_{HF}/R_{LF} = 0.135. This indicates that 13.5% of the total carriers in the system – that would otherwise recombine radiatively at high frequencies (via R_{HF}) – recombined non-radiatively through R_{LF} at times longer than the characteristic lifetime of 2.1 ms.

Table 3.1: Key parameters obtained from the fits of the relevant optical equivalent circuit models to the fast and slow processes.

Process	f_{char} (Hz)	τ_{char} (s)	R_{HF}/R_{LF} (%)
Fast	76±8	$(2.1\pm0.2)\times10^{-3}$	13.5
Slow	$(2.1\pm0.7)\times10^{-3}$	77±45	58.8

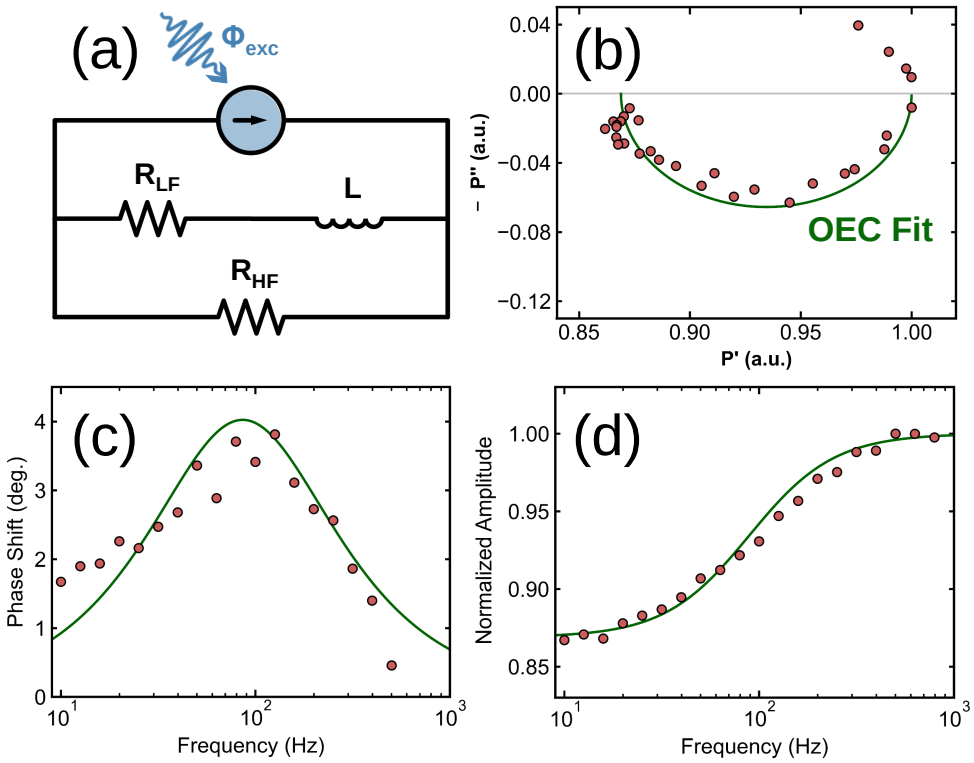

Figure 3.3: (a) The optical equivalent circuit model applied to fit the fast component of the IMPLS data. The resulting fit of the OEC model is shown in green in (b) the Nyquist plot, (c) the relative phase shift Bode plot and (d) the amplitude-normalized Bode plot.

To quantify the slow process, the OEC in Figure 3.4a was used to fit the blue curve shown in Figure 3.9. Unlike the ideal inductance-like behavior of the fast process (where the Nyquist arc is a perfect semicircle), the slow process exhibited non-ideal behavior. This is evident from the stretched Nyquist arc in Figure 3.4b[78]. The non-ideal inductor in this case is represented by L_α. Otherwise, the physical interpretation of the OEC is consistent with what was previously described. By extrapolating the fit (represented by the dashed green curves in Figure 3.4), we extract $f_{\text{char,slow}} = 2.1 \pm 0.7$ mHz, corresponding to a lifetime of $\tau_{\text{slow}} = 77 \pm 45$ s. The ratio between R_{HF} and R_{LF} for the slow process is much more substantial than the fast process, $R_{HF}/R_{LF} = 0.588$ – indicating that this is a significant loss process.

The remaining parameters obtained from the fit of the slow process are listed in Table 3.4, while key quantities are summarized in Table 3.1. The complete OEC diagram, which separates electronic processes from the fast and slow processes, is presented in Figure 3.11. Further discussion of OEC modeling is provided in Section 3.8.

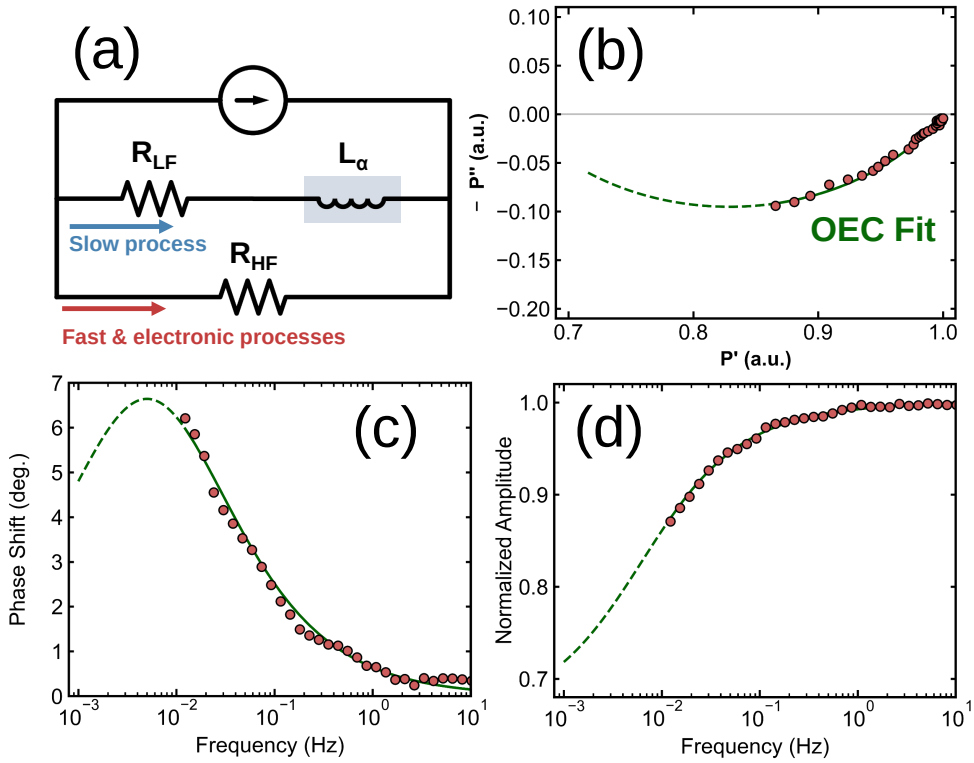

Figure 3.4: (a) The OEC applied to fit the slow component of the IMPLS data. The key difference between this OEC and the OEC applied to fit the fast process is the requirement of a non-ideal inductor (highlighted in gray) to account for the stretched Nyquist arc. (b) The Nyquist plot, (c) the relative phase shift Bode plot and (d) the amplitude-normalized Bode plot. The solid green curve in these panels represents the OEC fit to the data while the dashed green curve represents the extrapolation of the fit.

3.5. Mechanistic Insights

Considering the IMPLS-extracted characteristic frequencies, we tentatively propose that the mechanisms responsible for the fast and slow responses are likely the result of mobile ion or iodine species formation and diffusion. These mechanisms have already been proposed to describe the competing photobrightening/photodarkening PL features which have been observed in the time domain (Figure 3.1c)[41, 69, 204, 206]. In previous works, it has been postulated that the underlying driving force for the diffusion of mobile ion species is a consequence of the trap-state density distribution as a function of depth in the perovskite film (Figure 3.1c, left)[41, 204]. Under illumination, some traps of one type – particularly near the surface – are filled by the generated electronic carriers, leading to the formation of a light-induced electric field (Figure 3.1c, right). We similarly assume that during an IMPLS measurement, the superimposed AC and DC illumination from the LED generates a modulating electric field. As our sample is globally illuminated by

the LED, we further assume that this electric field is equally strong laterally and decays only along the transverse direction. If mobile ionic species are present in the sample (like those shown in Figure 3.1c), and if they diffuse through the entire film, we can calculate their diffusion coefficients using

$$D = W^2/\tau_{\text{diff}} \tag{3.7}$$

Where W is the thickness of the film (620 nm, measured with profilometry) and $\tau_{\text{diff}} = \tau_{\text{char}}$ in the case where diffusion is the rate-limiting step. The diffusion coefficient for the fast process would then be $D_{\text{fast}} = 1.8 \times 10^{-6}$ cm^2/s. However, based on the literature values for even the fastest diffusive species, halide vacancies, this coefficient is still several orders of magnitude higher than expected[48, 73, 82]. More likely, we anticipate that the fast process is related either to the light-induced formation of Frenkel defects, or to the formation of iodine species in the film[41, 69, 204]. Both of these are loss processes and consequently result in the reduction in the PL amplitude signal. This fast process therefore corresponds to the rapid initial drop in PL seen in the time domain (Figure 3.1b) upon illumination.

In contrast, the calculated diffusion coefficient of the slow process is $D_{\text{slow}} = 4.99 \times 10^{-11}$ cm^2/s. This value is consistent with literature values for the diffusion coefficient range for iodide vacancies in polycrystalline perovskite films, typically ranging from 10^{-10} – 10^{-12} cm^2/s[45, 48, 53]. It is therefore likely that we are observing the influence of iodide vacancies at the perovskite interface after they have diffused through the film. As the PL amplitude decreased for this process (corresponding to the slower PL reduction observed in the time domain in Figure 3.1b), it indicates that this interaction is a loss mechanism. This loss may result from the interaction of vacancies in the high trap-state density region at the interface, or potentially from vacancies screening other vacancies – preventing recombination with their corresponding iodide interstitials near the surface. The interpretation of the fast and slow processes as defect formation and diffusion, respectively, is also consistent with the ideal and non-ideal inductive-like behaviors observed in the corresponding OEC model; the physical interpretation of the ideal and non-ideal behavior is further described in Section 3.8. However, further investigation is required to fully elucidate the exact nature of these processes[78, 213].

3.6. Device Comparisons

From the experimental validation that IMPLS can resolve slower processes in perovskite films, we now consider its potential application as a contact-free diagnostic tool to fingerprint perovskite films for latent instability. Device degradation is predominantly a consequence of mobile ions creating carrier extraction barriers at the interfaces[25, 56, 57]. If IMPLS could indicate the presence of such effects prior to device fabrication, it would offer a valuable tool for optimizing both device stability and manufacturing processes. To assess this possibility, we examined whether the IMPLS responses observed above are similarly detectable in corresponding electrical measurements in perovskite solar cells. Full devices were fabricated using the same perovskite composition (Section 3.8.4 lists the device fabrication details). Figure 3.5a shows a representative device current density–voltage (JV) curve, from which a moderate device efficiency of 14.8% is calculated. The device exhibits inverted (inductive) hysteresis, which may tentatively be linked

to the inductive features observed in IMPLS[214]. Moreover, hysteresis in scan-rate-dependent IV measurements (Figure 3.14) suggests that mobile ions affect the device performance[52, 56]. However, such voltage scan-rate measurements are difficult to directly link to dynamic physical processes. As a frequency-domain alternative, we replicated IMPLS-like conditions by modulating the illumination of the full device using a 450 nm LED, with modulation frequencies ranging from 10 mHz to 100 Hz. The resulting IV curves (Figure 3.5b) reveal frequency-dependent variations which are more prominent at short-circuit current, I_{SC}, than at open-circuit voltage, V_{OC} (Figure 3.14c). Like the scan-rate dependent IV curves, this suggests that there is an induced mobile ion screening effect which also occurs under modulated light-soaking conditions.

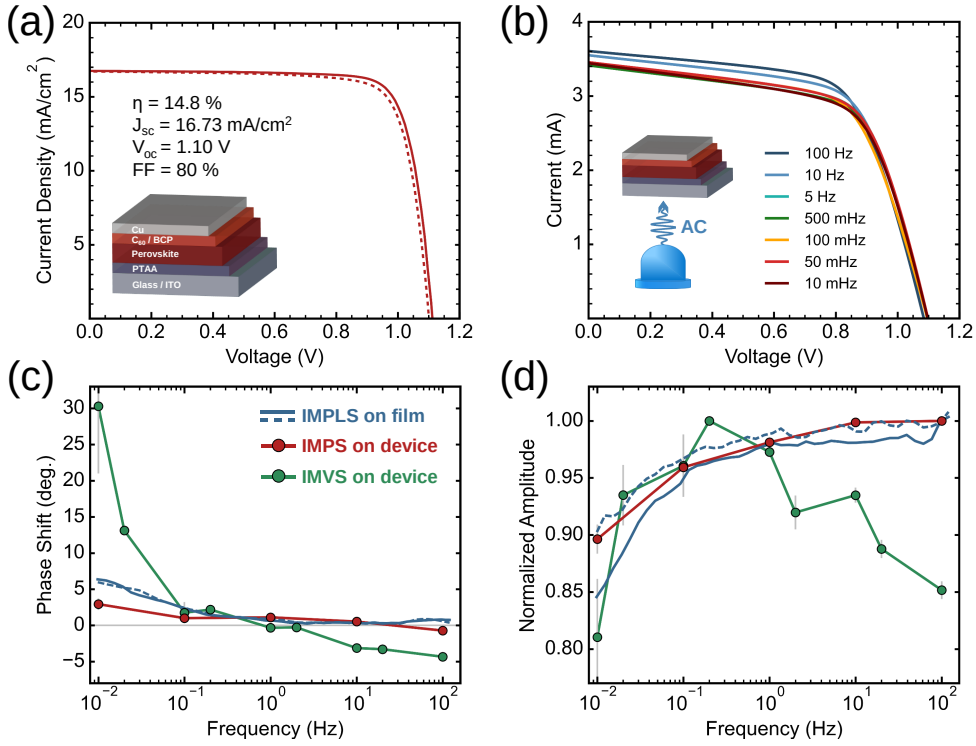

Figure 3.5: (a) JV curve of a representative perovskite solar cell measured under standard test conditions. The solid and dashed lines represent the forward and reverse scans. (b) Measured IV curves of an unmasked sample illuminated with a 450 nm LED. The IV curves were measured immediately after a modulated light-soaking treatment, where the LED was sinusoidally varied with modulation frequencies listed in the panel. (c) Comparison of the encapsulated perovskite film IMPLS phase shift (blue), the solar cell IMPS phase shift (red) and the solar cell IMVS phase shift (green). (d) Comparison of the normalized IMPLS amplitude (blue), IMPS amplitude (red) and IMVS amplitude (green). The light gray bars in (c) and (d) represent the associated error in the IMPS and IMVS measurements.

Given the strong current response in the device measurements, we performed IMPS at I_{SC}, and additionally measured IMVS at V_{OC} (as the PL intensity is directly related to the V_{OC})[89]. Figures 3.5c and 3.5d show the phase and amplitude responses of the IMVS (green), IMPS (red), and IMPLS (blue) measurements. Notably, all three techniques reveal inductive-like behavior at frequencies below 1 Hz. The amplitude responses from IMPS and IMPLS exhibit a particularly strong correlation across the entire frequency range, with a relative amplitude difference of less than 5% between them. This suggests that the low-frequency loss process identified in IMPLS may be linked to the same mobile ion screening mechanism responsible for reduced current extraction observed in IMPS. There is similarly a correlated reduction in the IMVS amplitude at low frequencies, which is expected based on the reduction in the IMPLS amplitude. Interestingly, the IMVS amplitude trend diverges from IMPLS/IMPS above 1 Hz. Additionally, the IMPLS phase measured for the complete device similarly follows the same trend as IMVS and IMPS at relatively higher frequencies (Figure 3.15a), while the amplitude deviation is also present in the solar cell IMPLS response (Figure 3.15b). These features signify that additional defect-related processes are occurring within the device which are absent in the symmetric SiO_2-encapsulated film. As only the contacts are different between the film and device, the defect formation is likely related to one or both of the electrical interfaces. While further investigation is required, the observed correlations highlight the promise of IMPLS as a contact-free screening method for perovskite device stability and performance.

3.7. Conclusion

In conclusion, we have presented IMPLS as a fully optical technique capable of quantifying and resolving ionic and other slow processes in metal halide perovskite materials. Through experimental validation of IMPLS on a SiO_2-encapsulated perovskite film, we demonstrated that in the 10 mHz to 1 kHz frequency range, at least two distinct loss processes occur within the material, likely corresponding to ionic species formation and mobile species diffusion to the perovskite interfaces. Additionally, we have shown that IMPLS data can be analyzed using an optical equivalent of the standard equivalent circuit model fitting procedure. The physical interpretation of this OEC model aligns with the carrier rate equation in the frequency domain, where frequency-dependent processes are represented by complex circuit components. Fitting IMPLS data to OEC models simplifies immediate data analysis, as standard EC models are already well-established in electrical analog techniques. Moreover, the interpretation of IMPLS data is simplified compared to electrical measurements as the influence of carrier extraction is eliminated, and interfacial recombination can be minimized by applying passivating contacts on either side of the film. However, IMPLS as a technique requires further benchmarking to confirm that the observed processes are indeed related to ionic species formation and diffusion, rather than other phenomena, such as slow chemical reactions at the interfaces. Temperature-dependent IMPLS measurements, combined with appropriate system modeling, could significantly enhance the interpretation and application of IMPLS in the near future.
From this foundational work, we postulate that IMPLS could eventually be applied to measure interfacial effects in halide perovskite devices by performing measurements at each step of the fabrication process – similar to sequential PLQY measurements, which are commonly used to quantify loss processes in many studies[25, 153, 215].

3.8. Supporting Information

3.8.1. Fabrication and Characterization of Perovskite Thin Films

The perovskite solution was prepared in a nitrogen-filled glovebox by separately dissolving PbI_2 (≥99.99%, TCI) and PbBr2 (≥98%, TCI) in 1.5 M solutions of DMF:DMSO (4:1) and stirring at 70 °C overnight. The PbI_2 solution was added to FAI powder (≥99%, TCI) with an excess of DMF:DMSO to achieve a 1.24 M solution of $FAPbI_3$ containing a 10%-molar excess of PbI_2. The $PbBr_2$ solution was added to MABr powder (≥99%, TCI) with an excess of DMF:DMSO to achieve a 1.24 M solution of $MAPbBr_3$, also containing a 10%-molar excess of $PbBr_2$. The perovskite solutions, and a 1.5 M solution of CsI (≥ 99.99%, Sigma-Aldrich) in DMSO, were stirred for a further 2 hours at 70 °C. The $FAPbI_3$ and $MAPbBr_3$ were then combined in an 83:17 ratio and the CsI solution was subsequently added to form the $Cs_{0.07}(FA_{0.83}MA_{0.17})_{0.93}Pb(I_{0.83}Br_{0.17})_3$ solution, and stirred again at 70 °C for a final 2 hours. Before deposition, the perovskite solution was cooled to room temperature and filtered with a 0.45 µm PTFE filter.

Glass substrates were cleaned by scrubbing with a 1% Hellmanex III solution in water, followed by three 15 minute sonication cycles: first in 70 °C water, then in acetone and finally in isopropanol. The substrates were dried under a nitrogen gas flow. Immediately before spin-coating, the clean substrates were treated with UV-ozone for 30 minutes.
For each sample, 120 µL of the perovskite solution was deposited on the glass substrate and then spin-coated at 4000 RPM for 30 seconds, with ramp-up time of 6 seconds. 15 seconds before the end of the cycle, the samples were quenched with 170 µL of filtered chlorobenzene (0.22 µm PTFE filter). The samples were then annealed at 100 °C on a hotplate for 30 minutes. Finally, the perovskite samples were encapsulated in SiO_2 using a Polyteknik Flextura M508E electron-beam evaporator. 60 nm of SiO_2 was deposited under vacuum directly from a SiO_2 target at an evaporation rate of 0.06 nm/s. The surface recombination velocity between the SiO_2 and perovskite interface is 200 cm/s – substantially lower than typical interfaces applied in corresponding solar cells[29]. The SiO_2 top layer additionally acts as a barrier to prevent the evaporation of volatile perovskite components.

The perovskite film formation was confirmed using x-ray diffraction (XRD, measured with a Bruker D2 Phaser with a Cu Kα tube), absorbance spectra (PerkinElmer LAMBDA 750 UV/Vis/NIR Spectrophotometer) and photoluminescence spectra (WiTEC alpha300 SR confocal imaging microscope coupled to a Thorlabs S1FC405 405nm CW diode laser). The results of these measurements are shown in Figure 3.6.

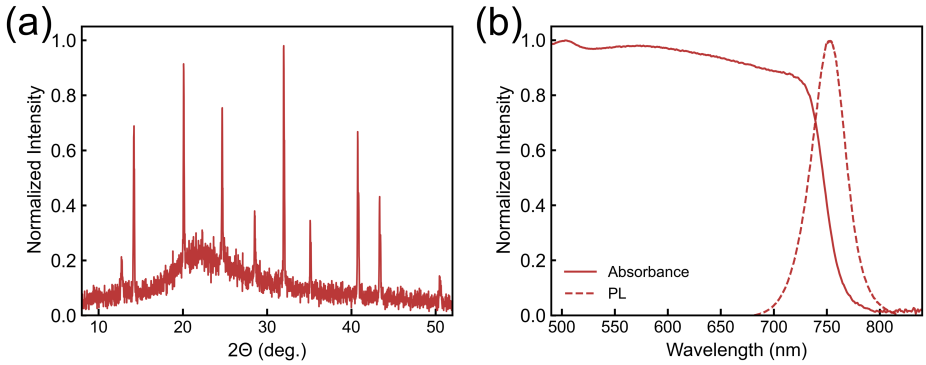

Figure 3.6: (a) The X-ray diffractogram of the metal halide perovskite sample following encapsulation in SiO_2 confirms the perovskite formation and correct perovskite phase. (b) The normalized absorbance (solid curve) and PL (dashed curve) of the same sample. The PL spectrum was obtained immediately after photoexcitation.

3.8.2. IMPLS Characterization

A comparison between IMPLS and the common modulated electrical and electrical-optical hybrid techniques are shown in Table 3.2[77, 216]. Impedance spectroscopy is most commonly performed with voltage acting as the modulating parameter and current as the response, however the converse configuration (using current modulation and measuring voltage) is also possible and still regarded as IS.

The IMPLS system, illustrated in Figure 3.2a was constructed inside a N_2-filled glovebox. The 465 nm blue LED (Cree LED) and the silicon photodiode (model BPW34, OSRAM, Infineon Technologies) were connected to a combined system-controller and system-readout unit (PAIOS from Fluxim AG). The 650 nm long-pass filter used to block the LED light was purchased from ThorLabs. IMPLS measurements for the encapsulated film were collected by configuring the PAIOS system to measure the photodiode signal under IMPS mode.
Reference measurements were performed as described in Section 3.3 and shown in Figure 3.7. While the low amplitude signal indicates that the effect of light leakage is negligible at all frequencies, the system response becomes relevant at relatively high frequencies. This response arises from the combined effects of the photodiode and LED response times, the system controller, and the system readout.
The complete forward and reverse scan from the exemplary measurement shown in Figure 3.2 is presented in Figures 3.8a and 3.8b. Notably, the fast process was quenched when measuring the reverse scan (Figure 3.8a). This quenching is also visible in the amplitude plot, which does not recover during the frequency sweep reversal (Figure 3.8b). After keeping the sample in the dark overnight, IMPLS was re-conducted on the same spot under the same conditions. Interestingly, the PL amplitude not only recovered but exceeded its initial value, and the previously quenched fast process re-emerged (Figures 3.8c and 3.8d). These results suggest that the observed changes are due to a reversible

Table 3.2: Summary of frequency-domain methods, their abbreviations and their transfer functions.

Method	Abbreviation	Perturbation	Response	Transfer Function
Impedance Spectroscopy	**IS**	Voltage, $\tilde{V}$	Current, $\tilde{j}_e$	$\mathbf{Z} = \tilde{V} / \tilde{j}_e$
Intensity-Modulated Photovoltage Spectroscopy	**IMVS**	Light in, $\tilde{\phi}_{\text{exc}}$	Voltage, $\tilde{V}$	$\mathbf{W} = \tilde{V} / \tilde{\phi}_{\text{exc}}$
Intensity-Modulated Photocurrent Spectroscopy	**IMPS**	Light in, $\tilde{\phi}_{\text{exc}}$	Current, $\tilde{j}_e$	$\mathbf{Q} = \tilde{j}_e / \tilde{\phi}_{\text{exc}}$
Intensity-Modulated Photoluminescence Spectroscopy	**IMPLS**	Light in, $\tilde{\phi}_{\text{exc}}$	Light out, $\tilde{\phi}_{\text{em}}$	$\mathbf{P} = \tilde{\phi}_{\text{em}} / \tilde{\phi}_{\text{exc}}$
Voltage-Modulated Emission Spectroscopy	**VMES**	Voltage, $\tilde{V}$	Light out, $\tilde{\phi}_{\text{em}}$	$\mathbf{S} = \tilde{\phi}_{\text{em}} / \tilde{V}$
Current-Modulated Emission Spectroscopy	**CMES**	Current, $\tilde{j}_{\text{in}}$	Light out, $\tilde{\phi}_{\text{em}}$	$\mathbf{R} = \tilde{\phi}_{\text{em}} / \tilde{j}_{\text{in}}$

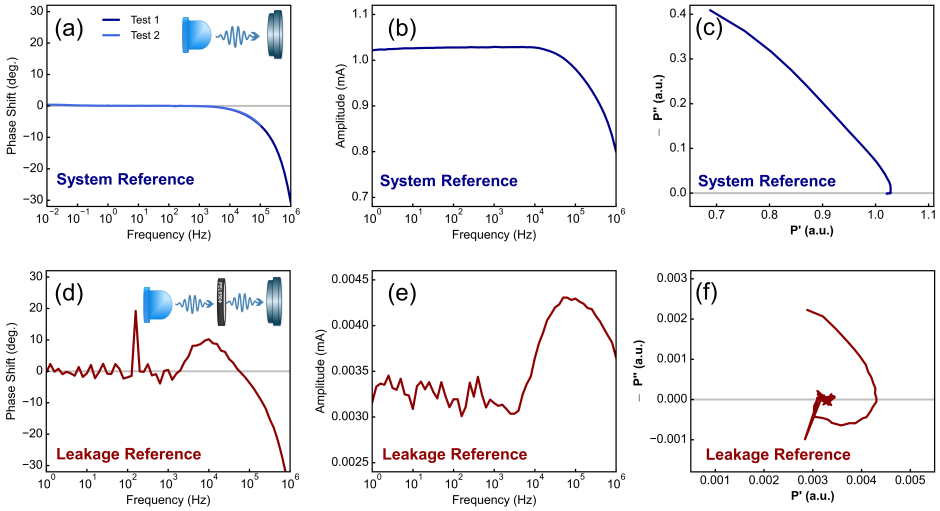

Figure 3.7: The top row represents the system reference measurement where the test configuration is depicted in the inset in panel (a). The results from the system reference are shown in blue, where (a) shows the relative phase shift across two separate frequency ranges, (b) shows the corresponding amplitude and (c) is the generated Nyquist plot from these values. The bottom row represents the reference measurement to determine the influence of light leakage through the long-pass filter. The configuration of this reference is visualized with the inset in panel (d). The relative phase shift, amplitude and corresponding Nyquist plot from the leakage reference measurement are shown in red in (d), (e) and (f), respectively.

state change in the material and not a consequence of permanent photodegradation. We then investigated the influence of starting frequency and scan direction on the perovskite's IMPLS response. A new experiment was conducted, which included a pre-conditioning step in which the sample was illuminated with DC light for 2 minutes before the IMPLS scan was measured. The first measurement started at 1 MHz, sweeping down to 10 mHz and back up. After recovery in the dark, a second measurement began at 10 mHz and was swept upward. The comparison of these measurements is shown in Figure 3.9. The red curve (starting at 1 MHz) shows trends similar to those in Figure 3.2, albeit with an amplitude enhancement at around 100 mHz. In contrast, the blue curve (starting at 10 mHz) shows no fast process in either direction. Furthermore, the PL amplitude of the slow process is reversible in the measurement starting at 10 mHz. The results indicate that one or more (possibly coupled) slow processes gradually quench the fast process under prolonged modulated light exposure. In order to quantify the fast process, the IMPLS measurement must be conducted relatively quickly so that this fast process remains in a quasi-stable state. Figures 3.10, 3.12a and 3.12b show that the fast process remained quasi-stable in a shortened IMPLS scan, verifying that separate measurements and analyses of the fast and slow processes are required.

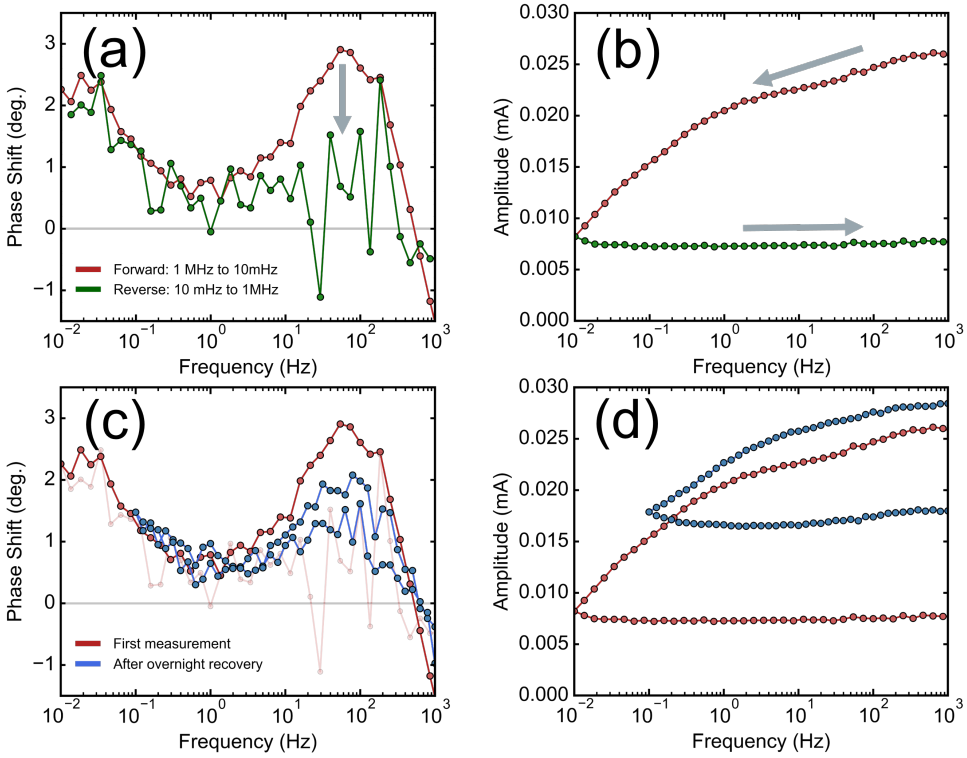

Figure 3.8: (a) The phase and (b) the amplitude for both the first half (red) and second half (green) of the IMPLS measurement presented in Figure 3.2. As shown with the gray arrow in (a), the fast response is quenched between the forward and reverse sweep in this case. This is accompanied by the quenched PL amplitude as shown in (b). (c) The phase and (d) amplitude of the same sample spot, re-measured after keeping the sample in the dark overnight. The fast process is re-observed in the phase plot and is accompanied with an absolute PL amplitude enhancement.

3.8.3. Optical Equivalent Circuit Modeling

Applying an OEC model is an effective, simple tool to fit the frequency-dependent rate equation to IMPLS data, where non-trivial, frequency-dependent processes can also be accounted for by including branches with their relevant circuit component proxies. The excess electronic minority carriers (Δn - which varies sinusoidally as a function of time during an IMPLS scan) corresponding to the OEC model described in this work is:

$$\frac{\mathrm{d}\Delta n(t)}{\mathrm{d}t} = G(t) - r_{\mathrm{rad}}(t) - r_{\mathrm{Auger}}(t) - r_{\mathrm{trap}}(t) - r_{LF}(t) \tag{3.8}$$

Where $G(t)$ is the generation rate and r represents each of the different processes' recombination rates. $r_{LF}(t)$ is a term which accounts for all non-electronic processes that occur at lower frequencies (such as ion migration and chemical reactions), which impact the carrier density. For sufficiently low frequencies, the fast electronic processes effectively behave as if in DC conditions. Then, this equation is simplified to:

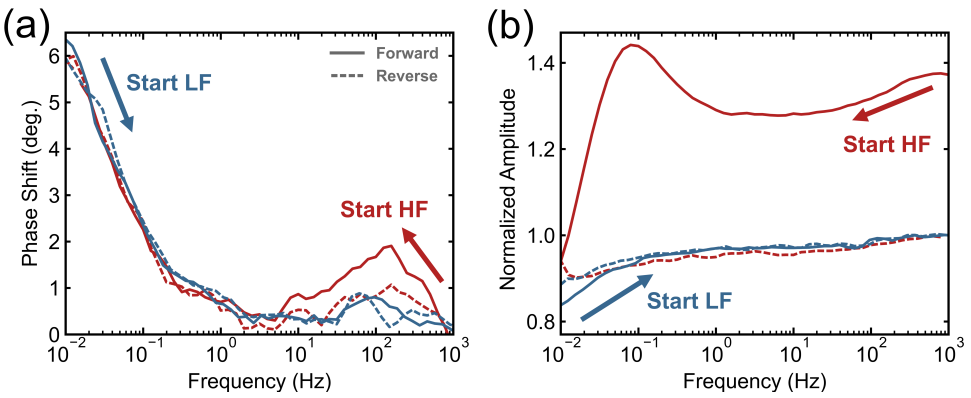

Figure 3.9: (a) Phase shift and (b) amplitude for two IMPLS measurements with different starting frequencies. The red curve in both panels represents the scan that begins at 1 MHz, with the solid red line showing the response during the first half of the scan (1 MHz to 10 mHz) and the dashed red line showing the response during the second half (10 mHz to 1 MHz). The blue curve represents the scan that begins at 10 mHz, with the solid blue line corresponding to the first half of the scan (10 mHz to 1 MHz) and the dashed blue line representing the second half (1 MHz to 10 mHz).

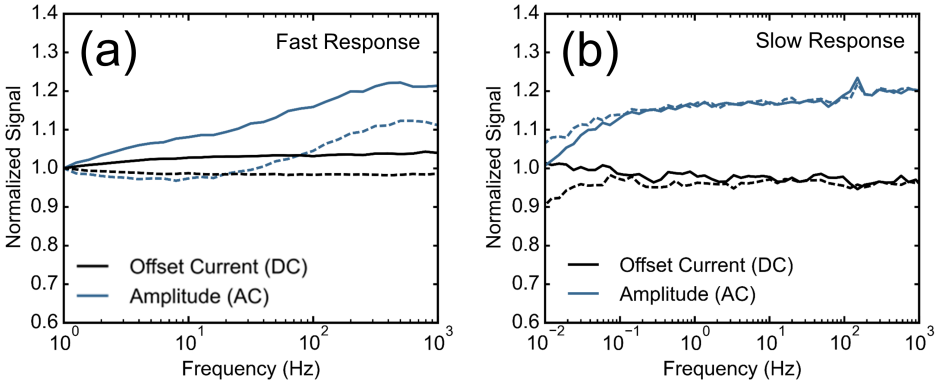

Figure 3.10: Comparison between the normalized AC (blue) and DC (black) current signals extracted for the (a) fast and (b) slow responses, corresponding to Figures 3.3 and 3.4, respectively. The solid lines represent the first halves of the scans and the dashed lines represent the second halves. In both measurements, the DC signal does not deviate by more than 10% from its starting value, indicating that the processes remain in a quasi-stable state for the duration of the IMPLS measurements.

$$\frac{\mathrm{d}\Delta n(t)}{\mathrm{d}t} = G - r_{HF} - r_{LF}(t) \tag{3.9}$$

Where only $r_{LF}(t)$ affects the frequency-dependent carrier density and thus the PL.

In principle, it is possible to separate these high frequency recombination processes with

IMPLS provided that the system components have sufficiently high response times. In this case, the HF branch would then be separated into the three branches representing each of the electronic recombination processes (Figure 3.11a). Using Kirchhoff's law for parallel circuits, the corresponding resistors for each of these processes relate to R_{HF} by:

$$\frac{1}{R_{HF}} = \frac{1}{R_{\text{rad}}} + \frac{1}{R_{\text{Auger}}} + \frac{1}{R_{\text{trap}}} \tag{3.10}$$

Note the capital-R terms denote resistances and should not be confused with recombination rates. Fitting at high frequencies thus allows for the extraction of the (modulated) PLQY.

This analysis ultimately means that when we are probing the slow process, the fast process is not relevant and can additionally be considered frequency-independent. Hence, the fast process is combined with the electronic processes in Figure 3.4a, and the analysis is simplified with the use of a single resistor. The converse is also true when we are measuring the fast process as in Figure 3.3a. However we emphasize that these separate analyses are not separate OECs. Rather, the schematics shown in Figures 3.3a and 3.4a are a simplification of the combined OEC which captures all of the electronic, fast and slow processes together. For completeness, this combined OEC is shown in Figure 3.11b. It is emphasized that the extracted values for R and L in Tables 3.3 and 3.4 do not correspond to physical electronic circuit components – rather, they simply correspond to fit parameters required to obtain the values of the characteristic frequency and lifetime in the OEC model fits.

Table 3.3: Extracted equivalent circuit parameters for the fast process using the simplified OEC shown in Figure 3.3a.

Direction	**R_{HF} (a.u.)**	**R_{LF} (a.u.)**	**L (ms)**	**f_{char} (Hz)**	**τ_{char} (ms)**
Forward	**1**	8.2 ± 0.2	18 ± 1	73 ± 4	2.2 ± 0.1
Reverse	**1**	6.6 ± 0.1	13.2 ± 0.6	79 ± 4	2.0 ± 0.1

Table 3.4: Extracted equivalent circuit parameters for the slow process using the OEC shown in Figure 3.4a.

Direction	**R_{HF} (a.u.)**	**R_{LF} (a.u.)**	**L (s)**	**α (a.u.)**	**f_{char} (mHz)**	**τ_{char} (s)**
Forward	1	1.9 ± 0.1	121 ± 8.4	0.65 ± 0.01	2.5 ± 0.3	63 ± 6
Reverse	1	1.5 ± 0.5	137 ± 8.9	0.67 ± 0.01	1.7 ± 0.6	91 ± 31

It is worth noting that the frequency at which the phase shift is at its maximum in the Bode plots does not necessarily correspond to the characteristic frequency of the process. This is because the characteristic frequency depends only on the process and is not coupled to any other effect in the system, as described in Equation 3.6. However, the measured phase in general is related to all processes occurring in parallel:

$$\theta(\omega) = \arctan \frac{\text{Im}|P_{\text{Total}}|}{\text{Re}|P_{\text{Total}}|} \tag{3.11}$$

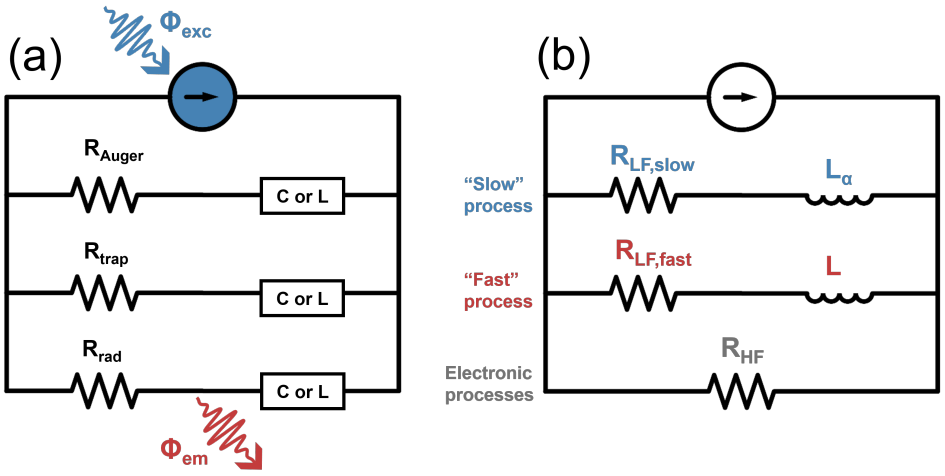

Figure 3.11: (a) A theoretical OEC model for when only electronic processes are considered. At sufficiently high frequencies, separate electronic responses (such as trap-assisted recombination) in principle can be resolved using a high-frequency adaptation of IMPLS combined with the appropriate OEC model to describe the data. As this OEC model is for exemplary purposes, only the influences of radiative, trap-assisted and Auger recombination are considered. The complex circuit components are exemplified with either an ideal capacitor or an ideal inductor (labeled as C or L), though other components may also be required to best fit and physically describe the electronic processes. (b) The complete OEC model separating the fast and slow processes observed in this work.

Where $\omega = 2\pi f$ and

$$\frac{1}{\mathrm{P_{Total}}} \propto \frac{1}{R_{HF}} + \frac{1}{R_{LF} + i\omega L} \tag{3.12}$$

As is often the case, the difference between using the OEC fitting and the peak in the Bode plot is small (79 Hz versus 86 Hz in the case of Figure 3.3), but we use the more accurate OEC fitting value.

It is also worth further discussing the relevance of the fractional exponent term, alpha (α), that was required to fit the slow process in this work. Mathematically, α alters Equation 3.12 by:

$$\frac{1}{\mathrm{P_{Total}}} \propto \frac{1}{R_{HF}} + \frac{1}{R_{LF} + i\omega^{\alpha} L^{\alpha}} \tag{3.13}$$

When $\alpha = 1$, the process is described by a singular, well-defined relaxation time. There is likely no coupling or external factors occurring within the system which alters such a process. This is similar to how trap-assisted recombination may be modeled using ECs in impedance spectroscopy. In the electrical analog, the process is effectively behaving

as a perfect inductor. In IMPLS, we assume that ion Frenkel pair formation and annihilation would similarly follow this ideal behavior. When $\alpha = 0.5$, the process is regarded to be entirely diffusive in nature and reflects mass transport limitations. This behavior aligns with that described by the Warburg element, which has previously been applied to model ion migration in perovskite devices in the past[79]. As shown in Table 3.4, α ranges from 0.64 to 0.68, which implies that the slow process we have measured is likely to be predominantly (but not perfectly) diffusive in nature. Simultaneous diffusion of different ionic species, grain boundaries, the thickness of the perovskite layer and reactions at the contact layers may impact the exact value for α. As we have speculated earlier in this chapter, the slow process may indeed be considered the combined effect of vacancy diffusion followed by further Frenkel pair formation, which in turn would ultimately place α somewhere between 0.5 and 1.

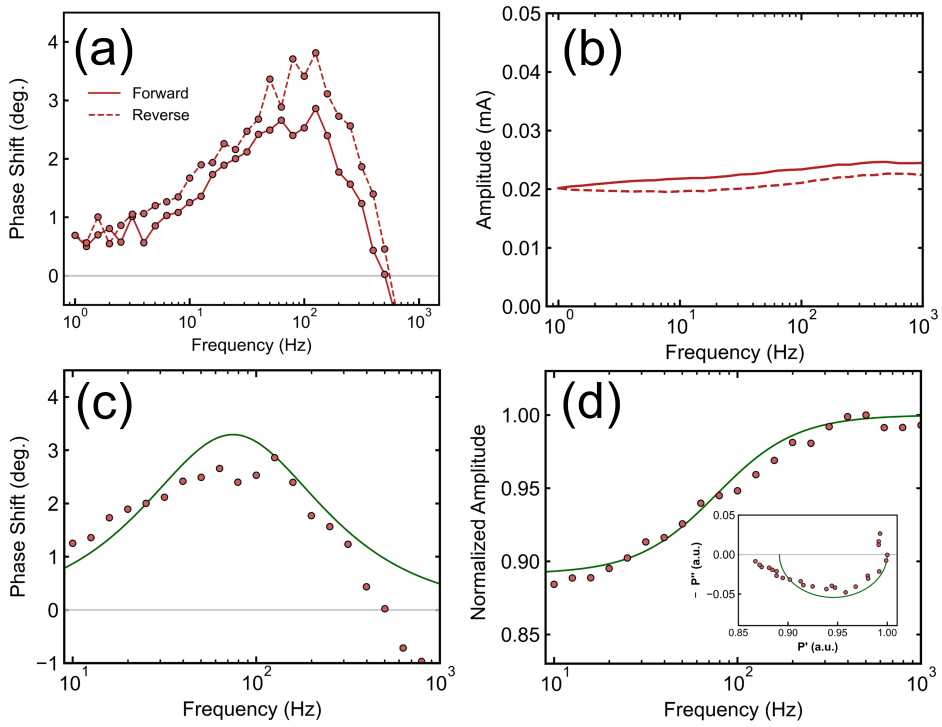

Figure 3.12: (a) The phase and (b) amplitude for the IMPLS measurement sweeping only from 1 kHz to 1 Hz (solid line) and back (dashed line). (c) The data (red) and corresponding OEC model fit (green) for the phase of the forward scan. (d) The data and OEC model fit for the amplitude of the forward scan. Inset in (d): the OEC model fit to the corresponding Nyquist plot.

All OEC fitting was conducted using the impedance.py package in Python[217]. The quality of each of these fits were assessed using the coefficient of determination, R^2, which is tabulated for the real and imaginary components of the OEC fits in Table 3.5. R^2 of the

imaginary component for the fast process is notably smaller than the slow component's imaginary fit, which we attribute to the onset of the system response in the fast process (occurring near 1 kHz). This system response is not present in the slow process frequency range which allows for a much higher R^2 for the imaginary component fits. However, as it is clear where the phase shift peaks in the Bode plots in Figure 3.3c and in Figure 3.12c, we can confirm that the fits still are well assessed for the given data.

Table 3.5: The coefficient of determination (R^2) for each of the four OEC fits.

	Fast (Forward)	Fast (Reverse)	Slow (Forward)	Slow (Reverse)
Real R^2	0.9733	0.9877	0.9963	0.9492
Imaginary R^2	0.5687	0.6479	0.9891	0.9758
Combined R^2	0.9390	0.9440	0.9937	0.9651

Sensitivity analyses in general show that the model is more sensitive to changes in R_{LF} than in L; this is exemplified in Figure 3.13 which shows the sensitivity analysis results for the forward scan fit of the fast process. The combined R^2 deviates by 3.3% when the value for L is reduced by 20%, and by only 2.2% when L is increased by 20%. However the combined R^2 deviates by 13.3% when R_{LF} is reduced by 20%, and 7.1% when R_{LF} is increased by 20%. The maxima shown in both Figures 3.13a and 3.13b further verify that the obtained fits are optimized for the IMPLS data.

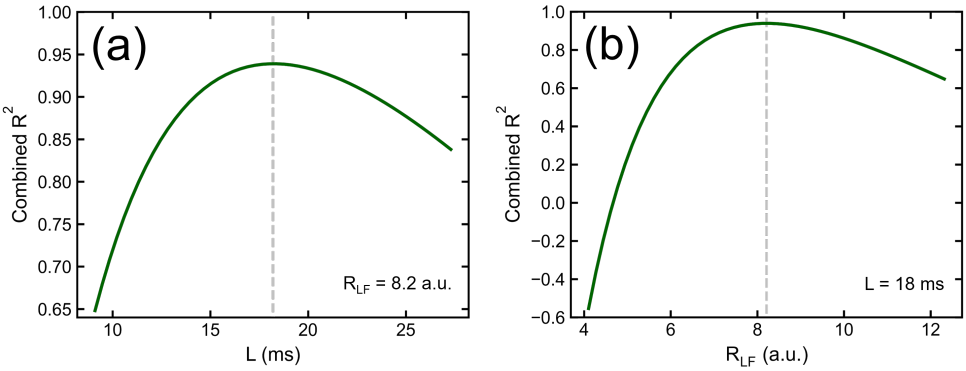

Figure 3.13: Sensitivity analysis for the forward scan of the fast process. (a) The sensitivity of the combined residuals when R_{LF} is fixed at 8.2 a.u., and L is swept ± 20% of its fitted value of 18 ms (shown with the gray dashed line). (b) The sensitivity of the combined residuals when L is fixed at 18 ms, and R_{LF} is similarly swept ± 20% of its fitted value of 8.2 a.u. (similarly shown with the gray dashed line).

3.8.4. Fabrication and Characterization of Perovskite Devices

Pre-patterned (2.5×2.5 cm^2, 15 Ω/sq) ITO substrates (Psiotec, UK) were sonicated for 10 minutes subsequently in acetone, 3% Hellmanex solution in deionized (DI) water,

DI-water and isopropanol in order to clean them. After an oxygen plasma treatment (4 min, 120 W), the substrates were transferred to a N_2-filled glovebox. To deposit the hole transport layer, 60 µL of PTAA (Poly-[bis-(4-phenyl)- (2,4,6-trimethylphenyl)-amin]) solution (Sigma-Aldrich, 1.75 mg/mL in toluene) was spin-coated onto the substrates at 6000 RPM for 30 seconds with a ramp of 2000 RPM/s. After 10 min annealing on a hotplate at 100 °C, the films were cooled down to room temperature. 60 µL of PFN-Br (Poly(9,9-bis(3'-(N,N-dimethyl)-N-ethylammonium-propyl-2,7-fluorene)-alt-2,7-(9,9-dioctylfluorene))dibromide) solution (1-Material, 0.5 mg/ml in methanol) was deposited on top of the PTAA layer dynamically at 4000 RPM for 30 s.

The solutions for the perovskite active layers were prepared in a similar manner to the bare films: 1.2 M $FAPbI_3$ solution was prepared by dissolving FAI and PbI_2 in DMF:DMSO (4:1 volume ratio) which contains a 10%-molar excess of PbI_2. The 1.2 M $MAPbBr_3$ solution was made by dissolving MABr and $PbBr_2$ in DMF:DMSO (4:1 volume ratio) which contains a 10%-molar excess of PbBr2. The solutions were stirred overnight at room temperature. By mixing these $FAPbI_3$ and $MAPbBr_3$ solutions in a ratio of 83:17 and adding 42 µL 1.5 M CsI solution in DMSO to 958 µL of the 83:17 mixture, the desired solution was obtained. The triple-cation perovskite films were prepared by depositing 120 µL and spin-coating at 4000 RPM for 400 s at a ramp of 1334 RPM/s. 10 s after the start of the spinning process, the spinning substrate was washed with 300 µL ethyl acetate for approximately 1 s (the anti-solvent was deposited in the center of the film). The perovskite film was then annealed at 100 °C for 1 h on a preheated hotplate. After annealing, the samples were transferred to an evaporation chamber where fullerene C_{60} (25 nm), 2,9-Dimethyl-4,7-diphenyl-1,10-phenanthroline (BCP, 8 nm) and copper (100 nm) were deposited under vacuum (10^{-7} mbar). The overlap of the copper and the ITO electrodes defined the active area of the pixel (6 mm^2).

The *JV* curves of these devices were measured under an N_2 atmosphere using a Keithley 2401 SMU and a G2V Pico LED solar simulator. The scan rate for the *JV* curve shown in Figure 3.5a was 0.1 V/s. The modulated *IV* curves (Figure 3.5b), the IMPS and IMVS scans (Figures 3.5c,d) and the scan-rate dependent *IV* curves were measured using an Agilent B2902A SMU with 450 nm blue LED (Cree LED). The devices were left unmasked for these measurements and the illumination power density was approximately 120 mW/cm^2.
IMPLS measurements of the solar cell (Figure 3.15) were obtained using the WiTEC alpha300 SR confocal imaging microscope acting as the PL detector and with the Agilent B2902A SMU coupled to a 450 nm blue LED (Cree LED) to supply the DC and AC light signal.

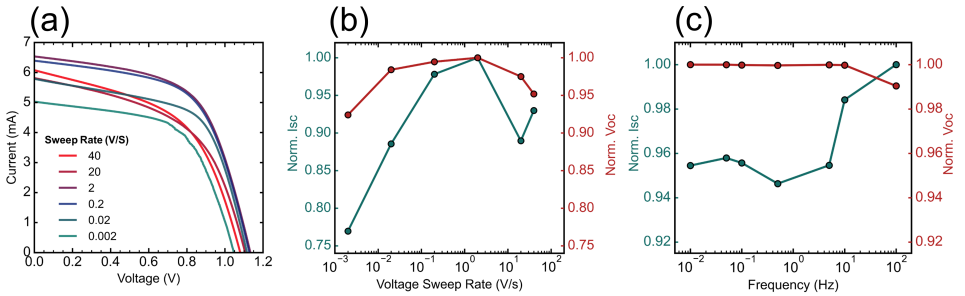

Figure 3.14: (a) Measured IV curves at different voltage scan rates, where the rates are shown in the legend. (b) The normalized I_{SC} (left) and normalized V_{OC} (right) as a function of the voltage scan rate, extracted from the device IV curves shown in panel (a). (c) The normalized I_{SC} (left) and normalized V_{OC} (right) as a function of AC modulation frequency for the data shown in Figure 3.5b. Panels (b) and (c) highlight that the current is more strongly influenced than the voltage in both the voltage scan rate measurements and light modulation frequency measurements.

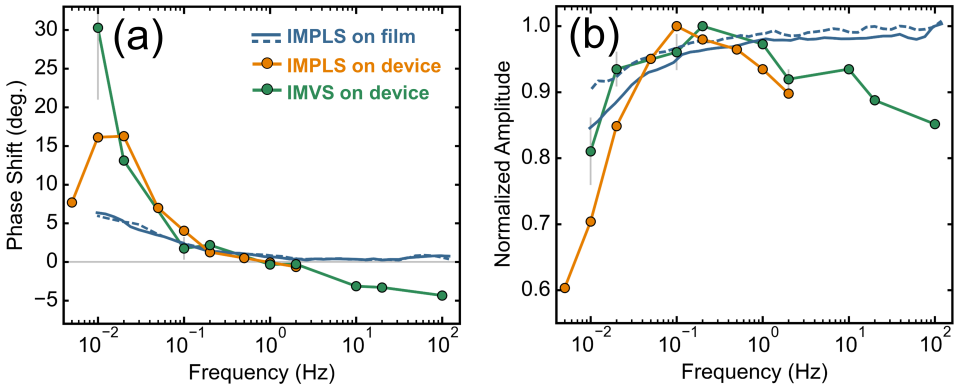

Figure 3.15: (a) Measured IMPLS phase shift for the solar cell (orange) overlaid with the IMPLS phase shift of the encapsulated film (blue) and the IMVS phase shift for the same device (green). (b) The corresponding normalized amplitudes for the same IMPLS and IMVS measurements.

4

Dynamic Contrasts
Mapping Mobile and Fixed Defects via Dual-Component PL Correlation

Metal halide perovskites exhibit coupled electronic–ionic properties that critically influence photovoltaic performance. Robust characterization of mobile ions is therefore essential for advancing perovskite technologies. Conventional electrical methods for probing ion dynamics, such as impedance spectroscopy, require fully operational devices, and their interpretation is often complicated by confounding factors including interfacial layer effects. In this chapter, we introduce localized intensity-modulated photoluminescence spectroscopy (IMPLS) to probe lateral ionic transport in perovskite films. We measure the IMPLS response as functions of modulation frequency and carrier injection level, and establish its correlation with the perovskite's photoluminescence quantum yield (PLQY). We propose a model in which mobile ionic defects – responsible for pinning the PLQY – laterally diffuse from high-intensity regions, thereby inducing the observed IMPLS signal. Ionic diffusion coefficients extracted from this purely optical analysis agree with reported values in the literature. Importantly, IMPLS mapping enables us to isolate the contributions of mobile and immobile defects, quantified through a parameter we define as the defect contrast coefficient. Overall, this chapter demonstrates that localized IMPLS provides a contact-free means to extract lateral ion diffusion coefficients while simultaneously distinguishing defect types across the sample.

This chapter is based on:

Sarah C. Gillespie, Jérôme Gautier, Linde M. van de Ven, Agustin O. Alvarez, Veronique S. Gevaerts, L.J. (Bart) Geerligs, Gianluca Coletti, Bruno Ehrler, and Erik C. Garnett. Photoluminescence Mapping of Mobile and Fixed Defects in Halide Perovskite Films. *Submitted* (2025).

Author contributions:

SCG fabricated the samples, measured IMPLS and TRPL, analyzed the data, and wrote the manuscript. JG measured and analyzed the IMPLS maps. LMV measured PLQY. ECG gave analytical guidance and reviewed the manuscript. VSG, LJG, GC, BE, AOA and ECG provided supervision.

4.1. Introduction

Metal halide perovskites are among the most promising materials for next-generation semiconductor applications, with over 74,000 publications in the past 10 years alone[64, 218]. Their exceptional optoelectronic properties have made them particularly attractive for high-efficiency photovoltaics (PV)[9, 12, 33, 136, 219]. Beyond PV, perovskites have potential applications in a wide range of technologies, including transistors, memristors, photo- and X-ray detectors, self-tracking solar concentrators, and more[183, 184, 220–230]. Many of these emerging applications exploit the coupled electronic–ionic properties inherent to the perovskite material itself. For example, halide segregation drives the self-tracking behavior in solar concentrators, while the operating principle of perovskite memristors relies on ionic migration and the associated memory effect, enabling information retention over extended periods and the formation of multiple resistive states within a device[65, 68, 183, 184, 231].

Among the available characterization tools, photoluminescence (PL) spectroscopy stands out as one of the most widely used for probing electronic charge-carrier processes in the perovskite community[31]. By tuning the excitation conditions such as energy, intensity, and repetition rate, PL measurements can be analyzed to determine key electronic properties, including carrier lifetimes, surface recombination velocities and carrier diffusion lengths[29, 37, 191, 232, 233]. PL time series have also been applied to study ionic phenomena such as halide segregation and mobile ion redistribution – however, the resulting information from these measurements has been largely limited to qualitative trends[41, 68, 69, 192]. Quantitative methods for determining ionic parameters, such as mobile ion densities and diffusion coefficients, are still predominantly in the domain of electrical measurements; techniques including transient ion drift and impedance spectroscopy (IS) are commonly applied to extract these ionic values[48, 53, 70, 79]. Despite this, all electrical approaches face inherent limitations: measurements are restricted to fully operational devices, while high recombination at the transport layers and interfacial ionic reactions tend to complicate the interpretation of results[72, 83].

In **Chapter 3**, we introduced a new PL characterization method, intensity-modulated photoluminescence spectroscopy (IMPLS), designed to resolve ion dynamics purely optically in perovskite films and devices[234]. Unlike time-domain PL measurements, where overlapping processes complicate interpretation, IMPLS separates contributions with distinct relaxation times by probing the PL response in the frequency domain.

As an analogy, IMPLS can be viewed as a fully optical equivalent of impedance spectroscopy. Typically in IS, the frequency-dependent current response is measured under a small voltage perturbation[75, 78]. In IMPLS, a sinusoidally modulating optical input is applied at varying frequencies (f), and the PL response for each frequency is measured. This response is quantified by both the relative PL amplitude ($|\widetilde{\phi}_{\mathrm{em}}|/|\widetilde{\phi}_{\mathrm{exc}}|$) and the phase shift between the excitation and emission (θ), which together provide direct insight into the underlying processes.

To analyze IMPLS data, we define the IMPLS transfer function, P, to be[193]:

$$P = \frac{\widetilde{\phi}_{\mathrm{em}}}{\widetilde{\phi}_{\mathrm{exc}}} = \frac{|\widetilde{\phi}_{\mathrm{em}}|}{|\widetilde{\phi}_{\mathrm{exc}}|} \exp(i\theta) \tag{4.1}$$

which enables the IMPLS data to be mapped on Nyquist plots and modeled with corresponding optical equivalent circuit (OEC) models.
Based on the transfer function definition, a requirement of IMPLS analysis is that the intensity of the PL must exhibit a dependence on the frequency of the applied optical excitation. In other words, an ionic process must alter the photoluminescence quantum yield (PLQY) when it is probed in order for its response to be observed.
This frequency-dependent PLQY response raises the key question: how can frequency modulations on the timescale of seconds influence the PLQY, a parameter typically governed by nanosecond-to-microsecond charge-carrier recombination dynamics? In this chapter, we address this question by correlating the IMPLS response with absolute PLQY measurements under localized excitation conditions. Specifically, we measure the IMPLS response of a halide perovskite thin film both as a function of frequency, and of excess minority carrier density, Δn. We directly compare the phase component of the IMPLS response to the absolute PLQY(Δn) and to the relative PLQY(f), and spatially resolve these correlations across the sample. From this analysis, we propose a model of the coupled electronic–ionic processes, in which the IMPLS signatures originate from lateral mobile ion diffusion between the laser-illuminated region and the surrounding background. The analysis indicates that, under localized experimental conditions, IMPLS can be applied as a means to determine mobile ion diffusion coefficients (D_{ion}) entirely without the requirement of electrical contacts. In the case where the total defect density in the halide perovskite is dominated by mobile ionic defects, the lateral diffusion coefficient can be correlated to the change in the PLQY[67]. Thus, analyzing differences between IMPLS and PLQY maps provides a route to spatially resolve regions where non-radiative recombination is dominated by either mobile or fixed defects.

4.2. Time-Dependent PLQY in Halide Perovskites

Before discussing the IMPLS results, we first consider the PLQY variations observed in halide perovskites under time-domain measurements, and discuss how these effects manifest in the frequency domain. Assuming no processes alter the semiconductor's electronic properties under continuous illumination, the PLQY is defined as the ratio of the radiative recombination rate, R_{rad}, to the total recombination rate under steady-state conditions:

$$\text{PLQY} = \frac{R_{\text{rad}}}{R_{\text{rad}} + R_{\text{trap}} + R_{\text{Auger}}} \tag{4.2}$$

Here, R_{trap} and R_{Auger} are the trap-assisted and Auger non-radiative recombination rates, respectively. In reality, the PLQY of halide perovskites can vary in time even under moderate illumination conditions. In Figure 4.1, we plot the measured PLQY time series of a $Cs_{0.07}(FA_{0.8}MA_{0.2})_{0.93}Pb(I_{0.8}Br_{0.2})_3$ thin film encapsulated in SiO_2. Sample fabrication and measurement details are listed in Section 4.9. We observe a rapid PLQY rise followed by a gradual plateau as the measurement time approaches 30 minutes. While this example exhibits a relatively straightforward bi-exponential rise, many studies have shown that the PL of perovskite films can alternate between photobrightening and photodarkening, depending on timescale and measurement conditions[205, 207, 235, 236]. Notable ionic processes that drive photobrightening or photodarkening include Frenkel pair generation and recombination, formation of complex species under specific illumination condi-

tions and ionic trap migration out of the illuminated region[41, 69, 192, 204]. To account for these changes under steady-state or quasi-steady-state excitation, we introduce an additional recombination term, $R_{\text{slow}}(t)$, in the PLQY definition. This time-varying non-radiative term encompasses changes in trap-state density, recombination coefficients, or other parameters that modify the total recombination rate over time. The time-dependent PLQY can thus be expressed as:

$$\text{PLQY}(t) = \frac{R_{\text{rad}}}{R_{\text{rad}} + R_{\text{trap}} + R_{\text{Auger}} + R_{\text{slow}}(t)} \tag{4.3}$$

Provided that the slow process affects only the minority-carrier lifetime, Equation 4.3 can instead be written with a time-dependent trap-assisted recombination rate, $R_{\text{trap}}(t)$. If the measured PLQY enhancement arises from ionic defect diffusion out of the illuminated region, or from vacancy–interstitial recombination, then $R_{\text{slow}}(t)$ gradually decreases over time[41, 69]. As a result, the ratio of radiative to non-radiative recombination increases, leading to an enhanced PLQY, as we show in Figure 4.1.

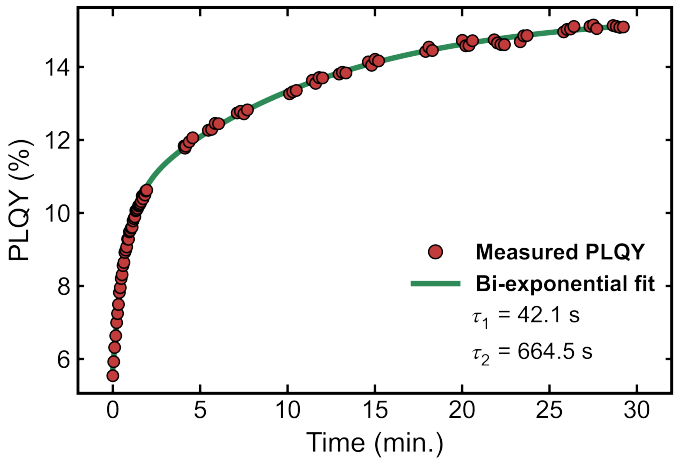

Figure 4.1: PLQY time series measured on an encapsulated triple-cation, mixed-halide perovskite film. The empty regions between the red data points are when the sample's absorptance was measured (see Section 4.9.2 for measurement details). The green curve represents the bi-exponential rise fit to the data, $\text{PLQY} = \text{PLQY}_{\text{saturation}} - A\exp(-t/\tau_1) - B\exp(-t/\tau_2)$. The PLQY saturation value from the fit is 15.5% and the extracted time constants are τ_1 = 42.1 seconds and τ_2 = 11.08 minutes.

In the corresponding frequency-domain analysis, the PLQY can vary depending on the applied excitation frequency. If the optical modulation frequency is much faster than the characteristic lifetime of the ionic process, $1/2\pi f \ll \tau_{\text{char}}$, then the modulations will not alter the PL response. This effect is analogous to the "ion-freeze" concept for perovskite solar cell JV sweeps, which occurs when the JV curve is measured at scan rates faster than the ionic response time[25]. In that case, the mobile ion contribution is suppressed at high JV scan rates, whereas at slower sweeps, their contribution becomes increasingly dominant in the JV response. Similarly, at high modulation frequencies,

ionic effects are frozen, resulting in an unchanged PLQY. Once the modulation frequency is sufficiently low to become comparable to the characteristic timescale of an ionic process, its influence appears through a measurable phase shift and amplitude change in the IMPLS measurements, corresponding to a changing $R_{\text{slow}}(t)$ in Equation 4.3, thus a change in the PLQY. This implies that the low frequency IMPLS response and PLQY changes on the timescale of seconds are both driven by the same ionic process. In this work, we test this hypothesis by directly correlating our measured IMPLS responses with absolute PLQY measurements.

4.3. IMPLS Results

The experimental setup used for the IMPLS measurements is schematically illustrated in Figure 4.2a. A perovskite sample, identical in composition to that shown in Figure 4.1, was placed above a 450 nm light-emitting diode (LED), which globally illuminated the sample. The LED provided an excitation density consisting of a sinusoidal (AC) modulation, $\widetilde{\phi}_{\text{exc,LED}}$, superimposed on a constant offset (DC) excitation, $\bar{\phi}_{\text{exc,LED}}$. The instantaneous LED excitation density at time t can be expressed as:

$$\phi_{\text{exc,LED}}(t) = \bar{\phi}_{\text{exc,LED}} + |\widetilde{\phi}_{\text{exc,LED}}| \sin(2\pi f t) \tag{4.4}$$

where $|\widetilde{\phi}_{\text{exc,LED}}|$ represents the sinusoidal modulation amplitude.
In parallel, a 405 nm laser provided additional high-intensity, localized excitation, $\phi_{\text{exc,laser}}$, focused onto a spot area of 78.5 μm^2. The total excitation density at the laser spot was therefore given by the sum of the LED and laser contributions:

$$\phi_{\text{exc}}(t) = \phi_{\text{exc,laser}} + \phi_{\text{exc,LED}}(t) \tag{4.5}$$

As illustrated in Figure 4.2a, the PL of the sample was collected through a 20× objective and recorded using a charge-coupled device (CCD) coupled to a spectrometer. The spectra were converted to the energy scale, and both the LED and PL signals were integrated and tracked in time[237]. The PL signal can thus be described as:

$$\phi_{\text{PL}}(t) = \bar{\phi}_{\text{PL}} + |\widetilde{\phi}_{\text{PL}}| \sin(2\pi f t + \theta) \tag{4.6}$$

where $\bar{\phi}_{\text{PL}}$ is the offset PL intensity (the DC component), $|\widetilde{\phi}_{\text{PL}}|$ is the amplitude of the PL modulation (the AC component), and θ denotes the relative phase shift between the modulated illumination input and the PL output. By fitting sinusoidal functions to the integrated LED and PL spectra, all three parameters were determined.
With the measurement procedure established, we conducted two key IMPLS experiments: (i) in the first experiment, we varied the LED modulation frequency while holding the offset illumination intensity constant, and recorded the IMPLS response as a function of f (Figure 4.2b); (ii) in the second experiment, we varied the excess minority carrier density by sweeping the laser intensity at a fixed f, and measured the IMPLS response as a function of Δn (Figure 4.2c). Although the scales in Figures 4.2b and 4.2c are exaggerated for visualization, the changes in PL phase shift, amplitude, and offset follow the trends that were experimentally obtained in this work.

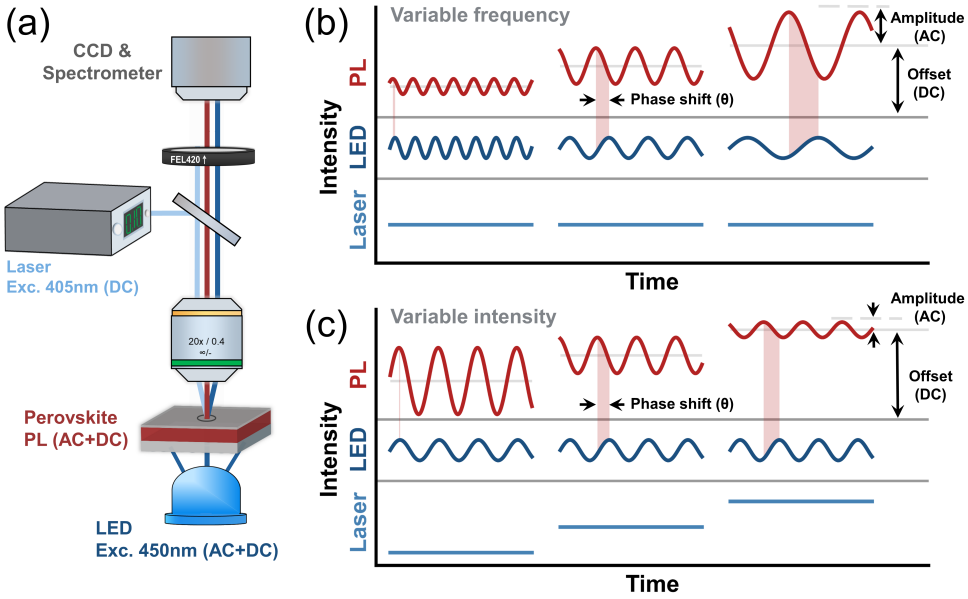

Figure 4.2: (a) Schematic of the experimental setup. Laser excitation was applied to the top of the sample via a dichroic mirror and its reflection was blocked using a 420 nm long-pass filter. The LED provided an offset intensity of 38.1 mW/cm^2, corresponding to a photon flux of $\Phi_{DC,LED}$ = 8.63×10^{16} cm^{-2}/s. The LED amplitude was set to 15.7 mW/cm^2 ($\Phi_{AC,LED}$ = 3.56×10^{16} cm^{-2}/s). For experiment (i) – the variable frequency experiment – the laser intensity was fixed at 33.104 W/cm^2 (Φ_{laser} = 6.75×10^{19} cm^{-2}/s). For experiment (ii) – the variable intensity experiment – the LED frequency was fixed at 50 mHz. (b) Schematic of experiment (i) for three representative modulation frequencies at a fixed offset intensity. As the modulation frequency decreases (dark blue LED curve), the PL AC amplitude and DC offset increase (red). The relative phase shift (exemplified by the shaded regions from the PL peak to the subsequent LED peak) also increases with decreasing frequency. (c) Schematic of experiment (ii) for three representative laser intensities at a fixed modulation frequency. Increasing laser intensity (light blue laser line) similarly increases the PL DC offset and phase shift. The PL AC amplitude decreases for increasing intensity. The amplitudes, offsets and phase shifts are exaggerated for clarity but follow the same trends observed experimentally in this work.

Focusing first on experiment (i), we measured the IMPLS response across modulation frequencies between 2 mHz and 1 Hz. To avoid perovskite memory effects, each frequency measurement was recorded at a fresh spot on the sample[225, 238]. Figure 4.3a presents the Bode plot of the phase shift across the frequency window; the positive phase shift indicates that the PL amplitude consistently led the LED amplitude across the entire range[75, 78]. Figure 4.3b shows the corresponding PL AC amplitude, and Figure 4.3c the PL DC offset. The associated uncertainty of the phase, arising from both the fitting procedure and sample inhomogeneity, ranged approximately 1% and 10%, depending on the applied frequency. This uncertainty was calculated based on repeated measurements across different sample points (Figure 4.11; see Section 4.9.3 for details).
Notably, both the PL amplitude and offset increased once $f \lesssim 100$ mHz. Since the incident

photon flux remained constant across all frequencies, this implies that a slow process with an onset time of $\tau_{onset} = 1/2\pi f = 1.6$ s locally improved the sample's PLQY. The increase in the PL DC offset reflects the time-averaged enhancement of the PLQY, whereas the enhancement in the PL AC amplitude quantifies the degree to which the process modulates the PLQY during the frequency sweep. Even at the lowest frequency measured (2 mHz, corresponding to $\tau_{meas.\ limit} = 79.6$ s), the sample's PLQY continued to increase. We further discuss this trend and the potential underlying mechanisms in Section 4.6.

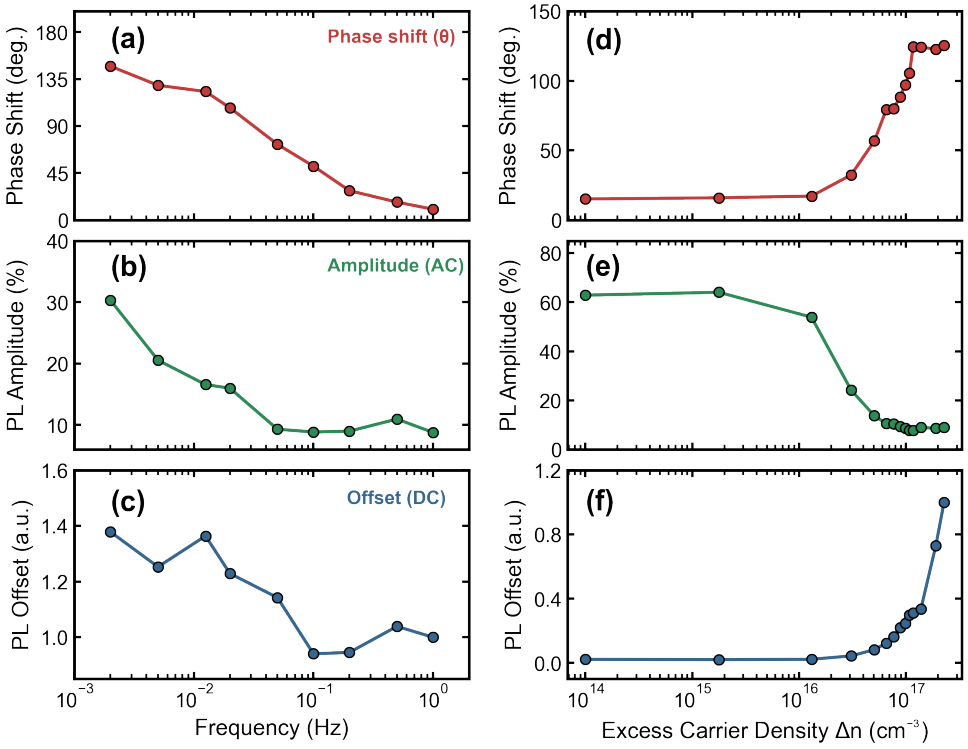

Figure 4.3: Panels (a) - (c) show results from experiment (i), corresponding to Figure 4.2b. Panels (d) - (f) show results from experiment (ii), corresponding to Figure 4.2c. (a) Bode plot of the PL phase shift as a function of LED modulation frequency. (b) PL amplitude and (c) PL offset Bode plots over the same frequency range. The PL offset was normalized to the PL offset signal collected at $f = 1$ Hz. (d) Bode plot of the PL phase shift as a function of the excess minority carrier density at a fixed modulation frequency of $f = 50$ mHz. The carrier density was calculated from the combined photon flux of the laser and LED. (e) Corresponding PL amplitude and (f) PL offset over the same Δn range, with the PL offset normalized to the signal collected at maximum Δn.

Turning to experiment (ii), the modulation frequency was fixed at $f = 50$ mHz, and Δn was varied by adjusting the laser intensity. The resulting incident photon flux (Φ) ranged from 7.7×10^{16} cm^{-2}/s (laser off) to 5.6×10^{20} cm^{-2}/s. Φ was converted to the carrier generation rate G using $G = A\Phi/W_{pvk}$, where the absorptance was $A = 72\pm2\%$, and the film thickness $W_{pvk} = 560$ nm. The excess carrier density was then obtained as $\Delta n = G\tau_{eff}(\Delta n)$, assuming

rapid spatial homogenization of the photogenerated excess carriers. This assumption is justified by the relatively high electronic mobilities ($\gtrsim 1$ cm^{2}V^{-1}s^{-1}) and long carrier lifetimes ($\gtrsim 100$ ns) for perovskite films[37, 239, 240]. The trap-assisted lifetime τ_{trap} was measured through time-resolved photoluminescence (TRPL) spectroscopy and applying the differential lifetime analysis method, as previously described in **Chapter 2**[29, 37]. The analysis yielded $\tau_{trap} = 100.5$ ns. Together with radiative and Auger recombination coefficients (determined from intensity-dependent PLQY, discussed in the following section), $\tau_{eff}(\Delta n)$ was evaluated.

Although $f = 50$ mHz was chosen here as a case study, experiment (ii) was repeated across several additional frequencies between $f = 10$ mHz – 1 Hz; these additional results are shown for completeness in Figure 4.12.

As illustrated in Figure 4.3d, the IMPLS phase remained constant up to $\Delta n_{threshold} \approx 10^{16}$ cm^{-3}, where $\theta \approx 16°$. Above this threshold, the phase increased with Δn before saturating at $\Delta n_{saturation} \approx 10^{17}$ cm^{-3}. The PL amplitude (Figure 4.3e) exhibited similar threshold and saturation points, but decreased in magnitude with increasing Δn.

Interestingly, the phase trend is qualitatively similar to the expected PLQY trend as it transitions from low injection levels (LIL) to high injection levels (HIL), provided that the doping density of the film is on the order of $10^{16} - 10^{17}$ cm^{-3}. Correspondingly, the unchanged phase and amplitude below $\Delta n_{threshold}$ would be linked to LIL, while $\Delta n_{saturation}$ would be linked to where Auger recombination begins to dominate over radiative recombination in the PLQY trend.

4.4. Phase Correlation with PLQY

To quantify this correlation, we measured the absolute PLQY across the same Δn range and on the same perovskite sample as that in Figure 4.2. Localized PLQY maps (25 μm^2) were collected as a function of Δn using a focused 660 nm laser in a custom-built integrating sphere microscopy setup (see Section 4.9.2 for measurement details). In Figure 4.4a, we overlay the measured PLQY(Δn) with $\theta(\Delta n)$. The scaling between θ (primary y-axis, in red) and PLQY (secondary y-axis, in blue) is arbitrary, but supports the correlation hypothesis. Using $\tau_{trap} = 100.5$ ns, we fit the experimental PLQY data to the analytical model:

$$\mathrm{PLQY}(\Delta n) = \frac{k_{rad}\Delta n(\Delta n + p_0)}{\Delta n/\tau_{trap} + k_{rad}\Delta n(\Delta n + p_0) + C_{Auger}\Delta n^2(\Delta n + p_0)} \tag{4.7}$$

from which, the radiative and Auger recombination coefficients, and the doping density were determined: $k_{rad} = (2.2 \pm 0.97) \times 10^{-11}$ cm^3/s, $C_{Auger} = (3.2 \pm 2.5) \times 10^{-28}$ cm^6/s and $p_0 = (4.8 \pm 3) \times 10^{16}$ cm^{-3}[31]. While C_{Auger} shows some deviation – most likely due to the limited data points collected in the Auger regime – k_{rad} and p_0 are consistent with our previously reported values for a similar perovskite composition (**Chapter 2**)[29]. The PLQY fit is shown by the blue curve in Figure 4.4a.

The phase data across the Δn range was then fit to a logarithmically-scaled Gaussian function:

$$\theta(\Delta n) = A\exp\left(\frac{-(\log_{10}(\Delta n) - \mu_{log})^2}{2\sigma_{log}^2}\right) + B \tag{4.8}$$

where $\mu_{\log}$ and $\sigma_{\log}$ represent the mean and standard distribution logarithmic space. This empirical fit is shown by the red curve in Figure 4.4a, with the fit coefficients and their uncertainties listed Table 4.1. Compared to the PLQY model, the phase shift transitions to its HIL-like regime at a higher Δn; θ reaches its maximum at $\Delta n = 8.06\times10^{17}$ cm^{-3}, compared to the PLQY peak at $\Delta n = 1.23\times10^{17}$ cm^{-3}. While this shift could reflect different processes separately influencing the phase and PLQY, we postulate that it is more likely a consequence of the different setups used for the two measurements. In particular, the beam diameter of the IMPLS configuration was 6.25 times larger than the beam diameter in the PLQY system. As we will show in the next section, the laser beam size significantly impacts the overall IMPLS response.

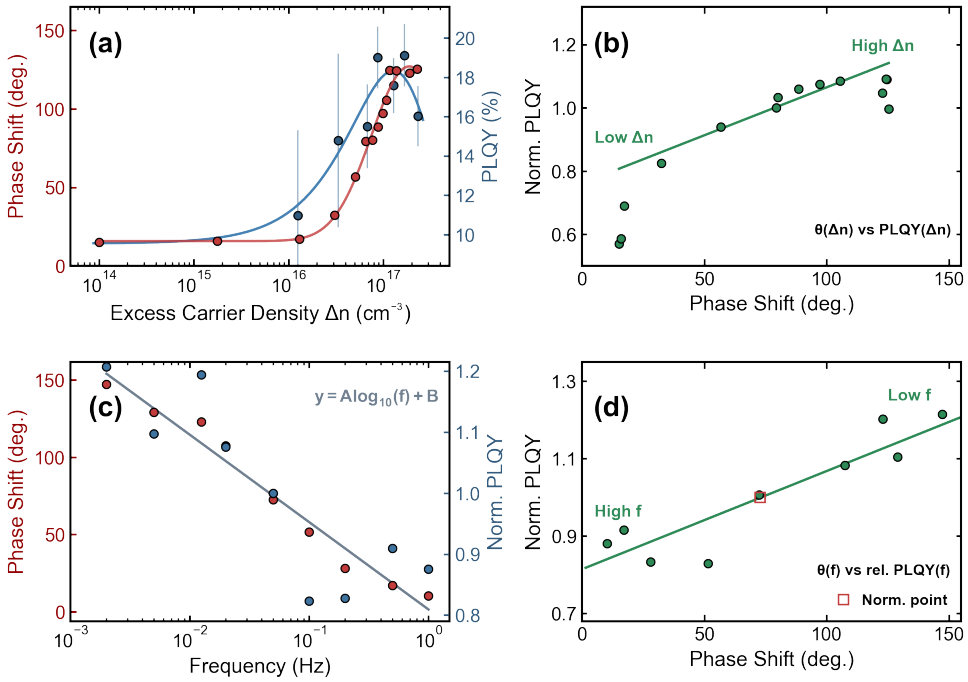

Figure 4.4: (a) PL phase shift data (red markers) as a function of excess minority carrier density (left axis). Averaged PLQY values (25 measurements per point), with standard deviation error bars are shown with the blue markers (right axis). The blue curve represents the PLQY fit using Equation 4.7 and red curve represents the phase fit using Equation 4.8. (b) Re-visualizing the data from panel (a) directly as the normalized PLQY versus θ. A linear fit (green line) was applied to the data to visualize the correlated trend. Outliers due to the difference in measurement setups at the high and low Δn limits were omitted from the fit. (c) PL intensity phase shift (red, left axis) and corresponding relative PLQY (blue, right axis) as functions of modulation frequency. Both datasets were fitted using a log-linear model, $y(f) = A\log_{10}(f) + B$. (d) Re-visualizing the data from panel (b) directly as the normalized PLQY versus θ. Both datasets in panels (b) and (d) are normalized to their common point (red square) at $f = 50$ mHz, $\Delta n = 6.6\times10^{16}$ cm^{-3}.

The relationship between the measured PLQY and the phase shift is shown in Figure 4.4b. We anticipate that under the same measurement conditions, the PLQY scales linearly with θ; this is illustrated by the fit in Figure 4.4b. The deviations from linearity at the high and low Δn limits are a consequence of the Δn offset between the curves.

Relating these observations to the frequency-dependent IMPLS response, if we consider θ to be directly correlated to the PLQY through ionic processes, then the increasing phase shift measured for decreasing frequency (Figure 4.3a) should also correspond to a rise in the PLQY. While we do not measure the absolute PLQY as a function of modulating frequency, we can quantify the frequency-dependent relative PLQY as the PL offset intensity in the IMPLS frequency-sweep measurement. Overlaying the relative PLQY with the phase shift show that they indeed both exhibit the same logarithmic dependence on f (Figure 4.4c), meaning a direct linear correlation to each other. The correlation shown in Figure 4.4d supports our claim that the PLQY and θ are linearly correlated also as a function of Δn. Both curves in Figures 4.4b and 4.4d are normalized to their common IMPLS point (f = 50 mHz, $\Delta n = 6.6\times10^{16}$ cm^{-3}, PLQY = 16.78%). The overall correlation suggests that IMPLS phase data may be considered a proxy for the PLQY under specific measurement conditions.

4.5. Impact of Beam Size and IMPLS Spatial Maps

To probe spatial variations across the perovskite film, we mapped the peak PL intensity – the maximum AC and DC PL signal – and the phase shift over a 25 µm × 25 µm area at f = 50 mHz. These measurements were performed on a different setup than described earlier, in which pixels were acquired in random order to minimize interference between neighboring points. Specifically, this approach prevented photobrightening or phase segregation effects from altering signals in adjacent pixels[41, 68].

Excitation was provided by a 405 nm pulsed laser (4 MHz repetition rate) at a fluence of 4.13 µJ/cm^2, focused to a beam radius of 1.7 µm (see Section 4.9.2 for details). The same 450 nm LED as before provided the sinusoidally modulating excitation. The resulting maps (Figures 4.5a and 4.5b) show strong spatial agreement between phase and PL intensity, further supporting that larger PL phase shifts coincide with higher PLQY.

To determine whether the beam size influences the IMPLS response, we mapped a different region of the same sample using a larger beam radius (3.2 µm) while keeping fluence, modulation frequency and all other parameters constant. The full maps are shown in Figure 4.14, while phase histograms comparing the two datasets are presented in Figure 4.5c. Notably, the histograms differ in distribution, revealing a clear beam-size dependence of the phase response. This suggests that localized IMPLS measurements are sensitive to the excitation volume and potentially to transport processes – such as ion diffusion – rather than solely local properties.

Finally, scatter plots of PL intensity versus phase for both spot sizes (Figure 4.5d) confirm the same positive correlation observed previously (Figure 4.3d), demonstrating that the general linear phase–PLQY relationship is robust across different excitation spot sizes.

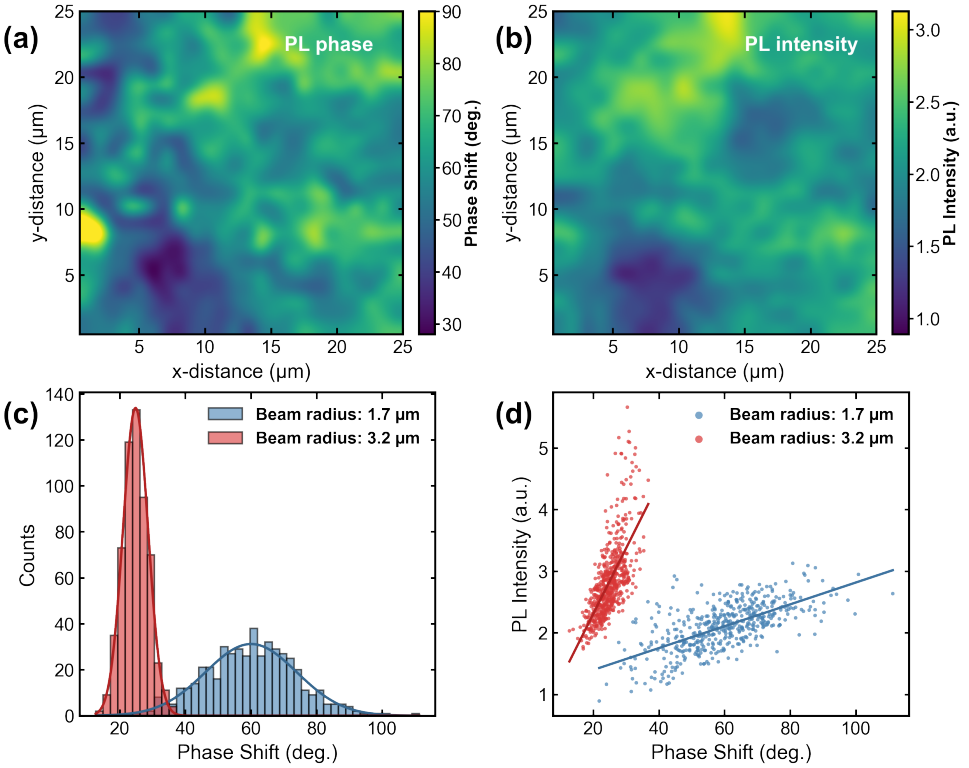

Figure 4.5: (a) Phase shift map and (b) corresponding peak PL intensity (the maximum AC and DC PL intensity signal, taken as the PLQY proxy) over a 25 µm × 25 µm region (1 µm step size) at f = 50 mHz, collected using the custom-built pulsed laser microscopy setup (Section 4.9.3). High-intensity (DC) excitation was provided by a focused 405 nm laser with a 1.7 µm beam radius, while modulating excitation was provided using the 450 nm LED. Maps are bicubic-smoothed for visualization; corresponding raw data maps are shown in Figure 4.14. (c) Phase histograms from the fluence-matched datasets, measured with laser beam radii of 1.7 µm (blue) and of 3.2 µm (red). (d) Scatter plots of the peak PL intensity versus phase shift for both beam sizes, with corresponding linear fits.

4.6. Mechanistic Insights

We now consider the underlying mechanism driving the IMPLS response observed in this work. In **Chapter 3**, we attributed the slow process with $\tau_{char,slow} \approx 77$ s to iodide vacancy diffusion across the depth of the sample. Given the similar timescales, it is possible that we are observing similar diffusive processes of mobile ions in our response here. However, unlike in **Chapter 3** – where the PL amplitude decreased with decreasing frequency – we now observe a PL amplitude enhancement[234]. To test whether this discrepancy arises from different excitation conditions, we repeated the frequency-dependent measurements without laser excitation and with the LED amplitude reduced to 20% of its

offset value. Under these conditions, the IMPLS trends are in agreement with our earlier findings (Figure 4.13 agrees with Figure 3.2). We previously attributed the decreasing PL amplitude to transverse (vertical) ionic diffusion toward the interface, leading to defect formation at the interface, thereby quenching the PL amplitude at low frequencies. In contrast, we propose that the PL enhancement observed under laser excitation (Figures 4.3b) is mediated by lateral ionic diffusion out of the beam spot[41]. At modulation frequencies comparable to the characteristic diffusion time of the mobile ions, more ionic defects can escape laterally, reducing the local defect density and thereby enhancing the PL. This lateral diffusion process is illustrated schematically by the green markers in Figure 4.6a. This schematic is constructed using the beam size and excitation conditions applied in experiment (i) in this work.

A potential driver for the ionic diffusion may arise when electronic traps of one charge carrier type are filled for longer times than the other[41, 69]. This asymmetric filling of traps would induce an electric field that decays radially with the beam spot size. The electric field would then drive charged ionic defects out of the beam spot.
As a proxy for this electric field gradient, in Figure 4.6b, we plot Δn (blue) across the same lateral distance as that in Figure 4.6a. Additionally, we plot intrinsic carrier density n_i (red), where the change in n_i is due to the bandgap difference between the iodide-rich region in the beam spot and the mixed-halide background. The quasi-Fermi level splitting (QFLS), calculated from Δn and n_i, is shown in Figure 4.6c. For these calculations, it is assumed that the charge carriers recombine close to where they were generated. If lateral diffusion of the electronic carriers were included, then the only difference would be a more gradual change in the Δn and QFLS curves, but the general physics remains the same. An important aspect of consideration is that while the LED's modulation strongly affects Δn and the QFLS outside the laser spot (Δn and QFLS amplitudes are indicated by the blue and green shaded regions), the amplitude variations in Δn and the QFLS within the 10 µm beam diameter are negligible (changes are <0.1%). This implies that mobile ions in the center of the beam spot are less likely to respond to the optical perturbation that would drive their oscillation; thus the IMPLS response is more likely to originate from the beam edge than from the center of the laser beam spot.

A notable point in this work is the PL phase shift and amplitude continued to increase even at the lowest frequency measured, corresponding to $\tau_{\text{meas. limit}} = 79.6$ s. From literature, diffusion coefficients for ionic species, such as halide vacancies in mixed halide films, typically range between $D_{\text{ion}} = 10^{-9} - 10^{-11}$ cm^2/s[48, 53, 54, 71]. We can relate these coefficients to the lateral diffusion length, L, of the ionic species by[79]:

$$L = \sqrt{D_{\text{ion}}\tau} \tag{4.9}$$

Using this equation, a time constant of τ= 79.6 s corresponds to L = 0.282 µm - 2.82 µm. These distance scales are relevant given the beam diameter size in Figure 4.6, but emphasize that diffusive ionic species well within the beam spot are not measured. As an alternative, if we consider a mobile ion to migrate from the beam center to the region where the modulated excitation becomes relevant ($L \sim$10 µm), the corresponding process time constant is estimated to range between 16 minutes and 27 hours ($f \approx$ 1 µHz - 0.1

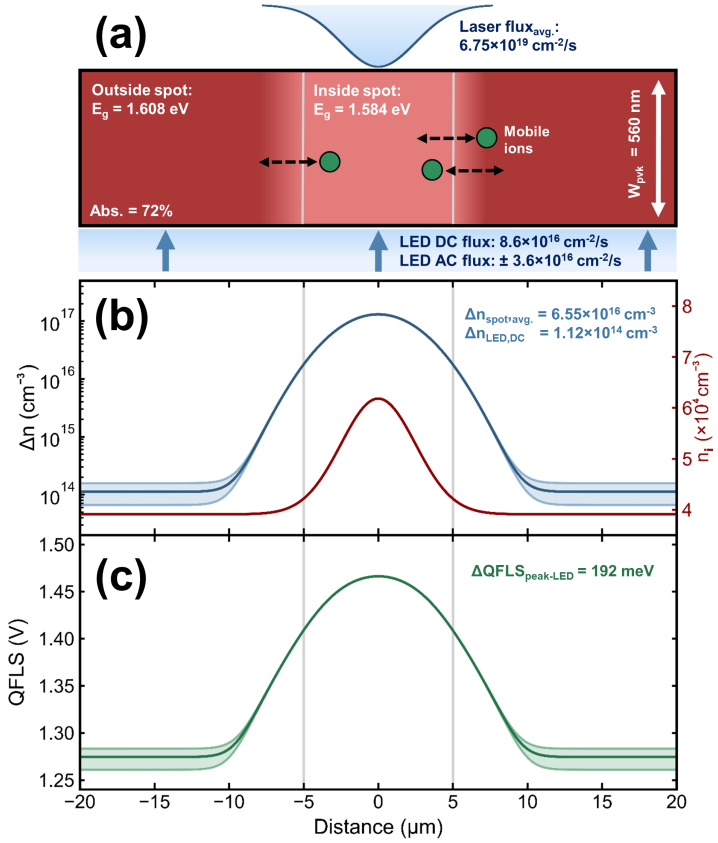

Figure 4.6: (a) Schematic of perovskite film during a frequency-dependent IMPLS measurement. Different shades of red represent the different bandgap regions due to laser-induced halide segregation. Vertical gray lines indicate the $1/e^2$ diameter of the focused laser beam. Green markers with black arrows represent the sinusoidal mobile ion oscillations that likely occur along the beam edge and at sufficiently low modulation frequencies. (b) The minority excess carrier density (dark blue curve, left axis) and its amplitude (blue shaded region) across the same lateral distance as in panel (a). The intrinsic carrier density, n_i, is shown in red (right axis). (c) The DC and AC QFLS, calculated from the values in (b) and from the extracted doping density in the PLQY fitting analysis.

mHz). This would thus explain why we do not observe PL amplitude saturation or reversal in phase trend as a function of frequency: these diffusive processes have time constants that are much longer than the measurement window. This hypothesis is corroborated by the fact that the beam diameter of the laser directly influences the absolute phase shift, even under matched irradiance conditions (Figure 4.5c).

We apply our hypothesis that lateral diffusion of mobile ions governs both the IMPLS and PLQY trends back to our original PLQY time series data in Figure 4.1. Accounting for the smaller beam diameter in the PLQY setup compared to the IMPLS setup and assuming

the change in PLQY is due to ionic diffusive effects, then the corresponding diffusion coefficient for the time constant $\tau_1 = 42.1$ s, is $D_{\text{ion},1} = 1.52 \times 10^{-10}$ cm^2/s. The slower diffusion coefficient for $\tau_2 = 664$ s is $D_{\text{ion},2} = 9.64 \times 10^{-12}$ cm^2/s. Both of these diffusion coefficients are in good agreement with the accepted literature values for ionic species, providing further evidence to support our proposed mechanism driving the correlated IMPLS and PLQY data[48, 53, 71]. This indicates that ionic defects generally dominate the PLQY for this perovskite composition[67]. In **Chapter 2**, we additionally showed that the carrier lifetime is surface-limited, ultimately implying that interfacial ionic defects are more influential than those in the bulk.

4.7. Spatially Resolving Dominant Defect Types

Building on the logic that correlating IMPLS and PLQY analysis can reveal whether mobile ionic defects pin the PLQY, we apply this approach to identify deviations from this trend across the collected maps. In principle, this enables differentiation between regions where non-radiative recombination is limited by mobile ions versus regions dominated by fixed defects or by processes with characteristic frequencies far from the applied modulation frequency.

To capture this behavior, we introduce a contrast parameter, κ, which we term the "defect contrast coefficient". This parameter is defined as the difference between the normalized PL intensity (PLI) and the normalized phase:

$$\kappa(x,y) = \frac{\text{PLI}(x,y)}{\text{PLI}_\mu} - \frac{\theta(x,y)}{\theta_\mu} \tag{4.10}$$

where PLI_μ and θ_μ are the mean values over the mapped area. From this definition, regions with $\kappa > 0$ correspond to areas where the phase shift contribution is less significant than the PL intensity contribution, suggesting that mobile ionic responses at the applied frequency play a relatively smaller role in limiting the PL. In these regions, trap-assisted carrier recombination is more strongly governed by fixed or slower-timescale defects. Conversely, regions with $\kappa < 0$ indicate that mobile ionic defects in resonance with the applied modulation frequency dominate the recombination process. This distinction allows separation of the influence of mobile ions from that of fixed defects or much slower ionic species.

Using this definition, we determined κ for both the 1.7 µm and 3.2 µm beam radii datasets. Histograms of κ for both maps are shown in Figures 4.7a and 4.7b. The corresponding spatial maps of κ for both beam radii are shown in Figures 4.7c and 4.7d, while the maps before smoothing are presented in Figure 4.15.

Notably, these maps exhibit spatial structure, suggesting that heterogeneity in defect types is resolvable using this approach. To statistically verify that the observed structure is not attributable to random noise, we calculated the global spatial autocorrelation coefficient using Moran's I[241, 242]. Calculation details and further description of this approach are provided in Section 4.9.4. For the map collected using the 1.7 µm beam radius, $I = 0.325$, while $I = 0.566$ for the 3.2 µm beam radius map. In both cases, $I > 0$ indicates statistically significant positive spatial autocorrelation, demonstrating that the κ maps capture genuine spatial heterogeneity rather than spatial noise.

While this analysis is already useful for benchmarking sample quality and identifying dominant non-radiative pathways, it can also be extended to solar cell half-stacks to probe the influence of mobile ions at transport layer interfaces. We envision that frequency sweeps of this approach, combined with PL spectral mapping, could enable differentiation of mobile defect species: lower modulation frequencies would resolve slower ionic species (for example cation versus halide migration), while red-shifted PL regions would correlate with iodide-rich domains[54, 68, 71]. Ultimately, this analysis provides a robust method to spatially resolve dominant loss pathways and distinguish competing recombination processes in perovskite films.

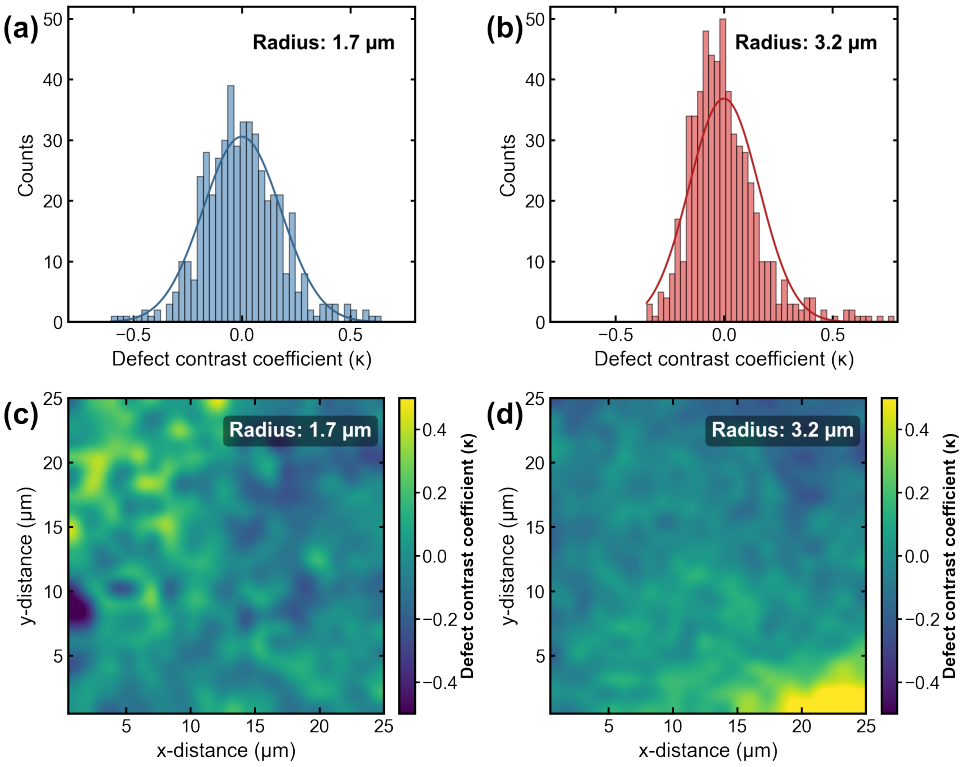

Figure 4.7: Histograms of the defect contrast coefficient (κ) for the spatial data collected using the (a) 1.7 µm and (b) 3.2 µm beam size. Corresponding spatial maps of κ for the same (c) 1.7 µm and (d) 3.2 µm radii, calculated using Equation 4.10 and shown after bicubic smoothing. Both maps exhibit notable spatial structure, while finer features are better resolved with the smaller 1.7 µm beam size.

4.8. Conclusion

In conclusion, across the narrow frequency range of 2 mHz to 1 Hz and carrier densities of $\Delta n \approx 10^{14} - 10^{17}$ cm^{-3}, we observed that IMPLS trends are directly linked to the sample's PLQY. We attribute these correlations to ionic defects diffusing laterally out of the high-intensity laser excitation spot. This interpretation is supported by the observed increase in PL amplitude at lower modulation frequencies, consistent with a reduction in the local trap-state density[41]. Additional evidence comes from beam-size-dependent mapping experiments, which demonstrate that the IMPLS response depends on the area of the high-intensity excitation, and from control measurements in the absence of laser excitation which reproduce the PL amplitude quenching described in **Chapter 3**. Together, these results indicate that mobile ionic defects – likely located at the surface – pin the PLQY across most regions of the perovskite film.

From a practical perspective, these findings suggest that lateral ion diffusion coefficients can be extracted either by extending IMPLS measurements across a broad frequency range or by systematically varying the laser beam size. Moreover, under the specific conditions where PLQY is limited by mobile ions, the phase response itself can serve as a direct proxy for material quality[67]. Spatial discrepancies between the phase response and PLQY thus provide a means to distinguish regions where non-radiative recombination is dominated by mobile ions from areas dominated by fixed or slower defects.

As an outlook, combining frequency- and beam-size-dependent IMPLS with spectral analysis could yield deeper insight into the specific defect species governing the response. With further benchmarking and complementary methods – such as direct ion-density quantification with drift–diffusion simulations – we aim to establish a comprehensive model of the coupled electronic–ionic processes underlying IMPLS in the near future[48, 53, 70, 72, 75, 77].

4.9. Supporting Information

4.9.1. Sample Fabrication

In a nitrogen-filled glovebox, two 1.5 M solutions of PbI_2 (≥99.99%, TCI) and $PbBr_2$ (≥98%, TCI) were prepared in DMF:DMSO (4:1 by volume) and stirred overnight at 70 °C. The PbI_2 solution was combined with FAI powder (≥99%, TCI) and excess DMF:DMSO solvent to yield a 1.24 M $FAPbI_3$ solution containing 10 mol% excess PbI_2. Similarly, the $PbBr_2$ solution was combined with MABr (≥99%, TCI) to form a 1.24 M $MAPbBr_3$ solution, also with a 10 mol% $PbBr_2$ excess. Both perovskite solutions were stirred for an additional 2 hours at 70 °C. The solutions were then mixed in an 80:20 ratio ($FAPbI_3$:$MAPbBr_3$), followed by the addition of a 1.5 M CsI solution in DMSO (≥99.99%, Sigma-Aldrich) to achieve the final composition $Cs_{0.07}(FA_{0.8}MA_{0.2})_{0.93}Pb(I_{0.8}Br_{0.2})_3$. The resulting solution was stirred at 70 °C for another 2 hours before cooling to room temperature and filtering through a 0.45 µm PTFE filter.

Glass substrates were cleaned by scrubbing them with a 1% Hellmanex III solution in deionized (DI) water, followed by applying sequential sonication steps (15 minutes each) in 70 °C water, acetone, and finally in isopropanol. Immediately before perovskite spin-coating, the substrates were treated under UV-ozone for 30 minutes and then transferred into the glovebox.

120 µL of the precursor solution was dispensed onto the glass substrate and subsequently spin-coated at 5000 RPM for 30 seconds after a 6 second ramp-up time. At 15 seconds before the end of the cycle, 170 µL of chlorobenzene filtered through a 0.22 µm PTFE filter was deposited as an antisolvent. The films were annealed on a hotplate at 100 °C for 45 minutes. Finally, the films were encapsulated with 60 nm of SiO_2, deposited by electron-beam evaporation (Polyteknik Flextura M508E), directly from a SiO_2 target at a deposition rate of 0.06 nm/s.

4.9.2. Measurement Details

The IMPLS setup shown in Figure 4.2a is comprised of a WITec alpha300 SR confocal imaging microscope, coupled to a S1DC405 405 nm CW diode laser (ThorLabs) and to a 450 nm light-emitting diode (Cree LED). The LED intensity and sinusoidal modulation was driven with a 33522A arbitrary waveform generator (Keysight Technologies). The 405 nm focused beam size was measured using the knife-edge technique and the power density and equivalent photon flux were determined with a wavelength-calibrated power meter (S120VC coupled to a PM100D, ThorLabs)[157].

IMPLS maps (Figures 4.5, 4.14) and uncertainty statistics (Figure 4.11) were obtained using a home-built pulsed laser microscopy setup. A tunable laser (Chameleon Discovery NX, Coherent) set to 405 nm was coupled to a pulse picker (pulseSelect, APE) to produce pulses (80 fs pulse width) at a repetition rate of 4 MHz. The beam was spatially filtered and then focused onto the sample using a Mitutoyo M Plan APO NIR B ×50 objective. The size of the beam on the sample was adjusted by changing the focal length of the collimating lens after the spatial filter, and the spot size was calibrated using the knife-edge technique. The sample was mounted on a TRITOR 100 SG piezo stage (Piezosystem Jena), and the same 450 nm LED as above provided sinusoidal AC illumination from the rear of the perovskite sample. To collect the maps, the measurement sequence was

randomized, with each consecutive point separated by at least 5 µm from the previous measurement. The total PL signal was collected using a Kymera 193i (Andor) and a ProEM electron-multiplying CCD (Princeton Instruments).

The time-resolved photoluminescence decay trace for the thin film was obtained with a time-correlated single-photon counting (TCSPC) system (PicoQuant), comprised of a PDL 828 Sepia II, a HydraHarp, a 485 nm pulsed diode laser and an Olympus ×60 Plan Apochromat water objective. The TRPL decay was measured following approximately 2 minutes of continuous light soaking. The total decay was averaged across an 80 µm×80 µm map with a 400 nm step size between each pixel. The laser repetition rate was set to 1 MHz, sufficiently low to capture the entire PL decay[13]. An arbitrary fit was applied to the TRPL signal to reduce noise, before the fit was background corrected by subtracting the noise floor from the signal. This decay is shown in Figure 4.8a. From measuring the film thickness by profilometry, absorptance, laser fluence (0.136 mJ/cm^2) and the laser spot size (1/e^2 diameter = 2 µm), the excess minority carrier density generated from each pulse was determined, $\Delta n_0 = 4.248\times10^{18}$ cm^{-3}. From this starting carrier density, the complete PL decay trace was converted to the decay of excess carrier density using $\Delta n \propto \sqrt{\text{PL}}$. Then, the differential lifetime was calculated as a function of Δn with the differential lifetime equation:

$$\tau_{\text{diff}}(\Delta n) = -\left(\frac{\mathrm{d}\ln\Delta n(t)}{\mathrm{d}t}\right)^{-1} \tag{4.11}$$

By definition, the saturation point of this curve is where $\tau_{\text{diff}} = \tau_{\text{trap}} = 100.5$ ns (Figure 4.8b)[37].

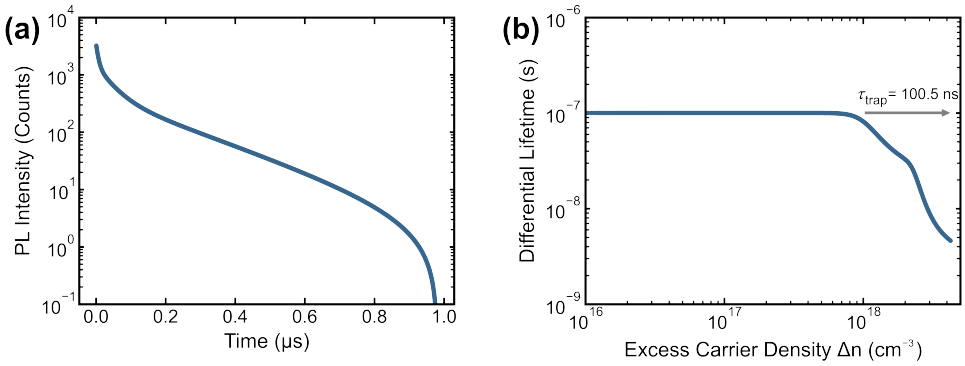

Figure 4.8: (a) Arbitrary fit of the averaged raw PL decay trace of the encapsulated perovskite thin film sample, following noise floor signal subtraction. (b) Differential lifetime as a function of excess minority carrier density, Δn. The saturation point is indicated with the gray arrow, in which $\tau_{\text{diff}} = \tau_{\text{trap}} = 100.5$ ns[37].

Photoluminescence quantum yield maps were collected using a custom-built integrating sphere microscopy setup and software (separate to the system described for IMPLS mapping above); a schematic is shown in our previous work[158]. 660 nm excitation was

provided using a 78 MHz supercontinuum laser (NKT Fianium FIU 15) coupled to an acousto-optical tunable filter (AOTF, with a Gooch & Housego AODS20200-8 driver). The AOTF was programmed to select the appropriate excitation wavelength, intensity and to modulate the laser light based on the input reference frequency. The beam radius was measured to be 800 nm using the knife-edge technique. Two PDA100A Si photodetectors were used as a beam monitor (BM) detector and as a reflection (R) detector. The BM detector collected the light emitted directly from the laser. The R detector collected light that was directly reflected or emitted within the acceptance angle of the objective lens from the integrating sphere after sample interaction. A calibrated Newport 818-UV photodetector was used to collect the transmitted and scattered light from the integrating sphere (IS), and to convert the signal intensity to photon counts. All detectors were connected to three lock-in amplifiers (LIA, Stanford Research Systems SR830). One LIA was used to set the reference frequency, which was transmitted to the AOTF and to the other LIAs. The reference frequency was set to 1.253 kHz. Four reference measurements were performed: a blank to calibrate the PDA100A detectors, a filter leakage reference, a 100% transmission reference, and a 100% reflection reference. The reflection reference was measured with a silver coated mirror placed at the same position as the sample during the PLQY measurement (ThorLabs PF10-03-P01). 700 nm short-pass and long-pass filters (placed in front of the reflection and IS detectors) were used to separate the absorptance and PL data, respectively. In addition to selecting the laser intensity using the AOTF, ND filters were applied to sweep the intensity range. The sample was mounted on an external piezo stage while in the integrating sphere, enabling the 5 µm×5 µm PLQY maps to be collected.

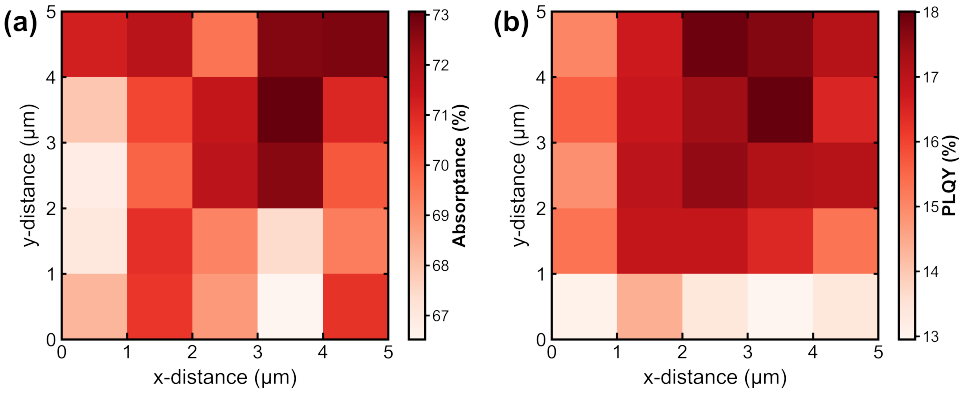

Figure 4.9: (a) Absorptance map of the perovskite thin film measured under an incident photon flux of $\Phi_{exc} = 5.88 \times 10^{20}$ cm^{-2}/s. Within this map, the average absorptance and standard deviation are $A = 70.1\%$ and $\sigma_A = 1.9\%$. (b) Corresponding PLQY map for the same area. The average PLQY and standard deviation within the map are PLQY= 16.0% and $\sigma_{PLQY} = 1.6\%$.

For every measurement, the emission data was obtained first, then the absorptance (A) data was collected. After calibration to convert the raw detector signals to number of photons (Φ) and accounting for the reference measurements, the PLQY was determined

using the standard:

$$\text{PLQY} = \frac{\Phi_{PL}}{\Phi_{\text{abs}}} = \frac{\Phi_{PL,R} + \Phi_{PL,IS}}{\Phi_{\text{exc}} \times A} \tag{4.12}$$

where $\Phi_{PL,R}$ and $\Phi_{PL,IS}$ represent the number of emitted photons incident on the R detector and the IS detector. The IS detector was used to collect both transmission, T, and scattering, S. With the short-pass filters before the detectors, the absorptance was calculated using $A = 1 - R - S - T$. Exemplary maps of the absorptance and PLQY are shown in Figure 4.9.

4.9.3. Supporting IMPLS Characterization

To maximize the signal-to-noise ratio across IMPLS measurements with different frequencies, different integration times were applied to acquire the spectra. To account for the differences in the integration times, the PL DC offset was scaled relative to the LED offset in each spectrum, as the absolute LED offset was constant for all measurements. Thus:

$$PL(f)_{\text{DC,relative}} = \frac{PL(f)_{\text{DC,counts}}}{LED(f)_{\text{DC,counts}}} \tag{4.13}$$

Where counts represent the integrated CCD counts for each spectrum. The PL amplitude was defined as the ratio between the PL peak value and the PL offset. Typically for other modulated techniques at high frequencies, the response amplitude is also scaled by the amplitude of the input parameter to correct for any frequency-dependent system response. However, given the low modulation frequency range explored in this work, the LED amplitude did not vary as a function of frequency (Figure 4.10) and so the PL amplitude did not need to be corrected further.

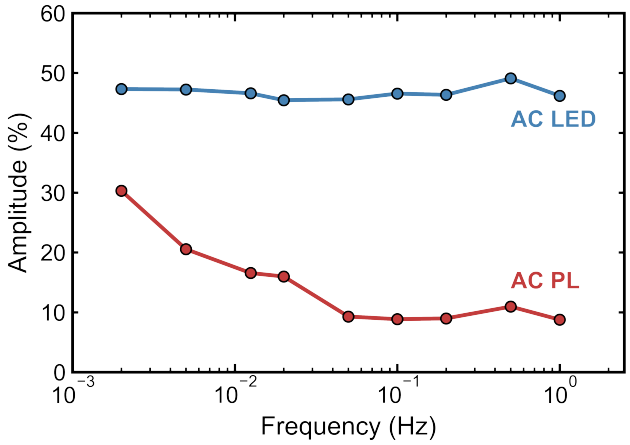

Figure 4.10: Comparison between the LED amplitude (blue) and the PL amplitude (red) as a function of frequency. The LED amplitude is independent of frequency, signifying that the change in the PL amplitude is due to the sample-related processes.

To estimate the uncertainty arising from both the fitting procedure and sample inhomogeneity, we performed repeated measurements at three modulation frequencies (f = 100, 50, 20 mHz) across different points on the sample. For the 100 mHz and 50 mHz cases, N = 400 data points were collected, while for the 20 mHz case only N = 47 data points were obtained due to the longer measurement time required. The resulting histograms of the phase shift distributions are shown in Figure 4.11. At all three frequencies, the distributions are well described by Gaussian statistics (solid curves). As illustrated by the inset, the extracted standard deviation (σ) of the fits decreases with increasing frequency. The relative error, defined as RE = $100\% \times \sigma/(\mu\sqrt{N})$ with respect to the mean (μ), ranged between 1.5% and 7% for the three measured frequencies. The offset in the absolute phase values relative to Figure 4.3a arises from the different excitation conditions and beam size; these statistical measurements were collected using the custom-built ultrafast laser setup with 405 nm pulsed laser excitation.

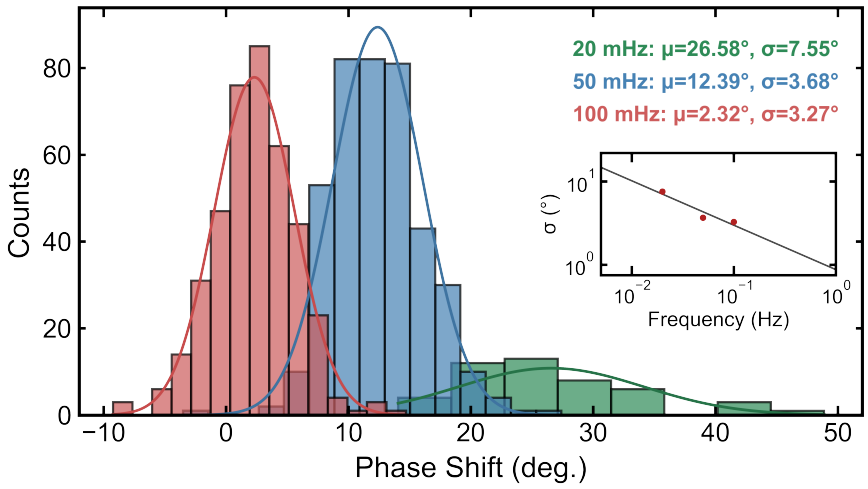

Figure 4.11: Histograms of the phase shift distributions measured at three modulation frequencies: f = 100 mHz (red), 50 mHz (blue) and 20 mHz (green). Solid curves indicate Gaussian fits to the data, from which the mean μ and standard deviation σ were extracted. The inset shows the frequency dependence of σ, with the dark gray line indicating the fit.

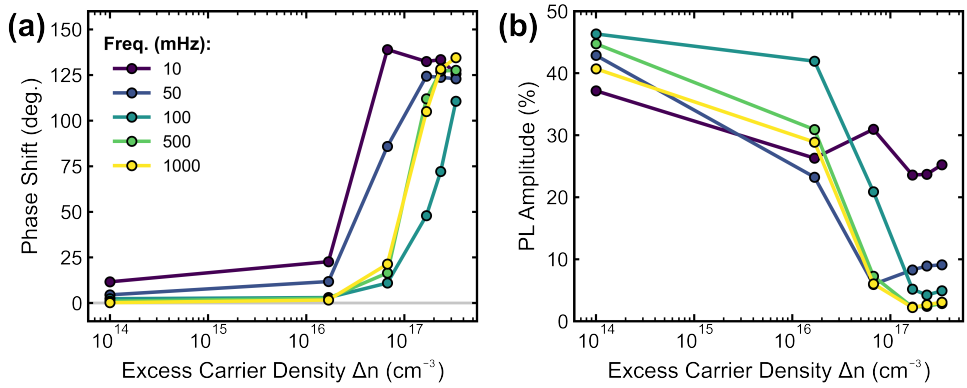

Figure 4.12: Line scans of the (a) PL phase shift and (b) PL amplitude as functions of Δn. Each color represents a different frequency applied during the measurement, labeled in the top left corner in panel (a).

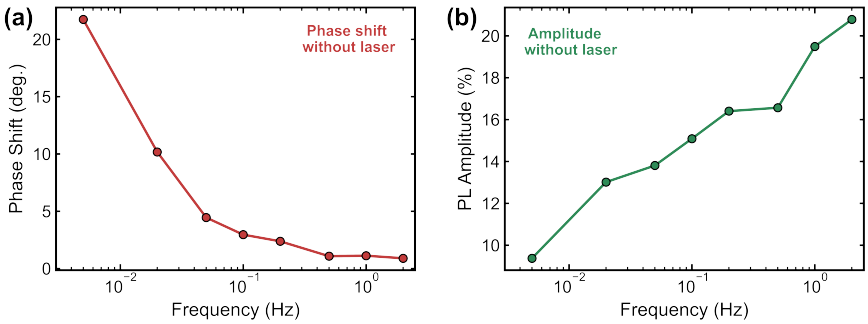

Figure 4.13: (a) PL phase shift and (b) PL amplitude as functions of modulating frequency without the additional laser excitation. For this measurement, the LED amplitude was reduced to 20% of its offset value. The sample's amplitude is reduced as frequency is reduced and the extent of the phase shift is significantly reduced without the additional laser excitation, compared to Figure 4.3. These trends in panels (a) and (b) agree with those observed for a similar perovskite composition in **Chapter 3**[234].

Table 4.1: Parameters obtained from fitting $\theta(\Delta n)$ to the logarithmically-scaled Gaussian model (Equation 4.8). The associated uncertainties of this empirical model were determined directly from nonlinear least-squares analysis.

A (deg.)	B (deg.)	μ (cm^{-3})	$\mu_{\log}$	$\sigma_{\log}$
111.1 ± 4.5	15.81 ± 3.3	$(1.88 \pm 0.16) \times 10^{17}$	17.27 ± 0.04	0.398 ± 0.038

4.9.4. Supporting IMPLS Maps Analysis

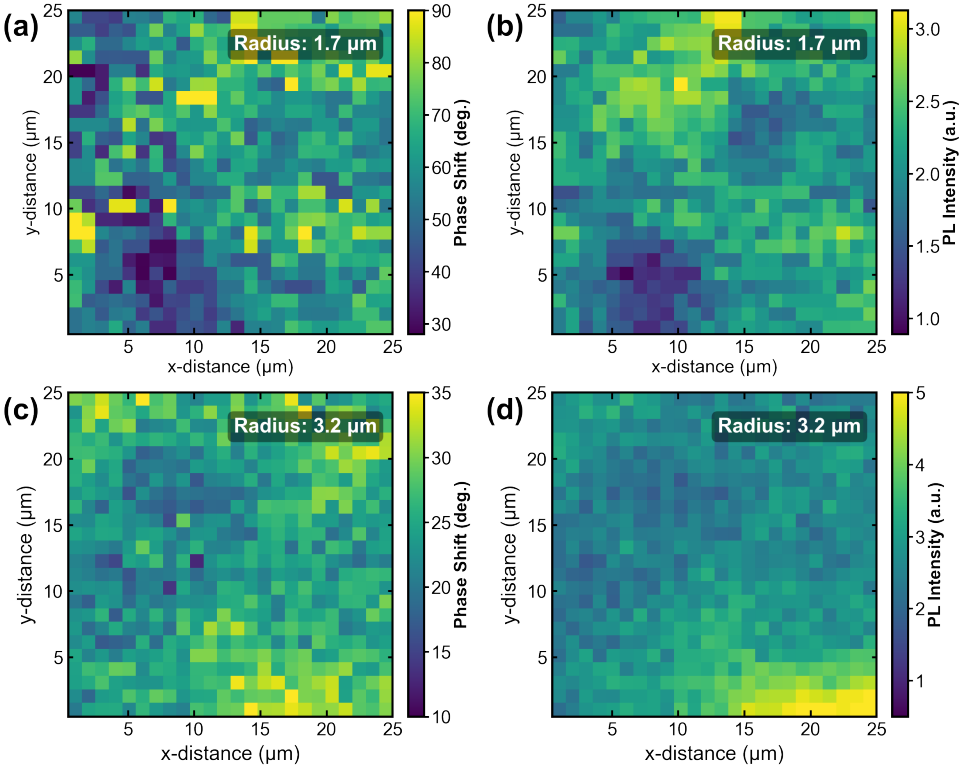

Figure 4.14: (a) Phase shift and (b) PL intensity raw signal maps (before bicubic smoothing) for a beam radius of 1.7 µm. (c) Phase shift and (d) PL intensity raw signal maps for a beam radius of 3.2 µm. The 3.2µm measurement was performed on a different area of the same sample, at matched fluence and with the same modulation frequency (f = 50 mHz).

To quantify whether the observed κ maps exhibit spatial structure beyond random noise, we calculated the global Moran's I statistic for spatial autocorrelation[241]. Moran's I quantifies spatial autocorrelation on a scale from $I = -1$ (perfect dispersion) to $I = 1$ (perfect clustering), with $I = 0$ corresponding to spatial randomness. While Moran's I is widely used in geographical applications, it has recently also been applied to analyze chemical disorder with scanning transmission electron microscopy (STEM) maps[242]. Moran's I for a map containing N pixels is defined as:

$$I = \frac{N}{\sum_i \sum_j w_{ij}} \frac{\sum_i \sum_j w_{ij}(x_i - \bar{x})(x_j - \bar{x})}{\sum_i (x_i - \bar{x})^2}, \tag{4.14}$$

where x_i is the value at pixel i, $\bar{x}$ is the mean value over all pixels, and w_{ij} is the spatial weight between pixels i and j. Specifically, w_{ij} determines whether a pair of pixels is considered close enough to contribute to the measure of spatial autocorrelation. Here, we adopted a nearest-neighbor weighting scheme: we set $w_{ij} = 1$ if pixel j is one of the four nearest neighbors of pixel$i$, and $w_{ij} = 0$ otherwise.
Both κ maps contain $N = 625$ pixels. Statistical significance was assessed using permutation testing with 5,999 random reassignments of pixel values to spatial locations for both κ maps of different beam radii. In both cases the p-values were $< 10^{-4}$, indicating highly significant positive spatial autocorrelation.

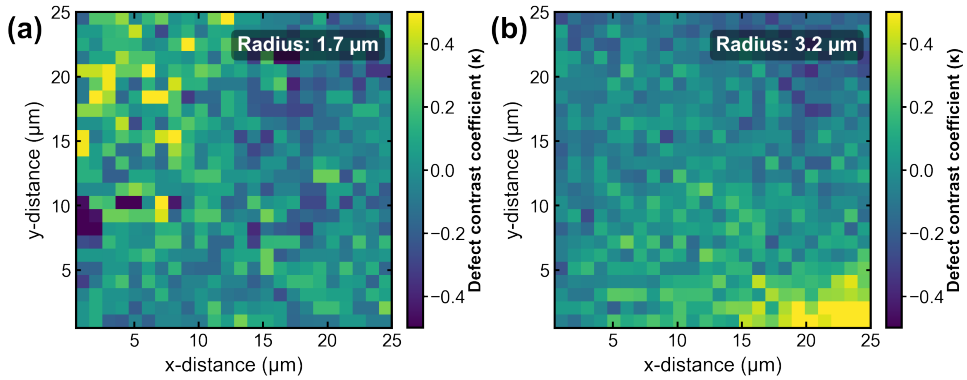

Figure 4.15: Defect contrast coefficient (κ) maps obtained using Equation 4.10 for beam radii of (a) 1.7 µm and (b) 3.2 µm, prior to bicubic smoothing.

5

Theme & Variation
Influence of Halide Composition on Spectrally Resolved IMPLS

Intensity-modulated photoluminescence spectroscopy (IMPLS) is a frequency-domain characterization technique that probes ionic processes and dominant recombination pathways in halide perovskite materials. A key advantage of IMPLS is its ability to resolve photoluminescence (PL) spectra as a function of modulation frequency – a capability that is impossible with purely electrical techniques such as impedance spectroscopy. For halide perovskites in particular, the PL spectrum offers additional chemical information relating to the local halide composition and chemical disorder. In this chapter, we apply a variation of IMPLS to spectrally track the PL peak energy and bandwidth for a triple-cation, mixed-halide perovskite composition across a modulation frequency window from 2 mHz to 1 Hz. The results reveal spectral responses that are distinct from our previously reported PL intensity trends. To identify the dominant halide species influencing the response, we measure IMPLS on four simplified perovskite compositions, $MAPb(I_xBr_{1-x})_3$ where $x = 1, 0.8, 0.5, 0$. The results indicate that bromide contributes little to the signals obtained across the frequency range. Moreover, the onset frequency differences between the pure-bromide and pure-iodide samples align with the diffusion coefficient differences reported in the literature. These findings demonstrate the additional benefits of spectrally resolving the IMPLS response – providing chemical insight into reactive species and enabling improved modeling through joint analysis of spectral and intensity components.

This chapter is based on:

Sarah C. Gillespie, Agustin O. Alvarez, Veronique S. Gevaerts, L.J. (Bart) Geerligs, Gianluca Coletti, Bruno Ehrler, and Erik C. Garnett. Resolving Mobile Ionic Contributions in Halide Perovskites through Frequency-Domain PL Analysis. *Submitted* (2025).

Author contributions:

SCG fabricated the samples, performed the measurements, and wrote the manuscript. AOA, VSG, LJG, GC, BE, and ECG provided feedback and supervision.

5.1. Introduction

Despite achieving power conversion efficiencies on par with record efficiencies of silicon solar cells, large-scale commercialization of perovskite photovoltaics (PV) is hindered by their limited operational stability[9, 171, 243]. While extrinsic degradation pathways, such as those induced by moisture or oxygen, can largely be mitigated through advanced encapsulation strategies, intrinsic instability arising from ion migration remains a major challenge[65, 174, 175]. Due to their low migration energies, ionic defects readily redistribute across the perovskite layer in solar cells under even moderate electrical bias or illumination[45, 49]. These defects can accumulate at interfaces and chemically react with charge transport layers or screen the electric field, which can alter both carrier extraction efficiencies and recombination rates over time[25, 58]. Such processes complicate both the accurate assessment of device efficiency and the development of reliable long-term stability testing protocols[81, 244, 245].

In this context, supporting electrical characterization methods, such as transient and frequency-domain techniques, have been employed to quantify ionic properties, including activation energies and diffusion coefficients, in complete devices[48, 53, 70, 76, 79, 246].

Among the available frequency-domain techniques, impedance spectroscopy (IS) is widely utilized for characterizing perovskite solar cells[75, 247]. In IS, a small sinusoidal electrical perturbation is applied to the device, and the resulting response is measured as a function of frequency[75, 78, 213]. Typically, the perturbation is introduced through a voltage modulation while the current response is recorded, although the inverse configuration is also possible with IS[78]. The response is characterized by both the amplitude of the current $|\widetilde{I}|$ and the relative phase shift θ between the applied and measured oscillating signals. Together with the voltage amplitude $|\widetilde{V}|$, the impedance transfer function is defined as

$$Z = \frac{|\widetilde{V}|}{|\widetilde{I}|} \exp(i\theta) \tag{5.1}$$

from which the real and imaginary components of the impedance can be extracted and represented in Bode or Nyquist plots. Distinct processes with characteristic relaxation times can be resolved across the frequency range; these processes are then physically interpreted using representative equivalent circuit (EC) models or drift–diffusion simulations[48, 74, 194]. IS can be performed under different offset voltages, temperatures, and illumination conditions, and is often combined with corresponding transient methods. Using such approaches, electronic and ionic diffusion lengths, ion activation energies and defect densities have been derived[48, 70, 79, 248, 249].

Despite the benefits of IS for perovskite device characterization, the interpretation of ion-related IS features remains challenging. This difficulty arises from several factors, including the wide range of spectral features that can be obtained (with various Nyquist arc shapes), device degradation during the measurement (often resulting in loops in the spectra), interfacial ionic reactions and recombination at the transport layers[74, 80, 250]. The interfacial effects in particular can dominate the IS signal and obscure fundamental ionic processes[72, 83]. In response to these challenges, several studies have provided essential guidelines for ensuring that IS measurements are both correctly performed and

meaningfully interpreted[74, 75, 78, 194, 209, 251]. Nevertheless, the need for electrical contacts imposes inherent limitations on IS and on all other electrical methods.

In response to this limitation, in **Chapter 3**, we introduced intensity-modulated photoluminescence spectroscopy (IMPLS) as an optical analog to IS. In IMPLS, the modulated photoluminescence (PL) response is monitored under sinusoidal optical excitation, where the IMPLS transfer function is defined as

$$\mathrm{P} = \frac{\widetilde{\phi}_{\mathrm{PL}}}{\widetilde{\phi}_{\mathrm{exc}}} = \frac{|\widetilde{\phi}_{\mathrm{PL}}|}{|\widetilde{\phi}_{\mathrm{exc}}|}\exp(i\theta_{\mathrm{PL}}) \tag{5.2}$$

Here, θ_{PL} is the phase shift between the excitation and PL, and $|\widetilde{\phi}_{\mathrm{PL}}|/|\widetilde{\phi}_{\mathrm{exc}}|$ is the ratio of PL to excitation amplitudes (Figure 5.1a). This transfer function is analogous to the IS transfer function in Equation 5.1, allowing similar analysis procedures and Nyquist representations to be applied to IMPLS data[234].
Both IMPLS and IS offer complementary perspectives on material properties. For instance, IMPLS can be performed on perovskite films without electrical contacts, thereby avoiding complications introduced by charge transport layers. However, unlike IS, IMPLS on such films is restricted to open-circuit voltage (V_{OC}) measurement conditions.
In addition, IMPLS enables an expanded set of measurement strategies, including full-field (**Chapter 3**) and localized point (**Chapter 4**) illumination conditions. Moreover, we have already shown that IMPLS can be conducted across a broad dynamic range of offset excitation intensities, and the response can even be spatially mapped across the sample surface (**Chapter 4**).

A distinguishing feature of IMPLS, with no direct analog in IS, is the ability to resolve the spectral component of the PL response in the frequency domain. The PL spectral shape of a thin-film semiconductor is sensitive to numerous material properties, including the band gap, temperature and film thickness[86, 87, 252]. For halide perovskites in particular, PL spectral features serve as a proxy for visualizing photoinduced halide phase segregation; both the extent and kinetics of segregation can be monitored through PL time-series measurements[68, 202, 232, 253]. While some works recognize the technological novelty of halide segregation, its presence is generally regarded as detrimental to perovskite PV stability[184, 238, 254]. Consequently, PL time-series analysis – thus IMPLS in the frequency-domain counterpart – provides additional compositional information linked to material performance that is inaccessible to purely electrical characterization approaches.

In this chapter, we demonstrate that frequency-domain responses of the PL spectra can be resolved using IMPLS. We quantify the frequency dependence of the PL peak energy and bandwidth (full width at half maximum, FWHM) for the same triple-cation, mixed-halide (TCMH) perovskite studied in **Chapter 4**. We further show that the *spectral* components can be visualized using Bode and Nyquist representations. To confirm that the frequency-dependent spectral features originate from halide-specific processes, we then compare the IMPLS responses of four simplified perovskite compositions with varying halide ratios. Notably, we resolve distinct features which we attribute to different halide contributions, with the pure-bromide sample showing minimal response across the

measured frequency window. This chapter ultimately highlights the simplicity of IMPLS as a powerful characterization method for probing and differentiating ionic processes in halide perovskites.

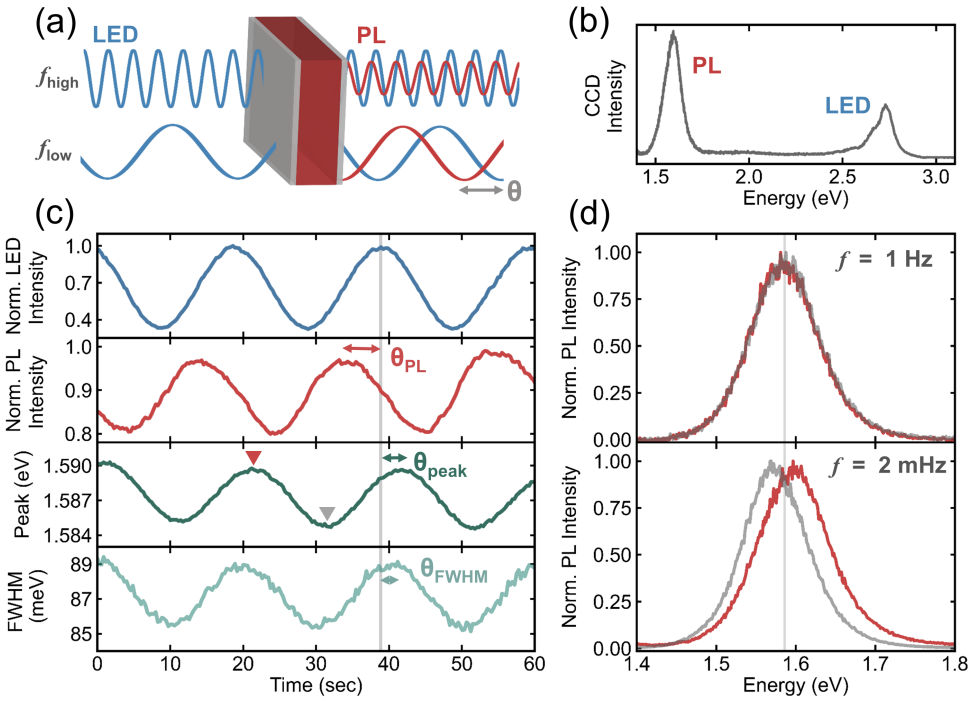

Figure 5.1: Schematic of IMPLS: optical excitation is sinusoidally modulated by a 450 nm LED source (blue), and both the PL (red) and LED outputs from the perovskite sample are monitored. The PL response, measured as the phase shift (θ) and amplitude, varies with modulation frequency, as illustrated here by the relatively stronger phase shift and larger amplitude at f_{low} compared to f_{high}. (b) Representative spectrum collected at a single time point (235 ms integration time), showing resolvable, non-overlapping PL (red) and LED (blue) peaks across the spectral range. (c) Time series at $f = 50$ mHz over 60 s (three periods), showing the integrated LED intensity (blue), PL intensity (red), PL peak energy (dark green) and FWHM (light green). The peak energy and FWHM were extracted from Lorentzian fits to each PL spectrum. The solid gray line marks a timestamp where the LED intensity reached its maximum over a cycle, and is extended across all four sub-panels as a visual guide. Distinct phase shifts are evident for all three PL components: the PL intensity leads the LED intensity ($\theta_{PL} > 0$), whereas both peak energy and FWHM lag the LED ($\theta_{peak}, \theta_{FWHM} < 0$). (d) Comparison of the PL spectral trends at $f = 1$ Hz (top) and $f = 2$ mHz (bottom). Red spectra correspond to the most blue-shifted state (corresponding to the peak energy maximum during a modulation), while gray spectra represent the most red-shifted state. These locations are indicated by the corresponding color-coded markers in panel (c). At high modulation frequencies, the PL spectrum remains effectively constant, whereas at low frequencies it exhibits measurable oscillations.

5.2. Frequency-Domain Response of the PL Spectrum

To investigate the frequency-dependent response of the PL peak energy and FWHM, we analyzed the spectral components of the data previously presented in **Chapter 4**, Figures 4.3a - 4.3c. Localized IMPLS on a SiO_2-encapsulated $Cs_{0.07}(FA_{0.8}MA_{0.2})_{0.93}Pb(I_{0.8}Br_{0.2})_3$ film was measured as a function of modulation frequency f between 2 mHz and 1 Hz. The global sinusoidal excitation was provided by a 450 nm LED, with an offset excitation intensity of 38.1 mW/cm^2 and a superimposed modulation amplitude of 15.7 mW/cm^2. A focused 405 nm laser supplied localized excitation at 33.1 W/cm^2. As previously shown in Figure 4.2a, both the LED and PL spectra were collected in time using a charge-coupled device (CCD) and spectrometer. An example of a single complete spectrum is presented in Figure 5.1b. All spectra were fit to Lorentzian profiles, which enabled us to quantify the intensity variations due to the excitation modulation over time. Representative LED (blue) and PL (red) intensity signals are shown for three periods at f = 50 mHz in the upper two sub-panels in Figure 5.1c. The fitting procedure additionally extracted the PL peak energy and the FWHM (third and fourth sub-panels in Figure 5.1c). By comparing the four traces, the relative phase shifts of the peak energy (θ_{peak}) and of the FWHM (θ_{FWHM}) are distinct from the PL intensity phase shift (θ_{PL}). This distinction already provides preliminary evidence that additional chemical information may be obtained from the spectral components of the IMPLS response.

The frequency dependence of the PL spectral shape is illustrated by comparing the spectra at the measurement limits of f = 1 Hz and f = 2 mHz in Figure 5.1d. At 1 Hz, the PL spectra show minimal variation across the modulation cycle, whereas at 2 mHz, pronounced oscillations in the spectral shape are evident. The gray traces correspond to the most red-shifted peaks and the red traces to the most blue-shifted ones (as indicated by the same color markers in Figure 5.1c). Further examples of the frequency-dependent spectral responses are presented in Figure 5.7, while applications of the switchable spectral oscillations are later described in Section 5.4.

In Figures 5.2a and 5.2b, the absolute changes in the peak energy amplitude and FWHM amplitude are presented in Bode plots. A particular advantage of resolving spectral features is that they can be tracked on an absolute scale, unlike IMPLS measurements (without an integrating sphere), where the PL intensity signal is only relative. Between f = 1 Hz and 100 mHz, both amplitudes remained constant; at lower frequencies, both increased. This inflection point occurred at the same frequency as the PL intensity response reported in **Chapter 4**, corresponding to a process onset time of $\tau_{onset} = 1/2\pi f$ = 1.6 s. Figure 5.2c further shows the phase shifts of the peak energy and FWHM relative to the LED intensity. Interestingly, these lagged behind the LED modulation, whereas the PL intensity led the LED (Figure 4.3a). Moreover, the phase shift differences between the PL intensity and LED intensity were found to be asymmetric when comparing the absolute values across all three responses, suggesting that additional relaxation pathways not captured by the intensity dynamics influence the spectral responses.

Based on the increasing phase and amplitude trends for reducing modulation frequency, it is unlikely that these variations were solely from thermal influences. In a purely thermal model with the substrate as the limiting layer, the thermal diffusivity of glass ($\alpha \approx 8 \times 10^{-3}$ cm^2/s) and thickness of the substrate (L = 1 mm) yield a characteristic thermal diffusion

time constant of $\tau_{\text{therm}} = L^2/\alpha \approx 1$ s[255]. Thus, for modulation frequencies below 1 Hz, the spectral responses would be expected to saturate. However, we observed the opposite, indicating that thermal diffusion cannot account for these trends alone. In any case, PL spectra were obtained under high-intensity localized excitation – about three orders of magnitude stronger than the modulating background – suggesting that thermal fluctuations from the LED modulation were negligible within the probed regions.

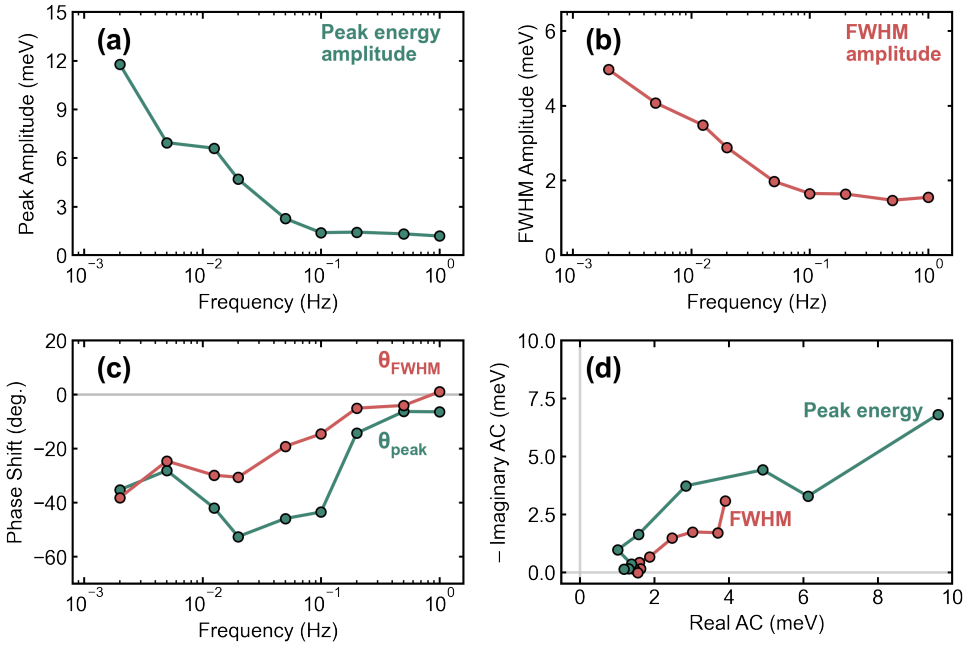

Figure 5.2: Amplitude Bode plots of (a) the PL peak energy and (b) the FWHM, measured between modulation frequencies of f =1 Hz to f =2 mHz. (c) Phase Bode plots for the same peak energy (green) and FWHM (red). (d) Corresponding Nyquist plots of the data, calculated using Equations 5.3 and 5.4 for the peak energy and FWHM, respectively. All spectral responses are plotted on the energy scale.

In addition to visualizing the spectral components in Bode plots, we distinguished the real from imaginary spectral components using Nyquist plots. To do this, we defined the transfer function of the peak energy, Pe, relative to the LED excitation as:

$$\text{Pe} = \text{Pe}' + i\text{Pe}'' = \frac{|\widetilde{\text{Pe}}|}{|\widetilde{\phi}_{\text{exc}}|}\exp(i\theta_{\text{peak}}) \tag{5.3}$$

and the FWHM transfer function, F, as:

$$\text{F} = \text{F}' + i\text{F}'' = \frac{|\widetilde{\text{F}}|}{|\widetilde{\phi}_{\text{exc}}|}\exp(i\theta_{\text{FWHM}}) \tag{5.4}$$

Since the LED amplitude remained constant across the frequency window during the measurements (Figure 4.10), we set $|\tilde{\phi}_{exc}| = 1$. This excitation normalization preserves the absolute energy scale in the Nyquist plots, as shown in Figure 5.2d. By inspecting the peak energy and FWHM arcs in analogy to IS, the spectral responses followed capacitive-like processes. This behavior contrasts with the inductive-like IMPLS response of the PL intensity, which exhibited a positive phase shift in **Chapter 4**.
A key element of this proof of concept is that the spectral features enable correlated and extended modeling on the same sample under identical measurement conditions. Just as IS is often combined with complementary electrical techniques to extract consistent parameters across methods, we argue that jointly analyzing the spectral and intensity components of IMPLS could likewise reduce model uncertainty when applying drift-diffusion simulations or optical EC fits to quantify the underlying processes[48, 70, 77].

5.3. IMPLS Analysis on $MAPb(I_xBr_{1-x})_3$ Films

Two key questions that follow from the spectral analysis are: what specifically governs the spectral response, and why does the IMPLS spectral element appear, to some extent, decoupled from the intensity element? Since the PL spectral shape is primarily influenced by the local halide composition, it is plausible that halide segregation effects play a role, with defect-driven processes further modifying both the spectral and intensity features[41, 53, 68, 232]. However, the relatively complex triple-cation, mixed-halide composition makes it challenging to attribute the observed responses solely to the halide distribution.
To investigate the influence of the X-site composition, we systematically measured the IMPLS response of pure-iodide, pure-bromide, and two mixed-halide perovskites. To reduce the A-site complexity, we focused solely on methylammonium-based films, $MAPb(I_xBr_{1-x})_3$, with $x = 1, 0.8, 0.5, 0$. This ensured that the PL response was not obscured by mixed-cation effects[17]. These films were encapsulated in SiO_2 to passivate the surfaces and minimize atmospheric influences on the PL[29, 205, 232, 256]. Fabrication details and supporting characterization are provided in Section 5.6.
We performed two IMPLS experiments on these materials. First, we measured the responses under full-field, low-intensity illumination (without additional localized excitation), which enabled direct comparison with the intensity response of the TCMH perovskite in **Chapter 3**. Second, we measured the responses under high-intensity localized excitation combined with global modulation, which allowed comparison with the IMPLS results in **Chapter 4**, along with the spectral results presented in Figure 5.2.

5.3.1. Full-Field Illumination Results

For the first experiment, the LED amplitude (AC) was set to 30% of its DC offset intensity (56.43 mW/cm^2), and the frequency was swept from 1 Hz to 2 mHz. The resulting PL intensity phase shifts (θ_{PL}) and normalized amplitudes are presented in Figure 5.3. Comparing these results with those for the TCMH compositions shown in Figures 3.2 and 4.13, we found that the pure-iodide and mixed-halide perovskites exhibited similar phase and

amplitude trends. Specifically, as the frequency decreased, the PL amplitude was reduced for all three iodide-containing perovskite films, consistent with the behavior of the TCMH perovskite. In contrast, the PL amplitude of $MAPbBr_3$ remained nearly constant across the frequency range, aside from the slight enhancement at $f \lesssim 20$ mHz, which coincided with its phase-shift inflection point.

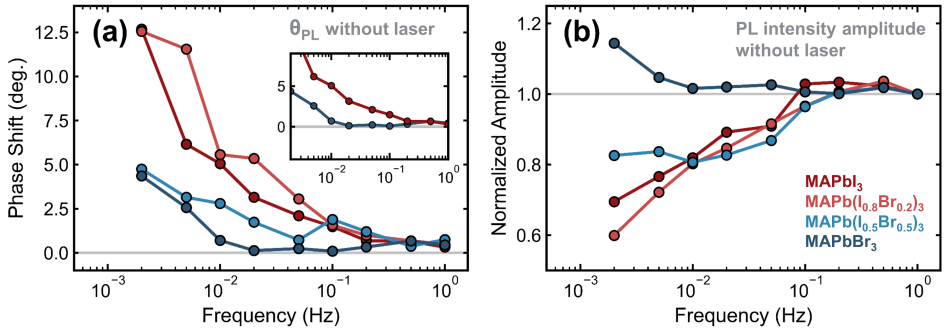

Figure 5.3: (a) Phase shift and (b) amplitude of the integrated PL intensity for four simplified perovskite compositions encapsulated in SiO_2: $MAPbI_3$ (dark red); MAPb($I_{0.8}Br_{0.2}$)$_3$ (light red); MAPb($I_{0.5}Br_{0.5}$)$_3$ (light blue); and $MAPbBr_3$ (dark blue). The pure-bromide sample exhibits a response onset frequency approximately one order of magnitude lower than that of the pure-iodide sample, as shown in the inset of panel (a). The pure-bromide sample additionally does not exhibit amplitude quenching at reduced frequencies, unlike the mixed-halide and pure-iodide perovskite samples.

The onset of this process in $MAPbBr_3$ occurred at a frequency approximately one order of magnitude lower than that of $MAPbI_3$ (10 – 20 mHz versus 100 – 200 mHz, depending on whether the onset frequencies are read from the phase or amplitude plots). For clarity, the phase components of only $MAPbBr_3$ and $MAPbI_3$ are shown in the inset in Figure 5.3. In **Chapter 3**, we ascribed the process observed in the millihertz range to the diffusion of mobile halide species across the film thickness[234]. Since the ionic diffusion coefficient is proportional to the characteristic diffusion frequency, $D_{\text{ion}} \propto 1/\tau_{\text{char,diff}} \propto f_{\text{char,diff}}$, and assuming the same mechanism for the $MAPbI_3$ and $MAPbBr_3$ samples, the order-of-magnitude difference in onset frequencies is – within uncertainty limits – consistent with the difference in ionic diffusion coefficients reported in the literature from transient ion drift measurements: $D_{\text{ion}} = (3.21 \pm 2.8) \times 10^{-9}$ cm^2/s for $MAPbI_3$ and $D_{\text{ion}} = (8.4 \pm 3.9) \times 10^{-10}$ cm^2/s for $MAPbBr_3$[54, 71]. These comparisons under full-field illumination therefore suggest that measured IMPLS responses were mediated primarily by iodide transport, with comparatively little contribution from mobile bromide species.

Notably, transient ion drift measurements on mixed-halide MAPb(I_xBr_{1-x})$_3$ compositions reported similar halide diffusion coefficients across different mixing ratios ($D_{\text{ion}} \approx 7 \times 10^{-10}$ cm^2/s)[53]. This invariance in D_{ion} was attributed to halide segregation and accumulation at the transport layers, effectively creating locally de-mixed regions with diffusion coefficients comparable to those of the pure-halide perovskites. Here, the IMPLS

responses of the two mixed-halide films more closely followed the behavior of $MAPbI_3$ than of $MAPbBr_3$. Specifically, the amplitudes for both mixed-halide compositions were reduced at low frequencies to a similar extent as observed for the pure-iodide sample. This suggests that iodide dominates the IMPLS response – likely due to halide de-mixing – even in mixed-halide films.

5.3.2. Localized Spot High-Intensity Results

Next, we performed IMPLS with additional localized excitation using a 405 nm laser focused onto a spot area of 78.5 μm^2. This experiment enabled comparison with the spectral features discussed in Section 5.2, as well as with the IMPLS intensity trends presented earlier in **Chapter 4**. The LED amplitude was increased to 55% relative to its DC offset, which was kept identical between the full-field and localized experiments. The 405 nm laser was applied at a fixed intensity of 2.74 W/cm^2. The approximate order-of-magnitude reduction in excitation intensity compared to the experiments in **Chapter 4** was necessary as photodegradation occurred in iodide-containing $MAPb(I_xBr_{1-x})_3$ samples at higher excitation levels.

We first monitored the PL evolution in the time domain. Figure 5.4 presents the integrated PL intensity time series under laser excitation only (without LED excitation and without excitation modulation); the corresponding time-resolved spectra for the four samples are provided in Figure 5.9. The mixed-halide films exhibited pronounced temporal evolution under continuous excitation, whereas the single-halide films remained comparatively stable.

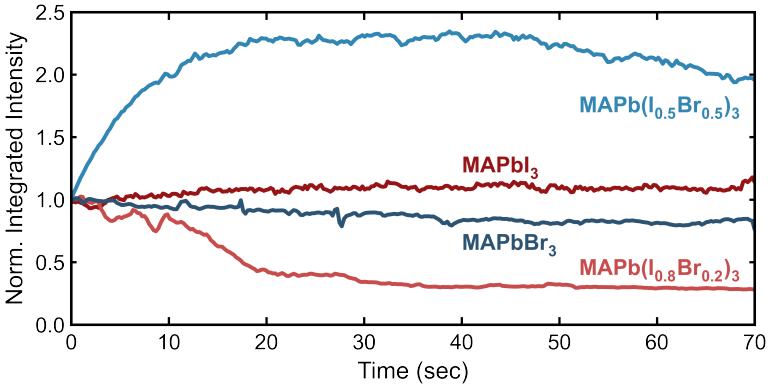

Figure 5.4: Integrated PL intensity time series for the four $MAPb(I_xBr_{1-x})_3$ compositions, measured with a focused 405 nm laser (without LED excitation and without modulation) at an intensity of 2.74 W/cm^2.

Figures 5.5a and 5.5b present the IMPLS response of the integrated PL intensity for the four sample compositions. These results follow the general trends observed for the TCMH perovskite in **Chapter 4**: as the modulation frequency decreased, both the phase and amplitude increased. A notable exception was the amplitude response of the

$MAPb(I_{0.8}Br_{0.2})_3$ sample, which initially decreased at higher frequencies before increasing again at lower frequencies. Broadly, the mixed-halide samples exhibited stronger IMPLS responses compared to the pure-halide samples, consistent with the PL time-series behavior in Figure 5.4. This difference is likely due to a combination of factors such as halide phase segregation and the higher defect densities previously reported in mixed-halide films, both of which can influence PL emission[41, 53, 68].
The larger absolute phase values observed in Figure 5.5a compared to Figure 5.3a are a consequence of the high-intensity localized excitation. As established in **Chapter 4**, the IMPLS response depends not only on the modulation frequency but also on the excess carrier density. Assuming that these perovskite films had comparable thicknesses and effective carrier lifetimes to the TCMH film ($W_{pvk} \sim 500$ nm, $\tau_{eff} \sim 100$ ns), the combined LED offset and localized laser excitation produced an average excess carrier density of approximately $\Delta n \sim 10^{16}$ cm^{-3}. Given that reported doping densities of these compositions are of similar magnitude, the larger absolute response values were likely driven by the transition to high-injection conditions[53].
Another difference between the phase response in Figure 5.5a and that in Figure 5.3a is the higher-frequency inflection point observed for $MAPbBr_3$ ($f \approx 50$ mHz). This shift suggests changes in ion-transport properties. One possible explanation is that the high-intensity excitation facilitated mobile-ion transport in $MAPbBr_3$, similar to light-enhanced ion transport previously reported for $MAPbI_3$[257]. Another possibility – relevant to all samples – is that local, laser-induced recrystallization may have altered ion-transport characteristics; grain-size variations are known to influence ion migration in $MAPbBr_3$ materials[61]. Such material changes could also contribute to the atypical FWHM phase variation for $MAPbBr_3$ (Figure 5.10), since grain-size differences affect optoelectronic properties including defect density and carrier lifetime[134]. However, these interpretations remain tentative and do not fully account for all features observed in the IMPLS response.

The corresponding IMPLS trends of the peak energy phase shift and amplitude are shown in Figures 5.5c and 5.5d, with additional spectral components presented in Figure 5.10. Unlike the TCMH peak energy response (Figure 5.2c), all $MAPb(I_xBr_{1-x})_3$ samples exhibited peak energies nearly perfectly out of phase at frequencies above approximately 20 mHz. At lower frequencies, however, the mixed-halide compositions diverged in their phase. This divergence indicates that the spectral behavior of mixed-halide systems (including TCMH) is at least partially governed by interactions between the two halide species, rather than by the response of a single halide or an unrelated process. This finding supports the conclusion that intensity and spectral IMPLS responses originate from somewhat distinct processes: halide segregation drives the spectral changes, whereas mobile-ion transport dominates the intensity response[68].

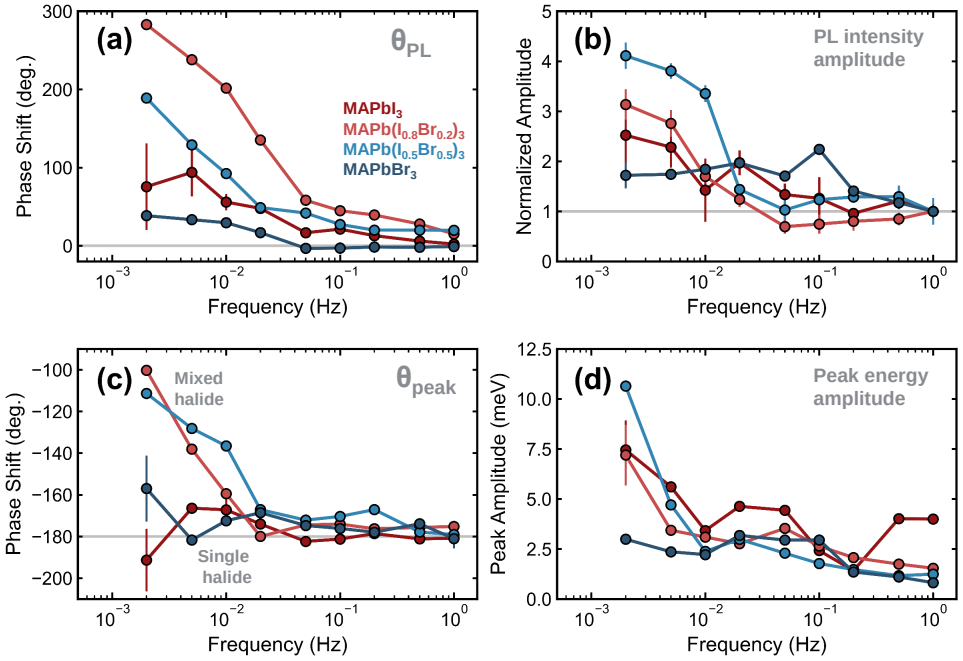

Figure 5.5: Localized spot IMPLS results for the four MAPb(I_xBr_{1-x})$_3$ compositions. (a) Phase shift and (b) amplitude of the integrated PL intensity. The increasing amplitude and large phase shifts for reducing frequency are generally consistent with the TCMH perovskite response presented in **Chapter 4**. The phase shift of the pure-bromide sample is similarly reduced compared to the iodide-containing samples, agreeing with the trends from Figures 5.3 and 5.4 (c) Phase shift and (d) amplitude of the peak energy for the same samples. While the amplitude trends are similar, the phase shifts of the peak energy are most pronounced in the mixed-halide samples, indicating that their peak energy response most likely arises from halide phase segregation and remixing.

5.4. Potential Applications

Before concluding, we briefly consider potential applications of the controllable PL spectral shapes achievable through modulated excitation. Specifically, the switchable PL spectra shown in Figure 5.1d – transitioning from a non-oscillating state at high f to an oscillating state at low f – highlight the potential of IMPLS in controllable optical materials. Switchable optical materials are an emerging research direction in photonics and biomedicine, with promising applications in ultrafast data processing, low-energy neuromorphic systems and fluorescence probes for bioimaging and sensing[258–263].

A broader application for spectrally resolved IMPLS is in PV and optoelectronics diagnostics and benchmarking. IMPLS offers a powerful, contact-free diagnostic tool for assessing perovskite material quality while directly probing ionic processes. When combined with established optical methods such as time-resolved photoluminescence spectroscopy (**Chapter 2**) and photoluminescence quantum yield analysis (**Chapter 4**), IMPLS provides complementary insights into the complex ionic–electronic interactions – including compositional insights from the spectral element – in halide perovskite films and perovskite

solar cells. With further development, IMPLS could be integrated into pilot-line and manufacturing workflows to enable scalable quality control and guide the design of more stable, high-efficiency perovskite optoelectronic devices.

5.5. Conclusion

In conclusion, we demonstrated as a proof of concept that the PL spectral components – specifically, the PL peak energy and FWHM – exhibit measurable responses under modulated excitation that are distinct from the corresponding PL intensity response. These spectral responses can be visualized on *spectral* Bode and Nyquist plots using the peak energy and FWHM transfer functions as we have defined here. We propose that quantifying these three separate PL components could reduce model uncertainty in fitting procedures for optical EC models and drift–diffusion simulations, analogous to the way impedance spectroscopy is typically combined with complementary electrical techniques[48, 70, 77].
We also performed a simple compositional analysis across two sets of experiments to elucidate the relative impact of the halide species on the IMPLS response. First, from the full-field experiment, we deduced that the reduction in IMPLS amplitude (signifying a loss process similar to that described in **Chapter 3**) is most likely mediated by mobile iodide rather than bromide species, since the $MAPbBr_3$ amplitude increased at sufficiently low frequencies. The approximate order-of-magnitude difference in onset frequencies between the pure-iodide and pure-bromide perovskites is consistent with the corresponding difference in their diffusion coefficients, supporting our previous hypothesis that the processes in both materials are diffusive in nature[53, 54, 71].
Second, from the high-intensity localized experiment, we found that the mixed-halide compositions exhibited stronger responses than the pure halides in terms of their spectral components, suggesting that these features are additionally influenced by combined halide effects, such as phase segregation, rather than a single halide dominating the spectral signal[68].
Despite this, complex additional factors may also contribute to the IMPLS response. Mixed-halide systems generally exhibit reduced ion-migration activation energies and higher mobile ion densities, which may lead to stronger IMPLS signals[53]. In addition, grain boundaries in polycrystalline thin films can facilitate ionic diffusion and introduce additional recombination pathways[61, 264]. Therefore, complementary measurements – such as electrical benchmarking of ion transport and spatially resolved mapping of mobile versus fixed defects under different excitation conditions (as implemented in **Chapter 4**) – will be essential for confirming the origins of the observed trends in both the spectral and intensity responses across various sample types and compositions.

5.6. Supporting Information

5.6.1. Fabrication and Characterization of Perovskite Films

The triple-cation, mixed-halide perovskite was fabricated as previously described in Section 4.9. To prepare the $MAPb(I_xBr_{1-x})_3$ films, under nitrogen conditions, PbI_2 (≥98%, TCI) and $PbBr_2$ (≥98%, TCI) were separately dissolved in 4:1 DMF:DMSO solvent mixtures (1.5 M) by stirring at 70 °C for three hours. The resulting PbI_2 and $PbBr_2$ solutions were then added to pre-weighed MAI (≥99%, TCI) and MABr (≥98%, TCI) precursors and further stirred (70 °C for two hours) to yield 1.24 M solutions of $MAPbI_3$ and $MAPbBr_3$, respectively. Parts of each solution were then combined in the appropriate ratios to prepare the $MAPb(I_{0.8}Br_{0.2})_3$ and $MAPb(I_{0.5}Br_{0.5})_3$ solutions, which were further stirred at 70 °C for one hour. The four solutions were then cooled to room temperature and filtered with 0.22 µm PTFE filters before spin coating.

Glass substrates were prepared by cleaning with 1% Hellmanex III solution in deionized (DI) water. They were then sonicated in 70 °C DI water (15 minutes), acetone (15 minutes) and finally isopropanol (15 minutes) before they were thoroughly dried under a high-pressure nitrogen gas flow. The substrates were further treated under UV-ozone for 45 minutes before they were immediately transferred to the glovebox. 120 µL of the perovskite solution was deposited on the glass substrates and then spin-coated at 5000 RPM for 30 seconds, with an 833 RPM/s ramp time. Halfway through the spin-coating procedure, the solution was quenched using 170 µL of filtered chlorobenzene. The perovskite films were then annealed at 100 °C for 20 minutes each. All films were encapsulated in 60 nm of SiO_2 by electron-beam evaporation (Polyteknik Flextura M508E) at 0.06 nm/s from an SiO_2 target.

5.6.2. Characterization of Mixed Halide Thin Films

X-ray diffraction (XRD; Bruker D2 Phaser with Cu Kα radiation) and absorbance spectra (PerkinElmer LAMBDA 750 UV/Vis/NIR spectrophotometer) were measured for the $MAPb(I_xBr_{1-x})_3$ samples to confirm material formation and to determine the band gaps[151]. The corresponding XRD patterns, absorbance spectra and instantaneous PL spectra are shown in Figure 5.6, with the extracted band gaps summarized in Table 5.1.

Table 5.1: Band gaps of $MAPb(I_xBr_{1-x})_3$ extracted from Tauc fitting of the absorbance data[151]. The uncertainties of the fitted band gaps are ±1 meV.

Composition	$MAPbI_3$	$MAPb(I_{0.8}Br_{0.2})_3$	$MAPb(I_{0.5}Br_{0.5})_3$	$MAPbBr_3$
Band gap (eV)	1.596	1.688	1.871	2.297

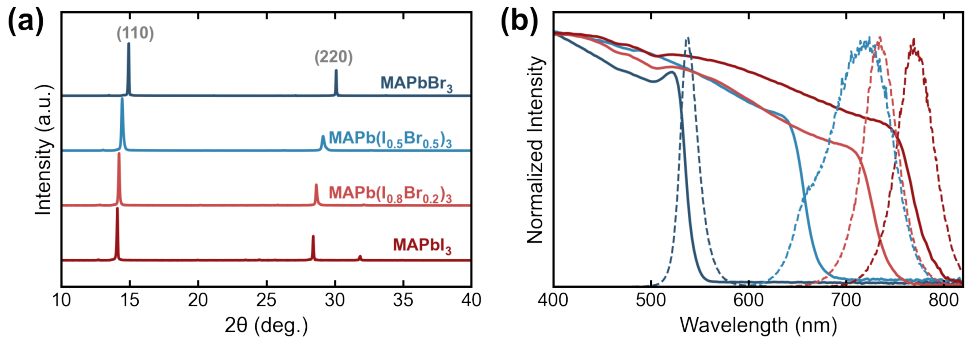

Figure 5.6: (a) XRD patterns of the MAPb(I_xBr_{1-x})$_3$ samples confirming perovskite formation. (b) Normalized absorbance spectra (solid curves) and PL spectra (dashed curves). The PL spectra were collected approximately 15 s after excitation was applied.

5.6.3. Supporting IMPLS Results

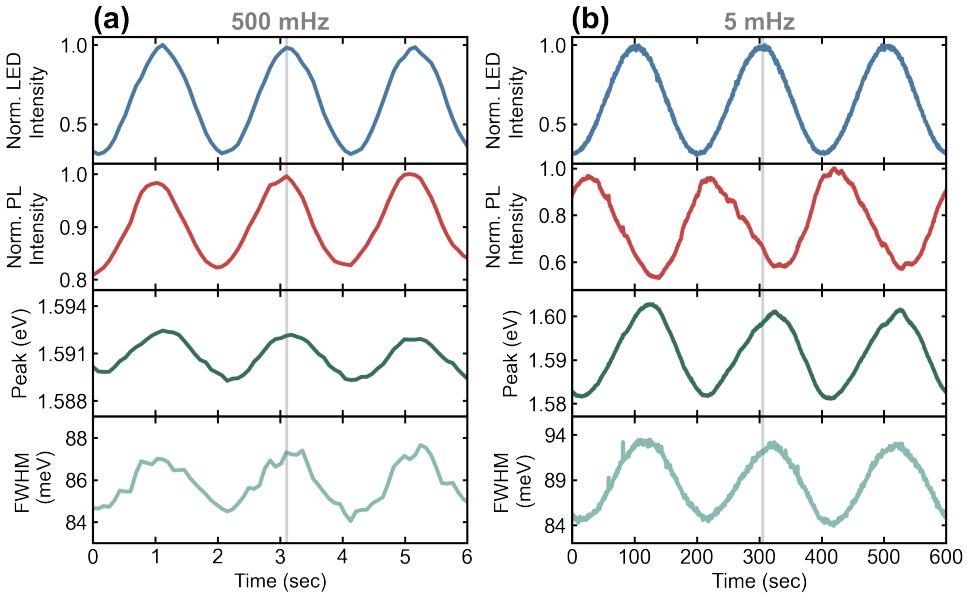

Figure 5.7: Time series at (a) f = 500 mHz (6 s), and (b) f = 5 mHz (600 s) of the integrated LED intensity (blue), integrated PL intensity (red), PL peak energy (dark green) and FWHM (light green). The gray solid line in both panels guides the eye to indicate frequency-dependent changes in the PL intensity and spectral responses.

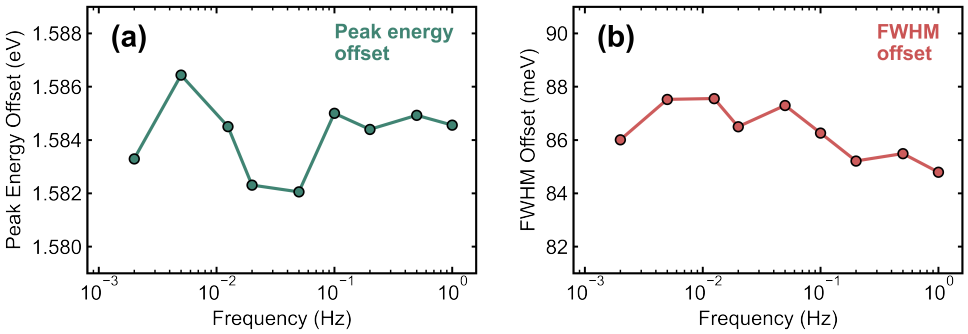

Figure 5.8: (a) Peak energy and (b) FWHM DC offsets for the TCMH perovskite sample corresponding to the results in Figure 5.2.

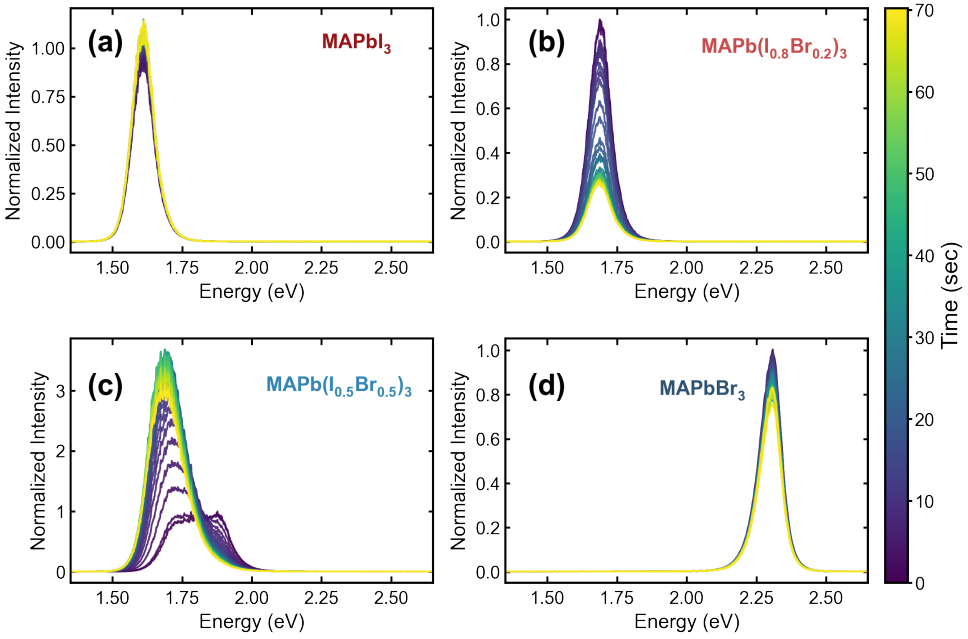

Figure 5.9: Stacked PL spectra (45 traces) of (a) $MAPbI_3$, (b) $MAPb(I_{0.8}Br_{0.2})_3$, (c) $MAPb(I_{0.5}Br_{0.5})_3$, and (d) $MAPbBr_3$ recorded between $t = 0$ and $t = 70$ s with an integration time of 83 ms. Spectra were obtained under 405 nm laser excitation only (without additional LED illumination or modulation).

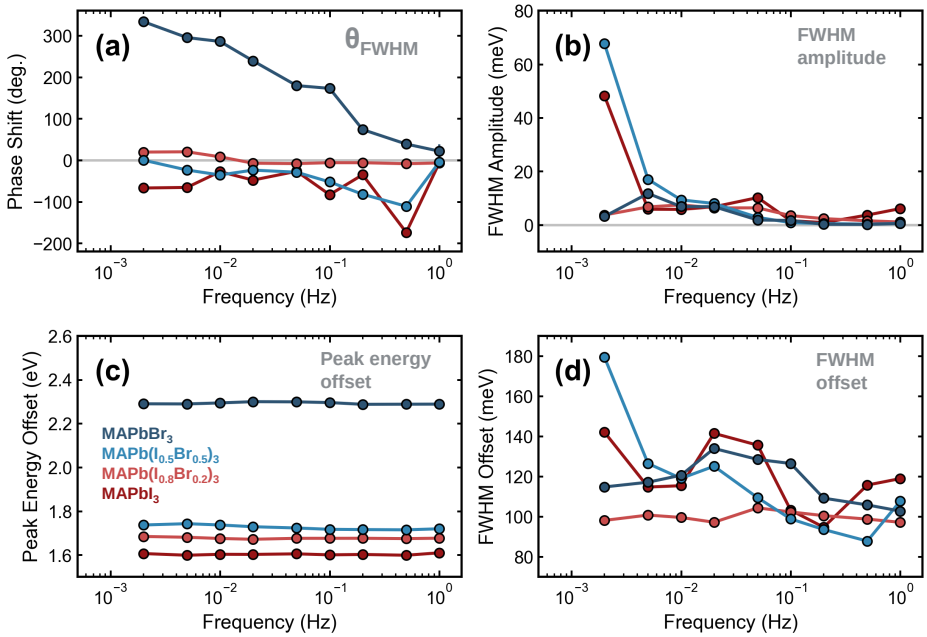

Figure 5.10: Supporting localized IMPLS results. (a) Phase shift and (b) amplitude of the FWHM for the four MAPb(I_xBr_{1-x})$_3$ perovskite compositions. (c) Peak energy DC offset and (d) FWHM DC offset for the same compositions.

6

Interludes

Excitation Intervals Enhance Performance in Perovskite Solar Cells

Halide perovskites face intrinsic stability challenges, primarily due to light- and bias-induced ion migration. To mitigate ion-mediated degradation on operationally relevant timescales, this chapter investigates how introducing brief periodic intervals of light and darkness (LD cycling) can stabilize the average efficiency of perovskite films and devices. Systematic photoluminescence (PL) studies reveal that dark intervals on the order of seconds significantly suppress non-radiative recombination and slow degradation. The extent of PL enhancement depends on the duration of the dark time, the material composition, and – critically – the sample's age. Remarkably, LD cycling increases PL by more than sevenfold even in aged samples that would otherwise undergo photodarkening under continuous illumination. Device measurements similarly show that LD cycling enhances power conversion efficiency compared to continuous illumination and mitigates deterioration over extended operation. We tentatively attribute these effects to coupled ionic-electronic processes at the perovskite interface, where dark periods allow mobile defects to redistribute and partially recombine, thus reducing the defect density and enabling performance enhancement. This strategy highlights a potential pathway to dynamically preserve, or even improve, perovskite performance in future optoelectronic applications.

This chapter is based on:

Sarah C. Gillespie, Jarla Thiesbrummel, Veronique S. Gevaerts, L.J. (Bart) Geerligs, Jeroen J. de Boer, Gianluca Coletti, and Erik C. Garnett. Excitation Intervals Enhance Performance in Perovskite Solar Cells. *ACS Applied Materials & Interfaces* **17**, 59476-59485 (2025).

Author contributions:

SCG fabricated perovskite films, performed all measurements and wrote the manuscript. JT fabricated the devices. JB fabricated the substrates for lateral devices. VSG, LJG, GC and ECG provided supervision. All authors contributed feedback on the manuscript.

6.1. Introduction

Metal halide perovskite semiconductors have huge potential in photovoltaics (PV), with a certified record device efficiency currently at standing at 27.3%[9]. Their impressive performance stems from excellent optoelectronic properties, including long charge-carrier lifetimes and diffusion lengths[9, 13, 41, 265, 266]. However, they typically also contain high densities of mobile ionic defects which, under even moderate illumination conditions or electrical bias, can migrate through the film, consequently altering the electronic properties over time[46, 47, 49, 204, 267]. These optoelectronic changes are particularly evident in the complex dynamics observed in photoluminescence (PL) time-series measurements[41, 69, 207, 208, 232, 236, 268]. The variability in perovskite PV performance has also prompted extensive discussion on how to accurately measure the efficiency of devices, including pre-conditioning steps and measurement scan rates[269, 270].

Recently, it has been shown that under standard test conditions for perovskite PV cells, ion accumulation at the perovskite surface leads to a reduction in the carrier extraction efficiency and can induce degradation in the device[25]. Despite this, computational studies indicate that the open-circuit voltage (V_{OC}) is higher with mobile ions present than if the ions were absent, due to their positive effect on the energy level alignment within the device[40, 42, 43]. Thus, the power conversion efficiency ultimately depends on the interplay between these ion-induced opposing effects.

Even with some ion-induced performance deterioration during a day of illumination, devices can (albeit not always) recover their initial performance after being stored in the dark overnight[59, 63, 245, 271–273]. This day/night recovery concept has resulted in renewed discussions on how to fairly assess the true degradation rate in perovskite solar cells compared to the standard stability tests based on crystalline silicon PV technology[81, 244]. Here, however, we do not address the various methods used to restore devices to their full performance between day and night. Rather, we focus on harnessing the light-responsive behavior of ions to yield an enhanced average power output during the course of a single day. Specifically, we report that dynamic illumination conditions – controlled intervals of light and darkness – can drive the perovskite into an optimized state. In this state, PV performance can be maximized without compromising device stability. The enhanced quasi-equilibrium state is sustained only due to the alternating cycles and, once the cycling is removed, the device performance deteriorates as anticipated. The results are corroborated with systematic PL studies, which further elucidate how dynamic light/dark cycling enhances the performance as a function of perovskite composition, dark time, sample age and more. These findings indicate that introducing unconventional light-harvesting protocols during the day, for example by incorporating switchable glass onto the device or by periodically tilting the module, could potentially mitigate the ion-induced degradative effects at the interface, thereby addressing some of the key remaining stability issues pertaining to perovskite solar cells[171, 274, 275].

6.2. Photoluminescence Results

We begin by presenting the PL time series observed for our triple-cation, mixed-halide perovskite films with a chemical composition of $Cs_{0.07}(FA_{0.8}MA_{0.2})_{0.93}Pb(I_{0.8}Br_{0.2})_3$, hereafter referred to as the 80:20 composition. All films were fabricated on glass substrates and encapsulated in 60 nm of electron-beam evaporated SiO_2; fabrication procedures are described in Section 6.8.1. Figure 6.1a shows a representative normalized PL time series acquired from the 80:20 sample during an excitation sequence alternating between illumination and darkness; Figure 6.5 presents the corresponding resolved PL spectra together with the time-series evolution of the PL peak wavelength over the same temporal range. Excitation was provided by a focused 405 nm continuous-wave laser set at an intensity of 220 W/cm^2 (2784 suns equivalent). At the start of the illumination, the PL initially exhibited an exponential decay with a decay constant of $\tau_{decay,1} = 0.72 \pm 0.01$ s. Approximately 10 seconds into the light soaking, the PL started to recover at a rate of 0.34 %/s (relative to the starting value); then, from 50 seconds onward, the PL continued to improve more slowly at a rate of 0.07 %/s. This dynamic behavior is typical for perovskite thin films and is attributed to several competing processes, most likely involving the initial formation of light-activated electronic traps, followed by a slow trap-annihilation process involving recombination of iodide vacancies and interstitials[41, 69, 204, 234, 273, 276]. When excitation was removed for 5 minutes and subsequently reapplied to the same spot, the PL intensity at the start of the second illumination sequence (indicated by the blue marker) was 2.02 times higher than at the end of the previous light soaking period (red marker). Even after the exponential decay ($\tau_{decay,2} = 7.64 \pm 0.02$ s), the PL intensity remained at least 1.14 times higher than the PL maximum during the first illumination period. This "dark-induced" enhancement was found to be reproducible across multiple cycles, as demonstrated by the continually enhanced third and subsequent light/dark (LD) periods.

The LD enhancement effect was not limited to the 80:20 perovskite composition. Among the five additional films tested in this work, all showed improved PL after a 5-minute dark period between illumination, which is illustrated by comparing the blue and green bars to the red bars in Figure 6.1b. The complete time series are shown in Figure 6.6a. This effect was observed regardless of whether the sample photobrightened or photodarkened during the initial 10 minutes of illumination as indicated by the relative positions of the red bars in the chart. These observations imply that the mechanism driving the LD enhancement is not simply a continuation of any light-activated photobrightening or photodarkening processes and therefore cannot be explained by any light-only mechanisms described in the literature[41, 69, 192, 273].

The magnitude of this LD PL enhancement depends not only on composition but also on the illumination intensity (Figure 6.6b), the interface applied (Figures 6.6c and 6.6d), and, importantly, the duration of the dark times. As shown in Figure 6.1c, the PL enhancement was maximized after a 10-minute dark interval, while the reversibility of the LD enhancement – the rate at which the sample returned to its initial state – was found to be significantly slower than its onset. Even after keeping the sample in the dark for 15 hours, the PL remained higher at the start of its second illumination period than at the end of its first illumination period. In Figure 6.1c, the PL signal was normalized to its value at the

end of the initial 5-minute light soaking to simplify the comparison. The blue curve represents the integrated PL measured immediately after the sample was illuminated, while the green curve represents the PL signal 5 minutes into the second light soaking period after the indicated dark time. To ensure that perovskite memory effects did not interfere with the experiment, the measurements for different dark times were all performed on a fresh spot on the sample[225, 238]. Notably, the long-term elevated PL was to some extent found to occur on samples that were exposed to full-field illumination and left in the dark for 12 hours (Figure 6.7a). This test was conducted with a blue, unfocused LED (10 mW/cm^2) and performed entirely under nitrogen conditions, further indicating that the dark enhancement is not the result of any atmospheric reactions[205, 207, 232, 256, 277].

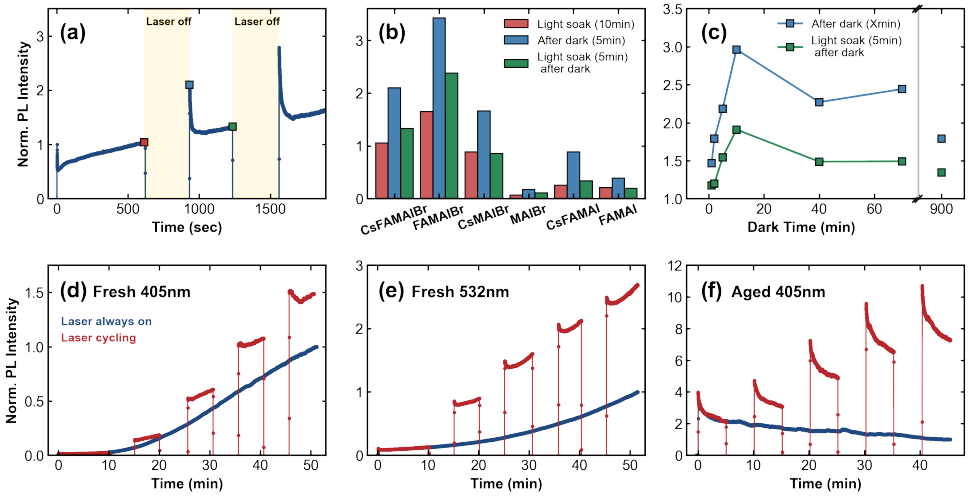

Figure 6.1: (a) Representative PL trace obtained from a SiO_2-encapsulated triple-cation, mixed-halide perovskite film (80:20 composition). (b) Comparative PL signals of the six perovskite compositions investigated in this work, with the bar chart values normalized to the PL at the start of the first illumination sequence. The x-axis labels show the chemical abbreviations for each composition, which are listed in full in Table 6.1. (c) The PL enhancement of the encapsulated 80:20 film as a function of dark time, where the blue points signify the PL immediately after re-excitation, similar to the blue marker shown in (a). The green points show the PL after five minutes of continuous illumination following the dark period. (d) Comparative PL time series measured under continuous excitation and under light/dark (LD) cycling. The sample was fabricated one day prior to measurement. (e) The same comparative PL time series but using 532 nm excitation. (f) The PL time series measured on the same sample shown in panel (d), but acquired after three weeks of dark storage in N_2. Panels (a) - (c) were measured at a 2784 suns-equivalent illumination, while panels (d) - (f) were measured at a reduced 1114 suns-equivalent illumination. Measuring under different intensities enabled us to elucidate the relative importance of applied intensity compared to other factors, such as the dark time duration.

6.3. Light/Dark Cycles Enhance Perovskite PL

Based on the initial PL findings, we next considered whether the rate of LD enhancement mirrored that of light-only enhancement. We compared the continuous and LD PL time series for a freshly prepared 80:20 sample under reduced illumination conditions (88 W/cm^2, 1114 suns equivalent). This comparison was conducted one day after fabrication, with the sample stored in the dark under nitrogen between fabrication and measurement. Figure 6.1d depicts the continuous illumination (blue) and LD cycling (red) signals, in which the PL was normalized to the end value of the continuous series. Despite having received a reduced total photon dose, the PL intensity in the LD cycling measurement was 50% higher after 50 minutes than in the continuous illumination case. A similar enhancement trend was observed using a focused 532 nm laser at comparable suns-equivalent intensity (Figure 6.1e). The relevance of the excitation energy is that the LD enhancement does not seem to be related to any selective PbI_2 formation process, as previously shown to occur at high excitation energies in $MAPbI_3$ films[192].

Importantly, after three weeks of dark nitrogen storage, the sample photodarkened when exposed to continuous illumination (blue curve, Figure 6.1f). Comparing the continuous curves in Figures 6.1d and 6.1f is significant; the only difference between these measurements is the age of the sample. This highlights that the dynamic PL response is potentially most critically influenced by the sample history, in addition to known variables such as excitation energy, excitation intensity, and applying pulsed rather than continuous excitation[69, 192, 232, 253]. Even under inert conditions with a fully encapsulated sample, intrinsic material changes significantly affect the PL response over time. This behavior may be related to factors such as strain relaxation, evaporation of volatile molecules at the edges of the film, or changes in the Urbach tail states[278–280]. Nevertheless, despite the change from photobrightening to photodarkening, applying LD cycles still resulted in a 7.3-fold PL enhancement at the final point of the measurement (red curve, Figure 6.1f), further emphasizing that this dark-driven enhancement is independent of the light-driven changes.

6.4. Correlating PL with Device Performance

Building on our initial findings that local PL in perovskite films can be enhanced by LD cycling, we next investigated the effects of such LD cycles on complete perovskite solar cells with a slightly different composition; see Section 6.8 for device fabrication details and measurement procedures. We compared the local PL changes of devices with the changes in their V_{OC}. During the device's PL measurement, as illustrated in Figure 6.2a, the PL was collected from a 113 μm^2 focused area on the sample, under 405 nm laser illumination at an intensity equivalent to 278 suns. The order-of-magnitude reduction in the applied illumination in the device case compared to the films was to verify that the applied intensity was not the dominant reason for general PL trends. In contrast, the V_{OC} time series was measured at 1 sun using a simulated AM1.5G spectrum (Figure 6.2b). Both PL and V_{OC} were monitored under periodic cycling: 30 seconds of illumination followed by 30 seconds of darkness, except for a 1-minute continuous illumination period at the start of the PL experiment. These cycles are shown in red in Figures 6.2c and 6.2d, while the blue curves represent the continuous illumination measurements. Over a short 10

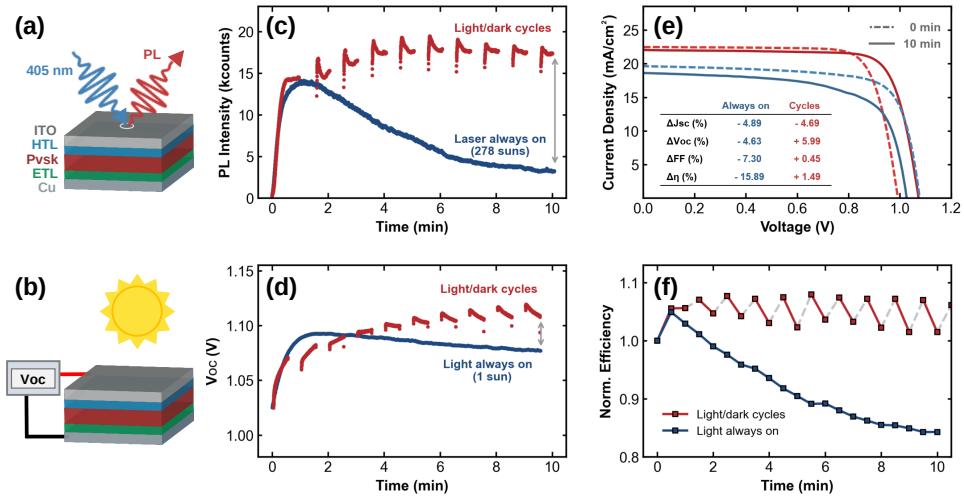

Figure 6.2: (a), (b) Schematics illustrating the measurement procedures for obtaining the solar cell's PL and V_{OC}. Panels (c) and (d) show the corresponding PL and V_{OC} time series under continuous illumination (blue) and LD cycling (red). (e) Representative JV curves comparing 10 minutes of continuous illumination (blue) with periodic 30-second LD cycles (red). The absolute differences in JV parameters arise from pixel-to-pixel variation. The dashed lines in both plots represent the starting curve, while the solid line represents the JV curve after the 10-minute experiment. Inset: table presenting the percentage change of the JV parameters for the always-on and cycled experiments. (f) Corresponding cell efficiency time series normalized to t = 0 min, highlighting the efficiency trends for the always-on (blue) and cycling (red) experiments.

minute period, both the PL and V_{OC} exhibited closely correlated dynamics. Both signals rose within the first minute, followed by a decay under continuous illumination. The accelerated degradation may be partially attributed to the interfacial reactions at the C_{60} interface, as shown in Figure 6.7b. Under LD cycling, both the PL and V_{OC} continued to increase, surpassing the continuous illumination maxima. In the second half of the experiment, both signals consistently exhibited some exponential decay, albeit with different decay constants. Upon averaging the final three cycles in both cases, $\tau_{decay,PL} = 5.3 \pm 0.2$ s and $\tau_{decay,Voc} = 27.4 \pm 0.6$ s. Interestingly, the PL decay constant of the device is similar to that of the pristine film measured earlier, despite the roughly tenfold lower excitation intensity applied to the full cell.

To quantitatively compare the differences between the solar cell's PL and measured V_{OC}, we use the established relation that linear differences in V_{OC} values correspond to logarithmic changes in PL[281]:

$$\Delta V_{OC,PL} = V_{therm} \ln\left(\frac{PL_{cycl}}{PL_{cont}}\right) \tag{6.1}$$

where PL_{cycl} and PL_{cont} are the PL intensities under LD cycling and continuous illumination, respectively. Using this equation, the PL-derived difference at the end of the

experiment in Figure 6.2c (gray double arrow) is $\Delta V_{OC,PL} = 44.8$ mV. By comparison, the directly measured $\Delta V_{OC} = 39.6$ mV at the gray double arrow in Figure 6.2d. The fact that these trends coincide despite the PL being performed under substantially higher excitation densities is striking. The nearly identical kinetics of the degradation highlight that localized high-intensity PL captures the same underlying processes as full-device V_{OC} measurements, and can serve as a reliable proxy for tracking device performance.

The magnitude of V_{OC} enhancement was found to depend on the duration of the dark time (Figure 6.8), mirroring the dependence shown in Figure 6.1c. The correlated PL-V_{OC} trends signify that the LD-driven enhancement is not the result of mobile defects diffusing out of the laser spot, thereby resulting in a local PL improvement[41]. Moreover, as shown in Figure 6.8, the V_{OC} continues to improve even after tens to hundreds of seconds of dark time – timescales comparable to the diffusion of mobile ionic species in perovskite films[45, 48, 53, 73, 82, 234]. We therefore suggest that the correlated LD enhancement is most likely driven by an interfacial, defect-mediated mechanism involving the diffusion of mobile ions across the sample and their recombination at the surface. This is corroborated by the fact that, without appropriate passivation, the PL tends to be interface-limited in perovskite devices (**Chapter 2**)[26, 41, 156, 236]. Even with the higher surface recombination from the C_{60} contact in our measured half-stack, the PL still enhanced under LD cycling (Figure 6.6)[29, 153]. This overall hypothesis is further validated by the full-field LED measurements discussed earlier in this work.

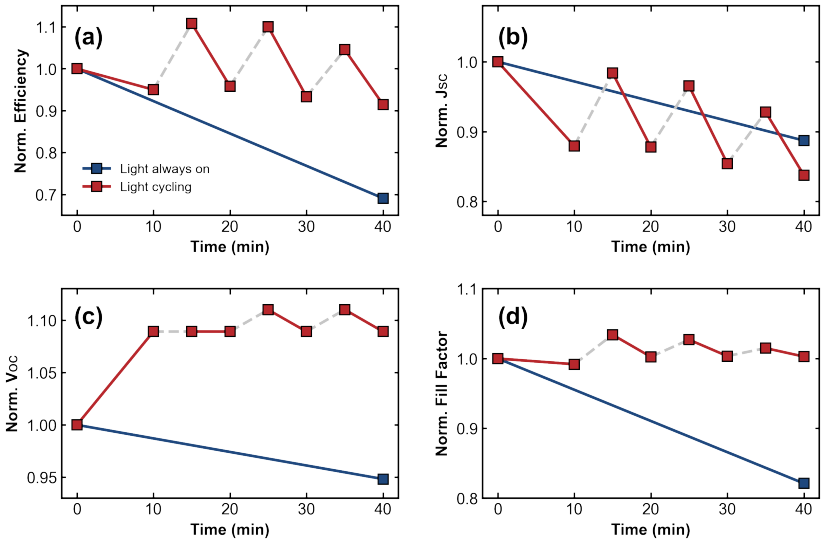

Figure 6.3: The normalized (a) efficiency, (b) J_{SC}, (c) V_{OC}, and (d) fill factor (FF) are shown for a 40-minute comparison between continuous illumination (blue) and LD cycling (red). The gray dashed lines represent the times at which the light was removed during the LD cycling measurement.

Extending to additional device parameters, we subsequently compared JV curves between devices that were illuminated continuously at 1 sun and held at V_{OC} between JV sweeps (ISOS-L1) and devices that underwent 30-second LD cycling for 10 minutes. Holding at V_{OC} between sweeps was based on community recommendations and was intended to further accelerate any rate of performance deterioration in the device[81, 271]. A representative comparison between these curves is shown in Figure 6.2e, while the tracked change in device efficiency is presented in Figure 6.2f. Comparisons between all four device parameters are shown in Figure 6.9. By reading the table inset in Figure 6.2e, the short-circuit current density, J_{SC}, in both instances was reduced by approximately the same amount, while the V_{OC} in the LD cycling case was improved compared to the continuous illumination case, which agrees with the V_{OC} tracking comparison. This ultimately led to a moderate overall efficiency enhancement in the cycling case. With a separate device, we repeated the 30-second LD cycling for 10 minutes, then measured the JV curves under continuous illumination for an additional 10 minutes to determine the steady-state changes following the brief cycling period. As shown in Figure 6.10, the performance remained stable during the 10 minutes of cycling but deteriorated over the subsequent 10 minutes without dark intervals, emphasizing that dark intervals are necessary to maintain the enhanced quasi-stable state.

We then compared devices under extended LD cycling conditions, with light and dark times resembling the timescales previously considered in Figure 6.1. The normalized device parameters of this extended test are compared in Figure 6.3. In this case, the V_{OC} enhancement trend was found to be similar to that previously observed, while the J_{SC} on average tends to decrease in the LD cycle at an average rate similar to the continuous illumination reference. Notably, the J_{SC} values measured immediately after the dark times were enhanced compared to their values at the end of the previous light soak. This reveals a correlated enhancement between all four parameters and importantly signifies that the V_{OC} enhancement does not come with a trade-off in extraction efficiency, as may be the case if the LD enhancement mechanism was due to the formation of an inert, passivating layer at the interface. Symmetric devices with Au/Cr lateral contacts also showed reduced resistance and enhanced current under cycling conditions (see Figure 6.11), where the current enhancement was found to depend on the distance between the electrical contacts. Ultimately, this means that both carrier recombination can be temporarily reduced and carrier extraction can be temporarily enhanced if a dark interval on the timescale of seconds is introduced between illumination periods.

6.5. Stabilizing Photovoltaic Performance

With the combined short-term device enhancement introduced, we next consider whether this LD cycling could mitigate the short-term device degradation known to occur over several hours of continuous illumination[63, 244, 245, 272, 273, 282–285]. In Figure 6.4a, we show the measured efficiency of our reference cell under continuous light soaking conditions for more than 5 hours. The data points indicate the times at which a full JV sweep was measured, and the blue curve represents the combined exponential and linear fit that accurately models the efficiency trend within this time frame. Similar to the earlier tests, all devices were held at V_{OC} between JV sweeps. All four device parameters

over time are shown in Figure 6.12. The efficiency decreases exponentially in the first 10 minutes of illumination, then deteriorates linearly for the remaining time. This trend was reproducible across different samples (Figure 6.13), which enabled us to confidently apply the same fitting approach to extrapolate the likely linear degradation rates for devices that underwent LD cycles. In Figure 6.4b, we show the efficiency results for a device that alternated between 39 minutes of continuous illumination and 39 minutes of LD cycling (with the continuous illumination regions shaded in light gray). All four device parameters from this measurement are presented in Figure 6.14. During the asymmetric LD cycles, the device was kept in the dark for 30 seconds after every 270 seconds of illumination. Between continuous illumination and LD cycling, the device was kept in the dark for 60 seconds to separate these periods and to "reset" the device to a state that was close to its starting performance. In Figure 6.4b, the red line represents the measured efficiency output, while the dashed black line represents the expected continuous illumination degradation rate if the device had been measured under continuous illumination. The periods of constant illumination between LD cycling exhibited steady efficiency deterioration, confirming that the trends observed within the LD cycles were due to the introduced brief dark times and not attributable to some other device effect. Even with the rapid decays that occurred during the light intervals within the dynamic LD cycles, all three cycles at 40 minutes, 120 minutes, and 200 minutes exhibited reduced overall degradation rates compared to the extrapolated linear curve. In fact, in the second and third cycles, the device efficiency even increased during the 39 minutes, emphasizing that by introducing even brief dark times, LD recovery can outcompete light-induced degradation and therefore stabilize the overall time-averaged efficiency output.

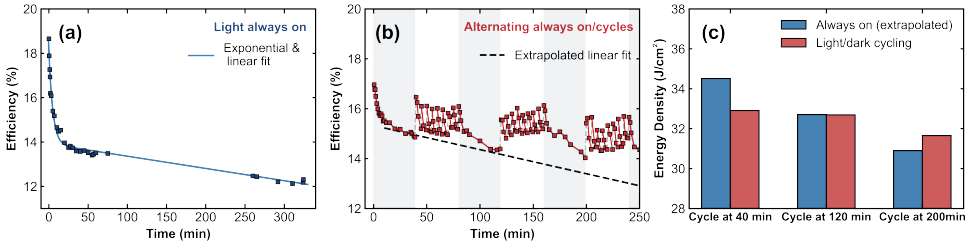

Figure 6.4: (a) Representative efficiency data for the devices studied in this work. These devices were measured under continuous 1 sun illumination conditions at AM1.5G at room temperature and indoors. The blue markers represent the points at which the JV sweeps were collected, with the combined exponential and linear fit shown by the blue line. (b) A second representative device efficiency curve plotted for alternating continuous illumination and asymmetric LD cycling periods. The red line and markers follow the actual measured data, with the black dashed line indicating the anticipated efficiency trend if the device had been continuously illuminated for the entire experiment. The gray background highlights when continuous illumination was applied, compared to the LD cycle periods (white background). (c) The total collected energy density for the 39 minutes of LD cycling (red) from (b). The hypothetical energy collected, determined from the extracted fit over the same time periods, is shown in blue.

We recognize that while there may be some relevance in stabilizing overall device performance using LD cycles, introducing dark time is only impactful if the average power output during these dynamic cycles is greater than the average power output from continuous illumination. This calculation should account for both the difference in degradation rates between the illumination conditions and the ≈10% dark time where no power is extracted at all during the LD cycles. In Figure 6.4c, we illustrate this comparison by plotting the integrated energy density harvested during the three LD cycles presented in Figure 6.4b. In blue, we additionally show the hypothetical total energy density that would be collected if the device did not undergo LD cycling. Comparing the results for the cycle at 40 minutes, the continuous illumination case is clearly preferable over LD cycling. However, the LD cycles in the second and third rounds resulted in either the same or greater electricity produced than in the continuous illumination case, respectively. These findings suggest that introducing brief, periodic intervals during which the device receives no sunlight over the course of a full day may result in both enhanced and stabilized overall device performance. We repeated the comparative LD experiment with longer dark intervals (60 seconds of dark time every 240 seconds) and with a higher frequency of dark intervals (30 seconds of dark time every 120 seconds); in both cases, we found that the dark-induced enhancement could not outcompete the extended time during which no energy could be collected. This indicates that the optimal percentage of dark time necessary within the LD cycles is somewhere below 20%.
We emphasize that while these measurements were performed on aged devices (to mimic real-world conditions in which PV modules are likely to be installed several weeks or months after fabrication), these are still preliminary findings and were tested only under indoor measurement conditions. Further research is necessary to elucidate the LD impact under real-world operating conditions, such as extended outdoor testing on different device structures, coupled LD cycling with day/night cycles, under various temperatures, humidity, and intensity levels[81, 245, 286, 287].

6.6. Discussion

We now consider possible mechanisms underlying the enhanced efficiency and PL observed with LD cycling, though we emphasize that mechanistic follow-up studies are needed for full validation. We first reiterate mechanisms which we have already ruled out. Because the samples were encapsulated and some measurements were further performed under nitrogen, atmospheric effects are unlikely to dominate the LD enhancement[205, 207, 232, 256, 277]. The comparison between excitation wavelengths (405 nm versus 532 nm) further indicates that passivating species such as PbI_2 are not responsible for the dark enhancement[192]. Finally, the enhancement cannot be attributed to mobile defect migration out of the illuminated region, as similar effects were observed under both localized and full-field illumination[41].
Instead, we propose that all PL and device changes are surface-driven. Our previous findings from **Chapter 2** support this: the bulk of the examined triple-cation, mixed-halide perovskite is of high quality (τ_{bulk} = 2 µs), whereas recombination losses are concentrated at the surfaces, which pin the PL[29]. Moreover, the timescales of the strongest enhancements – both in light and dark – align with mobile ion dynamics. In **Chapter 3**,

we measured a characteristic ionic diffusion time of 77 s in a 620 nm film, which directly altered the PL on that timescale, indicating that interfacial ionic reactions are a central driver of the observed dynamics[234].
Interestingly, the degradation and recovery kinetics resemble those reported by Nie and co-workers[273], who attributed photocurrent degradation to light-activated polaronic trap states at the perovskite interface. They showed that one minute in the dark was sufficient to deactivate these metastable traps, restoring J_{SC} without strongly affecting V_{OC}. However, trap deactivation alone cannot explain enhancements beyond the initial performance, nor the correlated improvements in both V_{OC} and PL reported here.
We therefore propose that LD enhancement arises from a combination of ion migration and interactions between mobile ions and metastable trap states. Under illumination, ions may accumulate at the interface alongside polaronic traps, reducing carrier extraction and increasing non-radiative recombination[25, 57, 273]. Once the light is removed, the traps deactivate rapidly (within 1 min), while slower-moving ions redistribute. It is possible that under illumination, polaronic defects screen ionic Frenkel pairs (vacancy–interstitial pairs), preventing their recombination[41, 204]. In the dark, these pairs may rearrange and recombine, lowering the interfacial defect density. The redistribution timescales – minutes – match the dark durations needed for maximum enhancement (Figure 6.1c and Figure 6.8)[48, 53, 79, 234].
The combined reduction in defect density and deactivation of trap states would then yield the correlated increases in PL, V_{OC}, and J_{SC} upon re-illumination. Repeated illumination could further drive ionic defects to the surface, while dark periods allow recombination, progressively reducing non-radiative losses over successive cycles (Figures 6.2c and 6.2d). This is effectively an optical zone refining process, where LD cycles anneal out interfacial defects. While this mechanism is consistent with our film and device observations and supported in part by the trap deactivation dynamics identified by Nie and co-workers, we emphasize that the specific role of ion migration remains speculative and alternative interpretations should not be excluded.

In addition to mechanistic validation, further investigation is needed to determine whether these enhancements can be permanently "locked-in" – that is, whether it is possible to prevent degradation once the enhanced state from LD cycling has been reached. This concept of inducing a permanent change may be achievable through recrystallization processes or through the incorporation of specific additives whose properties can be activated by laser or thermal annealing after fabrication[288–293]. Such strategies could potentially stabilize the beneficial ionic configurations established during LD cycling, with the goal of permanently forming a favorable energy landscape that suppresses detrimental ion migration and preserves device performance.
On a practical note, while engineering a complete system to implement LD cycling in perovskite solar cells is beyond the scope of this work, the integration of such a dynamic approach may not be as complex as one might expect. For example, if LD enhancement remains effective even under partial shading, then periodic module tilting could be employed to help maintain the enhanced state[294, 295]. Alternatively, with the development of smart glass – glass capable of selectively switching between transparent and opaque states – and its current applications in optimizing light and heat regulation within build-

ings, extending its application to perovskite PV is a justifiable consideration[274, 296]. Standard smart glass typically requires approximately 1 W/m^2 to maintain the opaque state and requires nearly zero power input for the transparent state; therefore, the additional energy consumption would remain below 1% if integrated into a high-efficiency module[297]. Notably, several studies have explored utilizing the dynamic properties of halide perovskites themselves for direct application as smart glass materials[298–300]. However, methods for stabilizing the average energy output from such dynamically operated modules, as well as the full integration costs, remain critical considerations for this hypothetical scenario. Finally, if the LD cycling mechanism could be replicated using a fully electrical approach, rather than an optical one, then it may be possible to retain the benefits of the induced enhanced state without reverting to additional dynamic layers or mechanical tilting.

6.7. Conclusion

In conclusion, we have demonstrated that localized high-intensity PL measurements can quantitatively reproduce device-level degradation trends. Systematic PL analyses revealed that light/dark cycling substantially enhances the emission compared to continuous excitation, with the magnitude of enhancement depending on dark time, composition and interface. Moreover, LD enhancement was observed under both localized and full-field excitation. Importantly, PL changes correlated directly with changes in the open-circuit voltage ($\Delta V_{OC} \approx 40$ mV). From this analysis, we established a simple LD protocol for complete perovskite devices under 1 sun conditions that yielded a higher energy output compared to continuous excitation.

Finally, we emphasize that after more than ten years of research into various stabilization strategies, perovskites remain entirely unconventional, dynamic semiconductors. Their material properties continually evolve over time due to ion-induced and other reactions, which are ultimately intrinsic to the material itself. It is therefore worth considering whether dynamic solutions are the key to maintaining stabilized photovoltaic performance. Beyond PV, if the ionic response in perovskites could be dynamically controlled, then these materials could even be exploited for novel applications, such as artificial synapses, adaptive materials, and more[181–184]. The simple consideration of dynamic light/dark cycling explored in this work yielded enhanced short-term results, though we argue that dynamic biasing, heating, or a combination of these parameters could ultimately result in enhanced material performance without compromising stability, for applications in perovskite photovoltaics and beyond.

6.8. Supporting Information

6.8.1. Fabrication Details

All materials were purchased from suppliers outlined in the materials sections of our previous works[29, 234]. The perovskite films were prepared on glass substrates. The glass was scrubbed with 1% Hellmanex III solution in deionized (DI) water, then sonicated for 15 minutes in 70 ^{o}C water, then for 15 minutes in acetone, and finally for 15 minutes in isopropanol. The glass was dried using N_2 and treated under UV-ozone for 30 minutes.
To prepare the perovskite films, 1.24 M solutions of PbI_2 in 4:1 DMF:DMSO and $PbBr_2$ in 4:1 DMF:DMSO were stirred overnight at 70 ^{o}C. A 1.5 M solution of CsI in DMSO was stirred at 70 ^{o}C for 2 hours. The PbI_2 solution was added separately to FAI powder and to MAI powder to form 1.24 M of $FAPbI_3$ and 1.24 M of $MAPbI_3$, respectively. Similarly, the $PbBr_2$ solution was added separately to FABr powder and to MABr powder to form 1.24 M of $FAPbBr_3$ and 1.24 M of $MAPbBr_3$. These perovskite solutions were then each stirred again at 70 ^{o}C for a further 2 hours before they were combined in the appropriate ratios, along with the CsI solution, to form the six compositions tested in this work. These compositions are listed in Table 6.1.
Before spin coating, all solutions were cooled to room temperature and filtered with a 0.45 µm PTFE filter. The solutions were spin coated at 4000 RPM for 30 seconds after a 6-second ramp-up time, and were quenched 15 seconds before the end of the spin coating using 170 µL of chlorobenzene. All samples were annealed at 100 ^{o}C for 30 minutes before being encapsulated in 60 nm of SiO_2 using a Polyteknik Flextura M508E electron-beam evaporator, where the evaporation rate was set to 0.06 nm/s.

Table 6.1: List of the six perovskite compositions studied by PL in this work, together with their chemical abbreviations, as referenced in Figure 6.1b.

Perovskite Composition	Abbreviation
$Cs_{0.07}(FA_{0.8}MA_{0.2})_{0.93}Pb(I_{0.8}Br_{0.2})_3$	CsFAMAIBr
$FA_{0.8}MA_{0.2}Pb(I_{0.8}Br_{0.2})_3$	FAMAIBr
$Cs_{0.07}MA_{0.93}Pb(I_{0.8}Br_{0.2})_3$	CsMAIBr
$MAPb(I_{0.8}Br_{0.2})_3$	MAIBr
$Cs_{0.07}(FA_{0.8}MA_{0.2})_{0.93}PbI_3$	CsFAMAI
$FA_{0.8}MA_{0.2}PbI_3$	FAMAI

For the interface comparison shown in Figures 6.6c, 6.6d and 6.7b, 25 nm of C_{60} and 7 nm of 2,9-Dimethyl-4,7-diphenyl-1,10-phenanthroline (BCP) were sequentially evaporated over the complete 80:20 film before either encapsulated further with 60 nm SiO_2, as described above, or left unencapsulated (for the comparison shown in Figure 6.7b).

Lateral devices were fabricated on glass substrates with a UV lithography lift-off procedure using MA-N1410 resist. The resist was UV-exposed on a Süss MA6/BA6 mask aligner and then developed in MA-D533/s. A 5 nm Cr adhesion layer and 80 nm of Au electrode material were deposited on the patterned resist by e-beam physical vapor deposition using the same evaporator listed above, both with a rate of 0.05 nm/s. Lift-off was performed by soaking in acetone for one hour. The substrates were treated un-

der a 1 minute oxygen plasma treatment before the perovskite solution of composition $Cs_{0.07}(FA_{0.83}MA_{0.17})_{0.93}Pb(I_{0.83}Br_{0.17})_3$ was spin coated on top of the substrate and contacts. The fabrication and spin coating of this perovskite follows similarly to what was described above. All lateral devices were encapsulated in 60 nm of SiO_2.

For the complete solar cells, the patterned ITO substrates were cleaned by sonication for 10 minutes, first in acetone, then in 3% Hellmanex III solution with DI water, then in DI water only, and finally in isopropanol. They were treated using oxygen plasma for 4 minutes. Poly[bis(4-phenyl)(2,4,6-trimethylphenyl)amine] (PTAA) was applied as the hole transport layer; the PTAA solution (1.75 mg/L in toluene) was spin coated onto the ITO at 6000 RPM for 30 seconds, following a ramp-up time of 3 seconds and then annealed at 100 ^oC for 10 minutes. After cooling to room temperature, PFN-Br(Poly(9,9-bis(3'-(N,N-dimethyl)-N-ethylammonium-propyl-2,7-fluorene)-alt-2,7-(9,9-dioctylfluorene))-dibromide) (0.05 mg/mL in methanol) was deposited on top of the PTAA layer dynamically at 4000 RPM for 30 seconds. A 1.2 M $Cs_{0.07}(FA_{0.83}MA_{0.17})_{0.93}Pb(I_{0.83}Br_{0.17})_3$ perovskite solution, with a 10% excess PbI_2 was prepared by similarly preparing the $FAPbI_3$, $MAPbBr_3$ and CsI solutions (although the perovskite solutions were stirred at room temperature overnight). The perovskite was spin coated on top of the hole transport layer at 4000 RPM for 400 seconds, following a ramp time of 3 seconds. 10 seconds into the spinning, the perovskite was quenched with 300 µL of ethylacetate. The samples were then annealed at 100 ^oC for 1 hour. 25 nm of C_{60}, 8 nm of BCP, and 100 nm of Cu were thermally evaporated on top of the perovskite through a mask to complete the devices.

6.8.2. Measurement Details

Photoluminescence measurements for all cases except for the full-field LED illumination test (Figure 6.7a) were performed using a WITEC alpha300 SR confocal imaging microscope coupled to a Thorlabs S1FC405 405 nm CW diode laser. The PL was collected in reflection mode, with a focused laser spot size of 113 μm^2. For the 532 nm excitation experiments, the WITEC system was instead coupled to a 532 nm Nd:YAG laser. Spectra were acquired using a charge-coupled device (CCD) and spectrometer, and the PL intensity was determined by integrating across the PL peak.
For the full-field PL experiment, the PL was collected in transmission mode. A 465 nm LED (Cree LED) was used as the excitation source and was set to an illumination intensity of approximately 10 mW/cm^2. An encapsulated 83:17 perovskite film was placed directly above the LED, and a Thorlabs 650 nm FEL long-pass filter was used to block the LED illumination from being detected by the silicon detector. The PL was monitored as the photocurrent generated by a BPW34 silicon photodiode (OSRAM, Infineon Technologies). The full-field PL experiment was conducted entirely within a N_2-filled glovebox.

All electrical measurements were performed using an Agilent B2902A Source-Measurement-Unit and the AM1.5G illumination was applied with an Oriel SOL2 94062A (6×6) Class ABA (Newport) solar simulator. For the *JV* curves, the voltage sweep rate was set to a high speed of 1 V/s to minimize hysteresis effects and reduce any influence from the measurement itself.

6.8.3. Supporting Characterization

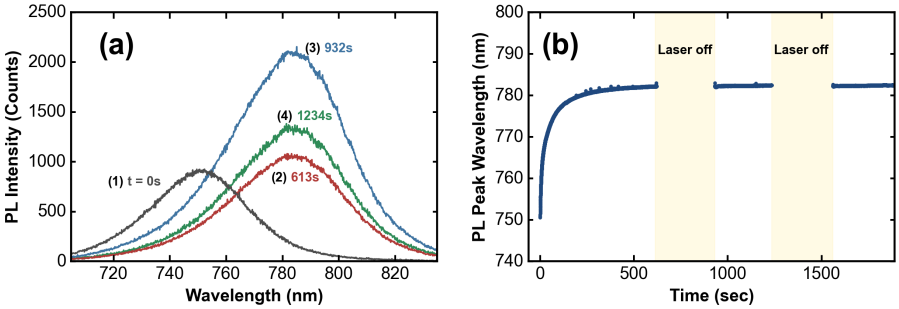

Figure 6.5: (a) PL spectra corresponding to the PL time series shown in Figure 6.1a. Each spectrum is color-coded to match the markers in Figure 6.1a. (b) Evolution of the PL peak energy over time, obtained from Lorentzian fits to the spectra.

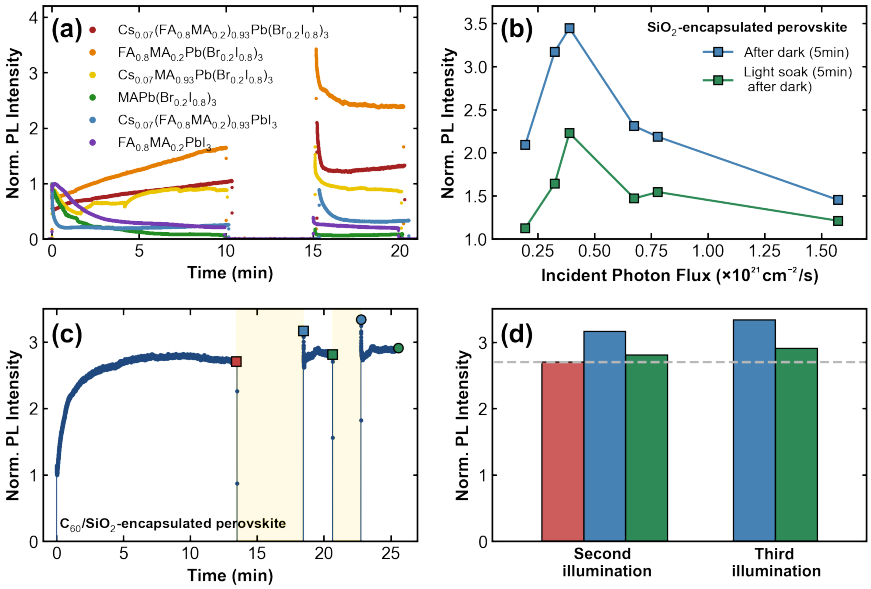

Figure 6.6: (a) PL time series of the six different perovskite compositions measured under 405 nm excitation at the same illumination intensity of 88 W/cm^2. (b) The measured PL of the 80:20 sample under different illumination intensities. In this panel, the PL is normalized to the end of the preceding light-soaking sequence (10 minutes of light soaking). The sample was kept in the dark for 5 minutes between illumination periods. The blue markers represent the PL immediately after re-excitation, while the green markers represent the PL following the second 5-minute light soak. (c) PL time series for an 80:20 sample with a 25 nm film of C_{60} and a 7 nm layer of BCP between the perovskite and SiO_2. (d) Bar chart highlighting the PL values of the square markers (second illumination period) and round markers (third illumination period) shown in panel (c).

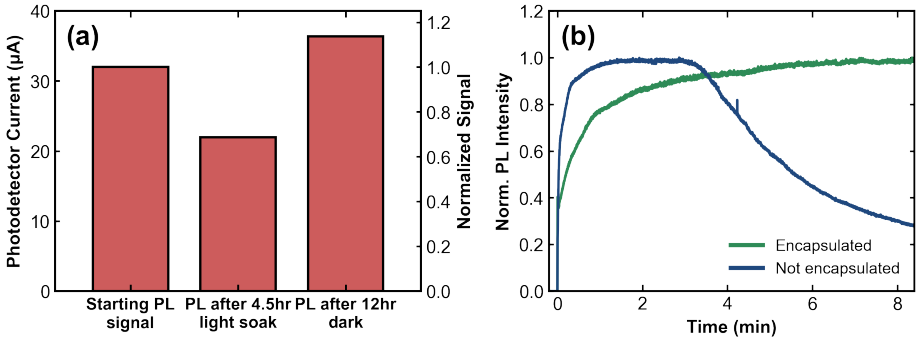

Figure 6.7: (a) Bar chart showing full-field PL as measured using a silicon photodetector. The absolute current signal is shown on the left side of the panel, and the normalized values (relative to the starting PL signal) are shown on the right side of the panel. After an extended illumination time of 4.5 hours, the full-field PL signal decreased, as shown by the middle bar. However, the full-field PL signal was enhanced to a level above the starting PL after allowing 12 hours in the dark. (b) Comparison between measuring the C_{60}-contacted film (previously shown in Figure 6.6c, in green) with a sample with C_{60} and BCP but not encapsulated in SiO_2 (blue).

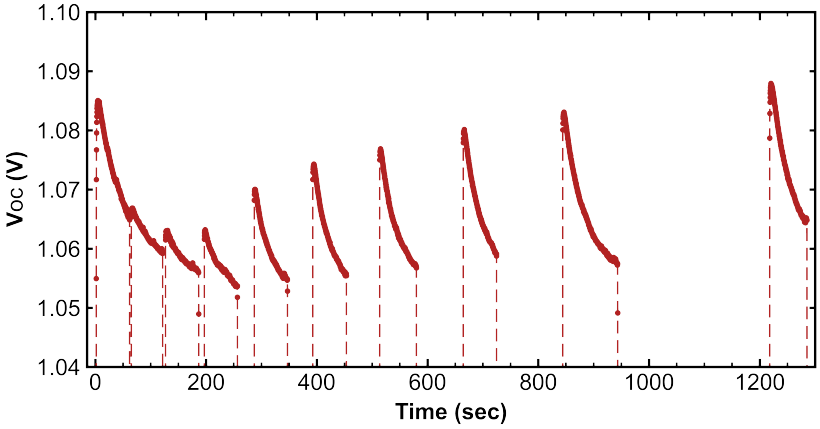

Figure 6.8: Time series of the open-circuit voltage, V_{OC}, for sequentially increasing dark times applied between 1-minute intervals of 1 sun equivalent AM1.5G illumination. Unlike the previous PL measurements, this time series was performed continuously on the same sample. The approximate duration of each dark interval was as follows (in chronological order): 3 seconds for the first two cycles, then 10 seconds, 30 seconds, 40 seconds, 60 seconds, 85 seconds, 120 seconds, and finally 260 seconds. Notably, the V_{OC} exhibits a steady improvement with increasing dark time.

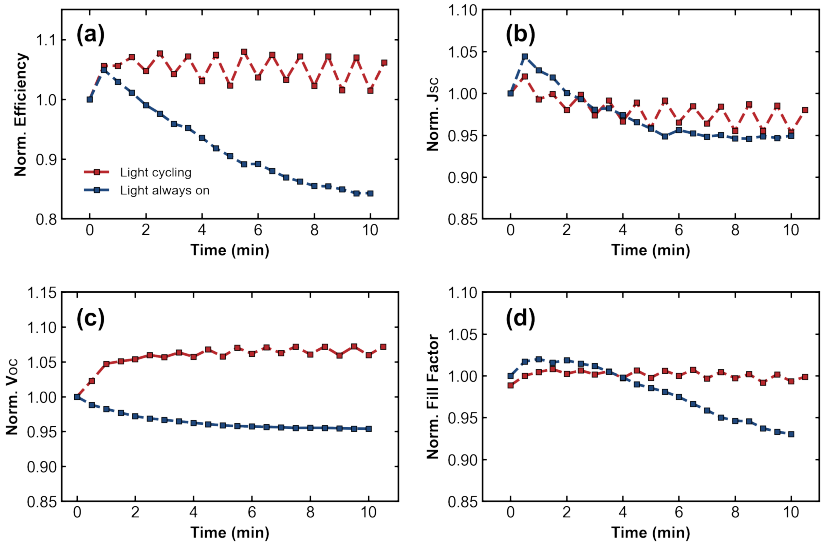

Figure 6.9: The complete normalized device parameter comparison between the devices shown in Figures 6.2e and 6.2f. The blue data represent the case where light was continuously applied, while the red data show the case in which light was periodically cycled between 30 seconds of illumination and 30 seconds of dark.

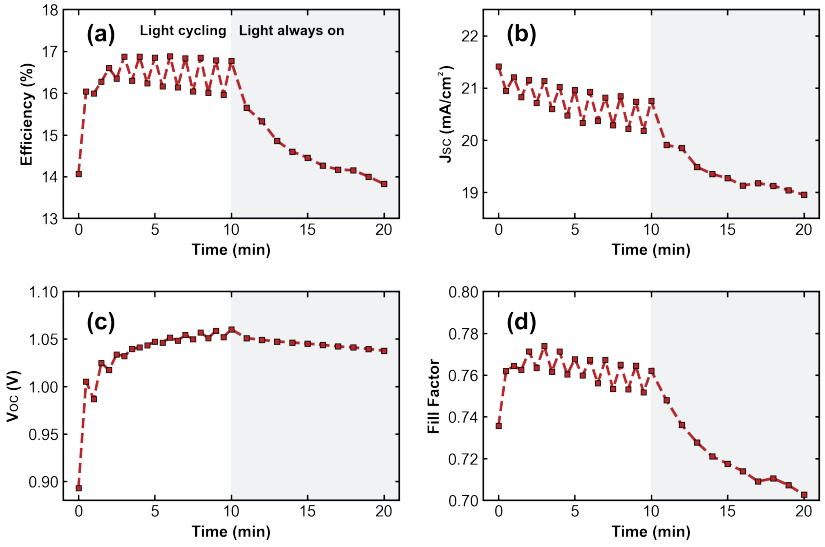

Figure 6.10: Measured device parameters over a 20 minute experiment in which the device was exposed to periodic LD cycles (30 seconds of light then 30 seconds of dark) for the first 10 minutes (white background), then continuously exposed under constant 1 sun illumination for the subsequent 10 minutes (gray background).

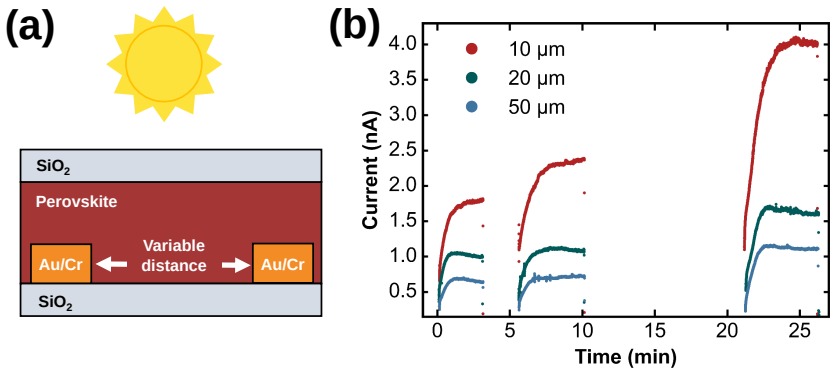

Figure 6.11: (a) Schematic of the symmetric lateral contact device measured. The distance between the lateral electrodes was defined by the evaporation mask, with values of either 10 µm, 20 µm, or 50 µm. The electrodes were 100 nm thick, and the 83:17 perovskite layer was approximately 600 nm thick. The excitation was applied at 1 sun equivalent with an AM1.5G solar spectrum. A 20 mV voltage bias was applied between the electrodes, and the current was measured. (b) The measured current for different samples with different lateral distances between the electrodes under an LD cycle. In all cases, the current was enhanced after the dark interval. Notably, the relative enhancement was highest for the sample with the smallest distance between the electrodes (10 µm, shown in red).

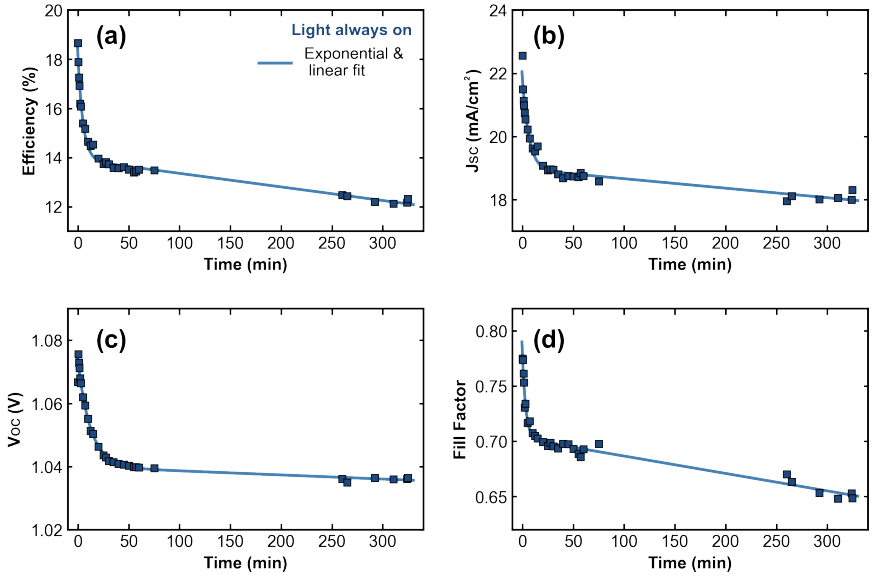

Figure 6.12: All four device parameter time series for the device that was continuously illuminated, shown in blue in Figure 6.4a. A combined exponential and linear fit was used to accurately model all four parameters, although the rates of degradation varied between them.

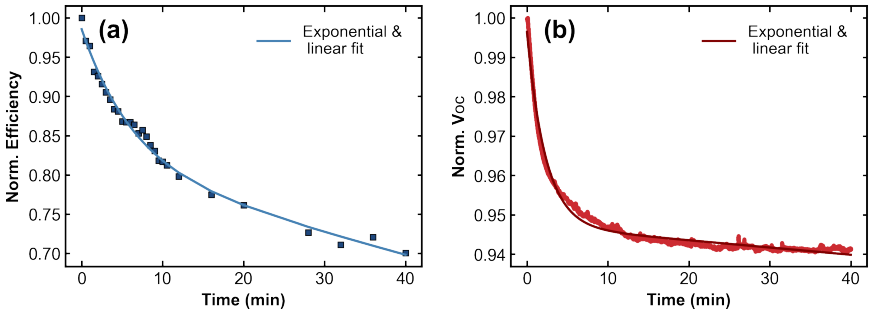

Figure 6.13: Supporting measurements indicating that a combined exponential and linear fit can empirically model the JV degradation trends. $Y = A\exp[-t/\tau] + Bt + C$, where Y is the JV parameter, t is time, and τ, A, B, C are the fit parameters. Panels (a) and (b) show the normalized efficiency and V_{OC} data for different devices. The solid curves represent the empirical fits.

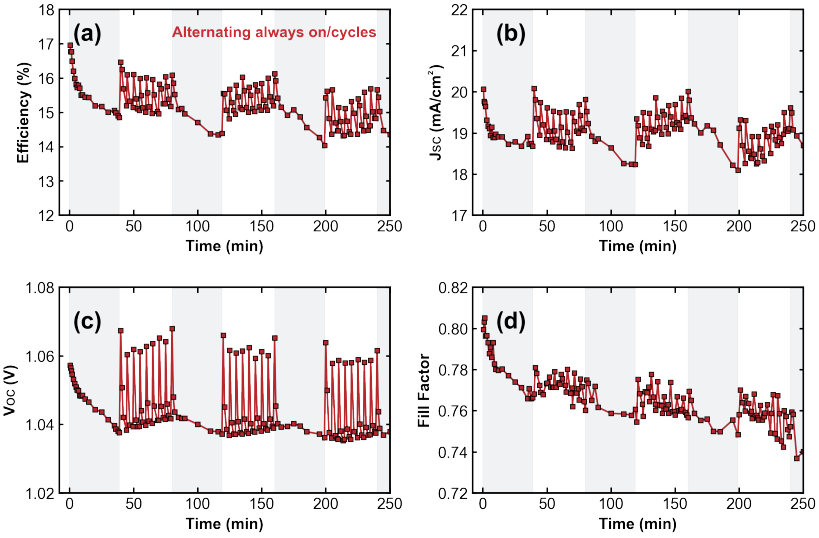

Figure 6.14: All four device parameter time series for the device that alternated between continuous illumination and LD cycling, shown in red in Figure 6.4b. Notably, a 30-second dark time enabled a significant enhancement in V_{OC}, consistent with the PL enhancement measured earlier in this chapter. The J_{SC} also increased immediately after the dark periods, while the fill factor did not significantly vary. The continuous illumination periods are highlighted with the gray background, compared to the white background for the LD cycle periods.

Summary

Meeting the global energy demands in the coming decades – without sacrificing the planet's natural environment – will require a full transition to primary energy sources that are affordable, abundant and entirely clean. This transformation will depend on effective policy, technological innovation and, critically, on fully utilizing renewable sources already available. Among these, solar energy is immensely valuable, with the Sun delivering many orders of magnitude more power to Earth than is currently consumed. Harnessing this resource requires high-performing photovoltaics (PV). While silicon PV is commercially established, it is now approaching its efficiency limits. For a successful global energy transition, PV efficiencies beyond those achievable with silicon alone will be essential.
Over the past 15 years, metal halide perovskites have emerged as a transformative class of semiconductors for PV applications. Their superb optoelectronic properties have already enabled perovskite solar cell efficiencies to be on par with those of silicon. In tandem architectures, perovskites can enhance PV efficiencies by more than 50%. However, their ionic nature introduces new challenges: mobile ions can migrate and alter their PV performance over time. Maximizing the potential of perovskite photovoltaics thus requires a detailed understanding of their coupled electronic and ionic dynamics at the fundamental level.
The focus of this thesis is to advance the understanding of perovskites by extracting the maximum information from their photoluminescence (PL). The PL is an intrinsic material property, inherently shaped by the interaction of both electronic and ionic processes. Each chapter of this thesis develops and applies various PL-based characterization methods to quantify key electronic and ionic properties.

Chapter 1 introduces the fundamentals of perovskite semiconductors. The importance of electronic charge-carrier management for photovoltaics is elucidated: maximizing the photogenerated carrier density increases current, while minimizing carrier recombination preserves voltage. The mechanisms of carrier generation and recombination under illumination are explained and related to the detailed balance limit.
Mobile ion dynamics in perovskites are then discussed, along with standard characterization techniques such as impedance spectroscopy, which is commonly applied to quantify ionic properties. Finally, the physics of photoluminescence is introduced by illustrating how the PL spectrum can be modeled in relation to the material's blackbody spectrum and absorption coefficient. The connection between PL and PV performance is established, and the key PL characterization methods employed in this thesis are briefly outlined.
Among the established PL methods for characterizing perovskites, time-resolved photoluminescence spectroscopy (TRPL) is already widely used to quantify carrier lifetimes, but it is not yet exploited to its full potential. Chapter 2 introduces an analysis framework to maximize the information attainable from TRPL. Like repeated *refrains* in musical terms, in TRPL, pulsed light excitation repeatedly excites the film and the PL decay is recorded

after every pulse. By fitting the PL decay beyond the conventional bi-exponential approximation, radiative, trap-assisted and Auger recombination coefficients are extracted. A systematic variation of perovskite layer thicknesses, under different top-surface encapsulation layers, is applied to separate the bulk lifetime from the surface recombination velocities (SRVs). These parameters are then used to extract the SRVs of 17 additional PV-relevant contacts, enabling both benchmarking of standard interfaces and the exploration of new contacts – for example, polysilicon. The trap-assisted recombination properties are compared with the sample's photoluminescence quantum yields (PLQY), from which the perovskite's doping density is estimated. The recombination values obtained from TRPL are then translated into device parameters and benchmarked against complete devices, from which the major loss channels are identified. This chapter demonstrates that the bulk perovskite quality (τ_{bulk} = 2 µs) is already exceptional, while limitations arise particularly at the C_{60} interface. Ultimately, it is shown that a comprehensive set of electronic properties – including doping density, recombination coefficients, and bulk versus surface recombination – can be obtained directly from TRPL analysis.

While Chapter 2 provides a means to quantify relevant electronic properties, a full understanding of perovskites also requires probing their ionic dynamics. To address this, Chapter 3 introduces a new characterization tool – intensity-modulated photoluminescence spectroscopy (IMPLS). The principles of IMPLS are described: light applied at modulation frequencies resonant with ionic processes in the perovskite induces a measurable response in the PL signal. In musical terms, scanning the modulation frequency is like tuning across notes to find the ionic *key signature*. The PL response, expressed as frequency-dependent changes in phase and amplitude, is demonstrated on a perovskite film. To interpret the measurements, optical equivalent circuit (OEC) modeling is introduced, and OEC models are fit to the data. The results reveal two distinct ionic processes with relaxation times of τ_{ion} = 2.1 ms and 77 s, which are attributed to ionic defect formation and diffusion. This chapter establishes the fundamentals of IMPLS, emphasizing its simplicity, contact-free nature and advantages as a complementary tool for studying ionic processes in halide perovskites.

Chapter 4 delves further into IMPLS using a different measurement configuration, in which a high dynamic range of excitation intensity is swept with a laser source. The IMPLS response of the perovskite sample indicates that the measured ionic processes are correlated with the PLQY. A rigorous comparison between IMPLS and PLQY demonstrates that mobile ionic defects pin the PLQY in many regions. Under low modulation frequencies, these ions laterally migrate out of the focused laser spot with diffusion coefficients in the range expected for halide species, $D_{ion} = 10^{-9} - 10^{-11}$ cm^2/s. Notably, correlated phase and PL intensity maps provide insight into where the effects of mobile ions dominate compared to fixed trap-assisted defects. These maps inspire the *dynamic contrast* chapter title.

The updated IMPLS configuration in Chapter 4 employs a charge-coupled detector and spectrometer, enabling the full PL spectrum to be collected at each data point. The PL spectrum provides additional information not accessible through electrical techniques. In perovskites, the peak energy and bandwidth specifically reflect local halide composition and chemical disorder. Chapter 5 extends IMPLS by resolving these spectral components in the frequency domain. The results provide further evidence that halides dictate the

IMPLS response. To identify the dominant halide response for these observed features, the perovskite composition is varied (*theme and variation*); the results indicate that iodide produces the strongest signal over the relevant frequency range. Together with Chapters 3 and 4, this work forms a trilogy of IMPLS studies, establishing the technique as a powerful characterization tool. IMPLS can be combined with other PL methods for comprehensive benchmarking of perovskite performance and stability, and it also holds potential for scalable quality control in both pilot and commercial production lines.
Finally, Chapter 6 explores how dynamic excitation protocols can optimize PL and device performance. Since PL serves as a proxy for recombination, systematic variations in perovskite composition, interfaces, excitation energy, and intensity are examined. A key observation is that PL intensity is enhanced after even brief periods of darkness. Repeated *interludes* between illumination and darkness amplify the PL beyond levels achieved under continuous illumination. When applied to full devices under 1-sun conditions, the same effect is observed, with stabilized performance maintained for hours. While dark recovery has been noted previously on overnight timescales, this work demonstrates that short light-dark cycling can actively enhance and stabilize PV performance. These findings suggest that conventional, continuous illumination protocols may not be optimal for perovskites, and that dynamic strategies such as smart glass or module tilting could be used to boost performance in practice.

Overall, this thesis demonstrates the profound potential of photoluminescence for characterizing and optimizing perovskite photovoltaics. It establishes how electronic and ionic dynamics can be probed and quantified through an *ensemble* of PL techniques. A single PL method – much like a soloist in music – yields only specific insights, but the collective arrangement of techniques presented here provides a deeper and more comprehensive understanding of perovskite physics.

Samenvatting

Om in de komende decennia aan de wereldwijde vraag naar energie te kunnen voldoen zonder de natuurlijke omgeving van de planeet op te offeren is het van groot belang om over te stappen op primaire energiebronnen die betaalbaar, ruimschoots aanwezig en volledig duurzaam zijn. Deze transitie zal afhangen van effectief beleid, technologische innovatie, en bovenal van het ten volste benutten van reeds beschikbare hernieuwbare bronnen. Zonne-energie is hierbij van bijzonder grote waarde, aangezien de zon vele malen meer energie aan de aarde levert dan momenteel wordt verbruikt. Het benutten van deze bron vereist hoogwaardige fotovoltaïsche (PV) zonnecellen. Hoewel siliciumtechnologie commercieel beschikbaar en betrouwbaar is, nadert deze nu haar efficiëntielimieten. Voor een succesvolle wereldwijde energietransitie is het essentieel om tot een hogere PV-efficientie te komen dan haalbaar is met alleen silicium.
In de afgelopen 15 jaar hebben metaalhalogenideperovskieten zich ontwikkeld tot een impactvolle klasse halfgeleiders voor PV-toepassingen. Hun superieure opto-elektronische eigenschappen hebben al geleid tot een rendement van perovskietzonnecellen dat vergelijkbaar is met dat van silicium. In tandemarchitecturen kunnen perovskieten de PV-efficiëntie met meer dan 50% verhogen. Hun ionische aard brengt echter nieuwe uitdagingen met zich mee: mobiele ionen kunnen migreren en hun PV-prestaties in de loop van de tijd veranderen. Het maximaliseren van het potentieel van perovskiet-zonnecellen vereist een gedetailleerd begrip van hun gekoppelde elektronische en ionische dynamiek op fundamenteel niveau.
De focus van dit proefschrift ligt op het vergroten van het begrip van perovskieten door de maximale informatie uit hun fotoluminescentie (PL) te halen. PL is een fundamentele materiaaleigenschap, inherent gevormd door de interactie van zowel elektronische als ionische processen. Elk hoofdstuk van dit proefschrift ontwikkelt en past verschillende op PL-gebaseerde karakteriseringsmethoden toe om belangrijke elektronische en ionische eigenschappen te kwantificeren.

Hoofdstuk 1 introduceert de basisprincipes van perovskiethalfgeleiders. Het belang van het beheer van elektronische ladingdragers voor fotovoltaïsche cellen wordt toegelicht: het maximaliseren van de fotogegenereerde ladingdragerdichtheid verhoogt de stroomsterkte, terwijl het minimaliseren van de recombinatie van ladingdragers de spanning behoudt. De mechanismen van de opwekking en recombinatie van ladingdragers worden verklaard en gerelateerd aan de detailed balance limit. De dynamiek van mobiele ionen in perovskites worden dan besproken, samen met standaard karakteriseringstechnieken zoals impedantiespectroscopie, wat vaak wordt toegepast om ionische eigenschappen te kwantificeren. Tot slot wordt de fysica van fotoluminescentie geïntroduceerd door te illustreren hoe het PL-spectrum kan worden gemodelleerd in relatie tot het spectrum van een zwarte straler en de absorptiecoëfficiënt van het materiaal. Het verband tussen PL en PV-prestaties wordt vastgesteld en de belangrijkste PL-karakteriseringsmethoden die in

dit proefschrift worden gebruikt, worden kort beschreven.
Onder de gevestigde PL-methoden voor de karakterisering van perovskieten wordt tijdgeresolueerde fotoluminescentiespectroscopie (TRPL) al veelvuldig gebruikt om de levensduur van ladingdragers te kwantificeren, maar deze wordt nog niet ten volle benut. Hoofdstuk 2 introduceert een analysekader om de informatie die uit TRPL kan worden verkregen te maximaliseren. Net als bij herhaalde *refreinen* in muzikale termen, exciteert bij TRPL een gepulseerde lichtexcitatie herhaaldelijk de perovskietlaag, en wordt het PL-verval vastgelegd na elke puls. Door het PL-verval buiten de conventionele bi-exponentiële benadering te fitten, worden stralings-, trap-geassisteerde en Auger-recombinatiecoëfficiënten geëxtraheerd. Een systematische variatie van de dikte van de perovskietlaag, onder verschillende encapsulatielagen aan het bovenoppervlak, wordt toegepast om de bulklevensduur te scheiden van de oppervlakterecombinatiesnelheden (SRV's). Deze parameters worden vervolgens gebruikt om de SRV's van 17 extra PV-relevante elektrische contacten te extraheren, wat zowel benchmarking van standaardinterfaces als de verkenning van potentiële nieuwe contacten mogelijk maakt, bijvoorbeeld polysilicium. De trap-geassisteerde recombinatie eigenschappen worden vergeleken met de fotoluminescentie kwantumopbrengst (PLQY) van het sample, op basis waarvan de dopingdichtheid van de perovskiet wordt geschat. De recombinatiewaarden worden vervolgens vertaald naar deviceparameters en vergeleken met complete devices, op basis waarvan de belangrijkste verlieskanalen worden geïdentificeerd. Dit hoofdstuk toont aan dat de kwaliteit van het bulkmateriaal (τ_{bulk} = 2 µs) al uitzonderlijk hoog is, en dat beperkingen voornamelijk aan de interface met de C_{60}-transportlaag ontstaan. Uiteindelijk wordt aangetoond dat een uitgebreide set elektronische eigenschappen – waaronder dopingdichtheid, recombinatiecoëfficiënten en bulk- versus oppervlakterecombinatie – direct kan worden verkregen uit TRPL-analyse.
Hoewel hoofdstuk 2 een manier biedt om relevante elektronische eigenschappen te kwantificeren, vereist een volledig begrip van perovskieten ook het onderzoeken van hun ionendynamiek. Om hierop in te gaan, introduceert hoofdstuk 3 een nieuwe karakteriseringsmethode: intensiteit gemoduleerde fotoluminescentiespectroscopie (IMPLS). De principes van IMPLS worden beschreven; licht met gemoduleerde frequenties die resoneren met ionische processen in het perovskiet induceert een meetbare respons in het PL-signaal. In muzikale termen, het scannen van de gemoduleerde frequenties lijkt op het stemmen langs verschillende noten om de ionische *toonsoort* te vinden. De PL-respons, uitgedrukt als frequentieafhankelijke veranderingen in fase en amplitude, wordt gedemonstreerd op een perovskietlaag. Om de metingen te interpreteren, wordt optische equivalente circuit (OEC)-modellering geïntroduceerd en worden OEC-modellen aan de data gefit. De resultaten onthullen twee verschillende ionische processen met relaxatietijden van τ_{ion} = 2 ms en 77 s, die worden toegeschreven aan de vorming en diffusie van ionische defecten. Dit hoofdstuk legt de basisprincipes van IMPLS uit en benadrukt de eenvoud, het contactloze karakter en de voordelen ervan als aanvullende tool voor het bestuderen van ionische processen in halogenide perovskieten.
Hoofdstuk 4 gaat dieper in op IMPLS met behulp van een andere meetconfiguratie, waarbij een hoog dynamisch bereik van excitatie-intensiteit wordt doorlopen met een laserbron. De IMPLS-respons van het perovskietsample geeft aan dat de gemeten ionische processen gecorreleerd zijn met de PLQY. Een grondige vergelijking tussen het duo

van IMPLS en PLQY toont aan dat mobiele ionische defecten de PLQY in veel gebieden vastpinnen; bij lage modulatiefrequenties migreren deze ionen lateraal uit de gefocuste laserspot, met diffusiecoëfficiënten in het bereik dat verwacht wordt voor halogenidesoorten, $D_{ion} = 10^{-9}$–10^{-11} cm^2/s. Gecorreleerde fase- en PL-intensiteitskaarten bieden met name inzicht in waar de effecten van mobiele ionen domineren in vergelijking met trap-geassisteerde defecten. Deze kaarten zijn de inspiratie van het *dynamisch contrast* hoofdstuk.
De geüpdatete IMPLS-configuratie in hoofdstuk 4 maakt gebruik van een ladingsgekoppelde detector en spectrometer, waardoor het volledige PL-spectrum op elk datapunt kan worden verzameld. Het PL-spectrum biedt aanvullende informatie die niet toegankelijk is via elektrische technieken. In perovskieten weerspiegelen de piekenergie en bandbreedte de lokale halogenidesamenstelling en chemische wanorde. Hoofdstuk 5 breidt IMPLS uit door deze spectrale componenten in het frequentiedomein te ontleden. De resultaten leveren verder bewijs dat halogeniden de IMPLS-respons domineren. Om de dominante halogenide te identificeren, wordt de perovskietsamenstelling gevarieerd (*thema en variaties*); de IMPLS-respons geeft aan dat jodide het sterkste signaal produceert in het relevante frequentiebereik. Samen met hoofdstukken 3 en 4 vormt dit werk een drieluik van IMPLS-studies, waarmee de techniek wordt neergezet als een krachtig karakteriseringsinstrument. IMPLS kan worden gecombineerd met andere PL-methoden voor uitgebreide benchmarking van de prestaties en stabiliteit van perovskiet, en biedt ook een groot potentieel voor schaalbare kwaliteitscontrole in zowel pilot- als commerciële productielijnen.
Tot slot onderzoekt hoofdstuk 6 hoe dynamische excitatieprotocollen PL en de prestaties van devices kunnen optimaliseren. Omdat PL als proxy dient voor recombinatie, worden systematische variaties in de samenstelling van perovskiet, interfaces, excitatieenergie en intensiteit onderzocht. Een belangrijke observatie is dat de PL-intensiteit zelfs na korte periodes van donkerte wordt versterkt. Herhaalde *interludes* tussen licht en donker versterken PL tot boven de niveaus die worden bereikt met continue belichting. Wanneer toegepast op volledige devices onder 1-zon-condities, wordt hetzelfde effect waargenomen, met gestabiliseerde prestaties die urenlang behouden blijven. Hoewel herstel van de donkere periode eerder is waargenomen binnen de tijdschaal van een nacht, toont dit werk aan dat korte licht-donkercycli de PV-prestaties actief kunnen verbeteren en stabiliseren. Deze bevindingen suggereren dat conventionele, continue belichtingsprotocollen mogelijk niet optimaal zijn voor perovskieten, en dat dynamische strategieën zoals slim glas of modulekanteling in de praktijk kunnen worden gebruikt om de prestaties te verbeteren.

Al met al toont dit proefschrift het enorme potentieel van fotoluminescentie aan voor het karakteriseren en optimaliseren van perovskiet-zonnecellen. Het laat zien hoe zowel elektronische als ionische dynamiek kan worden onderzocht en gekwantificeerd met behulp van een *ensemble* van PL-technieken. Eén enkele PL-methode – net als een solist in de muziek – levert slechts specifieke inzichten op, maar de hier gepresenteerde samenstelling van technieken biedt een dieper en uitgebreider begrip van de perovskietfysica.

References

[1] M. J. O'Kelly and C. O'Kelly, *Newgrange: Archaeology, Art and Legend* (Thames and Hudson, London, U.K., 1982).

[2] N. Nelson and A. Ben-Shem. The complex architecture of oxygenic photosynthesis, *Nature Reviews Molecular Cell Biology* **5**, 971–982 (2004).

[3] H. Ritchie, P. Rosado, and M. Roser. Energy production and consumption, *Our World in Data* (2020), https://ourworldindata.org/energy-production-consumption.

[4] U.S. Energy Information Administration, Energy Institute, and Our World in Data, Primary energy consumption per capita, Dataset (2025), U.S. Energy Information Administration, "International Energy Data"; Energy Institute, "Statistical Review of World Energy"; Various sources, "Population" (2024) – with major processing by Our World in Data. Retrieved August 11, 2025. Archived on July 17, 2025.

[5] C. MacFarling Meure, D. Etheridge, C. Trudinger, P. Steele, R. Langenfelds, T. van Ommen, A. Smith, and J. Elkins. Law dome CO_2, CH_4 and N_2O ice core records extended to 2000 years bp, *Geophysical Research Letters* **33** (2006).

[6] International Energy Agency, *Global Energy Review 2025*, Tech. Rep. (International Energy Agency, Paris, France, 2025).

[7] WWF International, *Living Planet Report 2024: A System in Peril*, Tech. Rep. (WWF International, Gland, Switzerland, 2024).

[8] IPCC, *Climate Change 2023: Synthesis Report. Contribution of Working Groups I, II and III to the Sixth Assessment Report of the Intergovernmental Panel on Climate Change*, Tech. Rep. (Intergovernmental Panel on Climate Change, Geneva, Switzerland, 2023).

[9] M. A. Green, E. D. Dunlop, M. Yoshita, N. Kopidakis, K. Bothe, G. Siefer, X. Hao, and J. Y. Jiang. Solar cell efficiency tables (version 66), *Progress in Photovoltaics: Research and Applications* **33**, 795–810 (2025).

[10] M. Green. Limits on the open-circuit voltage and efficiency of silicon solar cells imposed by intrinsic auger processes, *IEEE Transactions on Electron Devices* **31**, 671–678 (1984).

[11] VDMA Photovoltaic Equipment Sector Group, *International Technology Roadmap for Photovoltaics (ITRPV): 2023 Results, 15th Edition*, Tech. Rep. (VDMA, Mechanical Engineering Industry Association, Frankfurt am Main, Germany, 2024).

[12] S. D. Stranks, G. E. Eperon, G. Grancini, C. Menelaou, M. J. P. Alcocer, T. Leijtens, L. M. Herz, A. Petrozza, and H. J. Snaith. Electron-hole diffusion lengths exceeding 1 micrometer in an organometal trihalide perovskite absorber, *Science* **342**, 341–344 (2013).

[13] Y. Yuan, G. Yan, C. Dreessen, T. Rudolph, M. Hülsbeck, B. Klingebiel, J. Ye, U. Rau, and T. Kirchartz. Shallow defects and variable photoluminescence decay times up to 280 µs in triple-cation perovskites, *Nature Materials* **23**, 391–397 (2024).

[14] M. H. Futscher and B. Ehrler. Efficiency limit of perovskite/si tandem solar cells, *ACS Energy Letters* **1**, 863–868 (2016).

[15] G. E. Eperon, S. D. Stranks, C. Menelaou, M. B. Johnston, L. M. Herz, and H. J. Snaith. Formamidinium lead trihalide: a broadly tunable perovskite for efficient planar heterojunction solar cells, *Energy & Environmental Science* **7**, 982–988 (2014).

[16] D. Zhao, Y. Yu, C. Wang, W. Liao, N. Shrestha, C. R. Grice, A. J. Cimaroli, L. Guan, R. J. Ellingson, K. Zhu, X. Zhao, R.-G. Xiong, and Y. Yan. Low-bandgap mixed tin–lead iodide perovskite absorbers with long carrier lifetimes for all-perovskite tandem solar cells, *Nature Energy* **2**, 17018 (2017).

[17] M. Saliba, T. Matsui, J.-Y. Seo, K. Domanski, J.-P. Correa-Baena, M. K. Nazeeruddin, S. M. Zakeeruddin, W. Tress, A. Abate, A. Hagfeldt, and M. Grätzel. Cesium-containing triple cation perovskite solar cells: improved stability, reproducibility and high efficiency, *Energy & Environmental Science* **9**, 1989–1997 (2016).

[18] Z. Saki, M. M. Byranvand, N. Taghavinia, M. Kedia, and M. Saliba. Solution-processed perovskite thin-films: the journey from lab- to large-scale solar cells, *Energy & Environmental Science* **14**, 5690–5722 (2021).

[19] V. Kliner, T. Soto-Montero, J. Nespoli, T. J. Savenije, M. Ledinský, and M. Morales-Masis. Pulsed laser deposition of halide perovskites with over 10-fold enhanced deposition rates, *The Journal of Physical Chemistry Letters* **16**, 1453–1460 (2025).

[20] J. Li, H. Wang, X. Y. Chin, H. A. Dewi, K. Vergeer, T. W. Goh, J. W. M. Lim, J. H. Lew, K. P. Loh, C. Soci, T. C. Sum, H. J. Bolink, N. Mathews, S. Mhaisalkar, and A. Bruno. Highly efficient thermally co-evaporated perovskite solar cells and mini-modules, *Joule* **4**, 1035–1053 (2020).

[21] S. A. Kulkarni, T. Baikie, P. P. Boix, N. Yantara, N. Mathews, and S. Mhaisalkar. Band-gap tuning of lead halide perovskites using a sequential deposition process, *Journal of Materials Chemistry A* **2**, 9221–9225 (2014).

[22] Y. Chen, S. G. Motti, R. D. J. Oliver, A. D. Wright, H. J. Snaith, M. B. Johnston, L. M. Herz, and M. R. Filip. Optoelectronic properties of mixed iodide–bromide perovskites from first-principles computational modeling and experiment, *The Journal of Physical Chemistry Letters* **13**, 4184–4192 (2022).

[23] A. Smets, K. Jäger, O. Isabella, R. van Swaaij, and M. Zeman, *Solar Energy: The physics and engineering of photovoltaic conversion, technologies and systems* (UIT Cambridge Limited, Cambridge, U.K., 2016).

[24] W. Shockley and H. J. Queisser. Detailed balance limit of efficiency of p-n junction solar cells, *Journal of Applied Physics* **32**, 510–519 (1961).

[25] J. Thiesbrummel, S. Shah, E. Gutierrez-Partida, F. Zu, F. Peña-Camargo, S. Zeiske, J. Diekmann, F. Ye, K. P. Peters, K. O. Brinkmann, P. Caprioglio, A. Dasgupta, S. Seo, F. A. Adeleye, J. Warby, Q. Jeangros, F. Lang, S. Zhang, S. Albrecht, T. Riedl, A. Armin, D. Neher, N. Koch, Y. Wu, V. M. Le Corre, H. Snaith, and M. Stolterfoht. Ion-induced field screening as a dominant factor in perovskite solar cell operational stability, *Nature Energy* **9**, 664–676 (2024).

[26] J. Wang, W. Fu, S. Jariwala, I. Sinha, A. K.-Y. Jen, and D. S. Ginger. Reducing surface recombination velocities at the electrical contacts will improve perovskite photovoltaics, *ACS Energy Letters* **4**, 222–227 (2019).

[27] W. Peng, K. Mao, F. Cai, H. Meng, Z. Zhu, T. Li, S. Yuan, Z. Xu, X. Feng, J. Xu, M. D. McGehee, and J. Xu. Reducing nonradiative recombination in perovskite solar cells with a porous insulator contact, *Science* **379**, 683–690 (2023).

[28] C. M. Wolff, S. A. Bourelle, L. Q. Phuong, J. Kurpiers, S. Feldmann, P. Caprioglio, J. A. Marquez, J. Wolansky, T. Unold, M. Stolterfoht, S. Shoaee, F. Deschler, and D. Neher. Orders of recombination in complete perovskite solar cells – linking time-resolved and steady-state measurements, *Advanced Energy Materials* **11**, 2101823 (2021).

[29] S. C. Gillespie, J. Gautier, J. S. van der Burgt, J. Anker, B. L. Geerligs, G. Coletti, and E. C. Garnett. Silicon-inspired analysis of interfacial recombination in perovskite photovoltaics, *Advanced Energy Materials* **14**, 2400965 (2024).

[30] F. Peña-Camargo, J. Thiesbrummel, H. Hempel, A. Musiienko, V. M. Le Corre, J. Diekmann, J. Warby, T. Unold, F. Lang, D. Neher, and M. Stolterfoht. Revealing the doping density in perovskite solar cells and its impact on device performance, *Applied Physics Reviews* **9**, 021409 (2022).

[31] T. Kirchartz, J. A. Márquez, M. Stolterfoht, and T. Unold. Photoluminescence-based characterization of halide perovskites for photovoltaics, *Advanced Energy Materials* **10**, 1904134 (2020).

[32] M. Grundmann, *The Physics of Semiconductors: An Introduction Including Nanophysics and Applications*, 3rd ed., Graduate Texts in Physics (Springer, Cham, Switzerland, 2016).

[33] S. De Wolf, J. Holovsky, S.-J. Moon, P. Löper, B. Niesen, M. Ledinsky, F.-J. Haug, J.-H. Yum, and C. Ballif. Organometallic halide perovskites: Sharp optical absorption edge and its relation to photovoltaic performance, *The Journal of Physical Chemistry Letters* **5**, 1035–1039 (2014).

[34] B. Wenger, P. K. Nayak, X. Wen, S. V. Kesava, N. K. Noel, and H. J. Snaith. Consolidation of the optoelectronic properties of $CH_3NH_3PbBr_3$ perovskite single crystals, *Nature Communications* **8**, 590 (2017).

[35] A. Sproul. Dimensionless solution of the equation describing the effect of surface recombination on carrier decay in semiconductors, *Journal of Applied Physics* **76**, 2851 – 2854 (1994).

[36] W. Shockley and W. T. Read. Statistics of the recombinations of holes and electrons, *Physical Review* **87**, 835–842 (1952).

[37] L. Krückemeier, B. Krogmeier, Z. Liu, U. Rau, and T. Kirchartz. Understanding transient photoluminescence in halide perovskite layer stacks and solar cells, *Advanced Energy Materials* **11**, 2003489 (2021).

[38] A. Polman, M. Knight, E. C. Garnett, B. Ehrler, and W. C. Sinke. Photovoltaic materials: Present efficiencies and future challenges, *Science* **352**, aad4424 (2016).

[39] AMOLF, Detailed Balance (DB) Charts, https://amolf.nl/research/sustainable-energy-materials/detailed-balance-charts (2025), Figures updated June 6, 2025; accessed August 13, 2025.

[40] L. J. F. Hart, F. J. Angus, Y. Li, A. Khaleed, P. Calado, J. R. Durrant, A. B. Djurišić, P. Docampo, and P. R. F. Barnes. More is different: mobile ions improve the design tolerances of perovskite solar cells, *Energy & Environmental Science* **17**, 7107–7118 (2024).

[41] D. W. deQuilettes, W. Zhang, V. M. Burlakov, D. J. Graham, T. Leijtens, A. Osherov, V. Bulović, H. J. Snaith, D. S. Ginger, and S. D. Stranks. Photo-induced halide redistribution in organic–inorganic perovskite films, *Nature Communications* **7**, 11683 (2016).

[42] M. Córdoba and K. Taretto. Insight into the dependence of photovoltaic performance on interfacial energy alignment in solar cells with mobile ions, *Solar RRL* **8**, 2300742 (2024).

[43] J. Herterich, M. Unmüssig, G. Loukeris, M. Kohlstädt, and U. Würfel. Ion movement explains huge voc increase despite almost unchanged internal quasi-fermi-level splitting in planar perovskite solar cells, *Energy Technology* **9**, 2001104 (2021).

[44] W.-J. Yin, T. Shi, and Y. Yan. Unusual defect physics in $CH_3NH_3PbI_3$ perovskite solar cell absorber, *Applied Physics Letters* **104**, 063903 (2014).

[45] C. Eames, J. M. Frost, P. R. F. Barnes, B. C. O'Regan, A. Walsh, and M. S. Islam. Ionic transport in hybrid lead iodide perovskite solar cells, *Nature Communications* **6**, 7497 (2015).

[46] J. Diekmann, F. Peña-Camargo, N. Tokmoldin, J. Thiesbrummel, J. Warby, E. Gutierrez-Partida, S. Shah, D. Neher, and M. Stolterfoht. Determination of mobile ion densities in halide perovskites via low-frequency capacitance and charge

extraction techniques, *The Journal of Physical Chemistry Letters* **14**, 4200–4210 (2023).

[47] L. Bertoluzzi, C. C. Boyd, N. Rolston, J. Xu, R. Prasanna, B. C. O'Regan, and M. D. McGehee. Mobile ion concentration measurement and open-access band diagram simulation platform for halide perovskite solar cells, *Joule* **4**, 109–127 (2020).

[48] M. C. Schmidt, A. O. Alvarez, J. J. de Boer, L. J. van de Ven, and B. Ehrler. Consistent interpretation of time- and frequency-domain traces of ion migration in perovskite semiconductors, *ACS Energy Letters* **9**, 5850–5858 (2024).

[49] J. M. Azpiroz, E. Mosconi, J. Bisquert, and F. De Angelis. Defect migration in methylammonium lead iodide and its role in perovskite solar cell operation, *Energy & Environmental Science* **8**, 2118–2127 (2015).

[50] S. Meloni, T. Moehl, W. Tress, M. Franckevičius, M. Saliba, Y. H. Lee, P. Gao, M. K. Nazeeruddin, S. M. Zakeeruddin, U. Rothlisberger, and M. Graetzel. Ionic polarization-induced current–voltage hysteresis in $CH_3NH_3PbX_3$ perovskite solar cells, *Nature Communications* **7**, 10334 (2016).

[51] P. Delugas, C. Caddeo, A. Filippetti, and A. Mattoni. Thermally activated point defect diffusion in methylammonium lead trihalide: Anisotropic and ultrahigh mobility of iodine, *The Journal of Physical Chemistry Letters* **7**, 2356–2361 (2016).

[52] W. Tress, N. Marinova, T. Moehl, S. M. Zakeeruddin, M. K. Nazeeruddin, and M. Grätzel. Understanding the rate-dependent j–v hysteresis, slow time component, and aging in $CH_3NH_3PbI_3$ perovskite solar cells: the role of a compensated electric field, *Energy & Environmental Science* **8**, 995–1004 (2015).

[53] L. McGovern, G. Grimaldi, M. H. Futscher, E. M. Hutter, L. A. Muscarella, M. C. Schmidt, and B. Ehrler. Reduced barrier for ion migration in mixed-halide perovskites, *ACS Applied Energy Materials* **4**, 13431–13437 (2021).

[54] L. McGovern, M. H. Futscher, L. A. Muscarella, and B. Ehrler. Understanding the stability of $MAPbBr_3$ versus $MAPbI_3$: Suppression of methylammonium migration and reduction of halide migration, *The Journal of Physical Chemistry Letters* **11**, 7127–7132 (2020).

[55] G. Richardson, S. E. J. O'Kane, R. G. Niemann, T. A. Peltola, J. M. Foster, P. J. Cameron, and A. B. Walker. Can slow-moving ions explain hysteresis in the current–voltage curves of perovskite solar cells? *Energy & Environmental Science* **9**, 1476–1485 (2016).

[56] V. M. Le Corre, J. Diekmann, F. Peña-Camargo, J. Thiesbrummel, N. Tokmoldin, E. Gutierrez-Partida, K. P. Peters, L. Perdigón-Toro, M. H. Futscher, F. Lang, J. Warby, H. J. Snaith, D. Neher, and M. Stolterfoht. Quantification of efficiency losses due to mobile ions in perovskite solar cells via fast hysteresis measurements, *Solar RRL* **6**, 2100772 (2022).

[57] J. Thiesbrummel, V. M. Le Corre, F. Peña-Camargo, L. Perdigón-Toro, F. Lang, F. Yang, M. Grischek, E. Gutierrez-Partida, J. Warby, M. D. Farrar, S. Mahesh, P. Caprioglio, S. Albrecht, D. Neher, H. J. Snaith, and M. Stolterfoht. Universal current losses in perovskite solar cells due to mobile ions, *Advanced Energy Materials* **11**, 2101447 (2021).

[58] A. Guerrero, J. You, C. Aranda, Y. S. Kang, G. Garcia-Belmonte, H. Zhou, J. Bisquert, and Y. Yang. Interfacial degradation of planar lead halide perovskite solar cells, *ACS Nano* **10**, 218–224 (2016).

[59] K. Domanski, B. Roose, T. Matsui, M. Saliba, S.-H. Turren-Cruz, J.-P. Correa-Baena, C. R. Carmona, G. Richardson, J. M. Foster, F. De Angelis, J. M. Ball, A. Petrozza, N. Mine, M. K. Nazeeruddin, W. Tress, M. Grätzel, U. Steiner, A. Hagfeldt, and A. Abate. Migration of cations induces reversible performance losses over day/night cycling in perovskite solar cells, *Energy & Environmental Science* **10**, 604–613 (2017).

[60] W. Zhou, X. Chen, R. Zhou, H. Cai, Y. Wang, T. Zhang, Z. Zheng, F. Gao, Y. Zhang, and H. Yan. The role of grain boundaries on ion migration and charge recombination in halide perovskites, *Small* **20**, 2310368 (2024).

[61] L. McGovern, I. Koschany, G. Grimaldi, L. A. Muscarella, and B. Ehrler. Grain size influences activation energy and migration pathways in $MAPbBr_3$ perovskite solar cells, *The Journal of Physical Chemistry Letters* **12**, 2423–2428 (2021).

[62] I. M. Hermes, Y. Hou, V. W. Bergmann, C. J. Brabec, and S. A. L. Weber. The interplay of contact layers: How the electron transport layer influences interfacial recombination and hole extraction in perovskite solar cells, *The Journal of Physical Chemistry Letters* **9**, 6249–6256 (2018).

[63] L. Jiang, J. Lu, S. R. Raga, J. Sun, X. Lin, W. Huang, F. Huang, U. Bach, and Y.-B. Cheng. Fatigue stability of $CH_3NH_3PbI_3$ based perovskite solar cells in day/night cycling, *Nano Energy* **58**, 687–694 (2019).

[64] A. J. Olasoji, J. K. Park, H. J. Lee, Y. Song, D. S. Lee, and S. H. Im. Metal halide perovskites: a platform for next-generation multifunctional devices, *Advances in Industrial and Engineering Chemistry* **1**, 12 (2025).

[65] K. Sakhatskyi, R. A. John, A. Guerrero, S. Tsarev, S. Sabisch, T. Das, G. J. Matt, S. Yakunin, I. Cherniukh, M. Kotyrba, Y. Berezovska, M. I. Bodnarchuk, S. Chakraborty, J. Bisquert, and M. V. Kovalenko. Assessing the drawbacks and benefits of ion migration in lead halide perovskites, *ACS Energy Letters* **7**, 3401–3414 (2022).

[66] Y. Liu, A. V. Ievlev, N. Borodinov, M. Lorenz, K. Xiao, M. Ahmadi, B. Hu, S. V. Kalinin, and O. S. Ovchinnikova. Direct observation of photoinduced ion migration in lead halide perovskites, *Advanced Functional Materials* **31**, 2008777 (2021).

[67] Y. Luo, P. Khoram, S. Brittman, Z. Zhu, B. Lai, S. P. Ong, E. C. Garnett, and D. P. Fenning. Direct observation of halide migration and its effect on the photoluminescence of methylammonium lead bromide perovskite single crystals, *Advanced Materials* **29**, 1703451 (2017).

[68] D. J. Slotcavage, H. I. Karunadasa, and M. D. McGehee. Light-induced phase segregation in halide-perovskite absorbers, *ACS Energy Letters* **1**, 1199–1205 (2016).

[69] S. G. Motti, D. Meggiolaro, A. J. Barker, E. Mosconi, C. A. R. Perini, J. M. Ball, M. Gandini, M. Kim, F. De Angelis, and A. Petrozza. Controlling competing photochemical reactions stabilizes perovskite solar cells, *Nature Photonics* **13**, 532–539 (2019).

[70] M. H. Futscher, M. K. Gangishetty, D. N. Congreve, and B. Ehrler. Quantifying mobile ions and electronic defects in perovskite-based devices with temperature-dependent capacitance measurements: Frequency vs time domain, *The Journal of Chemical Physics* **152**, 044202 (2020).

[71] M. H. Futscher, J. M. Lee, L. McGovern, L. A. Muscarella, T. Wang, M. I. Haider, A. Fakharuddin, L. Schmidt-Mende, and B. Ehrler. Quantification of ion migration in $CH_3NH_3PbI_3$ perovskite solar cells by transient capacitance measurements, *Materials Horizons* **6**, 1497–1503 (2019).

[72] M. C. Schmidt, E. Gutierrez-Partida, M. Stolterfoht, and B. Ehrler. Impact of mobile ions on transient capacitance measurements of perovskite solar cells, *PRX Energy* **2**, 043011 (2023).

[73] C. Li, A. Guerrero, S. Huettner, and J. Bisquert. Unravelling the role of vacancies in lead halide perovskite through electrical switching of photoluminescence, *Nature Communications* **9**, 5113 (2018).

[74] W. Clarke, G. Richardson, and P. Cameron. Understanding the full zoo of perovskite solar cell impedance spectra with the standard drift-diffusion model, *Advanced Energy Materials* **14**, 2400955 (2024).

[75] E. von Hauff and D. Klotz. Impedance spectroscopy for perovskite solar cells: characterisation, analysis, and diagnosis, *Journal of Materials Chemistry C* **10**, 742–761 (2022).

[76] Y. Wang, H. Zheng, J. Xiao, Y. Liu, Q. Liu, X. Ma, J. Hu, D. Zou, and S. Hou. Intensity-modulated photocurrent and photovoltage spectroscopy for characterizing charge dynamics in solar cells, *Advanced Energy Materials* **14**, 2401585 (2024).

[77] A. O. Alvarez, S. Ravishankar, and F. Fabregat-Santiago. Combining modulated techniques for the analysis of photosensitive devices, *Small Methods* **5**, 2100661 (2021).

[78] A. C. Lazanas and M. I. Prodromidis. Electrochemical impedance spectroscopy - a tutorial, *ACS Measurement Science Au* **3**, 162–193 (2023).

[79] W. Peng, C. Aranda, O. M. Bakr, G. Garcia-Belmonte, J. Bisquert, and A. Guerrero. Quantification of ionic diffusion in lead halide perovskite single crystals, *ACS Energy Letters* **3**, 1477–1481 (2018).

[80] W. Clarke, P. Cameron, and G. Richardson. Predicting long-term stability from short-term measurement: Insights from modeling degradation in perovskite solar cells during voltage scans and impedance spectroscopy, *The Journal of Physical Chemistry Letters* **15**, 11730–11736 (2024).

[81] M. V. Khenkin, E. A. Katz, A. Abate, G. Bardizza, J. J. Berry, C. Brabec, F. Brunetti, V. Bulović, Q. Burlingame, A. Di Carlo, R. Cheacharoen, Y.-B. Cheng, A. Colsmann, S. Cros, K. Domanski, M. Dusza, C. J. Fell, S. R. Forrest, Y. Galagan, D. Di Girolamo, M. Grätzel, A. Hagfeldt, E. von Hauff, H. Hoppe, J. Kettle, H. Köbler, M. S. Leite, S. F. Liu, Y.-L. Loo, J. M. Luther, C.-Q. Ma, M. Madsen, M. Manceau, M. Matheron, M. McGehee, R. Meitzner, M. K. Nazeeruddin, A. F. Nogueira, Ç. Odabaşı, A. Osherov, N.-G. Park, M. O. Reese, F. De Rossi, M. Saliba, U. S. Schubert, H. J. Snaith, S. D. Stranks, W. Tress, P. A. Troshin, V. Turkovic, S. Veenstra, I. Visoly-Fisher, A. Walsh, T. Watson, H. Xie, R. Yıldırım, S. M. Zakeeruddin, K. Zhu, and M. Lira-Cantu. Consensus statement for stability assessment and reporting for perovskite photovoltaics based on isos procedures, *Nature Energy* **5**, 35–49 (2020).

[82] H. Wang, A. Guerrero, A. Bou, A. M. Al-Mayouf, and J. Bisquert. Kinetic and material properties of interfaces governing slow response and long timescale phenomena in perovskite solar cells, *Energy & Environmental Science* **12**, 2054–2079 (2019).

[83] M. T. Khan, M. Salado, A. Almohammedi, S. Kazim, and S. Ahmad. Elucidating the impact of charge selective contact in halide perovskite through impedance spectroscopy, *Advanced Materials Interfaces* **6**, 1901193 (2019).

[84] H. B. Bebb and E. W. Williams, Photoluminescence i: Theory, in *Semiconductors and Semimetals, Volume 8: Transport and Optical Phenomena*, Semiconductors and Semimetals, Vol. 8, edited by R. K. Willardson and A. C. Beer (Academic Press, New York and London, 1972) pp. 181–320.

[85] P. Wurfel. The chemical potential of radiation, *Journal of Physics C: Solid State Physics* **15**, 3967 (1982).

[86] T. Unold and L. Gütay, Photoluminescence analysis of thin-film solar cells, in *Advanced Characterization Techniques for Thin Film Solar Cells* (John Wiley and Sons, Ltd, Chichester, U.K., 2011) Chap. 7, pp. 151–175.

[87] J. K. Katahara and H. W. Hillhouse. Quasi-fermi level splitting and sub-bandgap absorptivity from semiconductor photoluminescence, *Journal of Applied Physics* **116**, 173504 (2014).

[88] I. L. Braly, D. W. deQuilettes, L. M. Pazos-Outón, S. Burke, M. E. Ziffer, D. S. Ginger, and H. W. Hillhouse. Hybrid perovskite films approaching the radiative limit with over 90% photoluminescence quantum efficiency, *Nature Photonics* **12**, 355–361 (2018).

[89] R. T. Ross. Some thermodynamics of photochemical systems, *The Journal of Chemical Physics* **46**, 4590–4593 (1967).

[90] J. C. de Mello, H. F. Wittmann, and R. H. Friend. An improved experimental determination of external photoluminescence quantum efficiency, *Advanced Materials* **9**, 230–232 (1997).

[91] S. Zeiske, O. J. Sandberg, N. Zarrabi, C. M. Wolff, M. Raoufi, F. Peña-Camargo, E. Gutierrez-Partida, P. Meredith, M. Stolterfoht, and A. Armin. Static disorder in lead halide perovskites, *The Journal of Physical Chemistry Letters* **13**, 7280–7285 (2022).

[92] R. Brüggemann and S. Reynolds. Modulated photoluminescence studies for lifetime determination in amorphous-silicon passivated crystalline-silicon wafers, *Journal of Non-Crystalline Solids* **352**, 1888–1891 (2006).

[93] M. Poplawski, F. Silva, J. C. Vanel, and P. R. i Cabarrocas. In situ minority carrier lifetime via fast modulated photoluminescence, *EPJ Photovoltaics* **14**, 19 (2023).

[94] N. Moron, B. Bérenguier, J. Alvarez, and J.-P. Kleider. Analytical model of the modulated photoluminescence in semiconductor materials, *Journal of Physics D: Applied Physics* **55**, 105103 (2021).

[95] Y. Zhao, F. Ma, Z. Qu, S. Yu, T. Shen, H.-X. Deng, X. Chu, X. Peng, Y. Yuan, X. Zhang, and J. You. Inactive (PbI_2)RbCl stabilizes perovskite films for efficient solar cells, *Science* **377**, 531–534 (2022).

[96] J. Yoo, G. Seo, M. Chua, T. G. Park, Y. Lu, F. Rotermund, Y.-K. Kim, C. Moon, N. Jeon, J.-P. Correa-Baena, V. Bulovic, S. S. Shin, M. Bawendi, and J. Seo. Efficient perovskite solar cells via improved carrier management, *Nature* **590**, 587–593 (2021).

[97] Q. Jiang, J. Tong, R. Scheidt, X. Wang, A. Louks, Y. Xian, R. Tirawat, A. Palmstrom, M. Hautzinger, S. Harvey, S. Johnston, L. Schelhas, B. Larson, E. Warren, M. Beard, J. Berry, Y. Yan, and K. Zhu. Compositional texture engineering for highly stable wide-bandgap perovskite solar cells, *Science* **378**, 1295–1300 (2022).

[98] M. J. Jeong, C. S. Moon, S. Lee, J. M. Im, M. Y. Woo, J. H. Lee, H. Cho, S. W. Jeon, and J. H. Noh. Boosting radiation of stacked halide layer for perovskite solar cells with efficiency over 25%, *Joule* **7**, 112–127 (2023).

[99] M. Degani, Q. An, M. Albaladejo-Siguan, Y. J. Hofstetter, C. Cho, F. Paulus, G. Grancini, and Y. Vaynzof. 23.7% efficient inverted perovskite solar cells by dual interfacial modification, *Science Advances* **7**, eabj7930 (2021).

[100] H. Sun, S. Gillespie, S. A. Rigter, J. S. van der Burgt, K. Datta, and E. C. Garnett. Spectroscopic analysis for the identification of loss mechanisms in back-contact perovskite solar cells, *Advanced Materials Technologies* **8**, 2300241 (2023).

[101] R. Sinton, A. Cuevas, and M. Stuckings, Quasi-steady-state photoconductance, a new method for solar cell material and device characterization, in *Conference Record of the Twenty Fifth IEEE Photovoltaic Specialists Conference* (1996) pp. 457–460.

[102] A. Cuevas and D. Macdonald. Measuring and interpreting the lifetime of silicon wafers, *Solar Energy* **76**, 255–262 (2004).

[103] K. McIntosh and R. Sinton. Uncertainty in photoconductance lifetime measurements that use an inductive-coil detector, *Proceedings of the 23rd European Photovoltaic Solar Energy Conference* (2008).

[104] H. D. Nagel, C. Berge, and A. G. Aberle. Generalized analysis of quasi-steady-state and quasi-transient measurements of carrier lifetimes in semiconductors, *Journal of Applied Physics* **86**, 6218–6221 (1999).

[105] E. Yablonovitch, D. L. Allara, C. C. Chang, T. Gmitter, and T. B. Bright. Unusually low surface-recombination velocity on silicon and germanium surfaces, *Physical Review Letters* **57**, 249–252 (1986).

[106] F. Wolny, M. Müller, A. Krause, and D. Neuhaus. Study of the bulk lifetime and material saturation current density of different p-type monocrystalline silicon materials, *Energy Procedia* **124**, 235–239 (2017).

[107] T. Niewelt, B. Steinhauser, A. Richter, B. Veith-Wolf, A. Fell, B. Hammann, N. Grant, L. Black, J. Tan, A. Youssef, J. Murphy, J. Schmidt, M. Schubert, and S. Glunz. Reassessment of the intrinsic bulk recombination in crystalline silicon, *Solar Energy Materials and Solar Cells* **235**, 111467 (2022).

[108] A. Cuevas and R. A. Sinton. Prediction of the open-circuit voltage of solar cells from the steady-state photoconductance, *Progress in Photovoltaics* **5**, 79–90 (1997).

[109] A. Kimmerle, P. Rothhardt, A. Wolf, and R. A. Sinton. Increased reliability for j0-analysis by qsspc, *Energy Procedia* **55**, 101–106 (2014).

[110] A. Kimmerle, J. Greulich, and A. Wolf. Carrier-diffusion corrected j0-analysis of charge carrier lifetime measurements for increased consistency, *Solar Energy Materials and Solar Cells* **142**, 116–122 (2015).

[111] L. M. Pazos-Outón, T. P. Xiao, and E. Yablonovitch. Fundamental efficiency limit of lead iodide perovskite solar cells, *The Journal of Physical Chemistry Letters* **9**, 1703–1711 (2018).

[112] T. Sherkar, C. Momblona, L. Gil-Escrig, J. Ávila, M. Sessolo, H. Bolink, and L. Koster. Recombination in perovskite solar cells: Significance of grain boundaries, interface traps and defect ions, *ACS Energy Letters* **2** (2017).

[113] D. Luo, R. Su, W. Zhang, Q. Gong, and R. Zhu. Minimizing non-radiative recombination losses in perovskite solar cells, *Nature Reviews Materials* **5**, 44–60 (2020).

[114] M. Müller. Reporting effective lifetimes at solar cell relevant injection densities, *Energy Procedia* **92**, 138–144 (2016).

[115] A. Richter, S. W. Glunz, F. Werner, J. Schmidt, and A. Cuevas. Improved quantitative description of auger recombination in crystalline silicon, *Physical Review B* **86**, 165202 (2012).

[116] D. Phillips, R. Drake, D. OConnor, and R. Christensen. Time correlated single-photon counting (tcspc) using laser excitation, *Instrumentation Science & Technology* **14**, 267–292 (1985).

[117] L. Kudriashova, D. Kiermasch, P. Rieder, M. Campbell, K. Tvingstedt, A. Baumann, G. Astakhov, and V. Dyakonov. Impact of interfaces and laser repetition rate on photocarrier dynamics in lead halide perovskites, *The Journal of Physical Chemistry Letters* **8** (2017).

[118] W. Chen, N. Pham, H. Wang, B. Jia, and X. Wen. Spectroscopic insight into efficient and stable hole transfer at the perovskite/spiro-ometad interface with alternative additives, *ACS Applied Materials & Interfaces* **13** (2021).

[119] P. Chen, Y. Xiao, L. Li, L. Zhao, M. Yu, S. Li, J. Hu, B. Liu, Y. Yang, D. Luo, C.-H. Hou, X. Guo, J.-J. Shyue, Z.-H. Lu, Q. Gong, H. J. Snaith, and R. Zhu. Efficient inverted perovskite solar cells via improved sequential deposition, *Advanced Materials* **35**, 2206345 (2023).

[120] A. Ren, H. Lai, X. Hao, Z. Tang, H. Xu, B. Yu Jeco-Espaldon, K. Watanabe, L. Wu, M. Sugiyama, J. Wu, and D. Zhao. Efficient perovskite solar modules with minimized nonradiative recombination and local carrier transport losses, *Joule* **4** (2020).

[121] B. Krogmeier, F. Staub, D. Grabowski, U. Rau, and T. Kirchartz. Quantitative analysis of the transient photoluminescence of $CH_3NH_3PbI_3/PC_{61}BM$ heterojunctions by numerical simulations, *Sustainable Energy & Fuels* **2** (2018).

[122] A. Al-Ashouri, E. Köhnen, B. Li, A. Magomedov, H. Hempel, P. Caprioglio, J. A. Márquez, A. B. M. Vilches, E. Kasparavicius, J. A. Smith, N. Phung, D. Menzel, M. Grischek, L. Kegelmann, D. Skroblin, C. Gollwitzer, T. Malinauskas, M. Jošt, G. Matič, B. Rech, R. Schlatmann, M. Topič, L. Korte, A. Abate, B. Stannowski, D. Neher, M. Stolterfoht, T. Unold, V. Getautis, and S. Albrecht. Monolithic perovskite/silicon tandem solar cell with 29% efficiency by enhanced hole extraction, *Science* **370**, 1300–1309 (2020).

[123] M. Liu, S. Dahlström, C. Ahläng, S. Wilken, A. Degterev, A. Matuhina, M. Hadadian, M. Markkanen, K. Aitola, A. Kamppinen, J. Deska, O. Mangs, M. Nyman, P. D. Lund, J.-H. Smått, R. Österbacka, and P. Vivo. Beyond hydrophobicity: how f4-tcnq doping of the hole transport material improves stability of mesoporous triple-cation perovskite solar cells, *Journal of Materials Chemistry A* **10**, 11721–11731 (2022).

[124] I. Allegro, Y. Li, B. S. Richards, U. W. Paetzold, U. Lemmer, and I. A. Howard. Bimolecular and auger recombination in phase-stable perovskite thin films from

cryogenic to room temperature and their effect on the amplified spontaneous emission threshold, *The Journal of Physical Chemistry Letters* **12**, 2293–2298 (2021).

[125] T. P. Weiss, B. Bissig, T. Feurer, R. Carron, S. Buecheler, and A. N. Tiwari. Bulk and surface recombination properties in thin film semiconductors with different surface treatments from time-resolved photoluminescence measurements, *Scientific Reports* **9**, 5385 (2019).

[126] E. Aydin, M. De Bastiani, and S. De Wolf. Defect and contact passivation for perovskite solar cells, *Advanced Materials* **31** (2019).

[127] R. Brenes, D. Guo, A. Osherov, N. K. Noel, C. Eames, E. M. Hutter, S. K. Pathak, F. Niroui, R. H. Friend, M. S. Islam, H. J. Snaith, V. Bulović, T. J. Savenije, and S. D. Stranks. Metal halide perovskite polycrystalline films exhibiting properties of single crystals, *Joule* **1**, 155–167 (2017).

[128] Y. Chen, H. T. Yi, X. Wu, R. Haroldson, Y. Gartstein, Y. Rodionov, K. Tikhonov, A. Zakhidov, X. Zhu, and V. Podzorov. Extended carrier lifetimes and diffusion in hybrid perovskites revealed by hall effect and photoconductivity measurements, *Nature Communications* **7**, 12253 (2016).

[129] Q. Dong, Y. Fang, Y. Shao, P. Mulligan, J. Qiu, L. Cao, and J. Huang. Electron-hole diffusion lengths >175 μm in solution-grown $CH_3NH_3PbI_3$ single crystals, *Science* **347**, 967–970 (2015).

[130] T. Savenije, C. Ponseca, L. Kunneman, M. Abdellah, K. Zheng, Y. Tian, Q. Zhu, S. Canton, I. Scheblykin, T. Pullerits, A. Yartsev, and V. Sundström. Thermally activated exciton dissociation and recombination control the carrier dynamics in organometal halide perovskite, *The Journal of Physical Chemistry Letters* **5**, 2189–2194 (2014).

[131] C. Wehrenfennig, G. E. Eperon, M. B. Johnston, H. J. Snaith, and L. M. Herz. High charge carrier mobilities and lifetimes in organolead trihalide perovskites, *Advanced Materials* **26**, 1584–1589 (2014).

[132] G. Xing, N. Mathews, S. Sun, S. S. Lim, Y. M. Lam, M. Grätzel, S. Mhaisalkar, and T. C. Sum. Long-range balanced electron- and hole-transport lengths in organic-inorganic $CH_3NH_3PbI_3$, *Science* **342**, 344–347 (2013).

[133] Y. Yang, M. Yang, T. Moore, David, Y. Yan, E. Miller, K. Zhu, and M. Beard. Top and bottom surfaces limit carrier lifetime in lead iodide perovskite films, *Nature Energy* **2**, 16207 (2017).

[134] G. Adhyaksa, S. Brittman, H. Abolins, A. Lof, X. Li, J. Keelor, Y. Luo, T. Duevski, R. Heeren, S. Ellis, D. Fenning, and E. Garnett. Understanding detrimental and beneficial grain boundary effects in halide perovskites, *Advanced Materials* **30**, 1804792 (2018).

[135] H. P. Pasanen, P. Vivo, L. Canil, H. Hempel, T. Unold, A. Abate, and N. V. Tkachenko. Monitoring charge carrier diffusion across a perovskite film with transient absorption spectroscopy, *The Journal of Physical Chemistry Letters* **11**, 445–450 (2020).

[136] D. W. deQuilettes, S. Koch, S. Burke, R. K. Paranji, A. J. Shropshire, M. E. Ziffer, and D. S. Ginger. Photoluminescence lifetimes exceeding 8 µs and quantum yields exceeding 30% in hybrid perovskite thin films by ligand passivation, *ACS Energy Letters* **1**, 438–444 (2016).

[137] A. F. Palechor-Ocampo, J. Caram, P. Hierrezuelo-Cardet, F. Ventosinos, D. Pérez-del Rey, H. J. Bolink, and J. A. Schmidt. Singular time-dependent photoconductivity response of $MAPbI_3$ samples deposited by vacuum processing on different substrates, *Energy Technology* **11**, 2200814 (2023).

[138] C. C. Boyd, R. C. Shallcross, T. Moot, R. Kerner, L. Bertoluzzi, A. Onno, S. Kavadiya, C. Chosy, E. J. Wolf, J. Werner, J. A. Raiford, C. de Paula, A. F. Palmstrom, Z. J. Yu, J. J. Berry, S. F. Bent, Z. C. Holman, J. M. Luther, E. L. Ratcliff, N. R. Armstrong, and M. D. McGehee. Overcoming redox reactions at perovskite-nickel oxide interfaces to boost voltages in perovskite solar cells, *Joule* **4**, 1759–1775 (2020).

[139] J. Holovský, E. Horynová, L. Horák, K. Ridzoňová, Z. Remeš, L. Landová, and R. K. Sharma. Pulsed laser deposition of high-transparency molybdenum oxide thin films, *Vacuum* **194**, 110613 (2021).

[140] Y. Wang, L. Duan, M. Zhang, Z. Hameiri, X. Liu, Y. Bai, and X. Hao. Ptaa as efficient hole transport materials in perovskite solar cells: A review, *Solar RRL* **6**, 2200234 (2022).

[141] M. Saliba, J.-P. Correa-Baena, C. Wolff, M. Stolterfoht, N. Phung, S. Albrecht, D. Neher, and A. Abate. How to make over 20% efficient perovskite solar cells in regular (n–i–p) and inverted (p–i–n) architectures, *Chemistry of Materials* **30** (2018).

[142] J. Warby, F. Zu, S. Zeiske, E. Gutierrez-Partida, L. Frohloff, S. Kahmann, K. Frohna, E. Mosconi, E. Radicchi, F. Lang, S. Shah, F. Peña-Camargo, H. Hempel, T. Unold, N. Koch, A. Armin, F. De Angelis, S. D. Stranks, D. Neher, and M. Stolterfoht. Understanding performance limiting interfacial recombination in pin perovskite solar cells, *Advanced Energy Materials* **12**, 2103567 (2022).

[143] L. Nakka, Y. Cheng, A. G. Aberle, and F. Lin. Analytical review of spiro-ometad hole transport materials: Paths toward stable and efficient perovskite solar cells, *Advanced Energy and Sustainability Research* **3**, 2200045 (2022).

[144] S. Olthof and K. Meerholz. Substrate-dependent electronic structure and film formation of $MAPbI_3$ perovskites, *Scientific Reports* **7**, 40267 (2017).

[145] A. Cuevas. The recombination parameter j0, *Energy Procedia* **55**, 53–62 (2014).

[146] T. Kirchartz. Photon management in perovskite solar cells, *The Journal of Physical Chemistry Letters* **10**, 5892–5896 (2019).

[147] J. M. Richter, M. Abdi-Jalebi, A. Sadhanala, M. Tabachnyk, J. P. Rivett, L. M. Pazos-Outón, K. C. Gödel, M. Price, F. Deschler, and R. H. Friend. Enhancing photoluminescence yields in lead halide perovskites by photon recycling and light outcoupling, *Nature Communications* **7**, 13941 (2016).

[148] J. M. Ball, S. D. Stranks, M. T. Hörantner, S. Hüttner, W. Zhang, E. J. W. Crossland, I. Ramirez, M. Riede, M. B. Johnston, R. H. Friend, and H. J. Snaith. Optical properties and limiting photocurrent of thin-film perovskite solar cells, *Energy & Environmental Science* **8**, 602–609 (2015).

[149] Y. Da, Y. Xuan, and Q. Li. Quantifying energy losses in planar perovskite solar cells, *Solar Energy Materials and Solar Cells* **174**, 206–213 (2018).

[150] D.-L. Wang, H.-J. Cui, G.-J. Hou, Z.-G. Zhu, Q.-B. Yan, and G. Su. Highly efficient light management for perovskite solar cells, *Scientific Reports* **6**, 18922 (2016).

[151] P. Makuła, M. Pacia, and W. Macyk. How to correctly determine the band gap energy of modified semiconductor photocatalysts based on uv–vis spectra, *The Journal of Physical Chemistry Letters* **9**, 6814–6817 (2018).

[152] D. Menzel, A. Al-Ashouri, A. Tejada, I. Levine, J. A. Guerra, B. Rech, S. Albrecht, and L. Korte. Field effect passivation in perovskite solar cells by a lif interlayer, *Advanced Energy Materials* **12**, 2201109 (2022).

[153] F. Ye, S. Zhang, J. Warby, J. Wu, E. Gutierrez-Partida, F. Lang, S. Shah, E. Saglamkaya, B. Sun, F. Zu, S. Shoaee, H. Wang, B. Stiller, D. Neher, W.-H. Zhu, M. Stolterfoht, and Y. Wu. Overcoming C_{60}-induced interfacial recombination in inverted perovskite solar cells by electron-transporting carborane, *Nature Communications* **13**, 7454 (2022).

[154] L. E. Black, Surface recombination theory, in *New Perspectives on Surface Passivation: Understanding the Si-Al_2O_3 Interface* (Springer International Publishing, Cham, Switzerland, 2016) pp. 15–28.

[155] Y. Shi, E. Rojas-Gatjens, J. Wang, J. Pothoof, R. Giridharagopal, K. Ho, F. Jiang, M. Taddei, Z. Yang, E. M. Sanehira, M. D. Irwin, C. Silva-Acuña, and D. S. Ginger. (3-aminopropyl)trimethoxysilane surface passivation improves perovskite solar cell performance by reducing surface recombination velocity, *ACS Energy Letters* **7**, 4081–4088 (2022).

[156] S. Jariwala, S. Burke, S. Dunfield, R. C. Shallcross, M. Taddei, J. Wang, G. E. Eperon, N. R. Armstrong, J. J. Berry, and D. S. Ginger. Reducing surface recombination velocity of methylammonium-free mixed-cation mixed-halide perovskites via surface passivation, *Chemistry of Materials* **33**, 5035–5044 (2021).

[157] M. A. de Araújo, R. Silva, E. de Lima, D. P. Pereira, and P. C. de Oliveira. Measurement of gaussian laser beam radius using the knife-edge technique: improvement on data analysis, *Applied Optics* **48**, 393–396 (2009).

[158] S. A. Mann, S. Z. Oener, A. Cavalli, J. E. M. Haverkort, E. P. A. M. Bakkers, and E. C. Garnett. Quantifying losses and thermodynamic limits in nanophotonic solar cells, *Nature Nanotechnology* **11**, 1071–1075 (2016).

[159] D. Grabowski, Z. Liu, G. Schöpe, U. Rau, and T. Kirchartz. Fill factor losses and deviations from the superposition principle in lead halide perovskite solar cells, *Solar RRL* **6**, 2200507 (2022).

[160] M. Saliba and L. Etgar. Current density mismatch in perovskite solar cells, *ACS Energy Letters* **5**, 2886–2888 (2020).

[161] M. Abdi-Jalebi, M. I. Dar, S. P. Senanayak, A. Sadhanala, Z. Andaji-Garmaroudi, L. M. Pazos-Outón, J. M. Richter, A. J. Pearson, H. Sirringhaus, M. Grätzel, and R. H. Friend. Charge extraction via graded doping of hole transport layers gives highly luminescent and stable metal halide perovskite devices, *Science Advances* **5**, eaav2012 (2019).

[162] Q. Dong, C. Zhu, M. Chen, C. Jiang, J. Guo, Y. Feng, Z. Dai, S. K. Yadavalli, M. Hu, X. Cao, Y. Li, Y. Huang, Z. Liu, Y. Shi, L. Wang, N. P. Padture, and Y. Zhou. Interpenetrating interfaces for efficient perovskite solar cells with high operational stability and mechanical robustness, *Nature Communications* **12**, 973 (2021).

[163] Y. Zhong, M. Hufnagel, M. Thelakkat, C. Li, and S. Huettner. Role of pcbm in the suppression of hysteresis in perovskite solar cells, *Advanced Functional Materials* **30**, 1908920 (2020).

[164] J. Luo, J. Xia, H. Yang, H. A. Malik, F. Han, H. Shu, X. Yao, Z. Wan, and C. Jia. Novel approach toward hole-transporting layer doped by hydrophobic lewis acid through infiltrated diffusion doping for perovskite solar cells, *Nano Energy* **70**, 104509 (2020).

[165] S.-K. Kim, H.-J. Seok, D.-H. Kim, D.-H. Choi, S.-J. Nam, S.-C. Kim, and H.-K. Kim. Comparison of NiOx thin film deposited by spin-coating or thermal evaporation for application as a hole transport layer of perovskite solar cells, *RSC Advances* **10**, 43847–43852 (2020).

[166] X. Li, Y. Meng, R. Liu, Z. Yang, Y. Zeng, Y. Yi, W. E. I. Sha, Y. Long, and J. Yang. High-efficiency and durable inverted perovskite solar cells with thermally-induced phase-change electron extraction layer, *Advanced Energy Materials* **11**, 2102844 (2021).

[167] Z. Liu, T. He, H. Wang, X. Song, H. Liu, J. Yang, K. Liu, and H. Ma. Improving the stability of the perovskite solar cells by v2o5 modified transport layer film, *RSC Advances* **7**, 18456–18465 (2017).

[168] M. A. Green, E. D. Dunlop, M. Yoshita, N. Kopidakis, K. Bothe, G. Siefer, X. Hao, and J. Y. Jiang. Solar cell efficiency tables (version 65), *Progress in Photovoltaics: Research and Applications* **33**, 3–15 (2025).

[169] H. Chen, C. Liu, J. Xu, A. Maxwell, W. Zhou, Y. Yang, Q. Zhou, A. S. R. Bati, H. Wan, Z. Wang, L. Zeng, J. Wang, P. Serles, Y. Liu, S. Teale, Y. Liu, M. I. Saidaminov, M. Li, N. Rolston, S. Hoogland, T. Filleter, M. G. Kanatzidis, B. Chen, Z. Ning, and E. H. Sargent. Improved charge extraction in inverted perovskite solar cells with dual-site-binding ligands, *Science* **384**, 189–193 (2024).

[170] Y. Cheng and L. Ding. Pushing commercialization of perovskite solar cells by improving their intrinsic stability, *Energy & Environmental Science* **14**, 3233–3255 (2021).

[171] Y. Rong, Y. Hu, A. Mei, H. Tan, M. I. Saidaminov, S. I. Seok, M. D. McGehee, E. H. Sargent, and H. Han. Challenges for commercializing perovskite solar cells, *Science* **361**, eaat8235 (2018).

[172] B. Conings, J. Drijkoningen, N. Gauquelin, A. Babayigit, J. D'Haen, L. D'Olieslaeger, A. Ethirajan, J. Verbeeck, J. Manca, E. Mosconi, F. D. Angelis, and H.-G. Boyen. Intrinsic thermal instability of methylammonium lead trihalide perovskite, *Advanced Energy Materials* **5**, 1500477 (2015).

[173] B. Chen, S. Wang, Y. Song, C. Li, and F. Hao. A critical review on the moisture stability of halide perovskite films and solar cells, *Chemical Engineering Journal* **430**, 132701 (2022).

[174] R. Cheacharoen, C. C. Boyd, G. F. Burkhard, T. Leijtens, J. A. Raiford, K. A. Bush, S. F. Bent, and M. D. McGehee. Encapsulating perovskite solar cells to withstand damp heat and thermal cycling, *Sustainable Energy Fuels* **2**, 2398–2406 (2018).

[175] S. S. Dipta, M. A. Rahim, and A. Uddin. Encapsulating perovskite solar cells for long-term stability and prevention of lead toxicity, *Applied Physics Reviews* **11**, 021301 (2024).

[176] A. R. Bowring, L. Bertoluzzi, B. C. O'Regan, and M. D. McGehee. Reverse bias behavior of halide perovskite solar cells, *Advanced Energy Materials* **8**, 1702365 (2018).

[177] Y. Zhao, W. Zhou, H. Tan, R. Fu, Q. Li, F. Lin, D. Yu, G. Walters, E. H. Sargent, and Q. Zhao. Mobile-ion-induced degradation of organic hole-selective layers in perovskite solar cells, *The Journal of Physical Chemistry C* **121**, 14517–14523 (2017).

[178] V. Nandal and P. R. Nair. Predictive modeling of ion migration induced degradation in perovskite solar cells, *ACS Nano* **11**, 11505–11512 (2017).

[179] J. A. Kress, C. Quarti, Q. An, S. Bitton, N. Tessler, D. Beljonne, and Y. Vaynzof. Persistent ion accumulation at interfaces improves the performance of perovskite solar cells, *ACS Energy Letters* **7**, 3302–3310 (2022).

[180] B. P. Finkenauer, Akriti, K. Ma, and L. Dou. Degradation and self-healing in perovskite solar cells, *ACS Applied Materials & Interfaces* **14**, 24073–24088 (2022).

[181] C. Gonzales, A. Bou, A. Guerrero, and J. Bisquert. Capacitive and inductive characteristics of volatile perovskite resistive switching devices with analog memory, *The Journal of Physical Chemistry Letters* **15**, 6496–6503 (2024).

[182] F. De Angelis. The revival of metal-halide perovskites transistors, *ACS Energy Letters* **7**, 1490–1491 (2022).

[183] J. J. de Boer and B. Ehrler. Scalable microscale artificial synapses of lead halide perovskite with femtojoule energy consumption, *ACS Energy Letters* **9**, 5787–5794 (2024).

[184] J. S. van der Burgt, S. A. Rigter, N. de Gaay Fortman, and E. C. Garnett. Self-tracking solar concentrator with absorption of diffuse sunlight, *Advanced Optical Materials* **11**, 2202013 (2023).

[185] S. Ravishankar, C. Aranda, S. Sanchez, J. Bisquert, M. Saliba, and G. Garcia-Belmonte. Perovskite solar cell modeling using light- and voltage-modulated techniques, *The Journal of Physical Chemistry C* **123**, 6444–6449 (2019).

[186] J. Bisquert and M. Janssen. From frequency domain to time transient methods for halide perovskite solar cells: The connections of imps, imvs, tpc, and tpv, *The Journal of Physical Chemistry Letters* **12**, 7964–7971 (2021).

[187] P. Calado, A. M. Telford, D. Bryant, X. Li, J. Nelson, B. C. O'Regan, and P. R. Barnes. Evidence for ion migration in hybrid perovskite solar cells with minimal hysteresis, *Nature Communications* **7**, 13831 (2016).

[188] Y. Wei, Z. Cheng, and J. Lin. An overview on enhancing the stability of lead halide perovskite quantum dots and their applications in phosphor-converted leds, *Chemical Society Reviews* **48**, 310–350 (2019).

[189] D. Zhou, D. Liu, G. Pan, X. Chen, D. Li, W. Xu, X. Bai, and H. Song. Cerium and ytterbium codoped halide perovskite quantum dots: A novel and efficient downconverter for improving the performance of silicon solar cells, *Advanced Materials* **29**, 1704149 (2017).

[190] H. C. Weerasinghe, N. Macadam, J.-E. Kim, L. J. Sutherland, D. Angmo, L. W. T. Ng, A. D. Scully, F. Glenn, R. Chantler, N. L. Chang, M. Dehghanimadvar, L. Shi, A. W. Y. Ho-Baillie, R. Egan, A. S. R. Chesman, M. Gao, J. J. Jasieniak, T. Hasan, and D. Vak. The first demonstration of entirely roll-to-roll fabricated perovskite solar cell modules under ambient room conditions, *Nature Communications* **15**, 1656 (2024).

[191] M. Taddei, S. Jariwala, R. J. E. Westbrook, S. Gallagher, A. C. Weaver, J. Pothoof, M. E. Ziffer, H. J. Snaith, and D. S. Ginger. Interpreting halide perovskite semiconductor photoluminescence kinetics, *ACS Energy Letters* **9**, 2508–2516 (2024).

[192] W.-A. Quitsch, D. W. deQuilettes, O. Pfingsten, A. Schmitz, S. Ognjanovic, S. Jariwala, S. Koch, M. Winterer, D. S. Ginger, and G. Bacher. The role of excitation energy in photobrightening and photodegradation of halide perovskite thin films, *The Journal of Physical Chemistry Letters* **9**, 2062–2069 (2018).

[193] M. Ansari-Rad and J. Bisquert. Theory of light-modulated emission spectroscopy, *The Journal of Physical Chemistry Letters* **8**, 3673–3677 (2017).

[194] E. von Hauff. Impedance spectroscopy for emerging photovoltaics, *The Journal of Physical Chemistry C* **123**, 11329–11346 (2019).

[195] J. A. Giesecke, M. C. Schubert, D. Walter, and W. Warta. Minority carrier lifetime in silicon wafers from quasi-steady-state photoluminescence, *Applied Physics Letters* **97**, 092109 (2010).

[196] A. Desthieux, M. Sreng, P. Bulkin, I. Florea, E. Drahi, B. Bazer-Bachi, J.-C. Vanel, F. Silva, J. Posada, and P. Roca i Cabarrocas. Detection of stable positive fixed charges in AlOx activated during annealing with in situ modulated photoluminescence, *Solar Energy Materials and Solar Cells* **230**, 111172 (2021).

[197] S. Ambros, R. Carius, and H. Wagner. Lifetime distribution in a-si:h: geminate-, nongeminate- and auger-processes, *Journal of Non-Crystalline Solids* **137-138**, 555–558 (1991).

[198] R. Stachowitz, M. Schubert, and W. Fuhs. Non-radiative distant pair recombination in amorphous silicon, *Journal of Non-Crystalline Solids* **227-230**, 190–196 (1998).

[199] T. Aoki, S. Komedoori, S. Kobayashi, T. Shimizu, A. Ganjoo, and K. Shimakawa. Photoluminescence lifetime distributions of chalcogenide glasses obtained by wide-band frequency resolved spectroscopy, *Journal of Non-Crystalline Solids* **326-327**, 273–278 (2003).

[200] T. Aoki. Understanding the photoluminescence over 13-decade lifetime distribution in a-si:h, *Journal of Non-Crystalline Solids* **352**, 1138–1143 (2006).

[201] B. Bérenguier, N. Barreau, A. Jaffre, D. Ory, J.-F. Guillemoles, J.-P. Kleider, and L. Lombez. Defects characterization in thin films photovoltaics materials by correlated high-frequency modulated and time resolved photoluminescence: An application to Cu(In_Ga)Se_2, *Thin Solid Films* **669**, 520–524 (2019).

[202] S. G. Motti, J. B. Patel, R. D. J. Oliver, H. J. Snaith, M. B. Johnston, and L. M. Herz. Phase segregation in mixed-halide perovskites affects charge-carrier dynamics while preserving mobility, *Nature Communications* **12**, 6955 (2021).

[203] S. Aharon, D. R. Ceratti, N. P. Jasti, L. Cremonesi, Y. Feldman, M. A. C. Potenza, G. Hodes, and D. Cahen. 2d Pb-halide perovskites can self-heal photodamage better than 3d ones, *Advanced Functional Materials* **32**, 2113354 (2022).

[204] E. Mosconi, D. Meggiolaro, H. J. Snaith, S. D. Stranks, and F. De Angelis. Light-induced annihilation of frenkel defects in organo-lead halide perovskites, *Energy & Environmental Science* **9**, 3180–3187 (2016).

[205] M. Anaya, J. F. Galisteo-López, M. E. Calvo, J. P. Espinós, and H. Míguez. Origin of light-induced photophysical effects in organic metal halide perovskites in the presence of oxygen, *The Journal of Physical Chemistry Letters* **9**, 3891–3896 (2018).

[206] Y. Zhou, S. C. W. van Laar, D. Meggiolaro, L. Gregori, S. Martani, J.-Y. Heng, K. Datta, J. Jiménez-López, F. Wang, E. L. Wong, I. Poli, A. Treglia, D. Cortecchia, M. Prato, L. Kobera, F. Gao, N. Zhao, R. A. J. Janssen, F. De Angelis, and A. Petrozza. How photogenerated I_2 induces i-rich phase formation in lead mixed halide perovskites, *Advanced Materials* **36**, 2305567 (2024).

[207] I. Riet, H.-H. Fang, S. Adjokatse, S. Kahmann, and M. Loi. Influence of morphology on photoluminescence properties of methylammonium lead tribromide films, *Journal of Luminescence* **220**, 117033 (2020).

[208] Z. Andaji-Garmaroudi, M. Anaya, A. J. Pearson, and S. D. Stranks. Photobrightening in lead halide perovskites: Observations, mechanisms, and future potential, *Advanced Energy Materials* **10**, 1903109 (2020).

[209] D. Pitarch-Tena, T. T. Ngo, M. Vallés-Pelarda, T. Pauporté, and I. Mora-Seró. Impedance spectroscopy measurements in perovskite solar cells: Device stability and noise reduction, *ACS Energy Letters* **3**, 1044–1048 (2018).

[210] R. A. Sinton and A. Cuevas, A quasi-steady-state open-circuit voltage method for solar cell characterization, in *16th European Photovoltaic Solar Energy Conference*, Vol. 25 (Taylor and Francis, Glasgow, Scotland, 2000) pp. 1152–1155.

[211] S. Schiefer, B. Zimmermann, and U. Würfel. Determination of the intrinsic and the injection dependent charge carrier density in organic solar cells using the suns-v_{OC} method, *Journal of Applied Physics* **115**, 044506 (2014).

[212] D. Grabowski, Z. Liu, G. Schöpe, U. Rau, and T. Kirchartz. Fill factor losses and deviations from the superposition principle in lead halide perovskite solar cells, *Solar RRL* **6**, 2200507 (2022).

[213] A. Guerrero, J. Bisquert, and G. Garcia-Belmonte. Impedance spectroscopy of metal halide perovskite solar cells from the perspective of equivalent circuits, *Chemical Reviews* **121**, 14430–14484 (2021).

[214] A. O. Alvarez, R. Arcas, C. A. Aranda, L. Bethencourt, E. Mas-Marzá, M. Saliba, and F. Fabregat-Santiago. Negative capacitance and inverted hysteresis: Matching features in perovskite solar cells, *The Journal of Physical Chemistry Letters* **11**, 8417–8423 (2020).

[215] C. M. Wolff, P. Caprioglio, M. Stolterfoht, and D. Neher. Nonradiative recombination in perovskite solar cells: The role of interfaces, *Advanced Materials* **31**, 1902762 (2019).

[216] R. Sánchez Sánchez, A. Villanueva-Antolí, A. Bou, M. Ruiz-Murillo, I. Mora-Seró, and J. Bisquert. Radiative recombination processes in halide perovskites observed by light emission voltage modulated spectroscopy, *Advanced Materials* **35** (2023).

[217] M. D. Murbach, B. Gerwe, N. Dawson-Elli, and L. kun Tsui. impedance.py: A python package for electrochemical impedance analysis, *Journal of Open Source Software* **5**, 2349 (2020).

[218] Google Scholar, Search results for "halide perovskite", https://scholar.google.com (2025), accessed: July 19, 2025.

[219] J. Guo, B. Wang, D. Lu, T. Wang, T. Liu, R. Wang, X. Dong, T. Zhou, N. Zheng, Q. Fu, Z. Xie, X. Wan, G. Xing, Y. Chen, and Y. Liu. Ultralong carrier lifetime exceeding 20 μs in lead halide perovskite film enable efficient solar cells, *Advanced Materials* **35**, 2212126 (2023).

[220] F. De Angelis. The revival of metal-halide perovskites transistors, *ACS Energy Letters* **7**, 1490–1491 (2022).

[221] R. A. John, N. Shah, S. K. Vishwanath, S. E. Ng, B. Febriansyah, M. Jagadeeswararao, C.-H. Chang, A. Basu, and N. Mathews. Halide perovskite memristors as flexible and reconfigurable physical unclonable functions, *Nature Communications* **12**, 3681 (2021).

[222] S. J. Kim, I. H. Im, J. H. Baek, S. Choi, S. H. Park, D. E. Lee, J. Y. Kim, S. Y. Kim, N.-G. Park, D. Lee, J. J. Yang, and H. W. Jang. Linearly programmable two-dimensional halide perovskite memristor arrays for neuromorphic computing, *Nature Nanotechnology* **20**, 83–92 (2025).

[223] K. Yan, M. Peng, X. Yu, X. Cai, S. Chen, H. Hu, B. Chen, X. Gao, B. Dong, and D. Zou. High-performance perovskite memristor based on methyl ammonium lead halides, *Journal of Materials Chemistry C* **4**, 1375–1381 (2016).

[224] Y. Park and J.-S. Lee. Metal halide perovskite-based memristors for emerging memory applications, *The Journal of Physical Chemistry Letters* **13**, 5638–5647 (2022).

[225] A. Marunchenko, J. Kumar, A. Kiligaridis, S. M. Rao, D. Tatarinov, I. Matchenya, E. Sapozhnikova, R. Ji, O. Telschow, J. Brunner, A. Yulin, A. Pushkarev, Y. Vaynzof, and I. G. Scheblykin. Charge trapping and defect dynamics as origin of memory effects in metal halide perovskite memlumors, *The Journal of Physical Chemistry Letters* **15**, 6256–6265 (2024).

[226] Y. Tang, P. Jin, Y. Wang, D. Li, Y. Chen, P. Ran, W. Fan, K. Liang, H. Ren, X. Xu, R. Wang, Y. M. Yang, and B. Zhu. Enabling low-drift flexible perovskite photodetectors by electrical modulation for wearable health monitoring and weak light imaging, *Nature Communications* **14**, 4961 (2023).

[227] Y. Ma, X. Xu, T. Li, Z. Wang, N. Li, X. Zhao, W. Wei, X. Zhan, and L. Shen. Amplified narrowband perovskite photodetectors enabled by independent multiplication layers for anti-interference light detection, *Science Advances* **11**, eadq1127 (2025).

[228] Y. Fang, Q. Dong, Y. Shao, Y. Yuan, and J. Huang. onemicron-crystal photodetectors enabled by surface-charge recombination, *Nature Photonics* **9**, 679–686 (2015).

[229] R. Liu, F. Li, F. Zeng, R. Zhao, and R. Zheng. Halide perovskite x-ray detectors: Fundamentals, progress, and outlook, *Applied Physics Reviews* **11**, 021327 (2024).

[230] H. Kim, J. S. Han, J. Choi, S. Y. Kim, and H. W. Jang. Halide perovskites for applications beyond photovoltaics, *Small Methods* **2**, 1700310 (2018).

[231] S.-Y. Kim, H. Zhang, and J. Rubio-Magnieto. Operating mechanism principles and advancements for halide perovskite-based memristors and neuromorphic devices, *The Journal of Physical Chemistry Letters* **15**, 10087–10103 (2024).

[232] A. J. Knight, A. D. Wright, J. B. Patel, D. P. McMeekin, H. J. Snaith, M. B. Johnston, and L. M. Herz. Electronic traps and phase segregation in lead mixed-halide perovskite, *ACS Energy Letters* **4**, 75–84 (2019).

[233] C. Cho, S. Feldmann, K. M. Yeom, Y.-W. Jang, S. Kahmann, J.-Y. Huang, T. C. Yang, M. N. T. Khayyat, Y.-R. Wu, M. Choi, J. H. Noh, S. D. Stranks, and N. C. Greenham. Efficient vertical charge transport in polycrystalline halide perovskites revealed by four-dimensional tracking of charge carriers, *Nature Materials* **21**, 1388–1395 (2022).

[234] S. C. Gillespie, A. O. Alvarez, J. Thiesbrummel, V. S. Gevaerts, L. Geerligs, B. Ehrler, G. Coletti, and E. C. Garnett. Intensity-modulated photoluminescence spectroscopy for revealing ionic processes in halide perovskites, *ACS Energy Letters* **10**, 3122–3131 (2025).

[235] E. V. Péan, C. S. De Castro, and M. L. Davies. Shining a light on the photoluminescence behaviour of methylammonium lead iodide perovskite: investigating the competing photobrightening and photodarkening processes, *Materials Letters* **243**, 191–194 (2019).

[236] J. S. Halpati, A. K. Samuel, T. M. Robert, and A. K. Chandiran. Real-time visualization of photobrightening in lead halide perovskites using confocal laser scanning microscopy, *The Journal of Physical Chemistry C* **127**, 3256–3267 (2023).

[237] J. Mooney and P. Kambhampati. Get the basics right: Jacobian conversion of wavelength and energy scales for quantitative analysis of emission spectra, *The Journal of Physical Chemistry Letters* **4**, 3316–3318 (2013).

[238] J. S. van der Burgt, F. Scalerandi, J. J. de Boer, S. A. Rigter, and E. C. Garnett. Perovskite plasticity: Exploiting instability for self-optimized performance, *Advanced Functional Materials* **32**, 2203771 (2022).

[239] L. M. Herz. Charge-carrier mobilities in metal halide perovskites: Fundamental mechanisms and limits, *ACS Energy Letters* **2**, 1539–1548 (2017).

[240] J. Lim, M. Kober-Czerny, Y.-H. Lin, J. M. Ball, N. Sakai, E. A. Duijnstee, M. J. Hong, J. G. Labram, B. Wenger, and H. J. Snaith. Long-range charge carrier mobility in metal halide perovskite thin-films and single crystals via transient photo-conductivity, *Nature Communications* **13**, 4201 (2022).

[241] P. A. P. Moran. Notes on continuous stochastic phenomena, *Biometrika* **37**, 17–23 (1950).

[242] M. Xu, A. Kumar, and J. M. LeBeau. Correlating local chemical and structural order using geographic information systems-based spatial statistics, *Ultramicroscopy* **243**, 113642 (2023).

[243] L. Duan, D. Walter, N. Chang, J. Bullock, D. Kang, S. P. Phang, K. Weber, T. White, D. Macdonald, K. Catchpole, and H. Shen. Stability challenges for the commercialization of perovskite–silicon tandem solar cells, *Nature Reviews Materials* **8**, 261–281 (2023).

[244] M. Saliba, M. Stolterfoht, C. M. Wolff, D. Neher, and A. Abate. Measuring aging stability of perovskite solar cells, *Joule* **2**, 1019–1024 (2018).

[245] M. Khenkin, H. Köbler, M. Remec, R. Roy, U. Erdil, J. Li, N. Phung, G. Adwan, G. Paramasivam, Q. Emery, E. Unger, R. Schlatmann, C. Ulbrich, and A. Abate. Light cycling as a key to understanding the outdoor behaviour of perovskite solar cells, *Energy & Environmental Science* **17**, 602–610 (2024).

[246] V. Srivastava, A. Alexander, B. Anitha, and M. A. Namboothiry. Impedance spectroscopy study of defect/ion mediated electric field and its effect on the photovoltaic performance of perovskite solar cells based on different active layers, *Solar Energy Materials and Solar Cells* **237**, 111548 (2022).

[247] T. Kirchartz. Challenges and opportunities for the characterization of electronic properties in halide perovskite solar cells, *Chemical Science* **16**, 8153–8195 (2025).

[248] S. R. Pering and P. J. Cameron. The effect of multiple ion substitutions on halide ion migration in perovskite solar cells, *Materials Advances* **3**, 7918–7924 (2022).

[249] V. Gonzalez-Pedro, E. J. Juarez-Perez, W.-S. Arsyad, E. M. Barea, F. Fabregat-Santiago, I. Mora-Sero, and J. Bisquert. General working principles of $CH_3NH_3PbX_3$ perovskite solar cells, *Nano Letters* **14**, 888–893 (2014).

[250] C. A. Aranda, W. Li, E. Martínez-Ferrero, P. Pistor, G. Oskam, E. Palomares, and J. A. Anta. Insights from impedance spectroscopy in perovskite solar cells with self-assembled monolayers: Decoding sam's tricks, *The Journal of Physical Chemistry Letters* **16**, 2301–2308 (2025).

[251] E. Ghahremanirad, O. Almora, S. Suresh, A. A. Drew, T. H. Chowdhury, and A. R. Uhl. Beyond protocols: Understanding the electrical behavior of perovskite solar cells by impedance spectroscopy, *Advanced Energy Materials* **13**, 2204370 (2023).

[252] T. P. A. van der Pol, K. Datta, M. M. Wienk, and R. A. J. Janssen. The intrinsic photoluminescence spectrum of perovskite films, *Advanced Optical Materials* **10**, 2102557 (2022).

[253] S. K. Gautam, M. Kim, D. R. Miquita, J.-E. Bourée, B. Geffroy, and O. Plantevin. Reversible photoinduced phase segregation and origin of long carrier lifetime in mixed-halide perovskite films, *Advanced Functional Materials* **30**, 2002622 (2020).

[254] A. J. Knight and L. M. Herz. Preventing phase segregation in mixed-halide perovskites: a perspective, *Energy & Environmental Science* **13**, 2024–2046 (2020).

[255] S. M. Eaton, H. Zhang, P. R. Herman, F. Yoshino, L. Shah, J. Bovatsek, and A. Y. Arai. Heat accumulation effects in femtosecond laser-written waveguides with variable repetition rate, *Optics Express* **13**, 4708–4716 (2005).

[256] Y. Tian, M. Peter, E. Unger, M. Abdellah, K. Zheng, T. Pullerits, A. Yartsev, V. Sundström, and I. G. Scheblykin. Mechanistic insights into perovskite photoluminescence enhancement: light curing with oxygen can boost yield thousandfold, *Physical Chemistry Chemical Physics* **17**, 24978–24987 (2015).

[257] Y.-C. Zhao, W.-K. Zhou, X. Zhou, K.-H. Liu, D.-P. Yu, and Q. Zhao. Quantification of light-enhanced ionic transport in lead iodide perovskite thin films and its solar cell applications, *Light: Science & Applications* **6**, e16243–e16243 (2017).

[258] P. L. McMahon. The physics of optical computing, *Nature Reviews Physics* **5**, 717–734 (2023).

[259] J. Feldmann, N. Youngblood, C. D. Wright, H. Bhaskaran, and W. H. P. Pernice. All-optical spiking neurosynaptic networks with self-learning capabilities, *Nature* **569**, 208–214 (2019).

[260] Y.-C. Yao, C.-J. Lee, Y.-J. Chen, J.-Z. Feng, H. Oh, C.-S. Lue, J.-K. Sheu, and Y.-J. Lee. All-inorganic perovskite quantum-dot optical neuromorphic synapses for near-sensor colored image recognition, *Advanced Science* **12**, 2409933 (2025).

[261] X. Zhou, F. Hu, Q. Hou, J. Hu, Y. Wang, and X. Chen. All-photonic artificial synapses based on photochromic perovskites for noncontact neuromorphic visual perception, *Communications Materials* **5**, 116 (2024).

[262] H. Fang, Y. Chen, Z. Jiang, W. He, and Z. Guo. Fluorescent probes for biological species and microenvironments: from rational design to bioimaging applications, *Accounts of Chemical Research* **56**, 258–269 (2023).

[263] H. Chen, J. Xu, Y. Wang, D. Wang, R. Ferrer-Espada, Y. Wang, J. Zhou, A. Pedrazo-Tardajos, M. Yang, J.-H. Tan, X. Yang, L. Zhang, I. Sychugov, S. Chen, S. Bals, J. Paulsson, and Z. Yang. Color-switchable nanosilicon fluorescent probes, *ACS Nano* **16**, 15450–15459 (2022).

[264] Y. Shao, Y. Fang, T. Li, Q. Wang, Q. Dong, Y. Deng, Y. Yuan, H. Wei, M. Wang, A. Gruverman, J. Shield, and J. Huang. Grain boundary dominated ion migration in polycrystalline organic–inorganic halide perovskite films, *Energy & Environmental Science* **9**, 1752–1759 (2016).

[265] C. Yang, W. Hu, J. Liu, C. Han, Q. Gao, A. Mei, Y. Zhou, F. Guo, and H. Han. Achievements, challenges, and future prospects for industrialization of perovskite solar cells, *Light: Science & Applications* **13**, 227 (2024).

[266] G. W. P. Adhyaksa, L. W. Veldhuizen, Y. Kuang, S. Brittman, R. E. I. Schropp, and E. C. Garnett. Carrier diffusion lengths in hybrid perovskites: Processing, composition, aging, and surface passivation effects, *Chemistry of Materials* **28**, 5259–5263 (2016).

[267] M. C. Schmidt and B. Ehrler. How many mobile ions can electrical measurements detect in perovskite solar cells? *ACS Energy Letters* **10**, 2457–2460 (2025).

[268] X. Fu, D. A. Jacobs, F. J. Beck, T. Duong, H. Shen, K. R. Catchpole, and T. P. White. Photoluminescence study of time- and spatial-dependent light induced trap deactivation in $CH_3NH_3PbI_3$ perovskite films, *Physical Chemistry Chemical Physics* **18**, 22557–22564 (2016).

[269] J. A. Christians, J. S. Manser, and P. V. Kamat. Best practices in perovskite solar cell efficiency measurements. avoiding the error of making bad cells look good, *The Journal of Physical Chemistry Letters* **6**, 852–857 (2015).

[270] R. B. Dunbar, B. C. Duck, T. Moriarty, K. F. Anderson, N. W. Duffy, C. J. Fell, J. Kim, A. Ho-Baillie, D. Vak, T. Duong, Y. Wu, K. Weber, A. Pascoe, Y.-B. Cheng, Q. Lin, P. L. Burn, R. Bhattacharjee, H. Wang, and G. J. Wilson. How reliable are efficiency measurements of perovskite solar cells? the first inter-comparison, between two accredited and eight non-accredited laboratories, *Journal of Materials Chemistry A* **5**, 22542–22558 (2017).

[271] K. Domanski, E. A. Alharbi, A. Hagfeldt, M. Grätzel, and W. Tress. Systematic investigation of the impact of operation conditions on the degradation behaviour of perovskite solar cells, *Nature Energy* **3**, 61–67 (2018).

[272] M. V. Khenkin, A. K. M., I. Visoly-Fisher, S. Kolusheva, Y. Galagan, F. Di Giacomo, O. Vukovic, B. R. Patil, G. Sherafatipour, V. Turkovic, H.-G. Rubahn, M. Madsen, A. V. Mazanik, and E. A. Katz. Dynamics of photoinduced degradation of perovskite photovoltaics: From reversible to irreversible processes, *ACS Applied Energy Materials* **1**, 799–806 (2018).

[273] W. Nie, J.-C. Blancon, A. J. Neukirch, K. Appavoo, H. Tsai, M. Chhowalla, M. A. Alam, M. Y. Sfeir, C. Katan, J. Even, S. Tretiak, J. J. Crochet, G. Gupta, and A. D. Mohite. Light-activated photocurrent degradation and self-healing in perovskite solar cells, *Nature Communications* **7**, 11574 (2016).

[274] M. Brzezicki. A systematic review of the most recent concepts in smart windows technologies with a focus on electrochromics, *Sustainability* **13** (2021).

[275] M. H. Miah, M. B. Rahman, M. Nur-E-Alam, M. A. Islam, M. Shahinuzzaman, M. R. Rahman, M. H. Ullah, and M. U. Khandaker. Key degradation mechanisms of perovskite solar cells and strategies for enhanced stability: issues and prospects, *RSC Advances* **15**, 628–654 (2025).

[276] H. Lou, C. Lin, Z. Fang, L. Jiang, X. Chen, Z. Ye, and H. He. Coexistence of light-induced photoluminescence enhancement and quenching in $CH_3NH_3PbBr_3$ perovskite films, *RSC Advances* **10**, 11054–11059 (2020).

[277] A. Senocrate, T. Acartürk, G. Y. Kim, R. Merkle, U. Starke, M. Grätzel, and J. Maier. Interaction of oxygen with halide perovskites, *Journal of Materials Chemistry A* **6**, 10847–10855 (2018).

[278] L. A. Muscarella and B. Ehrler. The influence of strain on phase stability in mixed-halide perovskites, *Joule* **6**, 2016–2031 (2022).

[279] B. Jin, J. Cao, R. Yuan, B. Cai, C. Wu, and X. Zheng. Strain relaxation for perovskite lattice reconfiguration, *Advanced Energy and Sustainability Research* **4**, 2200143 (2023).

[280] N. V, G. N. Nagy, A. Rahaman, S. K. Kalpathy, T. Thomas, S. T. P., and M. U. Kahaly. Unravelling the environmental degradation mechanism of perovskite thin films, *Materials Advances* **5**, 6426–6439 (2024).

[281] V. Sarritzu, N. Sestu, D. Marongiu, X. Chang, S. Masi, A. Rizzo, S. Colella, F. Quochi, M. Saba, A. Mura, and G. Bongiovanni. Optical determination of shockley-read-hall and interface recombination currents in hybrid perovskites, *Scientific Reports* **7**, 44629 (2017).

[282] K. Domanski, B. Roose, T. Matsui, M. Saliba, S.-H. Turren-Cruz, J.-P. Correa-Baena, C. R. Carmona, G. Richardson, J. M. Foster, F. De Angelis, J. M. Ball, A. Petrozza, N. Mine, M. K. Nazeeruddin, W. Tress, M. Grätzel, U. Steiner, A. Hagfeldt, and A. Abate. Migration of cations induces reversible performance losses over day/night cycling in perovskite solar cells, *Energy & Environmental Science* **10**, 604–613 (2017).

[283] J. A. Christians, P. Schulz, J. S. Tinkham, T. H. Schloemer, S. P. Harvey, B. J. Tremolet de Villers, A. Sellinger, J. J. Berry, and J. M. Luther. Tailored interfaces of unencapsulated perovskite solar cells for >1,000 hour operational stability, *Nature Energy* **3**, 68–74 (2018).

[284] X. Li, M. Tschumi, H. Han, S. S. Babkair, R. A. Alzubaydi, A. A. Ansari, S. S. Habib, M. K. Nazeeruddin, S. M. Zakeeruddin, and M. Grätzel. Outdoor performance and stability under elevated temperatures and long-term light soaking of triple-layer mesoporous perovskite photovoltaics, *Energy Technology* **3**, 551–555 (2015).

[285] T. Leijtens, G. E. Eperon, S. Pathak, A. Abate, M. M. Lee, and H. J. Snaith. Overcoming ultraviolet light instability of sensitized TiO_2 with meso-superstructured organometal tri-halide perovskite solar cells, *Nature Communications* **4**, 2885 (2013).

[286] W. Tress, K. Domanski, B. Carlsen, A. Agarwalla, E. A. Alharbi, M. Graetzel, and A. Hagfeldt. Performance of perovskite solar cells under simulated temperature-illumination real-world operating conditions, *Nature Energy* **4**, 568–574 (2019).

[287] G. M. Meheretu, A. K. Worku, M. T. Yihunie, R. K. Koech, and G. A. Wubetu. The recent advancement of outdoor performance of perovskite photovoltaic cells technology, *Heliyon* **10**, e36710 (2024).

[288] M. Kedia, M. Rai, H. Phirke, C. A. Aranda, C. Das, V. Chirvony, S. Boehringer, M. Kot, M. M. Byranvand, J. I. Flege, A. Redinger, and M. Saliba. Light makes right: Laser polishing for surface modification of perovskite solar cells, *ACS Energy Letters* **8**, 2603–2610 (2023).

[289] A. Hassan, Z. Ke, W. Lin, Y. Jin, Y. Cao, M. Azam, and W. Xue. Synergistic effect of additive engineering and ultrafast laser crystallization enabled efficient and stable air-processed perovskite solar cells, *Solar Energy Materials and Solar Cells* **287**, 113614 (2025).

[290] R. Gottesman, L. Gouda, B. S. Kalanoor, E. Haltzi, S. Tirosh, E. Rosh-Hodesh, Y. Tischler, A. Zaban, C. Quarti, E. Mosconi, and F. De Angelis. Photoinduced reversible structural transformations in free-standing $CH_3NH_3PbI_3$ perovskite films, *The Journal of Physical Chemistry Letters* **6**, 2332–2338 (2015).

[291] C. A. Aranda, A. O. Alvarez, V. S. Chivrony, C. Das, M. Rai, and M. Saliba. Overcoming ionic migration in perovskite solar cells through alkali metals, *Joule* **8**, 241–254 (2024).

[292] T. Ma, X. Zhao, X. Yang, J. Yan, D. Luo, M. Li, X. Li, C. Chen, H. Song, and J. Tang. Inhibiting ion migration and oxidation in Sn–Pb perovskite by multidentate chelating additive strategy, *Advanced Functional Materials* **35**, 2412216 (2025).

[293] S. Liu, Y. Guan, Y. Sheng, Y. Hu, Y. Rong, A. Mei, and H. Han. A review on additives for halide perovskite solar cells, *Advanced Energy Materials* **10**, 1902492 (2020).

[294] A. Amelia, Y. Irwan, I. Safwati, W. Leow, M. Mat, and M. S. A. Rahim. Technologies of solar tracking systems: A review, *IOP Conference Series: Materials Science and Engineering* **767**, 012052 (2020).

[295] H. Mousazadeh, A. Keyhani, A. Javadi, H. Mobli, K. Abrinia, and A. Sharifi. A review of principle and sun-tracking methods for maximizing solar systems output, *Renewable and Sustainable Energy Reviews* **13**, 1800–1818 (2009).

[296] S. W. Tong, W. P. Goh, X. Huang, and C. Jiang. A review of transparent-reflective switchable glass technologies for building facades, *Renewable and Sustainable Energy Reviews* **152**, 111615 (2021).

[297] A. Ghosh, R. Hafnaoui, A. Mesloub, K. Elkhayat, G. Albaqawy, M. M. Alnaim, and M. Mayhoub. Active smart switchable glazing for smart city: A review, *Journal of Building Engineering* **84**, 108644 (2024).

[298] B. A. Rosales, L. E. Mundt, T. G. Allen, D. T. Moore, K. J. Prince, C. A. Wolden, G. Rumbles, L. T. Schelhas, and L. M. Wheeler. Reversible multicolor chromism in layered formamidinium metal halide perovskites, *Nature Communications* **11**, 5234 (2020).

[299] A. A. Zhumekenov, M. I. Saidaminov, O. F. Mohammed, and O. M. Bakr. Stimuli-responsive switchable halide perovskites: Taking advantage of instability, *Joule* **5**, 2027–2046 (2021).

[300] S. Liu, Y. Du, R. Zhang, H. He, A. Pan, T. C. Ho, Y. Zhu, Y. Li, H.-L. Yip, A. K. Jen, and C. Y. Tso. Perovskite smart windows: The light manipulator in energy-efficient buildings, *Advanced Materials* **36**, 2306423 (2024).

List of Publications

This thesis is based on the following publications:

- **Chapter 2:** Sarah C. Gillespie, Jérôme Gautier, Julia S. van der Burgt, John Anker, L.J. (Bart) Geerligs, Gianluca Coletti, and Erik C. Garnett. Silicon-Inspired Analysis of Interfacial Recombination in Perovskite Photovoltaics. *Advanced Energy Materials* **14**, 2400965 (2024).

- **Chapter 3:** Sarah C. Gillespie, Agustin O. Alvarez, Jarla Thiesbrummel, Veronique S. Gevaerts, L.J. (Bart) Geerligs, Bruno Ehrler, Gianluca Coletti, and Erik C. Garnett. Intensity-Modulated Photoluminescence Spectroscopy for Revealing Ionic Processes in Halide Perovskites. *ACS Energy Letters* **10**, 3122-3131 (2025).

- **Chapter 4:** Sarah C. Gillespie, Jérôme Gautier, Linde M. van de Ven, Agustin O. Alvarez, Veronique S. Gevaerts, L.J. (Bart) Geerligs, Gianluca Coletti, Bruno Ehrler, and Erik C. Garnett. Photoluminescence Mapping of Mobile and Fixed Defects in Halide Perovskite Films. *Submitted* (2025).

- **Chapter 5:** Sarah C. Gillespie, Agustin O. Alvarez, Veronique S. Gevaerts, L.J. (Bart) Geerligs, Gianluca Coletti, Bruno Ehrler, and Erik C. Garnett. Resolving Mobile Ionic Contributions in Halide Perovskites through Frequency-Domain PL Analysis. *Submitted* (2025).

- **Chapter 6:** Sarah C. Gillespie, Jarla Thiesbrummel, Veronique S. Gevaerts, L.J. (Bart) Geerligs, Jeroen J. de Boer, Gianluca Coletti, and Erik C. Garnett. Excitation Intervals Enhance Performance in Perovskite Solar Cells. *ACS Applied Materials & Interfaces* **17**, 59476-59485 (2025).

Parts of this thesis are related to the following patent:

- Sarah C. Gillespie*, Agustin O. Alvarez*, Bruno Ehrler*, Erik C. Garnett*. *Modulated Photoluminescence Spectroscopy*. EU patent filing initiated (Feb. 2025).
  **equal contribution*

Other publications by the author:

- Sarah C. Gillespie*, Marco van der Laan*, Deepika Poonia, Sourav Maiti, Sachin Kinge, Laurens D. A. Siebbeles, and Peter Schall. Optical Signatures of Charge- and Energy Transfer in TMDC/TMDC and TMDC/Perovskite Heterostructures. *2D Materials* **11**, 022005 (2024).
  * *equal contribution*

- Hongyu Sun, Sarah C. Gillespie, Susan A. Rigter, Julia S. van der Burgt, Kunal Datta, and Erik C. Garnett. Spectroscopic Analysis for the Identification of Loss Mechanisms in Back-Contact Perovskite Solar Cells. *Advanced Materials Technologies* **8**, 2300241 (2023).

- Marcel Kouwenhoven, Jérôme Gautier, Fanny Thorimbert, Sarah C. Gillespie, and Erik C. Garnett. Reconfigurable Multistate Optical Memory in Mixed Halide Perovskites. *Submitted* (2025).

- Jérôme Gautier, Anton Bouter, Sarah C. Gillespie, Vanessa Volz, and Erik C. Garnett. Directed Material Evolution in Halide Perovskites. *In preparation.*

Acknowledgements

I could not have completed this thesis without the support and encouragement of so many amazing people, all of whom I wish to credit here. I was fortunate enough to pursue a joint PhD split between AMOLF and TNO, and I have learned a tremendous amount from the brilliant scientists and dedicated support staff at both institutes. I am also deeply grateful to my loving friends and family for giving me a wonderful life beyond my work.

First, I want to express my gratitude to **Erik Garnett**, who has been an incredible supervisor and an inspiration to me. **Erik**, thank you for offering me the opportunity to pursue a PhD in your group. I'm grateful for your endless stream of creative and wild ideas, for all our scientific discussions, for your expert guidance on so many topics, and, of course, for your contagiously positive and passionate attitude towards research. You are an exceptional group leader and mentor; I am proud of the scientist I have become today, and I have you to thank for that.
I also want to thank my co-promotor, **Gianluca Coletti**, for our many stimulating scientific discussions, for your innovative ideas on bridging the gap between silicon and perovskite characterization methods, and for encouraging me to start giving conference talks so early in my PhD. I have learned so much from you about the commercial side of PV, which has provided invaluable context for this thesis. I am sincerely grateful for all your support.
Each week, I was fortunate to have meetings with two more remarkable scientists at TNO, **Bart Geerligs** and **Veronique Gevaerts**. **Bart**, thank you for your incredibly clear and critical assessment of this research, for your detailed feedback, and for providing your exceptional expertise as a whole. Your input has been invaluable and I sincerely appreciate everything you have done to help me over the four years. **Veronique**, you brought new and exciting perspectives, especially during the second half of my PhD. I was delighted that you were also willing to join our weekly meetings. Thank you for your excellent guidance, enthusiasm, and for always providing such clear and constructive feedback on our research and papers.

It was a phenomenal experience to be part of the LMPV team at AMOLF. Everyone – at colloquia, poster sessions, and summer schools – has taught me so much, often on topics well beyond the scope of this thesis. I am especially grateful to the LMPV group leaders for creating such a wonderfully welcoming and collaborative scientific environment. **Bruno**, thank you for our engaging discussions, for your critical questions, and your insightful feedback – especially on all things IMPLS and ion migration. **Wiebke**, I learned so much from you about electron microscopy, nanomaterials, and various simulation methods. Your expertise in TEM is truly inspirational; thank you for sharing your wisdom during your talks and at LMPV tutorial sessions. **Albert**, thank you for your foundational work in developing the LMPV team and for your exceedingly practical advice on startups and career planning over the past year. **Esther**, I deeply admire your leadership skills and am

always inspired by your captivating scientific talks. The earliest LMPV tutorial I remember attending was your session on Raman spectroscopy, and from then until now, I have continued to learn so much from your work. I also want to thank you for serving on my PhD committee.
Alongside **Esther**, I sincerely thank the rest of my PhD committee – **Elizabeth**, **Monica**, **Jorik** and **Sander** – for taking the time to read and assess my thesis.

Then, of course, I have the amazing Nanoscale Solar Cells group to thank – each of whom has made every single day of my PhD so enjoyable and fulfilling! I want to start off by thanking **Linde**. I was lucky to meet you on the first day of our master's back in 2019, and since then, you have been an amazing and dear friend to me. I deeply admire your brilliance both in science and music, and I genuinely don't know anyone who is more sociable than you. You're *literally the best person ever*! Thanks for being an incredible friend, a fantastic colleague, for sharing our mutual love of drama, and for being a wonderful paranymph!
Elaina, I'm so grateful to have you as a close and genuinely dear friend. Of course, I find your research to be so fascinating – you are really incredible at what you do! But beyond that, you made me reflect on the bigger things in life, maybe without you even realizing it. I cherish all of our conversations about science and on life; I have learned so much from you. Thank you for being both an amazing paranymph and a perfect cat/fish/mouse *mom*.
Rohit, I think that you're the warmest, most welcoming person I've ever met! I want to sincerely thank you for all of our conversations about the challenges and joys of doing a PhD, and for our discussions on career decisions beyond it. You're a brilliant office mate (and I'm so sorry for my aggressively loud typing)! I'm also very grateful for your help with the setup downstairs. I have so much respect and admiration for you – you are *epic*!
Jérôme, since you joined the group shortly after my PhD began, you have been both an incredible scientist and a wonderful friend. You have such a warm and passionate personality, and I've learned more about optics from you than from anyone else – knowledge that has been invaluable for this thesis. Thank you so much for your SSPG measurements and for your IMPLS maps. I love our board-game evenings and the great cocktail nights you host, and I hope they won't end anytime soon!
Daan, thank you for bringing your passion, creativity, and energy to the group. I deeply admire your scientific work. But – more importantly (obviously) – I've loved every arm-in-the-air, onion-eating, and beer-related competition we've had together. You were a phenomenal head of the PV – every event was *literally the best thing ever*. Thank you for being an incredibly fun and sincere colleague and friend.
Fanny, I really admire your brilliance as a scientist, and I always find your work – along with your meticulous scientific approach – incredibly inspiring. You're so much fun, and you always make me laugh during our group outings. I think you're an outstanding postdoc, and I'm grateful for everything I've learned from you.
Marcel, I must admit that your directness and your grounded approach to science have helped me reshape my own way of working. Thank you for all our conversations, for sharing your knowledge on everything related to BBB, for your brilliant posters and tutorials, and for being a wonderful group member!

Omolara, I'm always inspired by your diligence and passion for science. Thank you for being a wonderful office mate, and for sharing your culture and food with us – it's truly fascinating and insightful. On top of your scientific expertise, have such a kind and warm personality; thank you for everything!
Shi Wei, even though you only joined the group this year, it feels like you've already been here for ages! I really enjoy all our conversations – your stories are always so interesting, and I'm perpetually amazed by how many fun facts you know. I'm lucky to have you as a colleague, and I'm certain that you have a brilliant PhD ahead of you. I also really have to emphasize *again* how iconic your quiz round was at that PV borrel – *I loved it*!
Nikolai, thank you for sharing your expertise on so many complex scientific topics. I'm especially grateful for all of your hands-on tutorials on AI, ML, and EBSD. I've learned so much about these increasingly relevant subjects from you; it's been a true pleasure working with you. Thank you for being such a dedicated postdoc in the group.
Basita, even before you joined the group, I had already learned a vast amount from you through your many insightful and fascinating research papers. Since you joined, I have greatly appreciated your thoughtful questions and valuable advice during our weekly group meetings – thank you!
To the newest member of our group, **Lucienne**, I'm delighted that you'll be starting in December, and I wish you all the very best with your PhD!
I also want to give an especially big thanks to **Marc Duursma**, our incredible lab technician. **Marc**, you've been such a huge help in the chemistry lab, especially in my early days when I knew next to nothing. I've always gone straight to you whenever something didn't seem right in the lab — and you always managed to solve the problem! I'm so grateful to have had such a knowledgeable, helpful, and approachable technician. Thank you for everything.
On top of all the current members, I also want to thank the past members of the NSC group. Most recently, thank you to **Jyoti** for being a truly remarkable postdoc. Your approach to science is deeply admirable – you are a brilliant researcher and a phenomenal teacher. Your tutorials were so insightful; I have learned so much about chemistry and plasmonics from you. Thank you for also being an amazing HF buddy in the cleanroom whenever I needed one! **Max** – you are an amazing scientist and even better person! It was a genuine pleasure working with you when you were in our group, and I was so delighted when you returned to AMOLF for your master's project! **Wander**, you're so much fun, and the way you balance your work and studies while also being a ski coach, mixologist, and more is extraordinary! Your contributions to the IMPLS prototype have been invaluable – thank you! **Susan**, you provided excellent supervision during my master's at AMOLF, and you're such an inspirational scientist – thank you for everything. **Hongyu**, you sat across from me during the early years of my PhD, and you were always so much fun! Thank you for teaching me how to fabricate and measure perovskite solar cells. I still miss your heavy metal/Dua Lipa playlists blasting at full volume in the lab. **Julia**, you were a great inspiration to me when I started my PhD. You taught me the optical setup and how to measure PLQY in my early days, which became essential for the work in this thesis. Thank you! **Sven** and **Eitan**, thank you both for being such knowledgeable and helpful postdocs when I joined the group.

I would also like to thank the many wonderful colleagues I've had the pleasure of working with beyond the Nanoscale Solar Cells group.
Most importantly, I want to express my deepest gratitude to **Agustin** – you are an exceptional and truly inspirational scientist. You've taught me so much about frequency-domain techniques, EC models, and so much more. I have great respect for you as a scientist and am genuinely in awe of your expertise in impedance spectroscopy, IMPS, and IMVS. You're amazing to work with, and I'm incredibly excited to continue working together in the future. On top of that, I deeply appreciate how genuine, warm, and kind you are. Thank you – I really can't express enough how grateful I am for everything.
I want to thank **Daphne D.**, with whom I probably spent the most time in the chemistry lab over the years. Thank you for making that lab time enjoyable, even when solar cell fabrication was *not*. You are a great friend, and I deeply appreciate all our conversations about music and life. I love going to see many great bands with you at Tivoli and Paradiso, and I've had so much fun with you at all the conferences and parties over the years! I hope they continue (the parties more so than the conferences). **Larissa**, you're a wonderfully sincere and warm person – you radiate pure positivity! Your scientific questions at the LMPV colloquia are always brilliant and thought-provoking, and I've learned so much from you. You are such a joy to be around, and I hope the *visgraat vloer* is the only stress you'll ever have. **Lars**, thank you for humbling me when we tried to *achterop* together after *that* AMOLF outing. You're always *great craic* – I have so much fun with you at the AMOLF borrels! I also want to thank you for your amazing Spibo expertise, which has benefited everyone in the lab. **Jarla**, you've contributed to many chapters of this thesis – I want to sincerely thank you for your exceptional scientific insights and feedback, and also for making extra perovskite devices for me! **Athira**, I've thoroughly enjoyed our discussions at AMOLF so far, and I'm really looking forward to seeing how IMPLS develops with your research. **Imme**, I've learned a lot from our discussions and from your impressive expertise and sharp questions during the LMPV colloquia. Thank you for training me on the TCSPC – it was invaluable for this thesis. **Jeroen**, it's hard to believe that we both started our master's projects at AMOLF on the same day back in 2020! I'm grateful to have started at AMOLF with such a wonderful person and scientist. Thank you for making lateral devices for me, for all your equipment training, and for our many enjoyable conversations. **Moritz**, I've heavily relied on your work to understand several of the processes discussed in this thesis. Thank you for sharing your knowledge and valuable insights! **Sam**, you're a wonderful office buddy – thank you for all our conversations and for making the atmosphere in the office so *gezellig*! **Nika**, I honestly don't think AMOLF would have been the same without you. To me, you're the funniest person in LMPV! Your colloquium talks were always so clear and educational, and I still really regularly think about your "news of the week" on the future of antibiotics. Thank you for everything. **Robin**, I deeply enjoyed all the conferences we attended together – thank you for being such wonderful company, especially in Valencia! Your research is so fascinating, and I'm excited to see how it continues. **Daphne A.**, your work and thesis were truly inspirational. Thank you for your excellent talks – I've learned so much about AFM from you. **Alex**, your creative ideas and out-of-the-box thinking have always inspired me. Thank you for our discussions and for your practical solar cell tips over the past four years. **Mees**, you were a fantastic PV leader – thank you for coming up with the best party games at

conferences and at the AMOLF borrels! **Evelijn**, I'm always captivated by your talks and posters. I've learned so much from you and find your research fascinating – thank you for our discussions and for being such a great colleague. **Ethan**, your models are ridiculously cool and exciting – your work is amazing! Thank you for everything! **Hollie**, thank you for regularly hosting Jennie and me at your lovely home for dinner, games, and great conversations. **Loriane**, **Mike**, **Jaime**, **Margarita**, **Antony**, and **Francesca** – thank you for our discussions and for all your great talks at colloquia and poster sessions. **Tom**, thank you so much for all your support within LMPV. I'm also grateful for your guidance on the IDF and patenting process, your advice on startups, the WITec training, and much more. **Marco**, thank you for being a great supervisor during my master's literature project and for all our engaging discussions. **Deba**, thank you for our many great conversations and for your incredibly practical thesis advice. **Chi**, thank you for your work on the ongoing and extremely exciting bio-IMPLS project – I'm looking forward to seeing how it evolves! **Lukas**, thank you for providing excellent startup advice. **Masha**, you're a brilliant PV member – I'm grateful to you for bringing so many exciting games to the PV events.
I also want to thank all other members of the **PV committee** for organizing the fantastic borrels, AMOLF outings, the annual AMOLF barbecue, and of course, the famous Christmas Lunch every year. On the subject of the Christmas Lunch, I'd like to extend a heartfelt thanks to **Katrien**, as well as **Sergio P.** and **Sofija**, for their dedication to the AMOLF Christmas Choir over the past few years. Singing in the choir was always my favourite part of the Christmas Lunch – it made the day feel especially festive and cheerful. Thank you for all the time and effort you've put into rehearsals, arranging sheet music, and making the choir such a wonderful tradition! I'd also like to acknowledge the organizers of the LMPV Summer School in France this year – **Saskia**, **Larissa**, **Antony**, **Linde**, and **Sergio**. It was an unforgettable week; thank you so much for all your work!
Next, I want to acknowledge the brilliant support staff at AMOLF. **Dion** and **Marko**, thank you both for training and assisting me with the WITec and the temperature-controlled PL setups, which were essential for the work in this thesis. **Ulaş**, you're a brilliant quiz buddy and friend! Thank you – and thanks also to **Jorijn** – for helping us with the software on the optical setup downstairs. **Alexander**, thank you for your integral role in developing the IMPLS prototype. Thanks to the NanoLab staff – **Bob**, **Igor**, **Isabelle**, **Laura**, and everyone – for all your training and incredible support. I'd like to give a special thanks to **Petra**, along with the entire communications department, for contributing to AMOLF's open and welcoming atmosphere. **Huib**, thank you for being an excellent director. **Paula**, thank you for being an incredible institute manager, and for providing us with excellent advice on the future of IMPLS, patents, and startups.
To all the support departments – the wonderful canteen staff, reception, library, engineering departments, IT support, cleaning staff, HR, secretarial office, finance, workshop, and more – every department at AMOLF is phenomenal. I'm deeply grateful to all the amazing staff who make this institute what it is. To everyone else I've met at AMOLF – **Wessel**, **Francesco**, **Saskia**, **Stan**, **Yorick**, **Luna**, **Konstantinos**, **Sergio**, **Antony**, **Roos**, **Alvaro**, **Larissa B.**, **Devin**, **Toon**, **Lucie**, **Matthias**, **Magda**, **Henk-Jan**, **Juliette**, **Clyde**, **Hinco**, **Jesse**, **Teressa**, **Dylan**, **Hans**, **Stefan**, **Evan**, and anyone I've surely forgotten – thank you all.

I have also had the pleasure to work with some brilliant colleagues at TNO. Thank you to the entire Solar Energy department, and in particular to **Astrid**, **Petra**, **John** and **Bas**, who helped me in the lab at TNO at the start of my PhD. Thank you to **Gert-Jan** for our many enjoyable conversations. I extend my sincerest thanks to **Nesjla** and **Peter** for their support and management. I also want to thank **Michiel** for being an excellent internal patent lawyer, and for taking the time to guide myself and Agustin through all the patent details. Finally, I want to thank **Sjoerd**, who was always so supportive, approachable and helpful throughout our AMOLF-TNO collaborations.

An essential part of earning a PhD is realizing the importance of a fulfilling and meaningful life beyond work. For that, I deeply appreciate having such a loving family and amazing friends. I first want to thank all my dear friends here in the Netherlands, who have each helped make this country feel like home. **Parva**, you're an incredibly important friend to me, and I'm so lucky to have met you. You've always been there for me – at my best and worst – and I'll always be so grateful to you for that. I have so many cherished memories with you, from Hamsterdam (RIP) to our chocolate cake nights during Covid, to our wonderful Christmas dinner tradition every year now. Thank you so much for everything, and I'm looking forward to making many more memories together. **Salome**, the fact that we basically had to learn a new language to understand each other is a special bond that nobody else will ever understand! Thank you for being such a wonderful and dear friend. **Cillian**, thank you for always being a superb host and for your wonderful parties and game nights – I always have so much fun with you! **Fiona**, our ten years of friendship mean the world to me. You're the person I've shared the most with – from our Belgrove days to now – and I'm so grateful to know you. Thank you for teaching me Python back in the day (I still use some of your functions!), and you're very welcome for all my perfectly perfect Quantum Mechanics notes (that you never needed again). Thank you for always being a loving friend.
Thanks to all the significant others that make me feel old and *burgerlijk* – **Javier**, **Joshua**, **Davit** and **Laurens** – you make life in Amsterdam all the more special! **Aisling** and **Nelson**, I'm so happy yous moved here; thank you for being such wonderful friends. **Aisling**, I'm grateful that you are even more competitive than I am at quizzes – you're the reason why we win and I can never thank you enough for that. I also want to thank **Hongyu**, **Jorien**, **Sanne** and **Annemijn** for all our parties and holidays together. My cousin, **Alan**, and **Katheryn**, I always love catching up with you both! **Fong**, **Aalok**, **Tim**, **Lydia**, **Katha**, **Merel**, **Roos** *en* **Eefke** – *Ik ben zo dankbaar dat ik jullie via Jennie heb leren kennen. Bedankt voor alle gezelligheid en dat jullie mij mijn Nederlands laten oefenen!* I also want to acknowledge everyone I met when I had just moved to Amsterdam, especially everyone from **SfES** – I've had incredible experiences with you all; thank you for everything! *Ik wil ook mijn oprechte dank uitspreken aan Jennie's lieve familie* – **Yvonne**, **Wim**, **Lianne**, **Yannick**, **Mieke**, *en de rest van de* **familie Broer** *en* **Spruit**. *Allereerst ben ik heel dankbaar dat jullie mij Nederlands geleerd hebben, maar nog belangrijker, dat jullie me zo'n warm welkom geheten hebben in jullie levens.*

I also want to thank my wonderful friends whom I've made and kept from growing up in Donegal and studying in Dublin. In true Irish spirit, we've now scattered ourselves all

over the globe, and I miss you all throughout the year. Coming home to Ireland and being with yous every Christmas and New Year's Eve means the world to me. Thank you all for being such lovely, loving, lifelong friends. To the entire UCD/MFATSF gang – **Lucy**, **Julia**, **Tara**, **Alanna**, **Aidan**, **Ian**, **Cathy**, **Adam**, **Caroline**, **Michelle**, **Avril**, and **Fiona** – I could write a whole *LetterLoop* about how each one of you has inspired me and how much I've learned from you over the years. I have so many cherished memories of our time in UCD together – our game nights in Sandyford and Stillorgan, our band, our cycles to Galway, and our singing in *almost* perfect harmony. I always love catching up during the holidays, and I really appreciate our tradition of spending New Year's Eve together, along with **Andy**, every year. Looking forward to Ballyshannon!
Speaking of Donegal, I want to sincerely thank my oldest friends – **Maria**, **Caitlin**, **Fiona Maguire**, **Sarah Gallagher**, **Eva**, **Shannon** and **Emily** – all of you are so incredibly important to me! I'm forever grateful to have grown up with all of you; I genuinely could not have asked for better friends. In connection to this thesis – thank you for all the lovely holidays together over the past four years. For me, Christmas in Ballybofey is only Christmas with yous all there too. It's truly inspiring to see how we're all leading such different lives since our St. Columba's days – and it's really beautiful how we've still stayed so close. I'm so proud of us and I love you all!
To my loving family: I have you to thank for so many things – above all, for my competitiveness, but also for shaping my beliefs, my morals, and my entire approach to life. I want to thank all my brilliant brothers and sisters – **Laurissa**, **Ryan**, **Anton**, **Niamh**, **Shaun-Henry** and **Luke** – all of whom I have learned so much from, am so proud of, and love so dearly. I also need to thank **Laurissa** *again*, for letting me briefly live with her I first moved here, and for being my family in Amsterdam (if I didn't say this, I wouldn't hear the end of it)! Thanks to all my extended family, most notably to my amazing brothers- and sisters in-law – **Caroline**, **Brendan**, **Laura**, **Rachel** and **Claire** – you have taught me so much and continue to shape my perspectives, both from when I was growing up and still today. It's so rewarding to see my wonderful nieces and nephews – **Molly**, **Lucy**, **Ryan**, **Ella**, **Grace**, **Lauren**, **Iarlaith**, **Odhran**, **Henry** and **Oliver** – grow and thrive. I miss you all whenever I'm away from Ireland!
I'm so blessed to have such loving, caring and incredibly kind parents, **Teresa** and **Tony**. **Mammy** – you have taught me the importance of charity, compassion and selflessness. You have always been an incredible mother, thank you so much for always supporting me in science, in music and in every other aspect of my life. I also couldn't ask for a better father. Thank you, **Daddy**, for your endless love and support. I cherish my childhood memories of our Sunday cycles after Mass to Trusk Lough with **Luke**. The way you tackle problems in machinery and problems on the farm is what sparked my interest in solving problems in science. I'm always grateful to be able to sing and play with you at the Brockagh music nights. Thank you both for everything.

Lieve **Jennie** – I met you just two months into this PhD, and throughout it all, you have grounded me, supported me, and inspired me in more ways than you could imagine. Thank you for your endless patience, kindness, and encouragement – especially during the hectic months while I was writing this thesis. Above all else, thank you for sharing your life with me.

About the Author

Sarah Gillespie was born on the 6th September 1996 in County Donegal, Ireland. After completing her secondary education in 2015, she was awarded a scholarship to pursue a bachelor's degree in Physics at University College Dublin. During her undergraduate studies, she spent a semester abroad at Villanova University in Pennsylvania, USA, and completed a summer internship in Beijing and in Shenzhen, China.

While at UCD, Sarah developed a strong interest in materials physics and renewable energy. After graduating, she moved to Amsterdam in 2019 to pursue a master's degree in Physics at the University of Amsterdam and the Vrije Universiteit, specializing in the Science for Energy and Sustainability track. In 2020, she carried out her master's research project at AMOLF under the supervision of Prof. Dr. Erik Garnett. Her work involved the synthesis and characterization of perovskite nanocrystals in silica molecular sieves. She completed her master's thesis and graduated cum laude in 2021.
She continued her research as a PhD candidate, with her doctoral project jointly carried out between AMOLF in Amsterdam and TNO in Petten, under the supervision of Prof. Dr. Erik Garnett, with Prof. Dr. Gianluca Coletti as her second supervisor. During her PhD, she has given five oral presentations at academic conferences in the USA, Italy, Spain, France, and the Netherlands. The results of her doctoral research are presented in this thesis.

Currently, together with her colleagues at AMOLF – Dr. Agustin Alvares, Prof. Dr. Bruno Ehrler, and Prof. Dr. Erik Garnett – Sarah is further developing IMPLS, the optical characterization technique introduced in this thesis. Their ongoing work aims to expand the technique's capabilities, with the goal of commercializing the technology for both academic research groups and industry.

Though she primarily played the trumpet in her youth, Sarah now spends her free time playing the guitar and learning the mandolin – hobbies that inspired the theme and cover art of this thesis. She also enjoys seeing live music, singing, hiking, reading, and particularly loves doing pub quizzes and escape rooms with friends.